Engineering Catalyst Layers for Next-Generation Polymer Electrolyte Fuel Cells: A Review of Design, Materials, and Methods

Theo A. M. Suter,* Keenan Smith, Jennifer Hack, Lara Rasha, Zahra Rana, Gyen Ming A. Angel, Paul R. Shearing, Thomas S. Miller, and Dan J. L. Brett*

Polymer electrolyte fuel cells (PEFCs) are a promising replacement for the fossil fuel–dependent automotive and energy sectors. They have become increasingly commercialized in the last decade; however, significant limitations on durability and performance limit their commercial uptake. Catalyst layer (CL) design is commonly reported to impact device power density and durability; although, a consensus is rarely reached due to differences in testing conditions, experimental design, and types of data reported. This is further exacerbated by aspects of CL design such as catalyst support, proton conduction, catalyst, fabrication, and morphology, being significantly interdependent; hence, a wider appreciation is required in order to optimize performance, improve durability, and reduce costs. Here, the cutting-edge research within the field of PEFCs is reviewed, investigating the effect of different manufacturing techniques, electrolyte distribution, support materials, surface chemistries, and total porosity on power density and durability. These are critically appraised from an applied perspective to inform the most relevant and promising pathways to make and test commercially viable cells. This holistic view of the competing aspects of CL design and preparation will facilitate the development of optimized CLs, especially the incorporation of novel catalyst support materials.

1. Background

1.1. Fuel Cell Basics

Global energy demands are expected to increase by up to 90% from current levels by 2040.[1,2] Within the same time scale,

T. A. M. Suter, K. Smith, J. Hack, L. Rasha, Z. Rana, G. M. A. Angel,
P. R. Shearing, T. S. Miller, D. J. L. Brett
Electrochemical Innovation Lab
Department of Chemical Engineering
University College London
London WC1H 0AJ, UK
E-mail: theo.suter.14@ucl.ac.uk; d.brett@ucl.ac.uk

world governments have agreed to reduce their reliance on traditional fossil fuels;[3,4] current estimates suggest only 28% of global electricity generation is from renewable sources. To meet this energy demand without compromising on supply sources, it is imperative and time-urgent to increase uptake of renewable and low-carbon energy generation technologies. Fuel cells can play a substantial role, both as energy storage and generation systems, which are in growing demand.[5] Their high-energy densities make them suitable for a large range of sectors, such as transport, where they can work in concert with other electrochemical power sources such as batteries and supercapacitors. Achieving high-performance and cost-effective fuel cells can therefore provide a major avenue in establishing a low carbon and sustainable future for the planet.

Fuel cells are electrochemical energy devices in which a reactant is oxidized to generate electrical power and water.[6] This process is facilitated by the transport of ions (protons, hydroxides or oxides) through an electrolyte from one electrode to the other. Fuel cells are categorized by their electrolyte, such as polymer electrolyte fuel cell (PEFC),[7] phosphoric acid fuel cell (PAFC),[8,9] alkaline anion exchange membrane (AAEM),[10] and molten carbonate fuel cell (MCFC),[11] among others.[12] The nature of the membrane used in a fuel cell is, in turn, dependent on the constraints of the operating temperature, the desired application and the fuel. While the basic working principles of all fuel cells are similar, a variety of different reagents have been shown to be effective as the fuel; this includes methanol,[13,14] urea,[15,16] as well as hydrocarbons and waste gases. The most commonly used is hydrogen, this is partly due to water being the sole product, making it a zero-carbon technology at point-of-use. The overall chemical reaction can be considered to be a combustion reaction with reagents reacting with oxygen to form standard combustion products. However, the reactants do not directly contact as the overall reaction is split between two half-cell reactions, with the oxidation reaction occurring on the anode and reduction on the cathode, as shown in the equations below. The movement of ions between electrodes is critical to drive the reaction and is

one of the limiting aspects of the reaction and fuel cell output. The subsequent migration of electrons from the redox reaction to an external circuit generates a current. This direct conversion of reactants into electricity results in the promisingly high theoretical energy efficiency of fuel cells.[17]
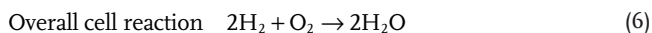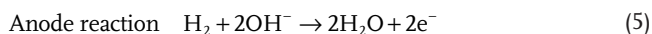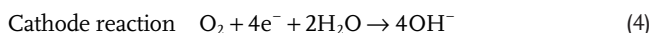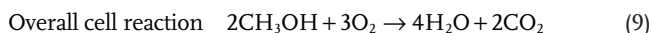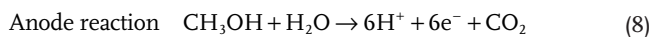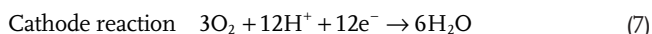
Acid PEFC:

Cathode reaction $\quad O_2 + 4e^- + 4H^+ \rightarrow 2H_2O$ (1)

Anode reaction $\quad H_2 \rightarrow 2H^+ + 2e^-$ (2)

Overall cell reaction $\quad 2H_2 + O_2 \rightarrow 2H_2O$ (3)

Alkaline PEFC (or AAEMFC):

Cathode reaction $\quad O_2 + 4e^- + 2H_2O \rightarrow 4OH^-$ (4)

Anode reaction $\quad H_2 + 2OH^- \rightarrow 2H_2O + 2e^-$ (5)

Overall cell reaction $\quad 2H_2 + O_2 \rightarrow 2H_2O$ (6)

Direct methanol fuel cells (DMFC):

Cathode reaction $\quad 3O_2 + 12H^+ + 12e^- \rightarrow 6H_2O$ (7)

Anode reaction $\quad CH_3OH + H_2O \rightarrow 6H^+ + 6e^- + CO_2$ (8)

Overall cell reaction $\quad 2CH_3OH + 3O_2 \rightarrow 4H_2O + 2CO_2$ (9)
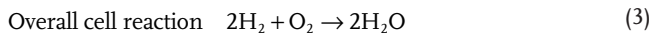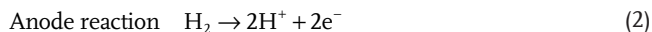
PEFC are among the most widely used and investigated fuel cells.[20] This is due to their relatively low operating temperature (60–180 °C), simple reagents, compact systems, and the commercial availability of components. PEFCs are constructed from an assembly of different layers with large variation in thickness and functions, as shown in **Figure 1**. Sandwiched between the cathode and anode catalyst layers (CLs) is the central part of any individual PEFC, the solid electrolyte membrane. CLs are formed from an amalgam of electrically conductive support, catalyst particles, and a proton conducting (for acidic FC) ionic polymer (ionomer). The microporous layer (MPL) is next in contact with the CL; it is a mix of carbon nanospheres and PTFE designed to maximize gas transport and electrical conductivity while expelling water generated in the CL. This layer is coated onto the gas diffusion layer (GDL), which is a weave of highly porous carbon fibers, designed to facilitate gas transport, and maintain electrical conductivity.[18,19] The combination of CL, MPL, and GDL is called a gas diffusion electrode (GDE). When the membrane and both GDEs are combined into one unit, they form a membrane electrode assembly (MEA) and this is the active part of the fuel cell. To operate a fuel cell system the MEA is placed into a cell assembly, a flow field is used to distribute the reactant gases and conducts electricity to the current collectors where the electrical current generated in the MEA feeds the external current. Finally, a pair of end plates on each side of the MEA are bolted together to provide pressure to the assembly and hold the system in place.

PEFCs use a solid electrolyte membrane to transfer protons or hydroxyl ions between electrodes.[7] Acidic PEFCs transfer a proton across the membrane, while alkaline PEFCs transfer a hydroxyl ion; each require differing chemistries for effective functionality, with commercially available acidic PEFC membranes being cheaper and more durable.[21] The membrane also acts as an electrically insulating and gas blocking barrier layer between the electrodes, avoiding electrical short circuits and
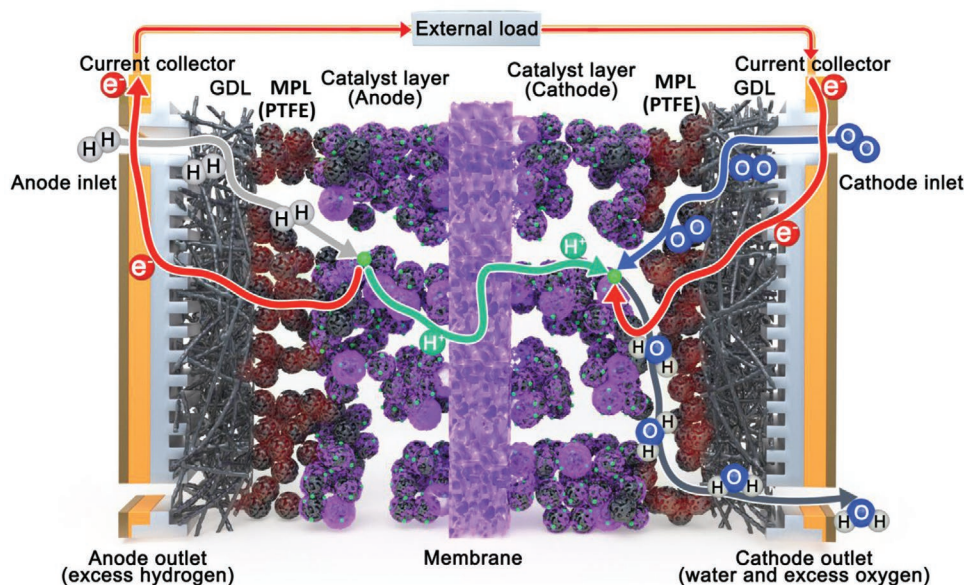
Figure 1. Schematic of an acid PEFC showing the different layers, their compositions, and reactant transport pathways. Black structures indicate carbon support, purple the ionomer, red the PTFE, and green the catalysts. The relative sizes and distances are not to scale and the catalyst layer, MPL, and GDL possess significantly different porosities and support material size.

**ADVANCED
SCIENCE NEWS**

www.advancedsciencenews.com

**ADVANCED
ENERGY
MATERIALS**

www.advenergymat.de

damaging direct gas reactions. PEFCs can be separated into two different groups, low-temperature PEFCs (LT-PEFCs) and high-temperature PEFCs (HT-PEFCs).[8,21–23] Operating temperature has a significant impact on performance as reaction rates increase with temperature and water management becomes a less significant issue.[21,22] LT-PEFCs typically operate between 60–80 °C and use perfluorosulfonic acid (PFSA) ionomers, such as Nafion, as the membrane and ionomer.[21,22] However, the majority of world leading PEFC membranes require high humidities and thus constant hydration of the input gases in order to provide high proton conductivity. Although water is a product of the redox reaction, excessive water can reduce performance.[21,22] This results in a LT-PEFC requiring constant water management and complication of the fuel cell stack design. HT-PEFCs typically operate between 120–180 °C.[8,21–23] Although Nafion composites have been shown to perform at the lower end of this range, PFSA membranes are generally not stable at these high temperatures so alternative membrane and ionomer chemistries are required. The most widely studied type of membrane for HT-PEFCs is polybenzimidazole (PBI) polymer doped with phosphoric acid.[21,23] While showing less dependence on membrane humidification, PBI-based membranes have issues with stability owing to the formation of water on the cathode and acid leaching.[21,22] Although there many similarities in the CL design between LT- and HT-PEFCs, this review will focus on acidic LT-PEFCs as they are more widely used commercially due to the more mature membrane technology. Although, some of the CL discussion within this review can be applied to the design, or aid in the understanding of, CLs for other fuel cell variants.[20] For further information on PFSA membranes we suggest the review by Kusoglu and Weber.[24]

1.2. The Commercial Landscape for PEFCs

The potential to generate hydrogen gas using renewable energy via water electrolysis has resulted in significant interest for PEFCs in many energy conversion applications, particularly relevant to sectors with increasing greenhouse gas regulation.[25] Stationary applications, such as residential combined heat and power (CHP), industrial backup power, and automotive applications are generally considered to be best suited to PEFCs where the stability and high power density has already been utilized commercially.[20] Fuel cells will likely play an essential role in the future of renewable energy, as part of a hydrogen energy storage system (HESS), in which excess electrical energy can be converted to hydrogen gas, stored in a range of scales from tanks to natural caverns, and then used to generate power in a fuel cell when required.[26–28] This would require sufficiently large renewable hydrogen generation capacity from either efficient electrolyser banks coupled with renewable energy or biomass to supply highly efficient fuel cells.[27] This basis for a closed green hydrogen economy system is understood to be a stable, renewable and efficient energy generation and consumption system,[5,29] a necessity for the global energy landscape.

The use of fuel cells for transport applications has seen the largest growth in the last 5 years.[20] PEFCs are currently commercialized in vehicles including the Toyota Mirai, the Hyundai Tucson, and Honda Clarity.[30–32] However, market penetration is limited, in part due to the relatively high cost when compared to fossil fuel-based cars. This is due, to some degree, to the use of platinum (Pt)-based catalysts that represent a large source of the vehicle cost.[33,34] However, due to maturing of automotive fuel cell technologies, the costs are expected to decrease from current prices, with a proportional market uptake anticipated.[30] The next iteration of the Toyota Mirai is expected to use 66% less Pt than the current generation (down to 10 g)[30] and if the use of Pt decreases even further, then it would approach the quantity of Pt in typical catalytic converters (2–4 g).[35] Although these technologies will increase demand for Pt metal, the total cost of the catalyst in a fuel cell vehicle is not predicted to increase due to a continued reduction in Pt loading from typically 0.4 mg_{Pt} cm^{-2} to 0.125 mg_{Pt} cm^{-2}, alongside other technical innovations.[35,36] Manufacturers expect the high cost of fuel cell vehicles and other fuel cell systems to decrease once the technology becomes more widespread, partly due to economies of scale for the non-catalyst components.[37,38] However, the public uptake of the technology is currently limited by the cost, lack of infrastructure, and safety concerns.[5,39] Governments and companies across the world are aware of these issues and have set policies and investments to help facilitate the growth of the hydrogen industry.[39–41] Recently, a publication from Toyota R&D labs detailed some of the central issues facing further PEFC commercialization and highlighted the need for further technological breakthroughs.[42] This direct feedback from companies and organizations about the direction that fuel cell technologies need to take is very useful in directing research efforts.

In typical fuel cell systems, the most expensive part is the fuel cell stack, owing to the large amounts of (typically) Pt catalyst in the CL. Thus, there is a commercial need to engineer low- and no-Pt-containing electrodes to drive down stack cost. As a result of this need, there has been a significant amount of research undertaken into catalysts, and the performance of laboratory-based nanostructured Pt and Pt alloy catalysts have improved significantly in the last decade, which has partly led to the reduced loading of Pt.[43,44] In addition, research into non-Pt group metal catalysts has expanded significantly and resulted in some promising materials.[45,46] However, non-platinum group metal (non-PGM) materials are less mature than Pt catalysts and suffer from durability and performance issues.[43] Given the costs and performance difference between the Pt and non-PGM catalysts, it is likely that they will both be commercially utilized in the future, but for different applications. Pt could achieve wider use in high-performance applications such as in the automotive sector, while non-PGM materials would be more suited to stationary applications such as CHP, and backup power. Due to the large number of reviews on novel catalysts and their development they are considered beyond the scope of this review.[43,47–49]

1.3. PEFC Structure–Performance Relationship

It is within the CL that the electrochemical reaction occurs. Given its significant role in fuel cell performance, as well as the clear potential for improvements, the CL has received a significant amount of research focus. This review will focus on CL engineering and the structure-performance relationships

unique to low-temperature acidic fuel cell electrodes. The development of novel fuel cell materials, particularly nanomaterials, will be also reviewed in regards to their reported impact on CL design and performance.

Standard CL design is based on highly dispersed Pt catalyst nanoparticles (NPs) deposited onto support materials at both the anode and the cathode. The support materials are generally spherical, high surface area carbon aggregates, known as carbon black (CB). The reactants must be transported through the CL onto the surface of the catalyst to be utilized. This transport of reactants is broadly defined as the mass transport, the pathways of which are shown for each species in **Figure 2**c. The reactant gases are transported through the empty voids between the support particles, which are dependent on the pore size distribution (PSD), determined by the size, distribution, and volume of the voids. The pores form as a result of the assembly of the support particles and the ionomer, which can significantly impact CL performance, as shown in Figure 2d. The electrons are transported to the CL via electrical contact between support particles, while the protons are typically transported via the PFSA ionomer or localized liquid water, produced by high humidity operating conditions or as the byproduct of the ORR reaction.[50–52] The combination of these three reactants at what is known as the triple phase boundary (TPB) is required for the reaction to occur, as shown in Figure 2b. If a catalyst particle is not connected to any one of these three then the catalyst will not be utilized in the reaction.

It is therefore key when fabricating and designing CLs to maximize utilization of the catalyst, achieved via the optimization of three reactant transport pathways. However, these pathways have significant impacts on each other, too much ionomer in the system will lead to greater proton transport at the cost of electrical contact between the support particles and increased resistance to gas transport across the CL.[53–57] High water content in the CL can improve proton conduction and catalyst utilization but can significantly reduce mass transport of reactant gases referred to as flooding (as shown in Figure 2c "Flooded Catalyst Layer").[50,58,59] Furthermore, the ionomer network typically forms a layer on top of the support/catalyst particles, a homogenous distribution of ionomer is desired although it is difficult to control during fabrication (Figure 2a). This heterogeneity can lead to areas with no ionomer, which results in catalyst particles not being utilized, or areas of excess ionomer which has a negative effect on gas transport. Catalyst poisoning by direct adsorption of ionomer sulfonate functional groups has been reported to reduce the available catalyst surface area, significantly reducing the mass activity.[60–69]

Developing new supports with high electrical conductivity, durability, and scalability, as well as highly active catalysts, has been a major avenue of research. The interaction between the catalysts and the support has been shown to significantly affect the performance and durability of fuel cells.[64,70–73] It has also been reported that support durability and CL performance can
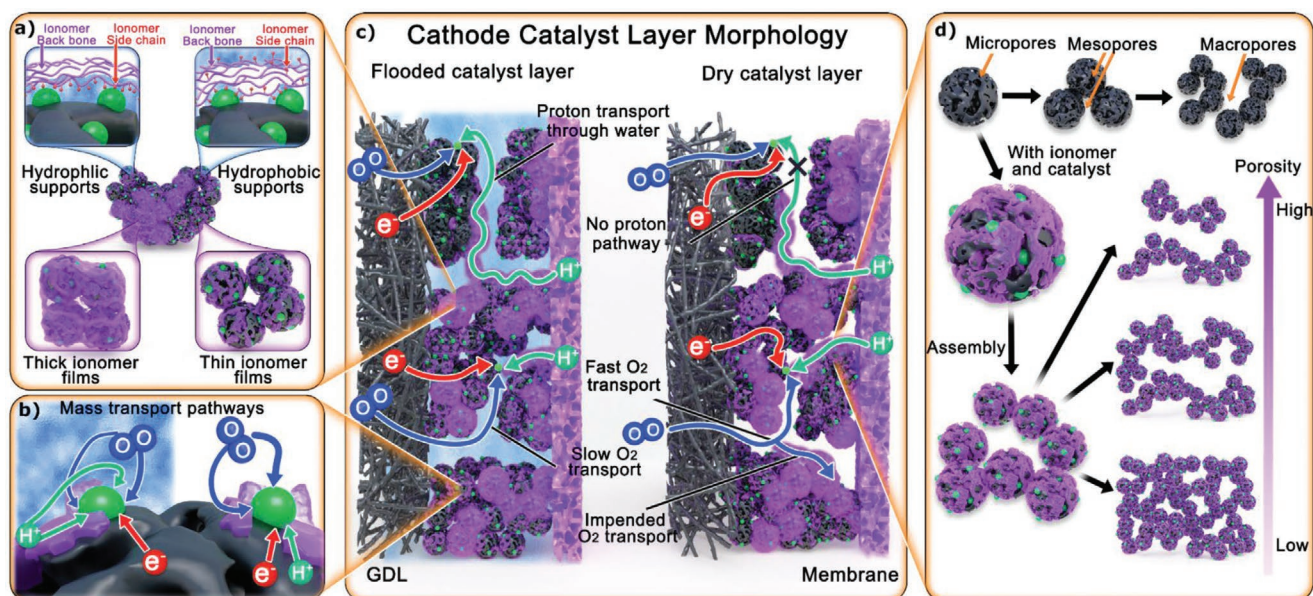
Figure 2. Schematic of the cathode catalyst layer morphology, reactant transport pathways, structure, and the factors that impact its performance. a) The ionomer coating over the carbon support and catalyst structure can be heterogeneous with areas of thin or thick coatings. The surface chemistry of the support impacts the surface-ionomer interactions changing the structure of the ionomer around the catalyst particles and the quantity of localized water. b) The mass transport of the reactants to the catalyst particles occurs via different routes, under flooding conditions more pathways are introduced for the proton conduction. Alterative reactant pathways are associated with different degrees of transport resistance as indicated by the relative size of the arrows, with the smallest being the most resistive. c) The cathode CL morphology has a significant impact on the mass transport pathways, with flooding allowing utilization of catalyst not connected to the ionomer network, although this increases reactant transport resistance. Limitations on catalyst utilization and performance can be induced by poor transport of any reactants across the CL or the absence of their transport pathways. d) The support materials have defined pore structures, both internally and as a consequence of assembly. Pores and porosity are discussed in more detail in Section 4.2.

2101025 (4 of 82)

significantly depend on the chemical composition of the support, as well as the degree and nature of its functionalization.[74–76] The support material does not just impact electrical conductivity and carbon corrosion, but also reactant mass transport and ionomer distribution, necessitating understanding of structure–performance relationships in the CL.[52,76–81] The morphology of the CL is usually defined by the structure of the support material and the manufacturing method, both of which play a role in shaping the morphology and therefore performance of the CL.[82–84] The mass transport of gases, particularly at high current regimes, is one of the limiting factors of performance and thus the CL morphology can have a huge impact on fuel cell performance. It should also be noted that performance gains from electrode structure innovations should be applicable to a wide range of Pt and non-PGM based catalysts.

It is clear that there are multiple challenges to advancing fuel cell technology and commercial uptake. Significant progress is being made by researchers in reducing catalyst loading, improving catalyst performance, and developing new materials. However, other factors that limit performance such as high mass transport resistances, low Pt utilization, and poor durability are all a consequence of CL composition and structure. These issues are a complex intertwined mix of bulk and surface chemistries, and multi-length scale structural issues that involve the interplay of catalysts, support, ionomer, and reactant transport in a porous media. The development of new catalyst and support materials is only part of the route to advance PEFC technologies. Without a simultaneous improvement in the understanding of CL structure–performance relationships, fuel cells will not reach a required level of technological maturity to achieve widespread commercialization. To make advancements in the performance of PEFCs, a combination of clear mechanistic understanding, focused characterization tools, and the ability to engineer structure across different length scales is required.

This review begins with an overview of CL performance characterization, focusing on how performance is determined in MEAs, and how operating conditions affect these (Section 2). Proton conduction is one of the key limitations of the CL, and is discussed in Section 3, detailing the mechanisms, structure and formation of the ionomer, and how this impacts performance. Section 4 considers and explains the support and morphology-based factors that impact the performance of the MEA, such as the implications of CL porosity, thickness, and novel CL design on performance. Finally, Section 5 covers the impact of fabrication and cell assembly on CL morphology and MEA performance, respectively. This review is intended as both an encompassing guide to those new to PEFCs and a thorough review of the many structure-performance relationships that are at play in CLs, intended to be understood by, and informative to, all.

2. Catalyst Layer Performance Characterization

2.1. Introduction

In order to build, operate, and develop commercial PEFC systems, it is necessary to develop a deep understanding of how different environmental factors affect the standard performance testing techniques. However, characterizing PEFCs is never trivial, for example, degradation heterogeneity is highly dependent on operating conditions and MEA size. This section details the manner in which PEFC performance is characterized and the limitations to these techniques. Furthermore, the impact of operating conditions such as gas flow, pressure, temperature, and humidity are discussed.

Testing methods are typically separated into two categories: ex situ or in situ. Ex situ methods occur in testing environments that do not, or only partly, resemble that of a fully operational PEFC system, such as a half-cell. Conversely, when the testing environment is representative of a complete PEFC, the method is known as in situ. In situ testing inevitably has additional layers of complexity (water management or mass transport limitations) compared to ex situ methods. Due to physical differences in the manners in which in situ and ex situ testing are carried out, the results are often reported differently. Ex situ testing will often present linear sweep voltammetry (LSV) and cyclic voltammetry (CV), while in situ testing will report polarization curves, CVs, hydrogen crossover, and electrochemical impedance spectroscopy (EIS) among others.

Various ex situ techniques are available to assess catalytic activity. These include the floating electrode technique (FET),[85] Gaskatel's "FlexCell", the rotating disk electrode (RDE) and the rotating ring disk electrode (RRDE).[86–88] The most commonly deployed is the RDE, which is a classic hydrodynamic electroanalytical technique[89] used to study the kinetics of interfacial processes. In this approach, the two integral PEFC half-cells can be investigated independently of each other. The half-cell approach allows for rapid and cost-effective investigation into catalyst activity, durability, and performance, often free from competing factors such as ionomer interaction and gas transport. Furthermore, RDE measurements only require a nominal amount of catalyst material, making it the ideal tool for preliminary screening of new materials. Hence, significant research has been devoted to understanding novel catalysts and materials using these ex situ techniques. While the results can be useful for understanding novel materials in idealized circumstances, the ex situ data does not always reflect the in situ reality due to the complex and non-ideal conditions within full devices. It is essential to comprehend the origin of these differences in the in/ex situ data.

In situ techniques are more representative of fully operational PEFCs, as they utilize operating parameters and constraints that are close to those in real devices. Additional operational constraints range from controlled cell temperature, humidity, gas flow rates, and gas pressure, all of which have a range of impacts on different aspects of PEFC performance. Understanding the mechanisms that drive the effects of operating conditions on performance allows for manipulation of the conditions in order to optimize performance for a particular system. The impact of the initial treatment before testing a cell (often called conditioning) is particularly important for in situ testing and has a large impact on the resulting performance and durability of the PEFC. However, this is relatively unstandardized. Accelerated stress tests (ASTs) are another tool that are used to simulate long-term degradation of an operational fuel cell in a timely manner. These studies typically follow set

**ADVANCED
SCIENCE NEWS**
www.advancedsciencenews.com

**ADVANCED
ENERGY
MATERIALS**
www.advenergymat.de

institutional testing regimes, and are highly informative about the durability of the materials and catalyst used in a PEFC.

2.2. Ex Situ Electrochemical Techniques

RDEs consist of a three-electrode system with a working electrode (WE), counter electrode, and reference electrode. The WE is a conductive disk onto which the catalyst material under study is deposited. The electrode is rotated at high speeds about its vertical axis during experimentation (between 400 to 10 000 rpm)[90] to drive high analyte flux, laminar flow, and ensure the WE is uniformly accessible.[91] The FET seeks to fill some of the middle ground between RDE and MEA testing and results in data that is more representative of fuel cell operation at high current densities.[85] In the FET, a porous gas diffusion electrode is "floated" with the membrane in contact with the aqueous electrolyte and the reactant gas supplied to the catalyst active sites from behind the CL. This arrangement can test thick electrodes in conditions similar to MEAs in a more facile system.

Microelectrodes (MEs), an often overlooked ex situ electrochemical technique, utilizing electrodes which have diameters on the micron scale. They function in a three-electrode setup similar to that of an RDE, but due to their small size they have been commonly used to investigate interfacial phenomena.[92–94] In particular, they have been successfully utilized in kinetic and mass transport studies of solid electrolyte membranes, which are significantly more difficult to directly measure accurately with in situ MEA tests. However, MEs do suffer from a number of issues with their low currents being easily impacted by room noise, sensitivity to contamination, and slow equilibrium times. In addition, as they have not been as widely explored in the literature compared to RDE, the standardization between studies is limited. A review and best practice article by Petrovick et al.[95] has recently made efforts to mitigate these issues.

When using ex situ techniques, the two principal tests are LSVs and CVs. These techniques were originally proposed in the 1950s,[96] and many years of development and increased knowledge of interpretation has made them invaluable tools for quick and easy data acquisition and elucidation of information on redox reactions. LSVs are the main performance measurement, allowing for the "diffusion" and "kinetic" components to be observed within a set voltage window.[97] The kinetic component is focused around the onset potential of the reaction (the overpotential that is required to drive the reaction). The onset potential is defined as the open circuit voltage (OCV) in MEA testing. It is a useful and easily accessible parameter for initial catalyst evaluation.[97,98] The diffusion component is typically given by the limiting current density at high overpotential,[99] and by comparing the Koutecky–Levich plot.[100,101]

In an RDE experiment, hydrogen ion transport occurs via a simple mechanism, as the acidic electrolyte solution is in direct contact with the catalysts surface. Direct contact with a liquid electrolyte achieves better proton availability to the catalyst than the ionomer network utilised in MEAs. This reduced Pt utilization is exacerbated by the thicker MEA electrodes. In some cases, ionomer is used as part of the electrode for RDEs as a binder; this has been reported to reduce RDE performance.[102]
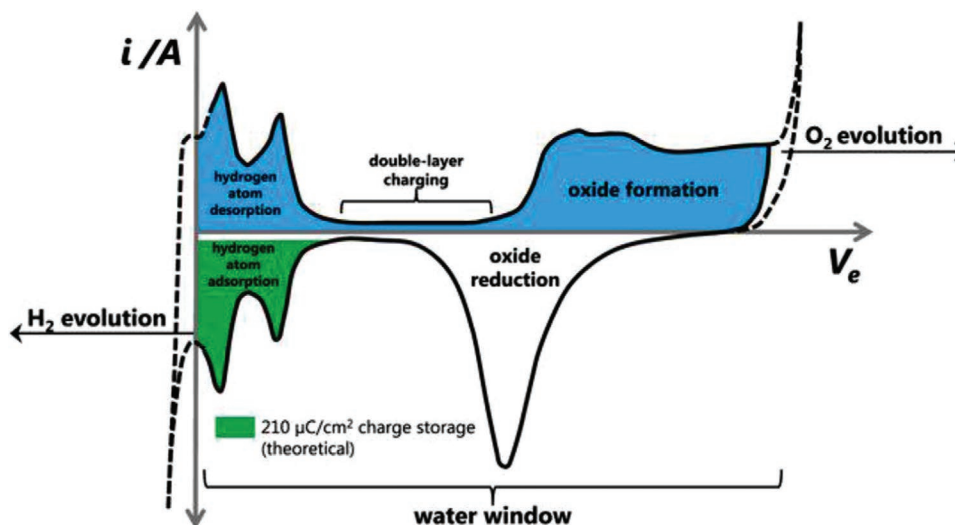
MEA CLs are typically formed with significantly more active material in thicker layers, incurring higher transport resistances. This is in contrast to RDE systems in which the liquid electrolyte is saturated with reactant gases delivered to the catalyst surface. In an MEA, the oxygen gas is delivered at a set gas flow rate to the catalyst via the GDL and MPL, and the tortuosity of this pathway can increase mass transport resistances. In addition, due to ionomer hydration requirements, inlet gases have to be humidified. In summary, RDE experiments are not restricted by a multitude of limitations common to MEA-based tests as they do not have membranes, significant ionomer contents, or bulk electrodes.

Perhaps one of the biggest issues with RDE systems is that despite their prevalence in literature, there are no single accepted protocols for testing, although attempts have been made to implement them.[103] This has led to a lack of reproducibility of results of even the same catalytic systems from different research groups. In an attempt to rectify the situation, a number of papers have suggested practices best adopted for reproducibility and reliability. In particular, Garsany et al.[104,105] and Takahashi et al.[106] have produced extensive papers focusing on the ways to test via RDEs that ensure verifiable performance and durability results. These cover everything from the best way to produce smooth catalytic thin films,[90] to the way glassware should be appropriately cleaned to avoid contamination.

While the various half-cell measurements are useful for screening materials, providing a relative measure against standard commercial materials such as Pt on carbon (often referred to as PtC) and identifying relevant kinetic and mechanistic information, they are artificial systems that do not fully represent practical technological electrode performance in an operating fuel cell. Testing MEAs in a single cell fuel cell provides much more accurate and representative information on how a CL will perform when it comes to catalytic activity, mass transport properties, and durability. While a single-cell lacks the additional engineering elements associated with parameters ranging from stack thermal management and the compatibility with other components, such as the bipolar plate (i.e., corrosion products and reactant flow implications), it provides the most reliable measure of how a CL/MEA system will operate in practice. As such, wherever possible, full cell data should be presented alongside RDE results.

2.3. In Situ Electrochemical Measurements: Membrane Electrode Assemblies

As mentioned, CVs are one of the most commonly used measurement methods for understanding catalyst activity under realistic operating conditions. CVs of Pt and Pt-based catalysts in an acidic electrolyte show three distinct regions, as shown in **Figure 3**: a region at low potentials due to hydrogen adsorption/desorption, a region at high potential due to oxide formation or reduction, and a double-layer capacitive region between the hydrogen and oxide regions (Figure 3). The current contribution shown in the peaks in the H_2 adsorption/desorption region are directly proportional to the number of hydrogen molecules in contact with any exposed and electrically connected Pt. Hence, the number of active catalyst surface sites can be calculated

**ADVANCED
SCIENCE NEWS**

www.advancedsciencenews.com

**ADVANCED
ENERGY
MATERIALS**

www.advenergymat.de

Figure 3. Typical CV of Pt electrode showing regions of hydrogen adsorption and desorption, formation, reduction of Pt oxides and oxygen or hydrogen evolution at either end. Reproduced under the terms of the Creative Commons Attribution 3.0 International (CC BY 3.0) license.[107] Copyright 2016, IOP Publishing Ltd.

from the total charge required for monolayer adsorption or desorption. This results in a parameter defined as the surface area of catalyst per gram of catalyst, often called the electrochemical surface area (ECSA). However, the measured ECSA has shown to be dependent on the nitrogen gas flow on the WE, with a gas flow of 4 L min^{-1} resulting in a 15% lower ECSA than the same electrode tested at 0.063 L min^{-1}.[108] It is recommended therefore, to measure ECSA with significantly reduced flow rates (0.001 L min^{-1} cm$^{-2}_{Electrode\ Area}$).[108] The ECSA of a Pt catalyst can be calculated[109] via Equation (10) below.

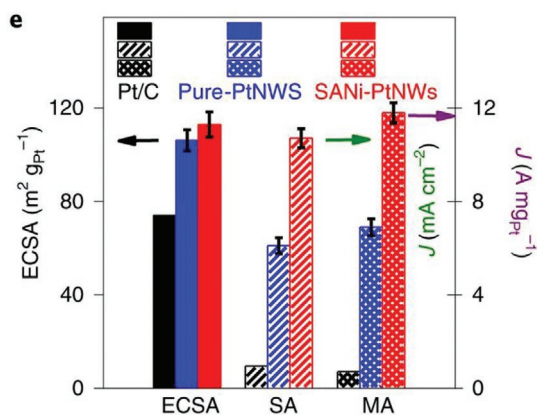$$ECSA_{Pt,\ Cat} = \left(\frac{Q_H}{\Gamma L}\right) \times 10^{-4} \qquad (10)$$

Q_H is the integrated charge density (µC cm$^{-2}_{electrode}$), Γ is the specific charge required to oxidize/reduce a monolayer of the adsorbed species (210 µC cm$^{-2}_{Pt}$), and L is the Pt loading of the electrode (g$_{Pt}$ cm$^{-2}_{electrode}$).[110,111] ECSA is an important quantitative metric as it indicates the surface area of catalyst per gram of catalyst that it is accessible to reactants independent of catalyst loading or electrode area. Since reactions occur on the surface of the CL, having a higher surface area increases the available catalyst and is key to improving performance. ECSA is best described as a measure of catalyst usage. Commercial PtC should typically achieve ECSA values of 60 m^2 g$^{-1}_{Pt}$.[71,81] Values above this show superior utilization, while values below show reduced access to active sites. ECSA units are m^2 (of available Pt surface)/ g(of Pt), catalysts with smaller average particle size typically have a higher surface area to volume ratio, hence show a higher ECSA. In practice, however, levels of Pt usage can vary for numerous other reasons, such as catalyst particles becoming isolated and therefore not connected to the ionomer or conductive network, poisoning of the catalyst surface, and changes in particle size during operation, among many others. ECSA values are typically lower when measured in an MEA compared to RDE due to inferior proton delivery system of the inhomogeneously

distributed ionomer network.[108] The difference between the ECSA, or mass activity, under MEA conditions as compared to those from RDE measurements is sometimes reported as a Pt utilization parameter, Ef_{Pt}.[77,112] This Ef_{Pt} is the quotient of the ECSA obtained under RDE conditions, which would be expected to measure all available catalyst surface area, and the ECSA measured under MEA conditions. Lower values of Ef_{Pt} indicate a significant loss of catalyst utilization when forming an MEA, which is typically due to either ionomer poisoning or isolated catalyst particles. In either case we would encourage the reporting of the Ef_{Pt} in future publications as is an easily measurable and a useful parameter to observe changes in the CL.

The observed ECSA of an MEA depends on the recent operating conditions, for example, flooded electrodes have been reported to have 10–15% higher ECSA.[108] The conductivity of the ionomer network's in the MEA improves upon water uptake and due to the generation of water during operation, this water also conduct protons to catalyst particles, some of which may not be accessible to the ionomer network. Given this, a measurement called dry proton accessibility, which measures the difference between ECSA at low and high humidity has been suggested.[113] Typically, this value is reported as a ratio of the ECSA at 20% relative humidity (RH) and at 100% RH. The high RH ECSA values should highlight all accessible Pt due to flooding, while low RH ECSA values should, in theory, only record the ECSA of catalyst particles in direct contact with the ionomer network.[63,113] While this measurement has been reported, there only are a few studies directly showing its validity and the protocol to ensure correct quantities of liquid water in each of the different RH measurements.[108] If a robust analysis and set of protocols could be established then this measurement would be a simple, highly effective method in which to record the ionomer distribution and catalyst accessibility of any MEA.

The specific activity (SA) is a common method to report catalyst activity, as it represents the intrinsic activity of the catalyst

ADVANCED
SCIENCE NEWS
www.advancedsciencenews.com

ADVANCED
ENERGY
MATERIALS
www.advenergymat.de

Figure 4. A comparison of ECSA, SA, and MA for the hydrogen evolution reaction for PtC, Pt nanowires, and single-atom nickel-modified Pt nanowires. Adapted with permission.[88] Copyright 2019, Springer Nature.

Figure 5. Model polarization curve for a PEFC. Reproduced with permission.[114] Copyright 2008, Elsevier.

surface. It is reported in µA cm$^{-2}_{Cat}$; hence, it is a measure of current generated relative to the surface area of the catalyst and is therefore independent of the total catalyst loading in an electrode. The mass activity (MA) of a catalyst is a similar measurement that is reported in units of µA mg$^{-1}_{Cat}$, as such it allows for easier comparison of different loaded electrodes. These parameters are highly dependent on the electrode and catalyst structure and should not be used as the only indicators of performance; they must be reported in conjunction with other parameters. For example, if solid catalyst particles were replaced with a core–shell type catalyst on an MEA with the same current density and ECSA, the SA of the new catalyst would not change, while the MA would significantly improve. Understanding what these parameters represent in any given situation requires a broad understanding of the electrodes and catalyst structure in question. There are numerous literature examples where this comparison is made, for example, Li et al.[88] used these parameters to compare their synthesized materials (single-atom nickel-modified Pt nanowires (SANi-PtNWs) and pure-Pt nanowires) with commercial PtC. **Figure 4** shows the variation in results of the three parameters and hence the importance of investigating all three.

Of the various electrochemical techniques used to analyze the performance of a fuel cell, the polarization curve has become the standard benchmark test. Typically, either the peak power density or the current density at 0.3 V is used to compare MEAs. The polarization curves are obtained by plotting cell potential against current density and is conventionally separated into three regions (**Figure 5**).[114] The OCV of the polarization curve is the voltage at which no current density is measured. It is the minimum overpotential required to drive an ORR reaction and is, in the most part, defined by the catalyst used. However, it is also dependant on other factors such as reactant gas pressure, voltage loss from hydrogen crossover and mixed potential from side reactions. Under standard operating conditions, the OCV of a Pt based fuel cell should typically be around 0.95–1 V,[115,116] although it can be reduced significantly by hydrogen cross over, particularly at very low Pt loadings. The first section of the curve between 1 and 0.7 V is typically described as the kinetic region, where the ORR overpotential
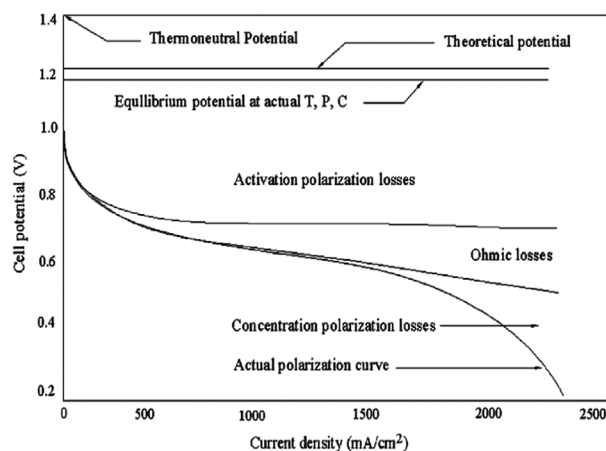
results in activation polarization losses. The kinetic region is mostly defined by the chemistry of the catalyst and the ECSA of the MEA, as more available surface area will increase the kinetic current. The central section of the polarization curve, nominally between 0.7 and 0.5 V, is typically referred to as the Ohmic polarization region. Losses in this region are mainly due to increased resistances due to increases in the current. The current density achieved is highly dependent on the electrical and proton conductivity of the CL as well as the contact between the different layers of the fuel cell. The third major region is the mass transport region, typically between 0.5 and 0.3 V, in which losses are due to the inability of reactants to reach the catalyst surface due to higher gas requirements at extreme currents, that is, mass transport limitations. In this situation, reactant gases are consumed in the reactions at the catalytic surface faster than they can diffuse to these active sites, either from the gas flow or as protons across the membrane. The losses in this region originate from proton and oxygen transport limitations, which can occur as a result of tortuous gas pathways and limited proton-conducting infrastructure.

At all points of the polarization curve, there are multiple interplaying factors that impact the current achieved at a set voltage, including catalyst accessibility, proton and electrical conductivity, reactant transport resistances, and H$_2$ crossover. The subdivisions of the polarization curve into the discrete units discussed above, and in literature widely, is an oversimplification that allows some separation of individual components of fuel cell performance. While this review will continue to use these terms for clarity of communication, it should be noted that the regions of the polarization curve are artificial divides. In reality, a polarization curve is a continuum and at every point there are influences from a multitude of different interacting factors.

Given the complex, hierarchical nature of MEAs, differences in materials or morphology will alter the shape of the polarization curve. This is useful as changes in the different regions can inform limitations of one MEA compared with another. For example, if a new material has lower current in the kinetic region compared to commercial samples, it would indicate a reduced catalyst utilization or turnover.

**ADVANCED
SCIENCE NEWS**
www.advancedsciencenews.com

**ADVANCED
ENERGY
MATERIALS**
www.advenergymat.de

Table 1. Conditioning strategies suggested in the literature.

Protocol name	Protocol steps	Total testing time (h)	Operating conditions
USFCC[137]	(1) CP: 0.6 V for 1 h. (2) Cycling CP: 0.7 and 0.5 V, 20 min each, 9 times. (3) CC: 0.25 A cm^{-2} for 12 h	19	80 °C, 100% RH, 172 kPa stoic: 1.2/2 (H$_2$/air)
CP[127]	0.6 V for 9 h	9	75 °C, 100% RH, 172 kPa bP
Three-step activation[532]	(1) Cell temperature 70 °C, 64% RH. (2) Cell temperature 60 °C, 157% RH. (3) Repeat of step (1)	No data provided	Variable temperature and humidity. No bP
Low thermal and pressure stress[511]	0.6 V for 9 h	9	55 °C, 34 kPa bP

Understanding why the polarization curve is changing compared to a reference cell is key to rationalizing the structural and chemical changes that occur in an MEA.
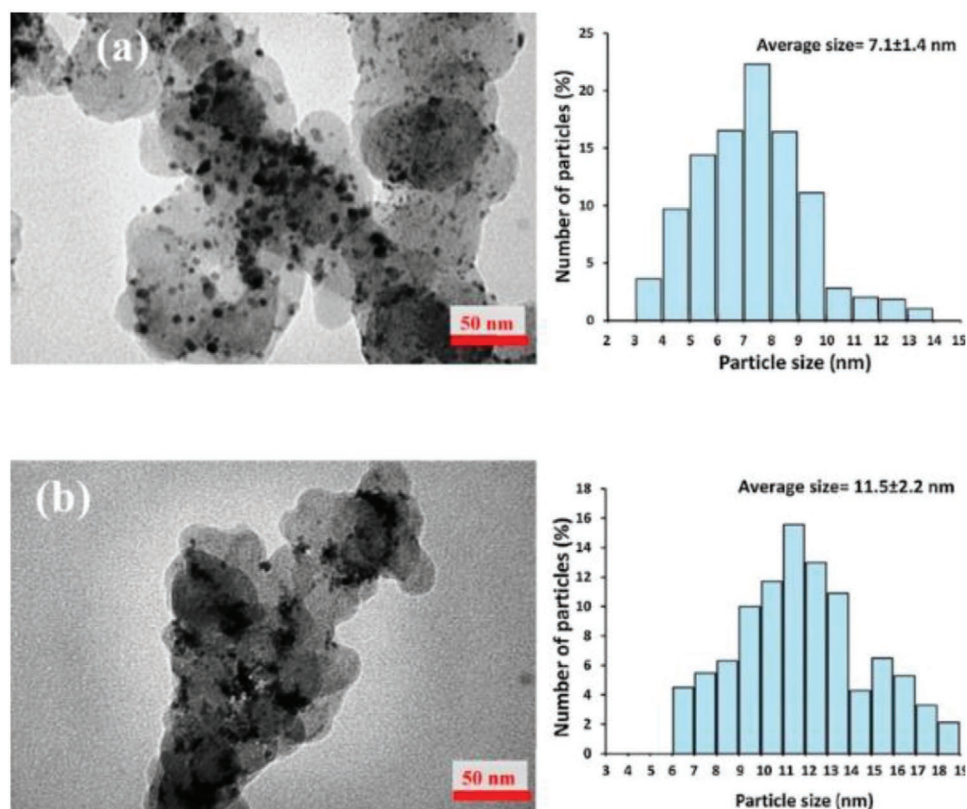
2.4. Impact of MEA Conditioning Procedures

Prior to fuel cell testing, a fresh MEA is subjected to an initial series of environmental conditions or electrochemical tests. This is called conditioning and typically follows a set of protocols to "activate" the MEA, thereby improving performance when fully operational. Throughout the conditioning process, the performance should gradually improve, due to physical changes that occur in the MEA.[117,118] These physical changes includes the expansion of the ionomer through hydration, but other changes that occur during conditioning are still not completely clear. Carrying out a conditioning protocol prior to MEA operation is crucial for ensuring the best performance of the MEA, though it should be noted that continuing the activation beyond the optimized condition could lead to the early onset of degradation mechanisms in the MEA.

Numerous conditioning protocols have been investigated and published, typically compared via final electrochemical performance and the rate of degradation over the lifetime of the MEA. Conditioning can be applied in two ways: through off-line methods such as steaming or boiling the electrodes prior to operation,[119,120] or on-line methods which employ fuel cell operation to condition the MEA. A comprehensive review by Yuan et al.[121] suggests three theories for the improvement in activity post-conditioning: activation leads to an improved catalyst surface, via processes such as stripping impurities from the CL introduced in the manufacturing processes; pathways are opened in the GDL for reactants to travel through and hydration of the ionomer[122] contained within the CL, facilitating better proton transport to the active catalyst sites. They concluded that the most important requirement for MEA activation is to develop adequate hydration, which is linked to cell temperature, as dehydration can result in membrane degradation,[123] while flooding will result in reactant starvation that can strip the CL.[124,125] The review also summarized a range of activation methods, including hydrogen pumping, temperature control, current control, potential control, and combined potential and current control. In hydrogen pumping, the cell has an external power source applied and hydrogen is supplied into the cell at the anode. The hydrogen is oxidized at the anode to form protons, which are "pumped" through the membrane and reduced at the cathode to form hydrogen. He et al.[126] found this method effective in improving the activity of the catalyst and the overall performance of the fuel cell. It was suggested that this resulted in changes to the porosity and tortuosity of the CL that occurred due to the evolution of hydrogen, activating more catalyst sites by exposing them to ionomer.

Zhiami et al.[127,128] compared three different conditioning strategies: constant potential hold (0.6 V for 9 h), constant current (CC) hold (0.25 A cm^{-2} for 19 h), and the US Fuel Cell Council (USFCC) protocol (listed in **Table 1**). For all strategies, the largest performance enhancement occurred after 1–2 h of operation. EIS analysis observed a reduction in Ohmic resistance with conditioning time, related to improved ionomer hydration. This has also been noted by Mason et al.,[122] who observed a direct relationship between ionomer conductivity and MEA swelling during initial hydration. Zhiami et al.[127,128] also measured EIS at 0.7 V showed a reduction in charge transfer, related to improved kinetics. The low-frequency arc measured at 0.5 and 0.3 V also reduced in diameter, due to improved mass transfer mechanisms. They went further to suggest that constant potential (CP) strategies, followed by the USFCC protocol, result in a better overall PEFC performance than constant current, in a much shorter time. The study also explored the effects of humidification on the activation process at low RH (30%), the ionomer inside the CL was found to not fully humidified. This was suggested to result in the shrinkage of ionic clusters and limiting both the O$_2$ permeability and proton transport to the catalyst/ionomer interface. This also links to the greater water production rate by the CP and USPCC protocol compared to CC. However, they did not suggest if higher current operation would solve the dehydration issue. Taghiabadi et al.[129] also investigated the long-term improved effects of the CP activation process on the MEA through aging cycles post-conditioning. CP conditioning at 0.6 V showed a slower voltage decay of 4.4 μV cycle^{-1} at 1 A cm^{-2}, compared to 11.33 μV cycle^{-1} for CC (0.25 A cm^{-2}) activation. ECSA decline as shown in **Figure 6** was also more prominent for CC compared to CP at 32% and 19%, respectively, linking to the performance decline. Yuan et al.[118] investigated the effects of temperature on the conditioning process. With full humidity of the reactants, conditioning at 90 °C achieved higher currents after a 6 h hold at 0.6 V than at lower temperatures, although this could be related to improved operating conditions rather than any structural improvements to the MEA. During the early 2000s, Qi et al.[130,131] pioneered MEA activation using a protocol that held the cell voltage in the range of 0.4–0.6 V (current density 1.0–1.5 A cm^{-2}) while varying the cell temperature, hydrogen, and air humidification. They found that a cell

**ADVANCED
SCIENCE NEWS**

www.advancedsciencenews.com

**ADVANCED
ENERGY
MATERIALS**

www.advenergymat.de

Figure 6. TEM images and catalyst particle size distribution of the cathode CL after aging cycles a) activated MEA by contact voltage procedure and b) activated MEA by constant low current method. Reproduced with permission.[129] Copyright 2019, Elsevier.

temperature of 75 °C and hydrogen and air humidification temperatures of 95 and 90 °C, respectively, produced the best performance post-activation. Catalysts with lower Pt loadings also experienced greater increases in activity compared to those with higher loadings. It was suggested that the performance improvement was due to the elevated temperatures "opening" regions of the CL by hydrating the ionomer, giving access to the Pt catalyst sites, which agrees with lower Pt loading exhibiting greater improvements when more sites are exposed. Although the importance of membrane and ionomer hydration as part of the conditioning procedure was not deeply discussed, it is likely that a large contribution of the performance improvement was due to this hydration.

Deliberate short-circuiting in PEFCs can be used to temporarily boost the performance by increasing the amount of water in the MEA and generating extra heat. Periodic shorting of a stack during operation, for example, 500 ms shorts every minute, is commonly employed in commercial systems.[132–134] Xie et al.[135] shorted their cell for a few minutes prior to feeding reactants, followed by CC operation at 1 A cm^{-2} for 6 h, obtaining a stable potential after 3 h. However, a recent study by Trogadas et al.[136] found that while immediate performance improvements are seen, in the long-term, severe Ostwald ripening and Pt migration occurs at the cathode CL of a short-circuited MEA compared to a non-shorted one.

Table 1 compares different conditioning strategies proposed in the literature. It is difficult to make direct comparisons

between the different methods as MEA variation, operating strategies, PEFC sizes, and environmental conditions mean that output power cannot be an accurately benchmarked. However, from our survey of the literature it appears that CP, high temperature and RH achieves the best performing devices. Although for ease of comparison between publication it is advised to follow procedures defined by independent bodies, such as the USFCC.[137]

2.5. Effect of Operating Parameters

The performance and operational stability of a fuel cell system is ultimately dependent on the operating parameters applied. These conditions include the operating temperature within the cell, humidification, gas purity, flow parameters within the feed lines, and pressure of the system. Poor optimization of these factors can result in inefficient operation or damage to the fuel cell components, such as overheating, ionomer dehydration, and pinhole formation. While each operating parameter can be individually investigated and optimized, they are ultimately interconnected and also dependent on the MEA properties and fuel cell design.[138] Basic performance comparison can be achieved through polarization and electrochemical analysis, where each operating parameter is expected to alter the kinetics, mass transport of gases, flooding/drying of the ionomer, etc. Understanding how these parameters affect each overpotential contribution is key, as it is possible to roughly
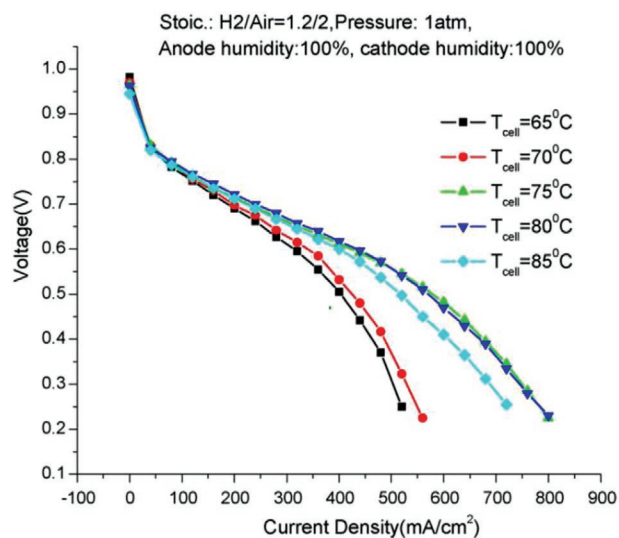
Figure 7. Polarization curves of a 5 cm² PEFC operated between 65 and 85 °C. Performance improved with increasing temperature between 65 and 75 °C, remained constant from 75 to 80 °C and then deteriorated at 85 °C. Reproduced with permission.[139] Copyright 2006, Elsevier.

deconvolute the impacts of various parameters on the overall activity of the PEFC and suggest improvements.[139]

2.5.1. Temperature and Relative Humidity

The choice of operating temperature influences the overall cell performance[140,141] and is particularly important for the activity of the CL. In a broad study examining the effects of various operating conditions on performance, Yan et al.[139] varied the operating temperature of a 25 cm² cell from 65 to 85 °C at 100% gas humidity. Using polarization curves (**Figure 7**), they observed an improvement in performance as the temperature increased from 65 to 75 °C; peformance then remained roughly constant from 75 to 80 °C, folllowed by deterioration after 85 °C. The authors suggest that the increase in performance be explained by the increase in ionomer conductivity and gas diffusivity at higher temperatures, increasing the amount of reactant available to the catalyst and thus reducing mass transport losses. The increase in temperature is also understood to enhance reaction kinetics at the catalyst site, reducing activation losses,[142–144] although this is not always observed as shown by the reduced OCV in Figure 7. As the temperature is increased further, the rate of water evaporation exceeds the rate of water production at the cathode, resulting in ionomer dehydration and impeding proton conduction within the CL and across the cell. Poor proton conductivity at higher temperatures leads to reduced cell activity, resulting in a feedback loop wherein even less water is produced in the cathode CL, leading to further dehydration of the membrane and potentially failure of the cell.[139,142]

Closely interlinked with the temperature is the humidity of the reactant feeds. Low humidity is typically considered to be between 20% and 50% RH, while above 70% RH is usually regarded as high humidities. Typically water is introduced into

the CL and membrane via gas humidification, this water is required to alleviate the negative feedback loop of dehydrated ionomer, particularly at higher temperatures. In a well-known study conducted by Wang et al.[144] in 2003, the cell temperature was varied while the gas humidification temperatures were held constant. At low current densities, when the operational temperature exceeded that of the humidification temperature, the water produced at the cathode was insufficient to maintain ionomer hydration within the CL, resulting in a decreased ECSA. When the operational temperature and humidification temperature were increased in step with each other, such that they remained equal, this effect was not observed and the performance increased consistently as the temperatures rose to 90 °C. Although this observation disagrees with the temperature impact on performance at a set humidification in Figure 7, we assign this to differences in cell design and testing protocols such as MEA size. It has further been found that the current density distribution across the MEA changes as a function of RH: at high humidity, the current density decreases from inlet to oulet; at low humidity this is reversed.[140] The performance and durability implications of cell heterogeneity is discussed more in Section 2.5.2.

Yan et al.[139] found that for a low air humidity, a high hydrogen humidity can be utilised to maintain membrane hydration by reversing the water gradient that normally causes back diffusion of water to the anode, while electroosmotic drag maintained water transport to, and hydration of, the cathode. As anode humidity was increasced, reduced cathode humiditiy was required to achieve peak current current density by increasing the water gradient between the electrodes. This is likely due to reduced excess water in the cathode and GDL impeding the access of oxygen to the cathode and results in larger mass transport resistances.[145] It was found that flooding under high cathode gas humidity also led to greater degradation of the CL, accelerating the agglomeration of Pt NPs, corroding the carbon support, and thus reducing the number of active catalyst sites.[146,147] Neyerlin et al.[148] observed poor ORR kinetics at low RH, due to poor proton conductivity and drop in ORR exchange current density, but this was unaffected above 50–60%.

Beyond the simple operation of a fuel cell at a given set of RH, it has been shown that the operational history of humidities of a fuel cell also has an impact on onward performance. Jomori et al.[149] studied the effects of low humidity operation on a 1 cm² cell, where the cell was left to operate for 18 h at a 20% RH. Using the current density achieved at 0.9 V after 200 s as a benchmark, they found that after 13 h of operating at low humidity, the normalized activity level of the cell had dropped by 68% when compared to the activity measured immediately after the cell's activation. While the cell activity could be mostly recovered via a number of protocols involving CP and high humidities (between 90% and 170% RH), it was not possible to regain the full activity observed immediately after activation. The loss in activity during the low humidity operation is suggested to be due to the adsorption of ionomer sulfonate groups onto the Pt surface, which in turn increases the oxygen transport resistance and poisons the Pt catalyst.

To conclude, higher temperatures directly improve catalytic activity and proton conductivity and thus, the kinetics of the

ADVANCED
SCIENCE NEWS
www.advancedsciencenews.com

ADVANCED
ENERGY
MATERIALS
www.advenergymat.de

electrochemical reaction. However, this is contingent on the hydration of the ionomer. It has been suggested that at low current densities, external humidification is required to achieve adequate performance, but MEAs operated continuously at high current densities can generate enough water to humidify the membrane and ionomer.[151] Hence, elevated temperatures can result in enhanced performance and higher attainable current densities, but the rate of water production may be insufficient to prevent ionomer dehydration, which ultimately leads to cell failure. Thus, suitable hydration of the feed streams or ionomer is crucial for maintaining the overall performance and stabilizing the water distribution within the cell. While this can be difficult to envisage prior to operation, as it can depend on the operating strategy, a comprehensive understanding of the interplay of temperature and humidity must be discerned by observing changes in performance. This interplay can be highly dependent on the size and design of a fuel cell and constrained by its intended application. In general, a higher temperature with a suitable level of hydration is desired, but this can also depend on the MEA material properties, such as the thickness of the GDL and ionomer. As a result of the difficulty in suggesting a universal operating temperature and gas humidification, the US department of energy (DoE) and the EU have synchronized their test protocols to suggest an operating temperature of 80 °C, but at varying RH as a base standard for comparison.[36,152]

2.5.2. Fuel Stoichiometry, Flow Operation and Cell Heterogeneity

There are two types of established fuel cell flow operations: through-flow anode (TFA) and dead-ended anode (DEA). DEA differs from TFA in that the anode outlet is closed, with intermittent purges acting to remove built-up N_2 in the system, replenish H_2 fuel, and instantaneously recover the cell voltage.[153] DEA mode has the benefit of requiring fewer auxiliary components, employing a single pressure regulator and a purging valve at the outlet. However, a highly heterogeneous current density distribution, caused by fuel starvation, has been observed in DEA operations induced by the accumulation of water and nitrogen in the anode channels.[154] This results in a higher local potential at the cathode, which corrodes the cathode carbon support, as shown by Yu et al.,[154] who reported a 25% decline in the cathode CL thickness from the regions of the hydrogen inlet to the outlet. Strahl et al.,[155] and Chevalier et al.[156] reported that the accumulation of water at the anode is more detrimental to performance than built-up N_2, with excess water aiding in accelerated carbon corrosion.[146]

In through-flow operation, the supply of reactant gases can either be at a constant flow rate for small cells or, most commonly, in stoichiometric ratios. In which the flow of reactant gas is defined by the load demand, calculated through Faraday's law,[157] and multiplied by a stoichiometric ratio to give a proportional excess of reagents for the reaction at the desired current. Insufficient reactant gas supply can cause fuel starvation which results in severe carbon corrosion.[158,159] Excessive reactant gas can result in low fuel utilization, a significant drawback in commercial systems, and a loss in membrane humidity as a result of the higher flow rate drying out the cell.[160–162] Degradation caused by local fuel starvation can be mitigated by supplying reactants above the minimum required for the electrochemical reaction. For laboratory MEA testing, over-supply of reactants prevents local degradation. However, in commercial systems, the enhanced durability from fuel over-supply has to be balanced with higher operating costs and lower combine paragraphs.

If reactants are supplied at the exact quantity required for reaction, it can, counterintuitively, lead to degradation due to significant heterogeneity in cell performance and humidity.[163] This is due to the reactant being consumed by the MEA along the flow path, which lowers the reactant content along the channel away from the inlet.[140,164] This inconsistent reactant distribution is present in all fuel cells and results in fuel starvation toward the outlet, reduced current density, and local cell reversal in which the anode voltage becomes large enough to drive water electrolysis via carbon oxidation.[140,163,165–168]

Similar to reactant, RH changes significantly across the electrode area as a result of local water generation and water absorption by the ionomer. This results in significant variation in local water content, which accelerates local carbon corrosion and is a key cause of membrane degradation which leads to overall system failure.[169] As such, many of the factors influencing degradation in an MEA do not relate to the materials themselves, but the geometries and conditions of the MEA. For example, Chen et al.[163] found that increased size of the cathode outlet opening reduced carbon corrosion, this was suggested to be related to more homogeneous water distribution across the active area of the MEA. Gas purging during operation has been reported to remove the excess water associated with increased carbon corrosion.[146] Taniguchi et al.[124] investigated the damage to a 10 cm^2 PEFC subjected to fuel starvation and detected catalyst dissolution on both electrodes, with severe loss at the fuel outlet regions. The effects of fuel starvation become more prominent with increasing cell size.

Current distribution mapping can be utilized to study fuel starvation, carbon corrosions and performance heterogeneities by capturing localized measured currents in-operando. Using a specially designed cell Liang et al.[168] detected high local interfacial potentials (~1.8–2.6 V) near the anode outlet, where hydrogen and water are oxidized, accelerating carbon corrosion and generating a water electrolysis current. Using current mapping Zhang et al.[170] observed unstable current densities and temperatures toward the outlet during hydrogen starvation when the cell was operated in CP, while for CC, local performance near the inlet rises, which accelerates their local degradation. Brett et al.[150] used a segmented electrode array along a single channel to measure local performance at different gas flow rates. **Figure 8** shows that with increasing flow rate, homogeneity in the current density profile is established. However, at high air flow rate and no humidification (Figure 8j), an increase in current is exhibited along the channel, which when analyzed through local EIS, was due to membrane dehydration near the inlet caused by the high gas flow. The larger cells are more prone to inhomogeneous distribution of humidity and current density due to the significantly longer flow path of reactant gases and water distribution. Using smaller size MEAs, 5–25 cm^2, will minimize the impact of localized
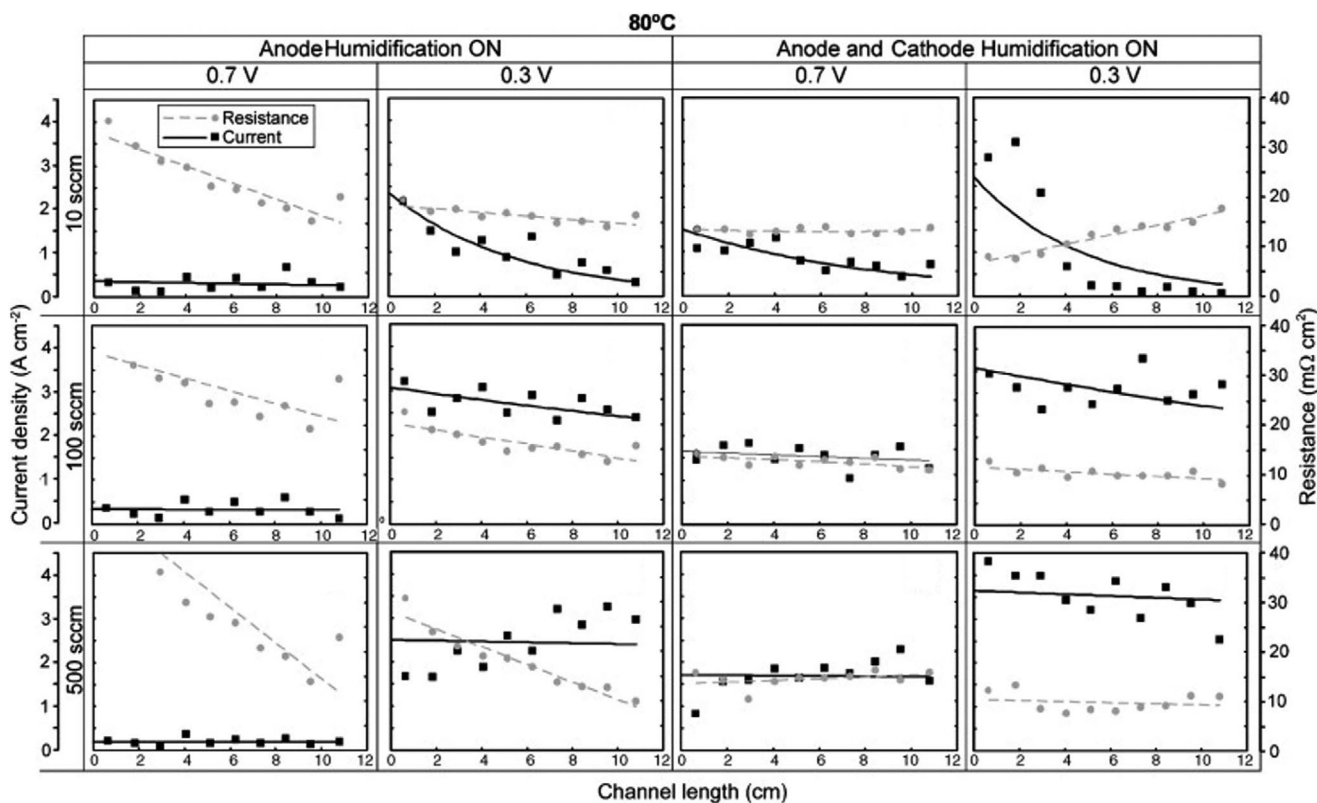
Figure 8. Current and ionomer distribution profiles during operation along channel length at different air flow rates at 80 °C. Reproduced with permission.[150] Copyright 2007, Elsevier.

degradation. However, significant research using current mapping systems is required to understand and optimize the MEA cell design and mitigate the localized durability loss.

2.5.3. Gas Pressure and Back Pressure

Gas pressure has several distinct impacts on fuel cell performance it is typically controlled via back pressure, in which a particular pressure is applied at the end of the systems flow path, after the active area. It impacts the thermodynamics of the ORR reaction, as the theoretical OCV is related to back pressure, with higher back pressure increasing the partial pressure of reactants and increasing the OCV.[171,172] It also has an impact on exchange current density, mass transfer, and to a lesser extent the membrane conductivity.[171,172] These factors result in increased current density as a function of back pressure, although this is often in conjunction with and limited by higher back pressure increasing H_2 crossover as shown in **Figure 9**.[171,172] Furthermore, at very high back pressure, sealing problems with the cell can lead to accidental gas loss. It has been reported that higher back pressure can cause a more homogenous distribution of local current density as more reactants are available to catalyst further along the flow path;[140] However, it has also been suggested that oxidant pressures above 3 atm do not significantly increase molar oxygen fraction

but does lead to durability issues and parasitic power loss associated with greater gas pressure.[173]

2.6. Accelerated Stress Tests (ASTs)

Degradation processes in fuel cells occur over thousands of hours, hence, ASTs are used to mimic degradation on a timescale that is more attainable for lab-based testing. Furthermore,
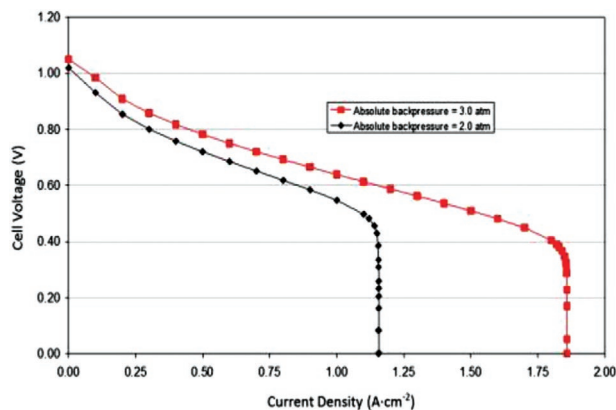
Figure 9. Calculated fuel cell polarization curves at back pressures of 2.0 and 3.0 atm. Reproduced with permission.[172] Copyright 2013, Elsevier.

ADVANCED
SCIENCE NEWS
www.advancedsciencenews.com

ADVANCED
ENERGY
MATERIALS
www.advenergymat.de

because each component has a unique degradation mechanism, the particular AST protocol used can target a specific mechanism, such that the processes can be partially disentangled. Similar to conditioning, a large range of protocols have been proposed, each with different voltage ranges, times, and cycling methods. Both the US DoE[36,174] and the EU[152] have outlined common standards to benchmark degradation of PEFC which are particularly useful for assessing the durability and lifetime of CLs and are essential for characterizing the suitability of new CL materials and compositions. Given the range of degradation mechanisms, including both mechanical and (electro-)chemical processes,[175] it is important to note that a range of such tests are necessary to fully understand a material's durability and suitability in real world applications.

For CLs, there are traditionally two key degradation pathways that occur, typically separated into the degradation of the catalyst particles and carbon corrosion of the support.[176,177] Although in practice, both mechanisms are interlinked and are consequences of Pt redox reactions that simultaneously occur to different degrees during fuel cell operation. Furthermore, changes to the ionomer distribution during operation can impact Pt utilization/poisoning, electrode thinning and mass transport. The two main mechanisms of catalyst degradation during fuel cell operation are Ostwald ripening, in which the catalyst detaches from the support and deposits somewhere electrochemically inactive, and particle coalescence, which results in the formation of larger particles with less catalytic surface area.[71,178] Regarding the catalyst, ASTs targeting this mode of degradation typically use voltage cycling in the region of 0.6–0.95 V (i.e., near OCV) for extended periods (30 000 cycles for the DoE protocol).[36,174] This voltage range is relevant for typical PEFC operating conditions and also encompasses the activation region of the polarization curve, where catalyst utilization is relevant. Within this range, Pt catalyst particles have been found to degrade via both particle coalescence and Ostwald ripening, which reduces the available ECSA as shown by in situ CV.[177] Some practitioners have found methods that can alleviate catalyst degradation, such as the reduction in catalyst particle size[179] or the use of additives, like graphene, for improving catalyst durability. This is more widely discussed in Section 4.[180]

To emulate carbon corrosion, which happens especially during cell start-up/shutdown where the cell is subject to high voltages caused by a hydrogen/air wavefront,[181,182] cells are cycled at higher voltages between 1 and 1.5 V for around 5000 cycles.[174] The result of extended cycling at extreme voltages includes the loss of oxygen-containing functional groups on the surface of supports,[159] formation of gases like CO and CO_2,[183] as well as increased cracking of the CL[184,185] and overall loss of carbon material.[177] The loss of carbon material itself also occurs, a side effect of this type of degradation is the loss of catalyst material via particle detachment,[186] which results in a loss of ECSA. Furthermore, ionomer is also lost from the CL during this carbon corrosion mechanism, which, along with increased cracking, thinning and collapse of the CL pore structure, can significantly reduce the water management abilities of the CL during operation.[187] Although the exact structure changes that occur during ASTs are beyond the scope of this review, we recommend other reviews on this topic.[188,189]

2.7. Conclusion and Outlook

While beneficial for screening the effectiveness of new catalyst materials due to facile operation, ex situ RDE does not provide data comparable with full fuel cell tests. It is therefore an appropriate starting point for catalyst development, allowing multiple new materials to be tested efficiently, but is not intended to replace MEA testing. In an MEA, interplay of additional factors such as the catalyst-support interaction, ionomer distribution, manufacturing processes, and non-CL components, provide a true representation of CL performance under realistic operating conditions. The natural progression for catalyst research and development follows the path of i) RDE screening with small amounts of novel catalysts to ii) single-cell MEA testing of batch samples and finally iii) short-stack testing of "design-freeze" scaled-up catalyst to assess long-term MEA performance in commercially relevant systems. As well as standard MEA electrochemical testing methods (polarization curve, ECSA), further quantitative information about the MEA can be obtained through metrics such as Ef_{Pt} and dry proton accessibility and are useful for understanding the Pt distribution within the CL. Furthermore, the role of conditioning on achieving optimized performance cannot be overlooked. A wide variety of conditioning protocols have been investigated and published, generally suggesting CV operation combined with CC. It is recommended that the US DoE protocols are adopted, as developing in-house conditioning requires extensive trial and error.[36] Much more work is required to understand the physical changes induced by conditioning and understanding this process could be used to optimize device performance.

It is not possible to recommend a single set of optimized operating conditions (i.e., temperature, humidity and gas flow) for PEFC operation since the values chosen depend on the design criteria of the system in question and their values relative to each other. For example, GDLs used for automotive applications will most likely be thicker, more porous, with greater amounts of hydrophobic coatings, best suited to low humidity operation as a significant amount of water will be produced in the stack. The optimum level of hydration is dependent on the operating current density, the thickness of the GDL, and the thickness of the membrane. Too little hydration will dehydrate the ionomer reducing performance and resulting in pinhole formation, while too much results in gas starvation. Higher operating temperatures are imposed in order to maximize catalytic activity, but ionomer dehydration is possible as the water produced by the electrochemical reaction is insufficient to maintain ionomer hydration. An elevated temperature can result in ionomer thinning and pinhole formation, and increased degradation rates of the support and Pt if the level of hydration is poor. Too low a temperature underutilizes the catalyst and is more likely to condense liquid water and flood the GDLs, restricting gas flow and thus causing reactant starvation.

Finding the right balance of operating conditions requires a solid understanding of how the operating parameters affect the overall performance as well as an awareness of how to identify and alleviate issues such as flooding or membrane dehydration. Defining the optimal operational parameters is further dependent on the size of MEA area, and number of cells in the stack, thus it is highly recommended to follow a

**ADVANCED
SCIENCE NEWS**

www.advancedsciencenews.com

**ADVANCED
ENERGY
MATERIALS**

www.advenergymat.de

well defined protocol. The degradation of PEFC components is an inevitable phenomenon, but operating parameters can significantly impact their durability. Carbon corrosion is accelerated under humidified conditions and higher temperatures, which results in Pt agglomeration/dissolution/migration. This degradation is not homogenously distributed over the entire MEA; localized membrane thinning leads to a negative feedback loop of deterioration and performance loss. Local condition heterogeneities are accentuated with larger active areas which will result in increased local degradation rates, predominantly at the outlet. This aggravates local fuel starvation leading to enhanced degradation. In general, commercial systems must carefully optimize the fuel ratio to minimize degradation mechanisms from local fuel starvation while maintaining fuel efficiency. Adjusting operating strategies such as flow-field design, gas flow, and humidity are required to reduce the inhomogeneous degradation, thus extending PEFC lifetime. While there is significant research looking at more complicated drive cycle corrosion testing, simple ASTs are a useful investigative tool that can simulate standard degradation in a reasonable timescale. Power density is a key performance indicator for PEFCs, however, the importance of durability cannot be understated, and all indications for PEFC targets, either from governments or companies, indicate that significant improvements to the durability of MEAs is needed.

3. Ionomer Distribution

3.1. Introduction

PEFCs utilize a solid electrolyte to act as a bulk ion-conducting membrane, typically 10–50 μm thick, to transfer protons between electrodes. The conduction of protons within the CL is typically achieved by the integration of a substantial proportion of polymeric ion conductor. The ion conductor coats catalyst support particles as thin films, 2–50 nm thick, as well as interpenetrating agglomerates and filling the regions between aggregates, as shown in Figure 2. PFSA ionomers are used due to their high proton conductivity as well as chemical and mechanical stability within the high voltage and corrosive fuel cell environment. However, good ionic conductivity is only achieved when properly humidified.[24,59,190] PFSA ionomers are typically formed from a combination of hydrophilic sulfonate (SO_3^-) bearing side chains and hydrophobic Teflon-like backbones, as shown in **Figure 10**.[59,191] This gives rise to their ability to conduct protons as the ionomer forms a crystalline phase-segregated structure with localized hydrophobic and hydrophilic domains.[59,192,193] Protons are transported in the hydrophilic region and the hydrophobic component provides mechanical support.[59,192]

PFSA ionomer chemical structure is commonly expressed by equivalent weight (EW), the mass of dry membrane per mole of acid groups, rather than molecular weight (MW). Backbone lengths are on the order of 100 nm, with side chains roughly 0.8 nm long regularly, but randomly, distributed on the order of every 0.6–1.2 nm for the most widely used ionomer Nafion with EW of 1100 g mol^{-1}.[191] Proton transport within ionomers relies upon the vehicular mechanism, via hydrated proton transfer, or
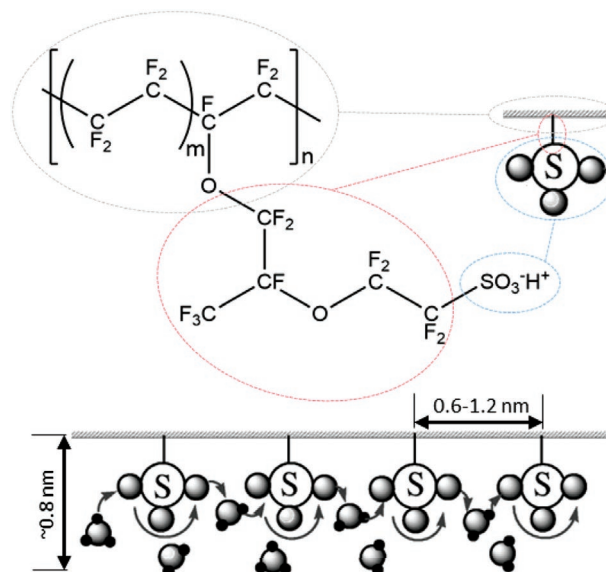
Figure 10. Molecular structure of Nafion ionomer with repeat unit, *n*, and EW determined by the repeat unit, *m*. The molecular structure corresponds to a simplified model of Nafion, with morphological dimensions and proton transfer via the Grotthuss mechanism in hydrated state detailed. Adapted with permission.[191] Copyright 2017, IOP Publishing, Ltd.

Grotthuss mechanism, via structural reorganization and "hopping" of protons within extended hydration structures.[194] The ionomer EW and morphology dictate the number and structural organization of bound counterions (SO_3^-), respectively. Therefore, the degree of acid dissociation (unbound protons) and long-range tortuosity can be influenced by the choice of ionomer and directed structure within the CL, with subsequent impact on long-range proton conductivity. Since this review is focused on the structure–performance relationship of the CL, it will discuss ionomers as a thin film within the CL. Although, the cathode/membrane interface has a large impact on performance.[195,196] Proton transport within the CL has also been reported to be supplemented by localized liquid water, which can act as a proton transport medium independent of the ionomer.[50,58,197] This can be seen in FPE[50] or nanostructured thin film (NSTF) electrodes which are designed to operate without ionomer in the CL and instead utilize only localized water to transfer protons.[52,61,197–200]

The ORR requires reagents to approach and adsorb onto the electrode surface, followed by a charge transfer between reactants and electrode and the resulting product to desorb from the electrode surface. Due to the competition for space on the surface of the catalyst, the structure and arrangement of the ionomer can have a serious effect on reactant transport, catalyst utilization, and durability.[201] Reducing the resistance to reactant diffusion and proton and electron conduction through the CL network improves the voltage and power density in the mass transport regime. Therefore, the nano- and micro-structure of the ionomer and relating physicochemical phenomena responsible for transport must be well understood. This knowledge of the structure–performance relationship can inform modification of the catalyst composition and morphology and allow researchers to develop efficient catalyst/ionomer support

interactions with optimum catalyst utilization and improved electrode performance.

3.2. Thin Film Morphology

Many morphological models of bulk Nafion have been proposed based on a variety of scattering, spectroscopy, and microscopy techniques. These include water-rich clusters that evolve into channels at high humidity,[202] water cylinders in a polymer matrix,[203] and elongated polymer aggregates that bundle,[204] possibly into ribbon-like units.[205] The structure and properties of Nafion confined to the nanoscale are significantly different from the bulk, and its exact structure and behavior is still not precisely understood.[206] The lack of certainty regarding mechanisms within Nafion thin films present in the CL has led to many studies using thin-film model samples to probe the analogous structures occurring at these low dimensions.[192,193,207] The morphology has been widely reported to change significantly across different length scales.[192,193,207,208] As thin films of Nafion become confined, self-assembly becomes constrained compared to bulk Nafion,[193,207] resulting in the hydrophobic and hydrophilic domains becoming more intermixed than in bulk Nafion.[209] Transport of active species is closely tied to the Nafion morphology, specifically the ionic domains that swell upon hydration and allow proton conduction, but also free volume and interfacial structuring that affect gas diffusion.[210] In addition to the complex morphology of Nafion, the ionic domain structure, chain dynamics, and mobility have a significant effect on functional properties such as the glass transition, water uptake (WU), mechanical properties, and anisotropic ionic conductivity.[17] Fabrication methods, including mode of deposition and thermal processing, can have

additional effects on the structure, which affects functionality within the electrode and thus fuel cell performance.[211] Therefore, it is imperative to achieve a complete understanding of the differences in the morphology of thin-film and bulk Nafion to comprehend the proton-conducting and mechanical properties present in optimized CL with varied catalyst and support chemistries. Over the past decade, significant work has elucidated the structures of thin-film ionomers based upon varying substrate, choice of deposition technique, thickness, processing, and environmental conditions. This has been achieved by the use of a range of techniques including neutron reflectivity (NR),[211,212] grazing-incidence small-angle X-ray scattering (GISAXS),[213] ellipsometry,[210] and quartz crystal microbalance (QCM).[192]

The separation of bulk-like properties and properties due to dimensional confinement and surface interactions has been demonstrated to start at around 60 nm.[192,211] Films between 12 and 60 nm, known as the "thin film regime", consist of a lamellae layer at the substrate interface and a layer of 3D phase-separated Nafion, with internal structure influenced by interactions with the substrate. Nafion assembled on a surface, that is, within the catalyst agglomerates, has been characterized as forming three thickness-dependent morphologies with varying degrees of ordering, as shown in **Figure 11**.[192] Quoted as the "truncated regime" by Dura et al.,[212] the morphology of films <12 nm are dominated by side-chain and sulfonate group interaction with the substrate resulting in in-plane orientation of polymer chains and multiple layered lamellae forming in extreme cases. This leads to polymer chains favoring alignment parallel to the surface, and hydrophilic sulfonic groups encouraged to orient toward the air–film interfaces.[192,207,214] The "thick-film" regime encompasses films >60 nm, which are composed of the two prior structures and an additional "bulk-like" layer. This "bulk-like" layer has properties and morphology
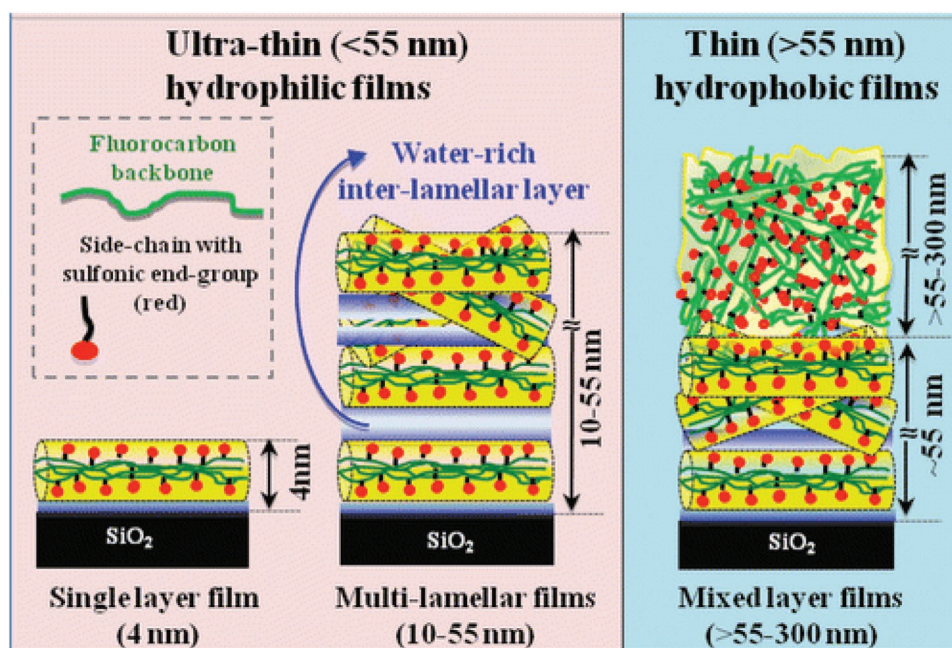
Figure 11. Proposed thickness–dependent nanostructure of ultrathin and thin Nafion films from 4–300 nm. Reproduced with permission.[192] Copyright 2013, American Chemical Society.

**ADVANCED
SCIENCE NEWS**

www.advancedsciencenews.com

**ADVANCED
ENERGY
MATERIALS**

www.advenergymat.de

equivalent to bulk Nafion, which remains relatively constant at all thicknesses greater than 60 nm, until the surface of the layer where a thin, hydrophobic, backbone-dominated layer forms, as is observed in bulk samples.[211] All Nafion films, regardless of thickness, exhibit the interfacial lamellae region. Therefore, understanding this lamellar region is imperative to the understanding of electrochemcial processes occuring at the TPB of fuel cell electrodes.
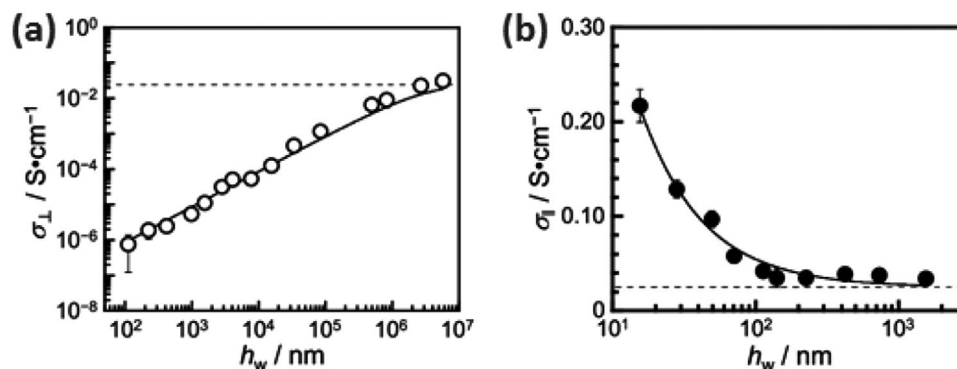
The lamellae region at the interface between a substrate and bulk Nafion is caused by a phase separation that develops few-nanometer, sheet-like crystallites that orient in-plane with the substrate. **Figure 12** shows the complex structure at the lamellae region, which is an interplay between ionomer/substrate interactions and water/ionomer interactions. The phase segregated ionomer structure is "locked into" the film, due to low mobility of the polymer groups under dry conditions. For hydrophilic substrates, such as SiO or PtO, the first lamella (in contact with the substrate), composed of primarily water when hydrated, is followed by a backbone-dominated water poor lamella. The side chains associated with the Nafion backbones in the second layer protrude through the first water-dominated lamella, and sulfonate groups interact with the hydrophilic substrate. The lamellae (1.5–2 nm) repeat with alternating water-rich, side chain-dominated layers, and water-poor lamella, with SO_3H groups lining the interfaces between the two. However, the exact crystallite structure is dependent on substrate and ionomer, as well as environmental condition. For example, when assembled on hydrophobic carbons the orientation of polymer chains is observed to be flipped so that the hydrophobic backbone component is in contact with the substrate.[215,216] The Nafion lamellae becomes less structured, with reduced phase separation away from the substrate, as the morphology is no longer defined by the surface interaction with the substrate, shown in Figure 11. Under dry conditions, a lack of internal water induces less phase separation, resulting in fewer lamellae layers.[215] Hydrophilic interactions entrap residual water molecules in the first lamella, but subsequent dehydrated side chain-dominated layers possess unfilled pores with limited side-chain mobility and low density. At RH between 0% and 100%, intermediate structures with increasing number and thickness of lamella are observed. The transition where structures resembles that in the fully hydrated state is 60–70% RH, this is in agreement with the RH where bulk-like water forms in bulk nafion.[24,213]

Molecular dynamics (MD) calculations of carbon agglomerates within a CL verified the existence of the lamellae structure with alternating hydrophobic and hydrophilic regions at the surface. The lamellae structure with tightly bound water and interfacial layering parallel to the substrate results in anisotropic tortuosity.[217] The formation of these structures favors water transport parallel to the substrate over the perpendicular direction and results in interfacial impedance in the electrode.[218,219]
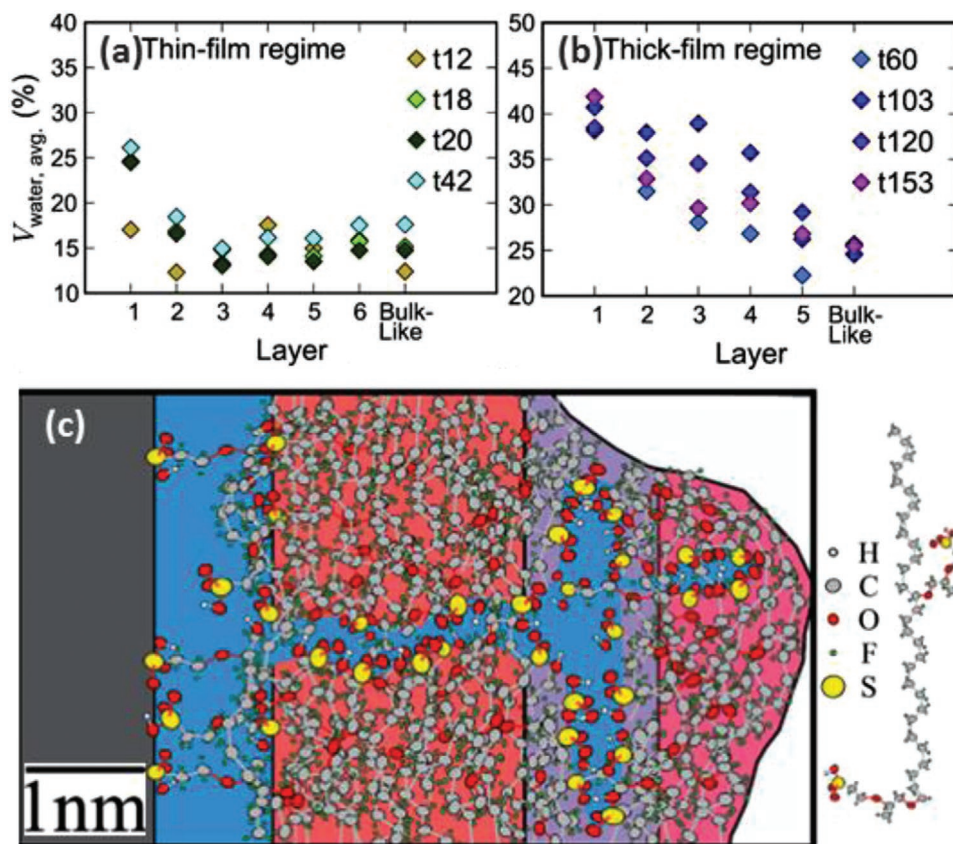
Figure 12. "Local average" water content in Nafion lamellae on SiO_x substrate, as a function of layer number in a) thin-film regime b) thick-film regime, where t12 denotes a 12 nm film. Reproduced with permission.[211] Copyright 2018, Elsevier. c) Proposed atomistic physical model of truncated Nafion on SiO_x, based on NR composition depth-profile. Adapted with permission.[215] Copyright 2005, The Royal Society of Chemistry.

ADVANCED
SCIENCE NEWS
www.advancedsciencenews.com

ADVANCED
ENERGY
MATERIALS
www.advenergymat.de

Figure 13. Plots of proton conductivity versus thin film thickness at 100% RH with dotted line showing proton conductivity of bulk Nafion. a) Through-plane conductivity proportional to thickness, while b) in-plane conductivity inversely proportional to thickness, demonstrating the effect of internal morphology with dimensional changes. Adapted with permission.[219] Copyright 2018, American Chemical Society.

Average film conductivity is highly dependent on thickness of this Nafion lamellae, with experimental and modeling studies observing water and thus hydronium ion transport widely fluctuating based on lamellae thickness and water-poor or -rich layer termination.[220] Increased interconnection of domains led to a ≈7 nm thick water-rich lamellae having the greatest and most isotropic dynamics. In contrast, lowest conductivities in the water-poor ≈5 nm lamellae were a result of both tightly bound water molecules and the continuous and impervious hydrophobic Nafion "skin" at the second lamella restricting through plane water connectivity.[212] The linear hydrophilic channels reported in 2.4 nm films likely provide a sufficient transport pathway.[220] This exemplifies the importance of an in-depth understanding of how the substrate/Nafion interactions defines the nanoscale structure and the resulting transport properties of the ionomeric binder and thus PEFC electrode.
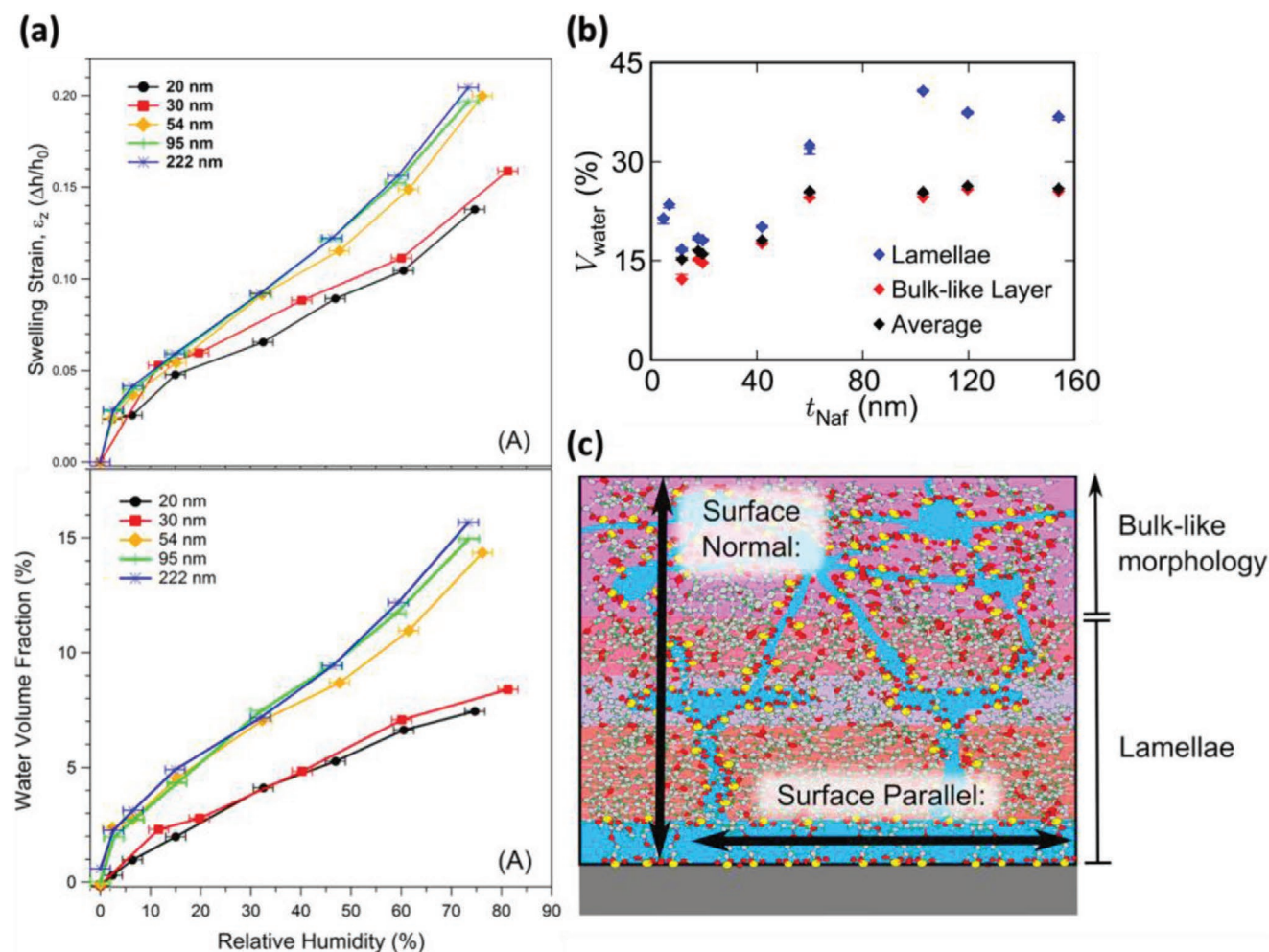
3.3. Thickness-Dependent Morphology

Film thickness impacts the internal film structure and degree of order, with thicker, less-confined films allowing the ionic domains to assume a more ordered and phase-separated structure. However, below 60 nm, interaction with the substrate results in frustrated packing of ionic domains and poor connection between hydrophilic phases, with non-uniform spatial distribution having a significant effect on swelling.[192] Using GISAXS, Eastman et al.[213] found that domains parallel with the substrate swell for all increases in RH, whereas domains perpendicular to the substrate swell only for RH increases above 60%. Above 60% RH, hydration of the interfacial layers reduces confining interactions and polymer plasticization induces 3D swelling of network channels. This non-affine swelling confirms that "thin films" are likely composed of an assembly of locally ordered flat domains that orient favorably in plane with the substrate, and this ordering decreases as the film exceeds 50–60 nm, at which point the matrix adopts a "bulk-like" phase separation.[24]

WU has a profound effect on the proton conduction of Nafion and the impeded transport properties of Nafion thin films are speculated to mainly arise from a poorer WU.[221,222] In bulk Nafion, separate conduction mechanisms are observed depending on λ (number of water molecules per sulfonate group).[24] At low water content ($\lambda < 2$), hydronium ions are tightly bound to the sulfonate groups and possess low mobility vehicular diffusion due to an incomplete hydrogen bond network. At intermediate water content ($2 < \lambda < 6$), the hydration shell grows forming more complex protonic species (Eigen and Zundel ions) and the hydrophilic domains swell to form a percolated network allowing long-range proton conduction via the Grotthuss mechanism. At high water content ($\lambda > 6$), Grotthuss mechanism hydronium transport dominates as the domains swell to accommodate bulk-water. It is thus critical to attain a comprehensive understanding of the WU and environment within thin films to understand their transport properties.

For thin films, interaction with the substrate leads to greater mechanical forces and a greater elastic modulus, which counteracts the thermodynamic drive for hydration, resulting in a lower WU for thinner films. A gradient in elastic modulus, decreasing further from the substrate, results in a gradient of water distribution with greater WU away from the substrate.[210,223,224] As the sample becomes thinner, domain size, free volume, polymer chain mobility, water content, and ordering decreases, with larger separations and less connections having a detrimental influence on anisotropic internal water mobility and proton diffusion, as shown in **Figure 13**.[213,217] **Figure 14**a demonstrates the total film WU and swelling at films of different thicknesses while Figure 14b provides isolated WU characteristics of the individual film components as total thickness varies, showing comparable results from studies using different techniques. In the "thick film" regime, WU in the lamellae remain roughly constant with the thickness increase, while it increases slightly in the "bulk like" layer. In the "thin film" regime, decreasing film thickness from 60 to 12 nm leads to a linear decrease in WU to the "bulk like" layer, but an abrupt and flattening-off decrease to the lamellae layer. The film's modulus gradient means that as the thickness decreases, and thus the proportion of material in the more confined near interface region (>12 nm) increases, overall WU decreases. Films in the "truncated" regime have significantly greater swelling and WU due to significant in-plane phase separation of hydrophilic and hydrophobic domains.[207] WU and swelling of the lamellae region is influenced by interactions with the substrate, bulk-like layer, and vapor surface. As shown in Figure 14, this results

**ADVANCED
SCIENCE NEWS**

www.advancedsciencenews.com

**ADVANCED
ENERGY
MATERIALS**

www.advenergymat.de

Figure 14. a) Swelling strain and water volume fraction determined for Nafion films of 20–222 nm as a function of RH measured from XR. Adapted with permission.[213] Copyright 2012, American Chemical Society. b) Water volume fraction as a function of Nafion thickness, including the interfacial lamellae, bulk-like layer, and whole-film average. c) Schematic illustration of Nafion thin-film structure at a hydrophilic interface, including the sheet-like lamellae and well-mixed, bulk-like outer layer. Adapted with permission.[211] Copyright 2018, Elsevier.

in lamellae WU changing from 23% for films in the truncated regime, to 17% in the thin-film regime, increasing slightly as the bulk-like layer reaches 60 nm, and increases to a relatively constant 35% in the thick-film regime.[211] While these values are obtained by ill-posed model fits (those with no unique solutions), constraining the fitting process by observing changes in an environment of light and heavy water and corroboration with other experimental techniques suggest that the general trend observed is accurate. It was found using MD simulations that thicker (2 and 3 nm) films have more contact points on the carbon support than 1 nm films and were thus less prone to "ball up" and form an inhomogeneous ionomer distribution revealing bare carbon surface.[225] This resulted in the 2 nm film retaining over double the water content of the 1 nm film at the same hydration level.

The presence of Pt NPs on the carbon surface changes the Nafion orientation due to strong interaction of sulfonic sites with Pt; this results in the hydrophilic domains of the ionomer connecting to the catalyst NP.[226] This hydrophilic region of ionomer causes a considerable number of water molecules to relocate close to the Pt NP in a favorable water cluster, and generally causing higher water retention of the film. This may provide a route for proton (and oxygen) to access the catalyst preferentially over the support. A similar phenomenon is observed upon Pt oxidation, with considerable preferential re-arrangement of sulfonate groups around the Pt.[225] Since poor coverage and water retention are suggested as the major reasons for poor proton transport and utilization of catalyst NPs, closer interactions between both water and Nafion to the Pt would be expected to improve performance.[227]

The performance and durability of a fuel cell can change significantly if the ion conducting network is disrupted or is assembled with different by film dimension and confinement.[228,229] As shown in Figure 13, the proton conductivity of Nafion films decreases with film thickness, with 100 nm thick films having conductivity an order of magnitude lower than, and activation energy twice that of bulk Nafion.[193,208,221] The relationship between λ and conductivity varies with distance

from the substrate. Due to orientational phase separation, through-plane ion conductivity is significantly limited in all layers, but it is highest at the substrate interface due to the lamellae. As the Nafion phase becomes thicker and transport becomes more isotropic, the difference between in- and out-of-plane transport decreases and becomes mostly negligible in the film volume >60 nm.[213] As the film expands with WU, increases in hydrophilic domain size and water volume fraction lead to development of more proton conducting pathways and loss of tortuosity, resembling the percolation threshold in bulk Nafion.[210] In regions thicker than the "thin film" regime, ionic domain morphology is similar to bulk Nafion with reduced anisotropic ordering, but the effect of dimensional confinement still suppresses the conductivity by restricting the mobility of the polymer chains. The significantly different morphologies and WU result in truncated films (5–10 nm) having an order of magnitude lower proton conductivity than thin films (50–160 nm).[230] Investigations using nuclear magnetic resonance (NMR) revealed equivalent local water dynamics for both 10 and 160 nm films characteristic of water that has exceeded the percolation threshold but without bulk water present.[231] While poor thin film conductivity could be a result of this lack of bulk water for effective Grotthus diffusion compared to bulk films, the same water environments in truncated versus thin film regimes could not be assigned as the cause of their differing conductivity. Therefore, it is more likely to be an effect of morphology and structuring within the water domains and polymer matrix that limit hydronium ion transport for truncated films. In the truncated regime, restricted chain dynamics and insufficient sulfonate group aggregation, leading to poorer domain formation, may collectively impede proton transport. Additionally, Paul et al.[208] also suggest that the mechanism of proton conduction in Nafion thin-films could be fundamentally different to bulk Nafion occurring by surface diffusion, rather than via the Grotthuss mechanism in the water phase. Further investigation is required to reveal these true atomic scale phenomena.

It is very important to note that while through-plane conductivities have been reported to be greater in thicker 'thin films', the total resistance to proton transport through ionomer films will be roughly proportional to the total diffusion distance, that is, the film thickness. Therefore, films in the "truncated" regime, with a shorter diffusion distance (<10 nm), minimize transport losses and thus a low Nafion content in the electrode that achieves these dimensions are a promising strategy to enhance performance.[211] Other transport resistances, such as gas transport resistance, will be impacted by Nafion film thickness and therefore their influence on performance and must be considered. A covering ionomer layer of ≈7 nm has repeatedly been identified as having high proton conductivity and exhibits the additional benefits of reduced gas transport resistance.[232] However, the offset between these effects is complex and dependent on the individual environments. For example, 60 nm films have been reported to have lower proton resistance than 42 nm films, and 200 nm films have been observed to have greater through-plane proton conductivity than both thinner and thicker layers.[233] This is likely an effect of the differing nanostructures and suggests that reducing the ionomer content in the CL to minimize proton resistance will only be successful if the covering ionomer films are homogenously maintained at ≈10 nm, rather than the heterogeneous layering commonly observed with areas <10 nm and >50 nm.

3.4. O$_2$ Diffusion Limitations and Low Pt Loading

One long-explored method to increase cost effectiveness of Pt-based CLs is reduction of Pt loading.[58,235,236] A trade-off between MEA costs and current density will define the Pt loading and fuel cell stack size, that is appropriate for different applications. The US DoE 2020 targets for Pt group metal loading on the anode and cathode combined is 0.125 mg$_{Pt}$ cm^{-2}.[234] However, with decreasing catalyst loading, an over-linear increase in transport resistance is observed, which significantly limits the performance of low loading Pt electrodes.[58,60,237–239] **Figure 15** shows that as Pt loading decreases, O$_2$ transport resistances increase.[237] At ultra-low Pt loading (roughness factor), O$_2$ transport resistance becomes the dominant factor causing performance loss.[236] This resistance has been simulated to cause just under half of the mass-transport voltage losses on a fuel cell operating at 1.75 A cm^{-2}, with 0.1 mg$_{Pt}$ cm^{-2}.[235] This effect has been reported to scale with available Pt surface area per cm^2 of MEA,[236,237,240–242] but is not related to the turnover frequency and is not a kinetic resistance.[235,237] Overcoming this transport resistance is necessary for achieving high performance in low Pt loading MEAs, one of the main routes to large scale commercialization of fuel cell technology.

The cause of O$_2$ diffusion limitations is widely reported to be related to the oxygen flux through the thin film ionomer coating on the Pt catalyst particles.[52,58,79,235,237–239] In addition, models of electrodes with identical overall Pt loading, but with different thickness have been reported to show the same O2 interfacial resistance increase as seen in thin low-Pt loaded electrodes, suggested to be also due to increased local O$_2$ flux.[228] However, a definitive effect of film thickness on O$_2$ diffusion eludes researchers due to the lack of control over
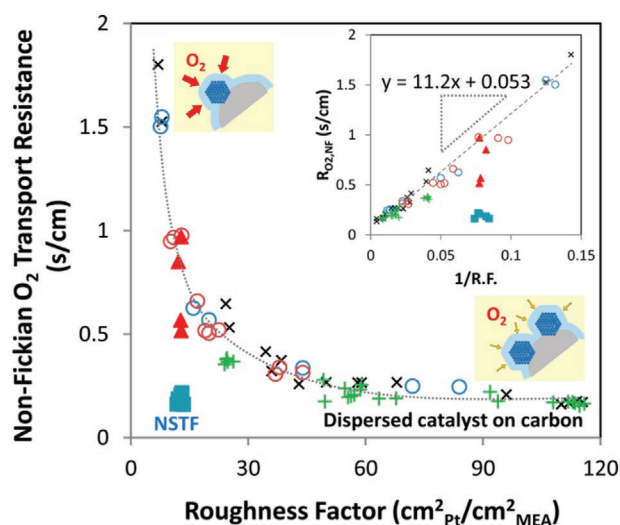

Figure 15. O$_2$ transport resistance dependence on specific current density or roughness factor. Reproduced with permission.[235] Copyright 2016, American Chemical Society.

ionomer homogeneity in the CL and variations in experimental setups.[237,243,244] Oxygen is speculated to diffuse via both free volume and hydrated hydrophilic domains in the ionomer bulk. As the Pt loading decreases, there is less catalyst surface area available, so a greater local O_2 flux is required to achieve the same current densities. It is the increased resistance caused by the additional O_2 flux that reduces performance.[245] Using small angle neutron scattering (SANS), Yoshimune et al.[246] showed that the ionomer shell layer adsorbed onto the PtC surface became thinner and denser with decreased Pt loading. The stronger hydrophobic interactions that occur between carbon and Nafion increase with lower Pt loading, leading to densification of the ionomer layer and thus poorer phase separation, impeding gas diffusivity via the minimal free volume.[247] Adding to the complexity of this system, it has been reported that the O_2 diffusion limiting process takes places at the Pt/Nafion interface, which has been reported to have diffusion resistance equivalent to 40–70 nm of Nafion, likely due to the lamellae phase separation.[61,235,243] Thinner films with lower WU have reduced swelling of hydrophilic domains, reducing the number of interconnected oxygen diffusivity pathways through the Nafion thin film.[248,249] However, the smaller oxygen diffusion distance in thinner Nafion layers has been reported to reduce O_2 diffusion resistance.[58,77,228,238] Oxygen transport resistance has been observed to decrease with increasing RH, due to lower interfacial resistance at the hydrated Pt–ionomer interface.[210,243] It may be considered that high interfacial water would reduce free volume at the interface because of strong affinities between ionomer, water, and Pt and therefore be detrimental.[250] However, as observed by neutron reflectivity (NR) investigations, the dry state mobility of the ionomer on the surface of the catalyst is reduced, which forces it to become a blocking layer to O_2 diffusion. The orientation of sulfonate groups to the Pt surface, via water molecules, has been shown to suppress O_2 adsorption resulting in reduced effective surface area of Pt.[251] Utilizing ionomers and supports with weaker adsorbing functional groups and short side chain ionomers could help reduce the formation of dense ionomer layers that impede O_2 transport and catalyst activity.[235,248] It is not clear which combination of these factors (Nafion layer thickness, density, and water content) has the most impact on O_2 diffusion resistance. Appropriate ionomer thickness, ionomer chemistries with higher WU, and pre-treatment may circumvent the O_2 diffusion issues on low Pt loaded CL.[224]

An alternative explanation for transport resistance at low Pt loadings has been proposed by Muzaffar et al,[50] who dispute the widely reported theory that transport resistance is caused only by limitations to the O_2 diffusion through the Nafion coating of the catalyst. It has been previously suggested via simple analysis of the surface area of the catalyst/support aggregates compared with the thickness of the ionomer layer that Nafion does not completely coat the catalyst particle surface.[252,253] While this analysis assumes an even distribution of ionomer across the support particles and no coalescence around Pt particles, many studies have reported that a significant proportion of Pt is not completely coated with ionomer.[248,252–254] On the other hand, catalyst particles in the porous aggregates are often not connected to the Nafion ionomer network, but still electrochemically active due to the water-filled pores.[209,255] NSTF electrodes have clearly shown that high current densities can be achieved using only water as the proton conductor.[50–52] However, since O_2 diffusion through water is slower than through air, excess localized liquid water can limit O_2 diffusion. Muzaffar et al.[50] suggest that the model of transport resistance-limited O_2 diffusion occurring only through the Pt-ionomer interface is insufficient, as the alternative proton conductivity pathway offered by localized water is largely ignored. Furthermore, the degree of ionomer coating is expected to be dependent on the support material functionalization, operating conditions, and ionomer content. In-depth analysis from neutron techniques or electron tomography is required to understand this ionomer-Pt interface and distribution. This analysis is key to determine if O_2 diffusion limitations stem entirely from transport through ionomer coating or if there is a significant contribution from O_2 diffusion through localized liquid water.

Muzaffar et al.[50] suggested the reduction in Pt loading creates CLs with reduced volume, which significantly affects the ratio between the rate of water vaporization and the rate of water generation within the layer, as shown in **Figure 16**.[50] This problem of water accumulation is made worse by increased local water content reducing the water removal rate,[146] resulting in the CL flooding as it is made thinner.[58,59] Thin, low-Pt loaded electrodes have been reported to be more prone to water management problems.[50,51,239] Hence, it is suggested the O_2 transport limitations are caused by the extended water diffusion pathways to the surface of the catalyst. This hypothesis suggests that thin CLs are more prone to flooding, and as such, water management is a high priority
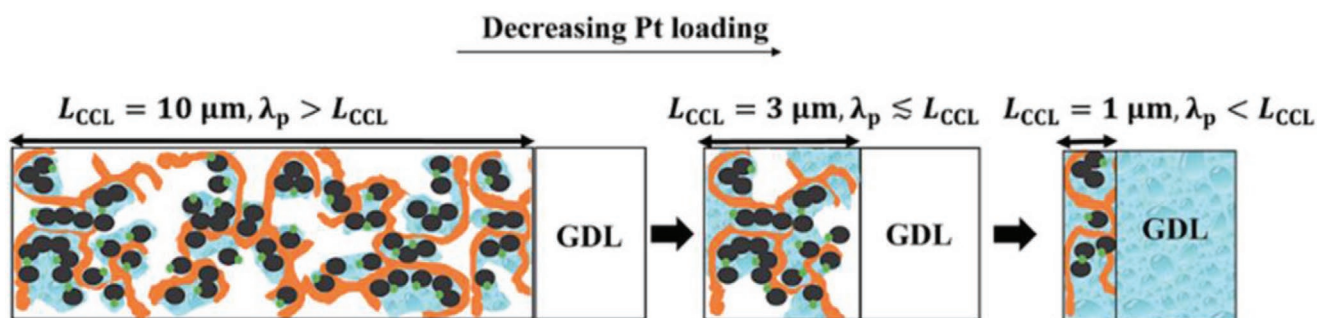
Figure 16. Schematic of water accumulation in the CL and GDL for electrodes of different thicknesses. Adapted with permission.[50] Copyright 2018, Royal Society of Chemistry.

ADVANCED
SCIENCE NEWS
www.advancedsciencenews.com

ADVANCED
ENERGY
MATERIALS
www.advenergymat.de

for low Pt loading electrodes. Models of very thin cathode CLs have reported limited current density due to oxygen transport resistance being inversely proportional to the thickness, with thinner CLs having lower currents.[256] Furthermore, other CL models have reported through-plane oxygen diffusivity limitations, from which they concluded that the electrodes are partially flooded.[239] It is key to the future development of low-Pt loaded electrodes to determine if water management is an independent, but still detrimental factor to electrode performance, or if flooding in thin CLs is the main cause of O_2 transport resistance.[50]

3.5. Role of Solvent in CL Structure

CL fabrication requires the use of ink composed of catalyst, support particles, ionomer, and solvent, which is deposited onto the substrate, dried, and sometimes exposed to further treatment. The formation of primary ionomer aggregates of varying size, shape, and dispersion, is dependent on solvent properties such as viscosity, dielectric constant (polarity), and surface tension. This influences how they interact with the catalyst and support particles, covering or penetrating and forming catalyst aggregates, or remaining as free ionomer. An appropriate dispersing medium (solvent) is required to tune the properties of the catalyst-ionomer interface. Solvent optimization is dependent on physicochemical properties of all ink components and must appropriately wet and stabilize the dispersion for useable ink. A complementary deposition method is also required to form appropriate CL structure. The ink structure is determined by nano-scale interactions of ionomer-solvent,[257] catalyst-ionomer,[258] and catalyst-solvent.[259] The DLVO (Derjaguin, Landau, Verwey, and Overbeek) model can be used to explain these multifarious interactions occurring in the ink leading to catalyst particle agglomeration, and should be considered when designing an experimental procedure.[260] For example, if electrostatic repulsion due to surface charges is sufficiently greater than Van der Waals attraction, the size of the particles remain small, but if Van der Waals attraction exceeds electrostatic repulsion, then particle aggregation produces larger particles resulting in an unstable ink and poorly performing heterogeneous CL.[259]

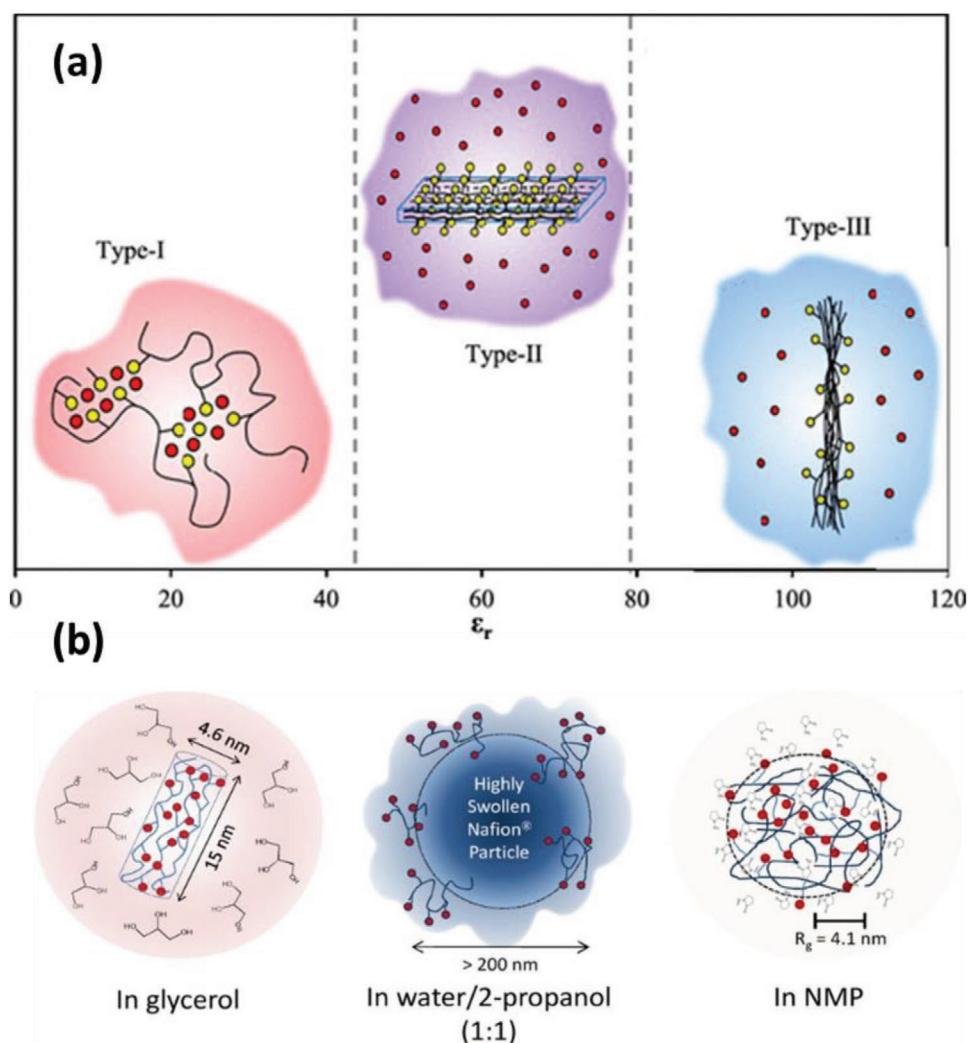#### 3.5.1. Ionomer Aggregate Structure

The solvent plays a key role in defining the shape and size of the ionomer aggregates in solution or suspension, due to the significant impact that polarity has on Nafion–solvent and Nafion–Nafion interactions.[261] PFSA-based ionomers are amphiphilic, hence the hydrophobic backbone has greater affinity to hydrophobic solvents, the ionic side chains have a greater affinity to hydrophilic solvents. Furthermore, ionic moieties (SO_3^-) with strong ionic interactions can further influence the molecular assembly. Therefore, the type and composition of the solvent determines the ionomer conformation and ion pair clustering, which then affects the morphology (size and shape) of the primary ionomer aggregates. A secondary aggregation produces larger particles based on the electrostatic interactions of side

chain ion pairs. The self-assembled ionomer structure in dilute solutions is the initial aggregation state for solution processing and has been shown to correlate with ionomer membrane morphology by Lin et al.,[262] who compared dynamic light scattering (DLS) with differential scanning calorimetry (DSC) and small angle X-ray scattering (SAXS). Aliphatic alcohol/water solutions exhibited larger aggregates and produced membranes with greater phase separation due to poor solvent-backbone compatibility. In contrast, DMF solutions showed molecular aggregates with reduced size and reduced phase separation because of the high compatibility with backbone and side chain. More recently an in situ GISAXS investigation by Dudenas et al.[263] directly observed the molecular transition of ionomer aggregates from dispersion phase to domain network during assembly of a 100 nm thin film. As the solvent evaporate over the first 50 s, the solution concentrated, inducing further primary particle aggregation with a decrease in d-spacing between cylindrical aggregates (≈0.8 nm radius backbone core with ≈1.8 nm side chain shell) from 12 to 6 nm. Concurrently crystallization is observed with a preferential alignment of crystallites through-plane. This is followed by formation of the ionomer peak, with a separation of ≈3 nm, indicating formation of the polymer network from ionomer aggregates. This directly demonstrates how the aggregate interactions in solution evolve into the film morphology. Subsequent gradual increase in domain spacing suggests coalescence of hydrophilic domains into fewer, but larger domains. Repeating the experiment with three water-alcohol ratios showed markedly different transitions from solution to film with varying interaction strengths and degrees of aggregate ordering. This study relates how the aggregate structure pre-determines the thin film morphology, corroborating models proposed previously, and consolidates the importance in understanding ionomer-solvent properties to CL structure.[192,211,213]

The solvent dielectric constant, (ε), has a large influence on conformation and size of PFSA ionomer aggregates by affecting the degree of ionic clustering.[257] The solvation characteristics of Nafion in 71 solvents were classified by Uchida et al.[264] as i) soluble ($\varepsilon > 10$), ii) dispersed ($3 < \varepsilon \leq 10$), or iii) precipitated ($\varepsilon < 3$), with the general conclusion that greater ε better solvates and thus reduces the size of ionomer aggregates. Direct methanol fuel cell performance was reported to be higher for CLs fabricated using low ε solvents, such as dipropyl ketone ($\varepsilon = 12.60$) and n-butyl acetate ($\varepsilon = 5.01$), which was attributed to the larger catalyst aggregates forming larger secondary pores with improved mass transport.[265] Using mixed solvents, all considered in the "soluble regime"[264] ranging from $\varepsilon = 74.9$ to $\varepsilon = 16.5$, obeyed the same trend of improved CL performance with decreasing dielectric constant, with highest performing being an ethanol:butyl-acetate:glycerol (45:40:15) composition of $\varepsilon = 16.5$.[266] This low ε solvent also facilitated impregnation of ionomer into the porous hydrophobic GDL during fabrication, providing a uniform structure, rather than highly polar solvents that remained at the surface of the GDL and had reduced intermixing.

While correlation of fuel cell performance with solvent properties has revealed insight to CL ink requirements, atomic-scale observation of the solvent-ionomer interactions provides a rigorous understanding of the factors that provide such performance. A MD study by Tarokh et al.[267] characterized the chain

**ADVANCED
SCIENCE NEWS**

www.advancedsciencenews.com

**ADVANCED
ENERGY
MATERIALS**

www.advenergymat.de

Figure 17. Aggregation phase diagram of Nafion in a) dispersions as a function of solvent dielectric media. Adapted with permission.[267] Copyright 2019, American Chemical Society. b) In glycerol and in ethylene glycol, water/isopropanol mixtures, and NMP. Adapted with permission.[269] Copyright 2012, American Chemical Society.

conformation and assembly, aggregate and ion-pair cluster shape and size, as well as inter-cluster distances of dispersions in solvents of varying ε and solubility parameter. This gives rise to variations in aggregate density and shape at specific ε ranges, as shown in **Figure 17**. For low ε solvents, hydrophobic-solvent interactions with the ionomer backbone dominate. Furthermore, the stronger attractive electrostatic interactions between SO_3^-/H_3O^+ ion pairs compared to the solvent-SO_3^- promote ionomer aggregation. This led to increased cross-linking and strong multipole–multipole interactions between ion-pair clusters forming aggregation of hydrophilic interiors and hydrophobic exteriors.[268] These interactions weaken with an increase in solvent polarity, such as with glycerol and formic acid, (42.5 < ε < 51.1), which increases shielding of charges between the ion-pairs. The balance of hydrophobic and hydrophilic attractive forces increases the dispersion of backbones and hydrophilic heads of the ionomer, which allows self-assembly into solvent-swollen 2D aggregates. For high polarity solvents (ε > 79, such as water and formamide), the hydrophilic tail of

the ionomer-solvent interactions are very strong and dominate. Combined with enhanced hydrophobicity of the solvent, the ionomer forms tightly packed elongated backbone aggregate with non-clustered sulfonic acid groups protruding into the solvent. The lamellar structure and tight aggregation formed in the mid-high ε solvents would likely provide more abrupt phase separation for proton and water transport, but the study provides no performance data. Previous solvent-dependent performance studies attributed benefits of low polarity solvents to gas transport in the large pores formed between larger aggregates,[265] but this study suggests that in addition, the less crystalline ionomer structure provides facile gas transport. These fundamental studies are particularly imperative for investigating CL components to minimize variable factors. Further research is required to understand how significantly the ionomer aggregate structure in the ink impacts the ionomer distribution and performance in the dried CL.

The aggregate structures formed can have a significant effect on performance and durability of the CL. Kim et al.[56] found

ADVANCED
SCIENCE NEWS
www.advancedsciencenews.com

ADVANCED
ENERGY
MATERIALS
www.advenergymat.de

that the use of glycerol as an ink solvent resulted in reduced degradation of the CL under AST, in line with the aggregates formed in solution. The large aggregates and inability to form polymer entanglements in water–alcohol solvents produced an electrode with numerous large-scale open cracks (>100 μm) and low mechanical strength. In contrast, aprotic polar solvents, such as NMP and DMF, can solvate the polymer backbone allowing polymer chain entanglements to give true solution behavior, forming random-coil conformations with a 41 Å radius of gyration.[269] Owing to the better solvent compatibility, fewer Nafion molecules aggregate, and this structure is transferred to the cast membranes with smaller phase-separated hydrophilic and hydrophobic domains.[215,262] The highly solvated polymer chains in NMP thus produced a crack-free, yet coarse microstructure in the CL. Polyhydric alcohols, such as glycerol and ethylene glycol, cannot completely solvate the polymer chain but, due to the number of alcohol groups, can disperse the Nafion in the form of very small, well-defined, cylindrical, rod-like structure with a radius of 22 Å and length of 150 Å.[269] The small micelles combined with the slow evaporation of glycerol enabled polymer mobility to be retained as the electrode dried, so that chain entanglements formed to give an intermediate mechanical strength and dispersed micro-cracks (<10 μm). It was found that once the mechanical stability was sufficient, as is the case for NMP and glycerol, other solvent factors determine CL degradation. Glycerol-cast electrodes form a favorable side-chain–Pt interface, leaving ionomer free to reorient during long-term testing, achieving better durability. In comparison, the strong solvation of both side and main chain in NMP produces highly mixed chains in the electrodes, and thus poor availability of side chains for TPB formation during electrode restructuring, agreeing with the "positive structural change" observed by Choi et al.[195] The exact nature of the interactions of ionomer with glycerol versus NMP and how they result in differing dynamic ionomer–Pt interactions are not clear from this study, and reinforce the need for further fundamental investigation of these systems.

3.5.2. Binary Solvents

Binary solvents containing both alcohol and water are the most common choice for catalyst ink preparation, due to their ease of use, low cost, and minimal toxicity.[192] The polar nature of water leads to a strong tendency for the backbones to aggregate via hydrophobic interactions,[270] whereas alcohols are considered to be moderate solvents for the fluorocarbon backbones. While 1.2 – 2.6 nm rod-like aggregates have been observed in pure water or pure ethanol,[271] a combination of these solvents is used to prevent the formation of inhomogeneous Nafion films.[192] The exact alcohol/water composition has a significant influence on the size, shape, and dispersion of nano-aggregates and their bundles. Park et al.[270] found the distances between aggregates to decrease from 25 nm in pure water to 20 nm above 50 mol% IPA or ethanol and ≈17 nm in 10–50 mol% IPA or ethanol. Water–methanol mixtures have been found to contain spherical aggregates,[272] in contrast to the rod-like nanoaggregate in water-1-propanol mixtures.[270] Studies have also shown alcohol–water solutions to exhibit nanophase

segregation of solvent, which is driven by PFSA's surfactant-like hydrophilic/hydrophobic character.[267,269] Despite the variation in the literature, consensus has built around the simplified model of binary solvents exhibiting rod-like nano-aggregates, on the order of 50 nm,[273] in which the non-polar backbones constitute the core of the aggregates while the anionic groups sit at the aggregate–solvent interface.[273–275]

The alcohol fraction in the solvent and the ionomer concentration heavily influence the size of the ionomer bundles and thus have a significant effect on CL performance. Mabuchi et al.[274] reported that higher ionomer concentration caused the number of Nafion chains in the aggregate and the aggregate size to increase, as shown in **Figure 18**. The effect of solvent ratio on aggregate size was also dependent on ionomer concentration, due to competing effects of dielectric constant and hydronium ion distribution. At ionomer concentrations below 5 wt% (common in CL fabrication), most of the hydronium ions are dispersed and repulsive interactions among the negatively charged sulfonate groups are dominant. In a high water content, poorly solvated backbones and side chain repulsion induce larger aggregates with side chains externally orientated to avoid interaction. On the other hand, increasing alcohol content with greater ability to solvate backbones disfavors aggregation, resulting in increased dispersion of smaller primary aggregates. In contrast to this dielectric constant effect, at high ionomer concentration (≥7.5 wt%), hydronium ions are strongly localized with the anionic groups and thus reduce the electrostatic repulsion between sulfonate groups. This favors aggregation and leads to significant aggregate expansion at high alcohol content. While catalyst inks are rarely composed of such high ionomer concentrations, it is worth considering the effect of ionomer concentration on molecular arrangement, as solvent evaporation during the drying process leads to gradual ionomer concentration increase. Ngo et al.[276] carried out an experimental investigation into the effect of increasing alcohol content from 20 – 100 wt%, which decreased the solubility parameter ε from 67.7 to 19.9 with increased alcohol content in water-IPA and water-methanol inks. Correlating performance with understanding from Mabuchi et al.,[274] the more dispersed, smaller ionomer aggregates formed in higher alcohol (lower ε) concentrations had a detrimental effect on the CL. This suggests that the smaller aggregates with greater surface density had greater drive to assemble on the catalyst surface in addition to the carbon support, which was preferentially coated by low alcohol fraction dispersions due to greater interaction energy as found by Andersen et al.[75,76,247] This led to greater coverage of the active Pt and decreased ECSA. Tightly packed smaller aggregates led to greater compaction of the total CL impeding micro-void formation and thus gas transport, increasing charge transfer resistance. Overall, these resulted in decreased cell power density, as seen in Figure 18. Methanol–water solvent mixtures with greater ε compared to IPA-water across the molar fractions investigated had increased aggregate sizes and thus improved performance for the same reasons.

As ionomers contain charged segments, electrostatic interactions between sulfonic acid ion-pairs have an additional impact on aggregation and can occur due to suspension pH and ionomer counter-ion. Changes to water–alcohol composition alter the suspension pH which impacts aggregate
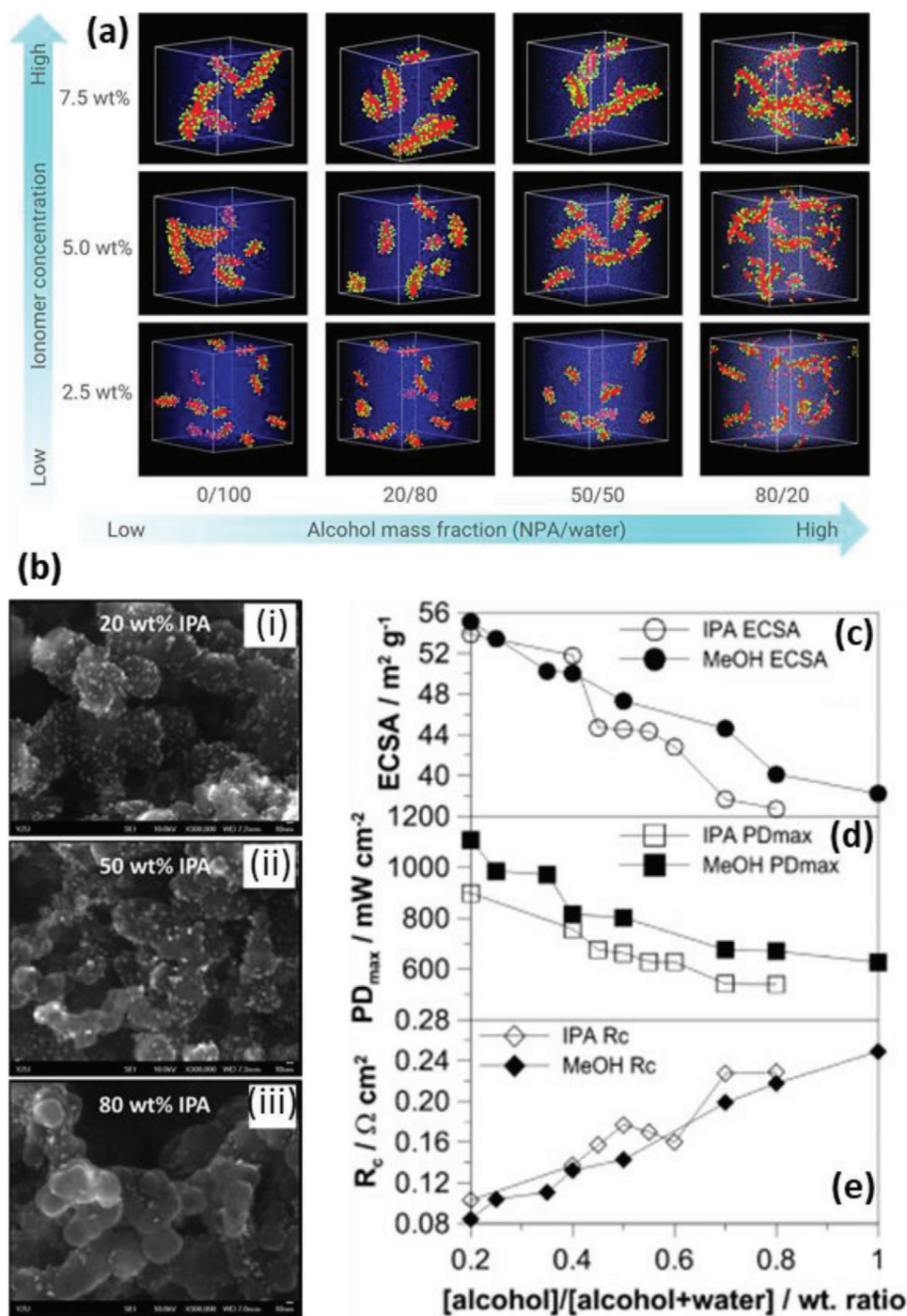
Figure 18. a) Snapshots of the cylindrical self-assembled ionomer aggregates at various ionomer concentrations and NPA/water fractions. Adapted with permission.[274] Copyright 2020, American Chemical Society. b) Field emission SEM micrographs of the PtC/Nafion layer on the surface of GDL. Carbon powder particles of diameters 60–80 nm are visible, but the bright spots from Pt particles with sizes <5 nm are covered in greater ionomer quantity at higher IPA fraction (i–iii). c) Pt electrochemical active surface area obtained by CV, d) fuel cell test maximum power density, and e) CL impedance cathode charge transfer resistance for CL fabricated from different water-IPA or water–methanol ratios. Adapted with permission.[276] Copyright 2013, Elsevier.

conformation, with increasing influence as ionomer concentration decreases.[277] Decreasing water content causes pH to decrease, with less hydronium ions, which reduces the magnitude of electrostatic interactions. This increases the favorability of side chains to extend into the solvent, reducing particle aggregation and favoring linear conformation, compared to highly aggregated and internally packed side chains in higher pH solvent systems. Ink pH should thus be considered when

ADVANCED
SCIENCE NEWS
www.advancedsciencenews.com

ADVANCED
ENERGY
MATERIALS
www.advenergymat.de
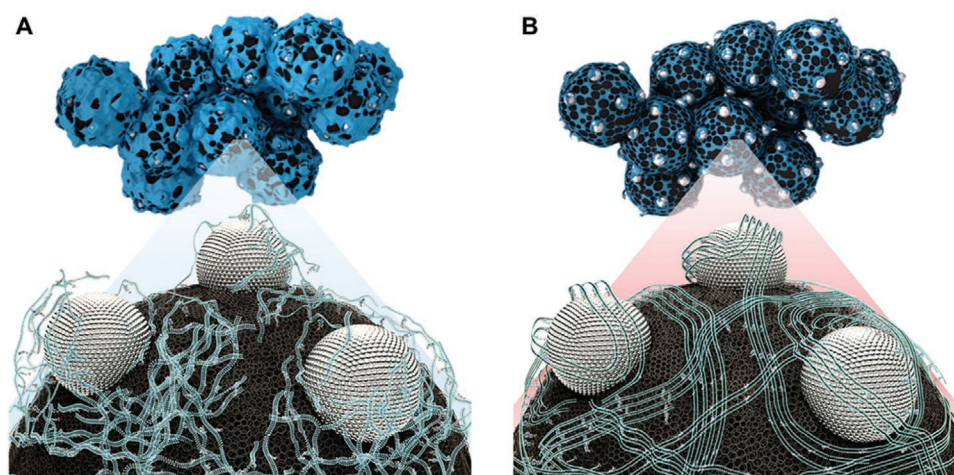
Figure 19. Schematics of Nafion ionomers on the catalyst surfaces. A) Distribution of conventional ionomers synthesized by emulsion polymerization. B) Distribution of the laboratory-made ionomers synthesized by SCF process. Enlarged conceptual diagram showing the distribution of both conventional and prepared ionomer on the Pt/C catalyst surface. The SCF process contributes to the formation of nanodispersed Nafion ionomer, leading to improved electrochemical performance and durability. Reproduced with permissions.[280] Copyright 2020, The Authors.

directing the morphology and size of the ionomer aggregates present in the ink. Vast pH change with ionomer concentration and counter-ion may rationalize the conflicting work that proposes differing structures for binary solutions.[267,269,273–275] Addition of salt (such as NaCl) to give cation-form Nafion dispersions has been shown to increase aggregate size and domain size in cast films.[274,278] The increasing tendency to form intra- and inter-chain associations with increasing ion valency cation size, polarity, and hydrophobicity have been shown to tune self-assembly thermodynamics of PFSA copolymers to control membrane morphology and transport properties.[279] Based on the globular, phase-separated model of binary solvents, the Na^+ form of Nafion has been found to possess fewer dispersed backbones and a less swollen structure.[207,267] These stronger attractive electrostatic interactions within and between ion-pair clusters result in larger ionic clusters. The localization of salts near sulfonate groups reduces electrostatic repulsion enhancing aggregation, and thus the number of ionomer chains in the aggregates increases with salt concentration. At low salt concentrations (≤0.1 M), ionomer aggregates remain cylindrical for all alcohol fractions, but at 1 M, aggregates increase in size and change shape. Due to the lack of repulsive sulfonate interactions in Na^+ form Nafion, the effect of water–alcohol fraction differs from H^+ form Nafion. The formation of a large aggregate with a single disk-like shape was observed at ≤50 wt% alcohol, while a large secondary-like aggregate was formed by multiple cylindrical aggregates bundled together at 80 wt% alcohol.[274]

Recent studies have used novel water–alcohol solvent systems to attain high-performance CLs. Ahn et al.[280] demonstrated the use of a supercritical IPA-water mixture with enhanced solvation strength to produce improved Nafion dispersion for a highly durable CL. This solvent reduced the entanglement of the polymer chains into particles below 100 nm, which then rearranged into smaller particles in the CL, providing a denser structure with greater crystalline content that had higher

mechanical toughness, chemical resistance, and proton conductivity. In addition, as in polar aprotic solvents,[281] the small colloidal PFSA particles easily assemble in the primary pores inside the catalyst support, providing a desirable TPB and well-developed secondary pores, that allow good mass transport as shown in **Figure 19**. Doo et al.[53] reported a method to reduce ionomer aggregate size (hydrodynamic diameter) by adding dipropylene glycol (DPG) to the solvent system, with correlative structural changes to the ionomer film. Smaller aggregates formed due to a greater DPG-ionomer affinity, with hydrophobic backbones being predominantly stabilized by DPG molecules.[282] The addition of DPG was observed via scanning electron microscopy (SEM) to produce a thinner, more homogeneous layer due to facile compaction of the smaller aggregates, which also reduced porosity. While the optimal DPG loading was dependant on operational RH, a 50:50 DPG-water mix consistently exhibited the greatest performance as a result of highly connected ionomer networks and porosity retention balancing proton and gas transport.

The studies mentioned highlight the significant effect of solvent properties, including dielectric constant, boiling point, pH, concentration, and hydrogen bonding capacity, as well as ionomer counter ion, on the size and shape of ionomer aggregates. This in turn has significant implication on the way an ionomer coats the catalyst particles and penetrates catalyst aggregates. This multitudinous combination of factors thus determines the surface and internal structure, durability, gas penetration, and mass transport within prepared CLs. While specific case conclusions can be proposed, such as larger aggregate size in binary solvents providing better initial performance, while smaller aggregates in NMP provide prolonged durability, the combination of numerous parameters requires a case-by-case solvent selection. A number of competing factors therefore result in CLs with heterogeneous structures and non-uniform particle size, distribution, and geometry. Moreover, a lack of consistency in experimental parameters have led to differing

**ADVANCED
SCIENCE NEWS**

www.advancedsciencenews.com

**ADVANCED
ENERGY
MATERIALS**

www.advenergymat.de

results, and therefore, this section is designed primarily to highlight the factors that must be considered when fabricating a CL.[261]

3.6. PtC-Ionomer Aggregate Structure

Addition of ionomer to catalyst-solvent mixtures leads to increased particle surface charge, increasing the electrostatic repulsion between catalyst particles, thereby stabilizing the ink.[283] A combination of interactions in the solvent/ionomer/catalyst ink determines the adsorption of ionomer on the catalyst and surface of the support material. This in turn governs the extent of ionomer coverage of catalyst particles and catalyst particle aggregation, providing the resultant structure with interspersing and covering "shell" ionomer. This self-assembly depends on the prior Nafion aggregates formed in solution. This formation can also be affected by mixing time and concentration of the Nafion solution, with reduced mixing times and concentrations providing thinner Nafion shells.[192] In addition to being a major cause of crack formation in the CL, the presence of free ionomer inhibits gas transport, durability, and control of CL structure.

As PtC-Nafion agglomerates start to form with a Nafion covering layer, the solvent-Nafion interaction becomes more deterministic in the wettability of the agglomerates than the solvent–catalyst interactions. Diverse chemical properties lead to ionomer-support and ionomer-catalyst interactions of different strengths, and thus agglomerates exhibit different ionomer morphology and coverage depending on active catalyst and support. In a series of publications, Andersen et al.[75,76,247] studied the self-assembly, orientation, and strength of the PtC/ionomer interactions with ^{19}F NMR. When deposited in a low concentration Nafion solution, primary adsorption onto the surface of the substrate followed a Langmuir isotherm and reached equilibrium, attributed to adsorption of ionomer film on the outer surface. At high ionomer concentration, secondary adsorption occurred, attributed to either ionomer adsorption to internal pores or rearrangement of the primary outer layer. The transition from the primary to the secondary adsorption was influenced by pore volume content. Greater pore volume (Ketjenblack > Shawinigan Black > Vulcan XC 72) resulted in a lower surface coverage before the secondary adsorption (to the internal pores) was activated. This suggests ionomer coverage of the total substrate surface is reduced by greater support porosity, which could provide a route to designed ionomer shell thickness. It was found that only a portion of the Nafion chain was in contact with the support, with the rest orienting itself away from the surface. Although the adsorption processes occurred simultaneously to both the carbon and noble metal catalyst components, the interaction was stronger between Nafion and carbon than between Nafion and catalyst. Furthermore, the introduction of Pt led to higher ionomer surface coverage reportedly due to surface roughness and porosity differences. In addition, the adsorption of Nafion onto the surface was found to correlate to the surface oxygen content of the substrate interacting with the hydrophilic tail, in agreement with thin layer NR and X-ray photoelectron spectroscopy (XPS) investigations.[215,284,285] While this method

provided insight into Nafion distribution on different supports, it did not measure the in situ ionomer distribution in the CL, but rather the relevant strength and coverage of surface adsorption. It is key to also investigate the complex interplay of substrate, deposition, and confinement effects that govern the chemical and mechanical properties of Nafion in situ under fuel cell testing conditions.

The highly solvated ionomer backbone and side-chain enhance hydrophilic and hydrophobic phase separation and lead to well-separated and closely connected hydrophilic domains increasing the water percolation.[286] As shown in **Figure 20**, Kim et al.[281] found that the main- and side-chain mobility of ionomer aggregates in the solvent heavily influenced their assembly onto the catalyst support, affecting ECSA and proton-conduction pathways, respectively. Nafion ionomers dispersed in solvents with low main-chain mobility (e.g. glycerol and IPA) distributed preferentially on the surface of PtC agglomerates, rather than permeating into the interior, resulting in a thick Nafion layer covering agglomerates, which develops a highly aggregated phase morphology with long diffusion paths for protons and gases. In contrast, NMP, which provides high main chain mobility, provided cast CLs with the highest ECSA, attributed to effective penetration of ionomer into support pores connecting internal Pt and minimizing covering shell for efficient utilization of external Pt particles.[281] Solvents that provide low side-chain mobility (e.g., glycerol) led to Nafion coating with an increased number of acid sites assembled into ion clusters. Thus, while the thick covering Nafion layer increases the diffusion pathway and is detrimental for solvents with high side chain mobility, the phase separation provides enhanced proton conducting capability.[267] Therefore, CLs prepared from glycerol achieved the highest performance at the low and intermediate current region, due to the lowest charge-transfer resistance, indicating an efficient proton-conduction network. Solvents with low main and high side-chain mobility, such as IPA, had the poorest performance, due to both reduced Nafion aggregate penetration reducing ECSA and reduced number of ion clustering acid sites producing a thickly covering Nafion layer with poor proton conductivity. This study details the benefits and drawbacks of having densely packed fine agglomerates with thin, well-covered ionomer, compared to more phase segregated morphology of larger agglomerates with greater proton-conducting capability. This demonstrates the competing processes that must be considered in an optimized CL.

3.7. Optimal Ionomer Content and Advanced Characterization

It is often assumed that the ionomer coating is evenly distributed across the carbon support and catalyst surface.[253] However, a variety of techniques have been used to show that the ionomer distribution is highly dependent on the catalyst properties, quantity of ionomer deposited, the deposition method, the material it is deposited onto, and how it is treated.[28,53,55,248,253] The target ionomer incorporation should provide sufficient ionomer percolation into and between catalyst aggregates for proton conduction, while retaining sufficient void space for unimpeded gas transport and a stable structure.

ADVANCED
SCIENCE NEWS
www.advancedsciencenews.com

ADVANCED
ENERGY
MATERIALS
www.advenergymat.de
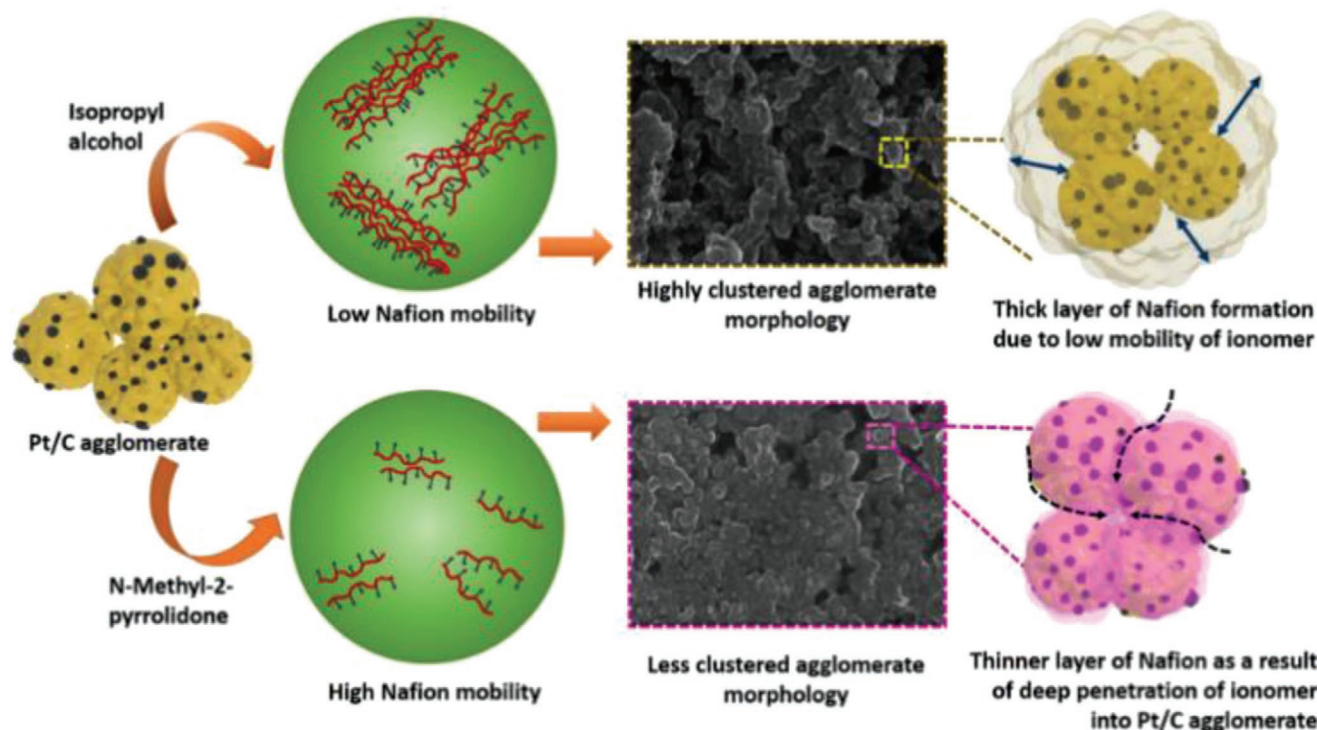
Figure 20. Illustration of greater Nafion aggregate mobility providing a thinner, more homogenous, morphology of ionomer films on PtC agglomerates resulting in improved reactant access and transport, in comparison to lower aggregate mobility. Reproduced with permission.[281] Copyright 2019, Elsevier.
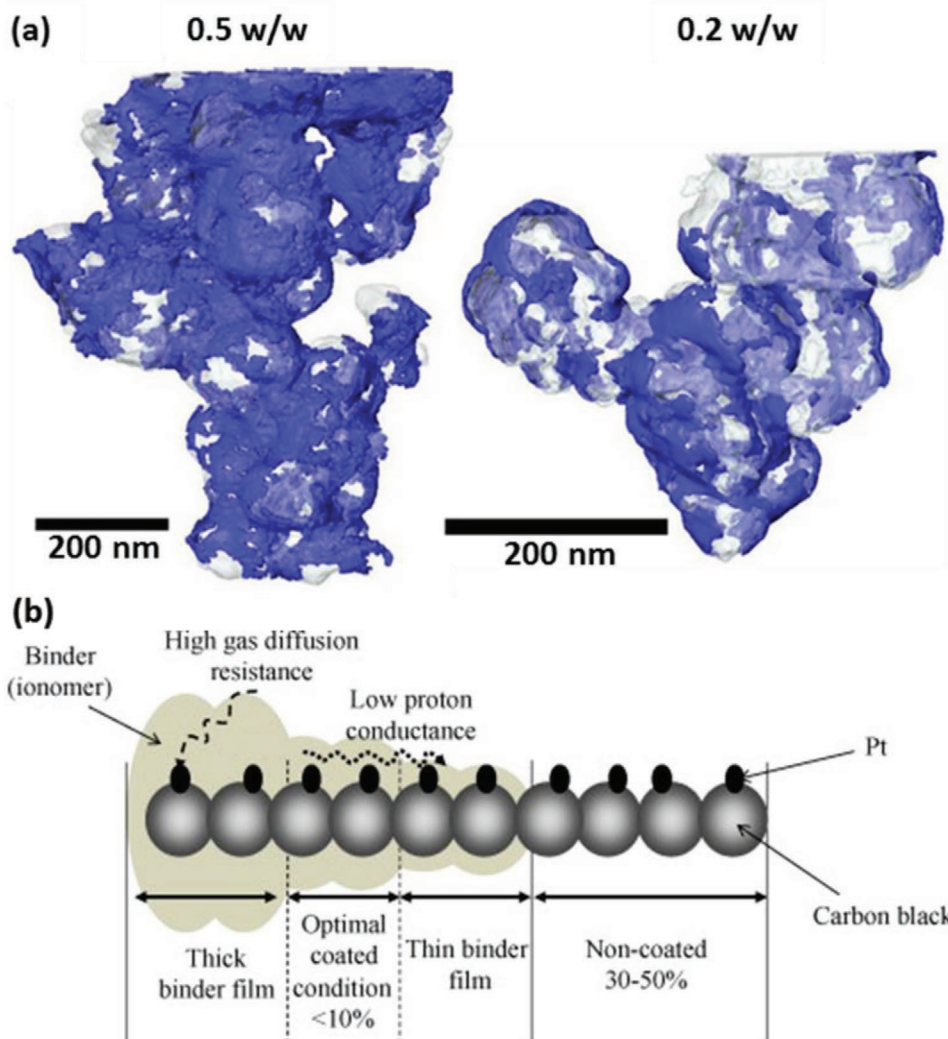
The optimal Nafion content in conventional PtC CLs has commonly been demonstrated on MEAs by use of ECSA, current density analysis, and EIS, to be roughly 33 wt% (ionomer to carbon ratio. (I/C. = 0.5).[57,287] This quantity avoids issues of poor electrical conductivity at high wt% and poor proton conductivity at low wt%. The use of an I/C above 0.5 causes the pore volume to decrease significantly, with the number of large pores found to particularly decrease.[288] Martin et al.[289] found that as Pt loadings decreased from 0.1 to 0.05 and 0.025 mg_{Pt} cm^{-2}, the optimal ionomer loading increased from 30 to 40 and 50 wt%, respectively. However, at 0.0125 mg_{Pt} cm^{-2}, the performance did not vary significantly with Nafion content, suggesting the Pt content was now the performance-limiting component. The ionomer loading not only affects the mass transport within the CL by changing the quantity of ionomer, but also how the support particles interact and deposit.

33 wt% ionomer has not been shown to be optimal for all carbon supports because of differences in carbon surface areas that accommodate differing quantities of covering and interpenetrating ionomer.[255] Lee et al.[290] reported the optimal composition to change slightly depending on carbon and solvent, due to the specific interactions in the ink influencing structural composition. For electrodes with the same I/C ratio, an amorphous carbon support exhibited a larger mean pore size, porosity, effective oxygen diffusivity, and smaller tortuosity, after co-deposition with ionomer, despite the PSD and porosities of the starting carbon particles being very similar. This dramatic difference in the electrode tortuosity indicated that the ionomer distributes more uniformly on amorphous versus graphitized carbon due to more consistent functional group distribution.

Furthermore, the ionomer ratio must be specifically adjusted for each catalyst support/ionomer couple, or novel catalyst with a different arrangement of active sites and surface group hydrophilicity to achieve optimum performance.[253] Extensive investigation is required for each unique system to optimize ionomer loading.

Advanced characterization techniques are useful in achieving this optimization, especially when new catalyst materials and supports are used. Transmission electron microscopy (TEM) imaging is a key technique that has been used to investigate the ionomer distribution, with ionomer thickness estimated from observing the edges of carbon agglomerates in the micrographs.[64,290] Despite the high-resolution nature of TEM, these boundaries can be somewhat difficult to resolve reliably, which raises questions about the accuracy of these measurements. Furthermore, sample deposition of small agglomerates onto a TEM gid may disrupt the ionomer distribution and the ultra-high vacuum experimental conditions are far from representative of operational fuel cells. Despite these drawbacks, TEM can contribute to the growing understanding of ionomer configuration within CLs. Lopez-Haro et al.[254] used high-angle annular dark field scanning TEM (HAADF-STEM) to obtain nanoscale 3D images of ionomer (Cs^+ form) distribution on CB. This analysis provided greater comprehension of the ionomer structures formed on aggregates at optimal ratios, as shown in **Figure 21**. Low ionomer CB ratio (I/C = 0.2) exhibited partial ionomer coverage (50%) that was predicted to provide poor proton conductivity. At higher ionomer-CB ratio (I/C = 0.5), the Nafion layer formed with comparable thickness, and higher coverage

**ADVANCED
SCIENCE NEWS**

www.advancedsciencenews.com
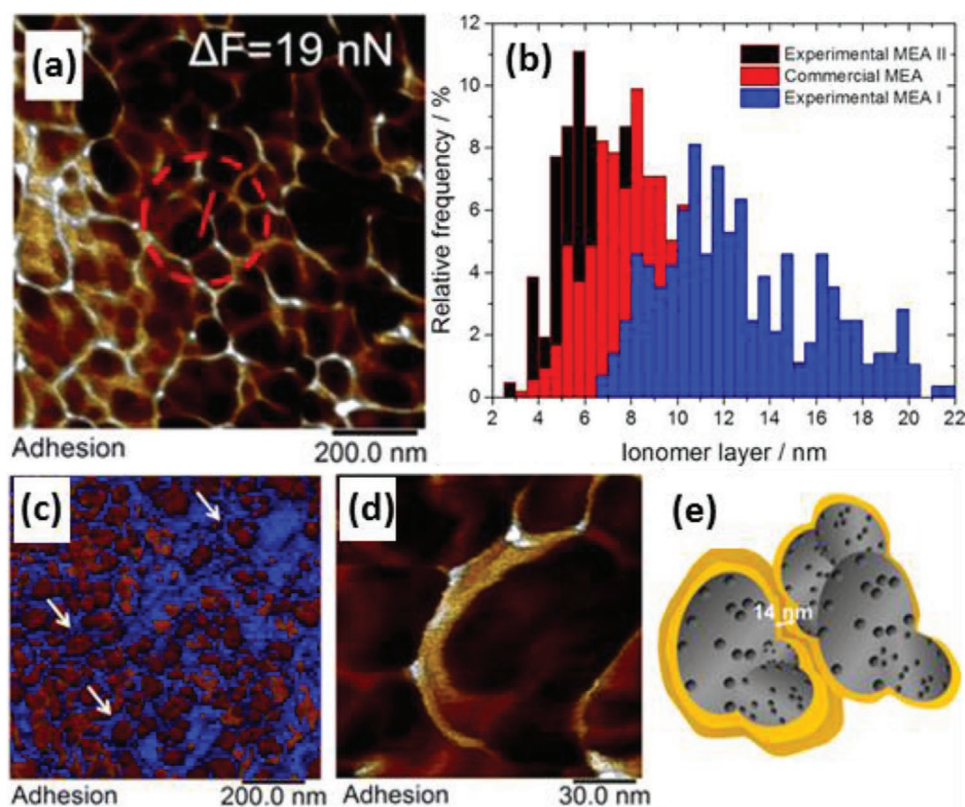
**ADVANCED
ENERGY
MATERIALS**

www.advenergymat.de

Figure 21. a) Rendered volume of the HAADF-STEM-reconstructed tomograms of Nafion-CB samples with ratios 0.5 and 0.2 w/w. The blue and grey regions correspond to the Cs+-stained Nafion and CB support, respectively. Adapted with permission.[254] Copyright 2014, Springer Nature. b) Schematic depiction of the variation of Nafion film thickness within the CL, showing the how thickness affects proton conduction and gas diffusion through the film. Adapted with permission.[112] Copyright 2010, Elsevier.

(80%). Increasing ionomer loading further to reach 100% coverage instead results in thicker layers and thus increased distances between catalyst agglomerates and diminishing returns to mass transport in the CL.

Another common method for characterizing ionomer distribution is atomic force microscopy (AFM), which is used to provide high-resolution surface topography. The use of AFM adhesion force, Young's modulus, and conduction mapping of cross sectional CL samples were successfully implemented by Morawietz et al.[291] to obtain the surface morphology of ionomer and carbon aggregates and inferred bulk morphology near to operational humidity and temperature. PtC-ionomer aggregates exhibited a linear size dependence from 60–100 nm, with Pt loading from 0.05–0.4 mg_{Pt} cm^{-2}. High-resolution mapping at 25% RH showed encapsulated agglomerates joined by ≈14 nm thick ionomer layers, constituted of separate layers equivalent to the lamellar structures described previously,

shown in **Figure 22**.[215] A broad, asymmetric distribution of ionomer layer thicknesses from 4–22 nm was observed in the CL sample at 50–60% RH and 25 °C. This corroborated thin-film investigations stating 4 nm to be the thinnest possible layer, likely due to the molecular dimensions and conformations of PFSA ionomers.[192] Total ionomer area of the sample decreased from 50% to 27%, with RH decrease from 60% to 30% due to domain shrinkage. As well as demonstrating large structural rearrangement with RH, this emphasized the significant difference in morphology for conditions commonly investigated and those present in operational fuel cells.

X-ray computed tomography (CT) is a widely used technique for 3D imaging of samples across multiple length scales. The technique is nondestructive, meaning the internal morphology of a sample can be investigated without deconstruction/destruction of the sample. Komini Babu et al.[292] reported the use of simulations and 3D X-ray CT to model Nafion

**ADVANCED
SCIENCE NEWS**
www.advancedsciencenews.com

**ADVANCED
ENERGY
MATERIALS**
www.advenergymat.de

Figure 22. AFM investigation of CL cross-section at 25 °C, a) Adhesion force map at 30–40% RH, with Pt-rich area appearing darker. b) Relative frequency of the ionomer layer thickness of three types of anode at 50–60% RH (red bars = Nafion ionomer and 0.2 mg$_{Pt}$ cm^{-2}; black bars = Aquivion ionomer and 0.05 mg$_{Pt}$ cm^{-2}; blue bars = Aquivion ionomer and 0.2 mg$_{Pt}$ cm^{-2}). c) High-resolution adhesion mapping of commercial MEA anode measured at 30–40% RH, with ionomer marked blue and arrows marking positions of separated layers. d) Zoomed-in high-resolution adhesion map of commercial MEA anode with two distinguishable layers around the PtC aggregates at 25% RH. e) Schematic depiction of ionomer-enclosed PtC aggregates. Adapted with permission.[291] Copyright 2016, American Chemical Society.

distribution in a 500 μm CL sample. At the lowest Nafion loading of 35 wt%, low activity was attributed to poor Nafion infiltration into the catalyst particles and agglomeration on the outside of the particles. In contrast, the highest level of Nafion loading of 60 wt%, caused excess Nafion to build up as films of 100s of nm on the outside of the catalyst particles with greater water retention, resulting in severe flooding and disappearance of macroporosity for gas infiltration. This structural effect of high ionomer concentration is well documented, with total porosity and pore size deviation decreasing as ionomer content increases.[293] This loss of both primary and secondary pores restricts Knudsen diffusion and gas transport through the CL, limiting cell performance. Cetinbas et al.[242] reported high-resolution X-ray CT of the CL, with ionomer distinguished from carbon and Pt. The observation-based model of pore distribution and shortest pore and solid pathways quantified the microstructure effect on transport properties at differing operational pressure and temperature. Local resistance at the catalyst surface constituted a large part of the mass transport resistance, but flooding of internal pores at 100% RH caused a resistance equally as significant that, in general, became the dominant mass transport limitation. Catalyst loading was shown to impact mass transport through the electrode roughness factor, as discussed in Section 3.4.[235]

CL structure is an extremely complex arrangement, providing many experimental challenges in its elucidation. A variety of techniques have been utilized to build a greater understanding of the structures present at varying length scales in differing conditions. This provides greater insight into the phenomena occurring within the structures and can help direct future directions for CL improvements. Further work should build on these investigations and utilize new material characterization developments to improve understanding of the morphology in operando or at least in operational conditions, due to the highly dynamic nature of the ionomer.

3.8. Ionomer in CL Durability

Much effort has focused on optimizing the composition and arrangement of CL components, but local environmental changes such as hydration, temperature, and potential lead to significant changes in the ionomer that must be considered and mitigated to ensure durable and long-lasting fuel cells.[294] Using NR, Wood et al.[79] showed that the long-range structure and hydrophobicity of Nafion at the catalyst/ionomer interface changes depending on Pt or PtO substrate. When the Pt metal is oxidized to form PtO, the Nafion film becomes hydrophilic at

ADVANCED
SCIENCE NEWS

www.advancedsciencenews.com

ADVANCED
ENERGY
MATERIALS

www.advenergymat.de

the interface, attributed to side-chain interaction, and restructures over a long-range, pushing itself away from the PtO interface.[79] In addition to the difference between hydrated PtO and hydrophobic contacted Pt, different side-chain hydrogen bond rearrangement occurs between Pt-H, Pt-O, and Pt-OH in the anode and cathode, even though all form a hydrated interface.[295] In the reducing environment at the anode, dissociated atomic hydrogen forms on the Pt surface, whereas exposure to oxygen at the cathode oxidizes the Pt surface. Adsorbed hydrogen provides a hydrophilic, but nonpolar, interface that forms hydrogen bonds with water in a similar manner to the sulfonate hydrogen bonds. In comparison, negatively charged oxygen groups on PtO are less hydrophilic but induce strong polar electrostatic interactions between hydronium ions in the hydrated interface and ionomer sulfonic acid groups. This restructuring of the ionomer can result in changes to packing density and WU to the bulk, as observed in aged samples that exhibited irreversible swelling with a resulting WU increase. Repeated rearrangement of ionomer at the surface, due to electrochemical environment, humidity, and temperature leaves the ionomer vulnerable to delamination and degradation in the electrode. In addition, transport of protons and gases must occur and be understood in a continually changing ionomer morphology as the Pt surface changes from Pt to Pt-O to Pt-OH during electrocatalysis.

Bulk CL degradation has been proposed by Yin et al.[296] to follow three typical phenomena: crack generation, the extension of existing cracks, and interaction of cracks. These microstructural changes were found to relate to ionomer aggregation and migration. Upon WU, ionomer swelling induces viscoelastic strain. Due to heterogeneous ionomer incorporation and film thickness, swelling and strain vary at different locations contributing to bulk tears and cracking. The observed structural changes correlate with increasing resistance due to a decrease in TPB caused by ionomer migration. Therefore, the durability of the overall CL can be tuned by reducing nanoscale dynamic changes of the ionomer within. Degradation is not only induced by changes to the ionomer, but other dynamic process occurring in the CL. Jomori et al.[240] observed the same high resistance, commonly presented in fuel cells with low Pt loadings, in standard fuel cells after ECSA decrease due to cycling-induced degradation. The agglomeration of Pt particles decreases ECSA and would be expected to cause higher O_2 transport resistance in the same manner as reducing Pt loading. This effect is more extreme under low humidity conditions, suggesting further mechanisms of ionomer change were occurring.[297] Ionomer sulfonic acid group adsorption to the Pt surface reduces the number of electrochemically active Pt sites, and the ionomer backbone forming a continuous layer can prohibit oxygen transport.[61,235,298] High WU in high RH conditions is suspected to mitigate Pt poisoning as the degree of sulfonic acid adsorption decreases with increased interfacial water.[295] While hydration fluctuations are the key parameter causing ionomer migration, temperature has a significant impact on hydration and subsequently structural deterioration.[299] AFM investigation of a CL cross-section showed an average doubling of inter-agglomerate ionomer layer thickness with increasing temperature from 25 to 75 °C at 30–40% RH.[291] This is expected based on WU and swelling increasing at higher temperatures. After cooling
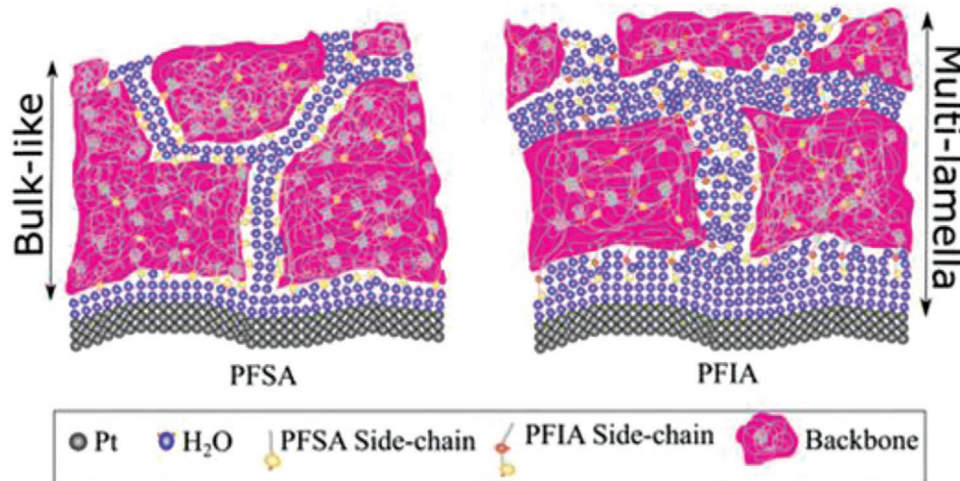
back to 25 °C, layer thickness remained ≈25% greater than initial thickness, due to residual irreversible extension force. In contrast, MEAs operated for 235 h exhibited ionomer layer thinning, due to low RH effects, with anode samples and thicker initial layers demonstrating greater degradation. This increased degradation from radical attack is due to the anode being more poorly hydrated. Therefore, maintaining optimum hydration during prolonged use is key to improving MEA durability and thus improved water management by system engineering to material advances is critical.

Prolonged usage of an MEA results in the formation of an ionomer structure that inhibits overall device performance. Thermal annealing above the glass transition temperature is commonly adopted to improve the mechanical and functional properties of Nafion.[300] By annealing below the ion hopping transition (≈100 °C), either sulfonic anhydride cross-linking or physical hydrogen bond cross-linking leads to stiffening of the film and enhancement of elastic modulus, which can counteract the swelling and rearrangement upon high RH and temperature.[301] A greater annealing temperature leads to a greater extent of crosslinking and crystallization and thus increased modulus and reduced WU and ion exchange capacity. Studying annealing of thin films allows insight to changes that occur to the ionomer within a CL during annealing. Paul et al.[302] found that films of thickness varying from 30–200 nm showed the same proportional modulus increase with thermal annealing conditions, indicating that all ionomer within the CL receives improved mechanical properties regardless of dimension. The enhanced durability of a CL that has been exposed to thermal treatments likely benefit from the increased mechanical properties that reduce ionomer migration, but also the reduced WU and therefore swelling and flooding that leads to crack propagation. Thin-film Nafion samples exposed to high temperatures had increased chain mobility and facilitated surface and bulk reorganization. Surface energy was minimized by sulfonic groups forming a hydrophobic skin to achieve thermodynamic stability and led to impeded WU kinetics. Corresponding bulk rearrangement formed static crystalline domains furthering retardation to WU and higher activation energy to proton transport. Upon exposure to liquid water, the sulfonic groups folded back up to the film surface due to their affinity for water, and bulk rearrangement induced lower proton conduction activation energy. Upon a subsequent second heat treatment, the hydrophobic surface is regenerated, but proton conductivity remained high. This emphasizes the effect of the conditioning step on the electrode properties and is one of the mechanisms by which it provides improved fuel cell performance. Moreover, it suggests that heat treatment of the CL can provide ionomer components with improved mechanical properties and stability, whilst also retaining high proton conductivity. Further investigation into the optimal balance between mechanical stability, proton conductivity and WU will allow realization of durable high performing CLs.

3.9. Non-Nafion Ionomers

The ionomer has two distinct contrasting roles in an MEA. It is required for high O_2 diffusion in its thin layer form within

ADVANCED
SCIENCE NEWS
www.advancedsciencenews.com

ADVANCED
ENERGY
MATERIALS
www.advenergymat.de

Figure 23. Depiction of the near-interface structure, due to composition and length of sulfonic group terminating side chains, confined as thin films (≈15 nm) of PFSA and PFIA on Pt at 30 °C and 97% RH. Reproduced with permission.[250] Copyright 2018, American Chemical Society.

the CL, and acts as a barrier to O_2 diffusion from the cathode to the anode in the membrane.[235,303] PFSAs provides these contrasting properties due to the changes to its crystalline structure when deposited as a thin film in the CL compared to bulk morphology in the PEM.[303] However, in an optimized system, different ionomer chemistries should be tailored to fit the unique requirements of the membrane and CL, while providing high proton conductivity and durability in both.[303]

Although Nafion is the industry standard for both PEM and CL ionomer, a variety of ionomers with alternative backbone and side-chain compositions have been developed. Differences in ionomer molecular architecture, that is, EW and side-chain length, alter both interactions with substrate and internal ionomer structure. The interfacial structure is affected little by EW, whereas side chain length and chemistry have a significant effect on the lamellae formed at interfaces, as shown in **Figure 23**.[250] PFSA ionomers with a single sulfonate group form a single interfacial layer on Pt under hydration, with water layer thickness dependent on side-chain length. Alternative side-chain chemistries, such as perfluoroimide acid ionomers (PFIA) that contain multiple sulfonate groups, induce an interfacial layer at lower humidities. This is likely due to uncollapsed voids created at the interface by the longer side chains bound to Pt via the many sulfonate groups. This side-chain variation also results in higher retention of water at the interface in hydrated conditions producing a lamellae structure with thicker hydrated layers. These differences in lamellae structure have a significant impact on transport properties at the catalyst surface, as detailed in Sections 3.2 and 3.4, and thus ionomer optimization must consider these effects.

EW significantly affects WU properties, with low EW ionomers accommodating greater total water and thus exhibiting greater total swelling. However, λ is lower because the higher density of sulfonic groups afford less space between domains to accommodate water, and so water domain spacing decreases.[304] PFIA ionomers with longer side chains, comprising two acidic sites to bind water, have higher total WU and λ, due to more SO_3H groups and greater domain size and connectivity.[305]

However, PFIA show lower mechanical stability, with a decrease in free volume upon hydration due to compression of the backbone that is induced via mechanical stress from WU.[250] Despite the greater WU providing improved proton conductivity, the increased swelling and lamellae formation may have a detrimental effect on the lifetime and stability of the ionomer and CL, as discussed previously. Oxygen diffusion may simultaneously be facilitated by the route provided by increased WU and be impeded by the loss of free volume. Therefore, ionomer design has many varying impacts on electrode performance and must be optimized to inhibit mass transport losses and degradation. High EW ionomers with reduced phase segregation have observed improved proton conductivity and promoted gas transport, leading to improved current density versus low EW ionomers with greater phase separation.[193,306] This trade-off is particularly important for ionomers in MEAs with low Pt loading. In a similar manner, changing the PFSA copolymer backbone structure was reported to form a less crystalline structure and benefitted from improved oxygen diffusion.[303,307]

Hydrocarbon-based ionomers have received extensive interest, as both membrane and ionomer, due to their tunable properties and lower synthetic cost.[308] One particular advantage of non-fluorinated ionomers is reduced catalyst poisoning due to formation of the degradation product, HF, when using PFSA ionomers. Many sulfonated poly-aromatic ionomers have been investigated for ionomer application, including poly-(arylene ether sulfone),[309] poly-(ether ether ketone),[310] and polyimide.[311] Current non-PFSA ionomers commonly yield slower ORR kinetics, which translates to larger activation polarization losses and poorer fuel cell performance. This is due to a combination of factors related to decreased pore sizes and decreased oxygen permeability. Unlike the side chains in PFSAs, sulfonic acid groups are directly attached to the polymer backbone, resulting in lower acidity, restricting the phase segregation of hydrophilic and hydrophobic domains and providing lower proton conductivity.[312] Despite the benefit of low O_2 crossover when used as electrolyte membrane, hydrocarbon ionomers exhibit reduced O_2 transport through the CL, due

**ADVANCED
SCIENCE NEWS**

www.advancedsciencenews.com

**ADVANCED
ENERGY
MATERIALS**

www.advenergymat.de

to lower oxygen solubility in the non-fluorinated backbone.[313] Despite this poorer performance, it is of interest to use hydrocarbon ionomer in the CL when a hydrocarbon PEM is used in the MEA, due to a reduction in interfacial resistance.[314] More efficient utilization of hydrocarbon ionomers is undergoing exploration to fully benefit from their advantages over PFSA ionomers. For example, Easton et al. found that adding PTFE in combination with SPEEK ionomer to the CL, greatly aided performance by enhancing hydrophobicity, which reduced electrode flooding and increased pore diameter and oxygen permeability, exceeding Nafion CL performance.[314]

3.10. Conclusion and Outlook

Fuel cell CLs are an intricate mix of components, with ionomer acting as a binder and main proton conduction pathway. Ionomer structure must be comprehensively understood and optimized to continue to improve PEFC technology. Reactant transport within the catalyst aggregates is a complex, 3D process and the ideal ionomer coating should have high and isotropic transport properties. For example, O_2 diffusion resistance is one of the main limiting factors in low Pt loading electrodes, and while it is clear that the ionomer/catalyst interface can cause this enhanced resistance, the role of other factors, such as incomplete ionomer coverage and CL flooding is not as well understood. With greater understanding, this O_2 diffusion resistance can be mitigated by utilizing different ionomers, CL design, or ensuring the ionomer thin film structure is deposited in such a morphology that can facilitate O_2 transport. Despite the use of appropriate ratios to optimize ionomer distribution, conventional fabrication procedures will inevitably lead to inhomogeneous ionomer distribution.[112] Furthermore, the ionomer can assemble on the Pt or carbon surface as ionomer agglomerates, films of fluctuating thickness, or be completely vacant, as depicted in Figure 21. As the incorporation of the ionomer will be affected by many factors, such as the support material and solvent, it is particularly hard to quantitatively determine the optimal ratio. The variety of structures, swelling, and changes that ionomers undergo in response to substrate and hydration will have a significant effect on electrode performance. Regardless of film thickness, the interfacial lamellae structure will influence short-range phenomena, such as electrochemistry, by affecting charge transfer reactions and adsorption of reactive species, whereas morphology and structure of water percolation in the "bulk" ionomer phase will impact the long-range transport of protons, O_2, or H_2 from gas phase through the ionomer to the active sites. Thick ionomer layers (>10 nm) provide facile proton conduction but poor gas diffusion, while bare Pt exhibits hindered proton transport, although it is facilitated by water and effective gas transport. An ultrathin layer (<10 nm) will likely provide the ideal transport scenario. Further detailed investigation of the ionomer structures present in the CL under different conditions are required to achieve optimization and subsequently significantly greater fuel cell performance.

A combination of techniques have shown that thin and consistent layers of ionomer (5–10 nm) covering catalyst particles and agglomerates, as well as some form of penetration into the aggregate, is desired, with thicker ionomer layers and inhomogeneous distribution impeding fuel cell performance.

To achieve this, the mechanics of ionomer distribution and deposition have been explored. Highly solvating solvents that induce well-dispersed aggregates of phase-separated ionomer are required to form contiguous proton-conducting networks adsorbed favorably to the catalyst support surface and internal porosity in the correct orientation. The catalyst ink ratio must be selected to ensure sufficient, but not excessive, ionomer coating and interconnection between catalyst aggregates and adequate time must be allowed for the ionomer to self-assemble on the particle surfaces during mixing. Maintaining this ideal structural composition over extended operation with changing humidity, temperature, and potential is a key step in the adoption of fuel cell technology. The current methodology has employed thermal treatment and appropriate combination of the above parameters, as well as using new solvent systems to achieve stable electrodes with long-lasting performance. Further fabrication parameters such as deposition method, Pt loading, and total CL thickness have a significant effect on the way in which ionomer permeates into the CL. These require further exploration to obtain optimized procedures for high-performing commercially viable devices.[315]

The majority of ink dispersion and ideal thin film studies (both experimental and computational) are carried out at room temperature. The molecular structure of the inks and organization of the polymer framework likely differ in the conditions present during CL fabrication (solvent removal) and fuel cell operation (≈80 °C). Similarly, microscopy investigations are commonly carried out under vacuum and are therefore not representative of the structures in an operating device under humidification. In addition, samples used for microscopy techniques are taken as small "sections" of the initial electrode, giving information that is unlikely representative of the true ionomer structure in the electrode.[185] To better understand these material properties in operating conditions, similar investigations, such as X-ray CT and electron microscopy, with adapted methodology must be carried out in situ or under environmental control. Moreover, techniques that are inherently more accommodating to high temperature and humidity, such as AFM, GISAXS, NR, and ellipsometry, should be utilized. High-speed AFM (HS-AFM) is one particular area that could provide more representative information of the surface by covering a greater and more representative sample size, as well as observing rapid surface changes upon temperature and RH change.[316] SANS and SAXS studies that can provide nanoscale understanding of the average structure have elucidated many morphological properties of catalyst inks and overcome issues of microscopy techniques. These same scattering techniques should be applied to the CL to understand the intricate morphology and interactions of ionomer and catalyst as a cast electrode in operation. As reiterated throughout this section, there are many factors that lead to different morphologies and dynamics within the CL. To ensure fair comparison and correct conclusion of the determining factors in CL performance, experimental studies should include a complete record of preparation parameters. At a minimum, the following should be included in the discussion: dielectric constant, boiling point, pH and concentration of solvent, and mixing time and PtC species (hydrophobicity) in the ink, ideally limiting these variables independently.

Through this increased understanding, many routes to optimized CL performance, via favorable ionomer interaction

ADVANCED
SCIENCE NEWS

www.advancedsciencenews.com

ADVANCED
ENERGY
MATERIALS

www.advenergymat.de

leading to optimized distribution, are conceivable. For example, non-carbon catalyst supports (e.g., Nb-SnO$_2$) have shown potential to overcome the issues of insufficient ionomer coating, and may help alleviate the limitations of low Pt loading electrodes.[253] Novel material approaches can benefit from the in-depth understanding of ionomer interactions and assembly, as well as a vast material library to choose specifically tuned supports/additives. This also highlights the important role of research into ionomer interactions that could lead to improved fuel cells.[76] Theoretical modeling and use of first principles must be further utilized to obtain greater understanding of interfacial reactions and charge transfer, as well as a fundamental understanding of the interplay between the many species in contact.[317,318] This theoretical understanding will provide support to experimental insight into optimal ionomer distribution and covering, especially as new materials are integrated.

4. Catalyst Layer Structure

4.1. Introduction

The ideal CL structure is an optimized balance between electrical conductivity, proton conductivity, gaseous reactant transport, and catalyst accessibility. This requires conductive support particles with close contact with ionomer; and is best achieved by forming dense, low-porosity electrodes. However, to facilitate gas transport and to aid water management, a high porosity and balanced PSD is needed, which encourages the use of highly porous morphologies. Achieving and optimizing this balance is key to high performing CLs. For commercial PtC-based CLs, this optimization has mostly been achieved, resulting in their leading performance. However, given sufficient optimization, other novel materials may achieve the same, or better, performance. Novel support materials such as metal oxides, graphene, or functionalized carbon supports have been widely proposed to promote aspects of the CL design, such as ionomer distribution and corrosion resistance.[74,178,324,186,225,253,319–323] The thickness and distribution of the Nafion film is dependent on the substrate surface composition and chemistry.[79,193,212] Hence, functionalization of the support material has the potential to alter ionomer distribution on the surface affecting the morphology of the resulting CL and improving electrode performance.[55,74,75,113] The structure of support materials affects CL morphology; for example, graphene-based CLs typically form re-stacked layers oriented in-plane with the membrane, which introduces limitations on the mass transport of protons and gases.[325,326] The typical solution to this morphological issue is to add different shaped carbon supports to act as spacers; however, in the case of graphene, this obviates the initial benefits. It is therefore important to understand the consequences of morphology on CL performance, in order to develop optimized design criteria. Furthermore, CL design from Nafion distribution to ink formulations is based on historic protocols used for small porous carbon nanospheres. However, these protocols may not be ideal for many novel supports, which may require different structures and support-solvent interactions for high-performance CLs.[178] Understanding the role that support

materials and CL morphology have on performance is key to moving from a trial and error-based optimization to an efficient rational approach to electrode engineering of novel materials.

CL components and structural durability are key design elements that need to be considered.[327,328] There are many degradation mechanisms that lead to MEA performance loss during cycling, including carbon corrosion, Pt catalyst loss, and electrode thinning. Carbon corrosion is the loss of support material leading to catalyst, ionomer, and conductivity losses and is typically more severe in the cathode compared to the anode.[146,329] It is a consequence of the electrode environment and the nature of the support material, and in principle can be managed by surface functionalization,[69,330] choice of support material,[74,178,186,225,322–324,329] or use of hydrophobic binders.[331,332] Catalyst loss is typically either driven by the aggregation or migration of the Pt catalyst, causing a loss of ECSA. It can also be impacted by surface functionalization,[69,333–338] support material,[253,333,339] and porosity.[71,178,186] Electrode thinning is often independent of carbon corrosion and leads to a loss of porosity which in turns impacts Pt accessibility and O$_2$ diffusion resistance.[159,340] For example, Pokhrel et al.[339] reported >50% reduction in performance during a carbon corrosion-specific AST and a change in porosity from 0.54% to 0.23% from the beginning-of-life (BoL) to end-of-life (EoL). Electrode thinning has been reported as being dependent on the structure and morphology of the CL.[159,320,341] All these degradation mechanics are highly dependent on the chemical nature of the support material and its surface functionalization. Tuning these surface groups or exploring the potential of new support materials such as metal oxides will allow for significantly longer-lasting fuel cells.

CL morphology and support chemistry (including surface functionalization) have an impact on other features of fuel cell operation too, particularly water management. Water management is not only an issue of CL flooding at high current densities but is also relevant to thinner electrodes and durability, particularly carbon corrosion. Thinner electrodes or those with a collapsed pore structure will not transport water as effectively through the layers of the MEA.[69]

It has been reported that the effects of carbon corrosion can be mitigated by adapting the fabrication method,[320,341] via electrode morphology improvements. Understanding the interactions between support materials, morphology, and corrosion mechanics may lead to significant improvements in device lifetimes without changing the fundamental materials.[320,341] Current research into the performance and durability implications of nanostructured CLs is limited, but shows great potential. The following sections provide a detailed discussion of different elements of CL structure and their influence on fuel cell performance.

4.2. Pore Distribution and Utilization

As described in Section 1.3, pores are the void spaces within and in between the solid-phase components of a fuel cell and they are a key requirement for an efficient CL, as it is via these empty channels that the reactant gases reach the catalyst surface. They also play an important role in water management,
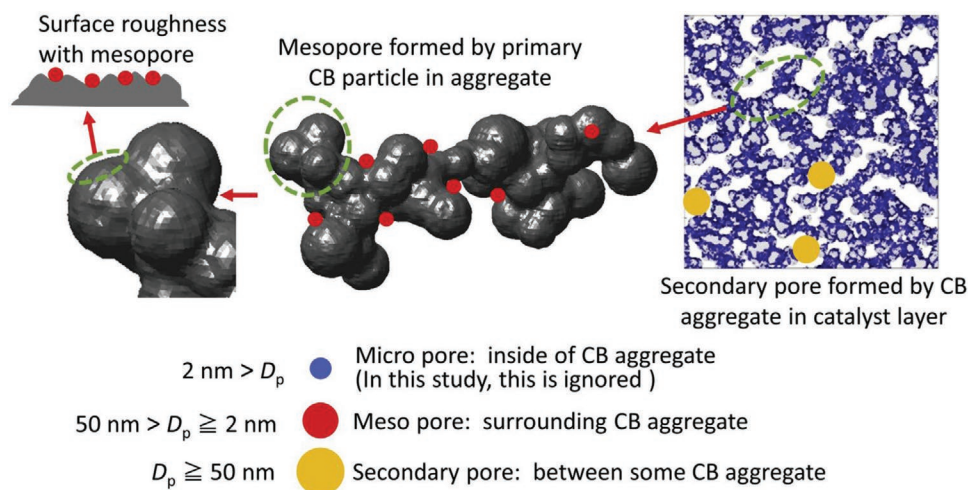
Figure 24. Schematic image of pore of CB aggregate and CL. Reproduced with permission.[80] Copyright 2019, Elsevier.

both removing excess water from the ORR reaction and maintaining hydrated membranes and ionomers.[342,343] Traditionally support particles are spherical and agglomerate into clusters (aggregates) separated by empty space or ionomer. The pores are the void space within each particle, between each particle in the cluster and the void space between each cluster, as shown in **Figure 24**. The synthesis method and pretreatment techniques of the support material help define the porosity.[344]

The terminology used to define the nature of porous materials follows from a technical report by Rouquerol et al.[345] Pore size is defined as the distance between two opposite walls of a pore. Porosity is the ratio of total pore volume as a proportion of the apparent total volume, typically expressed as a percentage or fraction.[346] Different sized pores are categorized into different broad definitions. Micropores are voids with a pore size smaller than 2 nm; they are typically due to channels in the interior of a particle.[255] Mesopores are pores between 2 and 50 nm, which can be due to larger channels within a particle or by the void space between particles.[63,113,255] Macropores are pores larger than 50 nm and are typically the voids between different particles or clusters.[347,348] Macropores have been referred to as O_2 diffusion highways as they are generally regarded as being key to low-tortuous gas diffusion, particularly in thicker CLs.[348] In some publications, pores are defined as either primary or secondary, with primary being between 6 and 20 nm and secondary pores between 20 and 100 nm.[255] It is widely considered that pores smaller than 20 nm do not have interiors coated with ionomer, although this has not been thoroughly determined or investigated. This likely stems from the constrained morphology formed at low dimensions being unfavorable versus ionomer deposition outside of the pore, and corroborates thin film studies of a "minimum" possible thickness due to phase separation.[255] Closed or isolated pores are pores that are completely enclosed by the support and therefore cannot be accessed by fluids or gases. Catalysts in closed pores will not be electrochemically active, even if they are electrically connected, although the pores themselves will still affect the overall CL structure/density.[349] A perfect electrode structure would contain

no closed pores, as these only serve to increase electrode thickness and reduce catalyst utilization. Macro-scale heterogeneous structures, particularly large isolated pores, have been suggested to be one of the key limitations of the CL, along with the morphology of the ionomer adhesion.[349] They have been reported to typically reduce Pt utilization by 25–30% in PtC electrodes.[350]

Typically, carbon supports are categorized into two broad definitions: solid carbons that possess low surface area and low microporosity, namely low surface area carbons (LSAC), and high surface area carbons (HSAC), which have high surface areas and a large number of micropores within each particle.[64,69,71,324,351] Ketjenblack is a prime example of an HSACs with a surface are of 900 m² g⁻¹, mostly due to the presence of micropores through the carbon particles.[255] Vulcan carbon is a classic example of a solid carbon or graphitized carbon black (GCB), which possesses a lower surface area (220 m² g⁻¹).[63,255] Other examples include acetylene black and most highly graphitized carbons. The relative pore structure and surface area of these carbons are a consequence of the synthetic methods used to make them and their chemical composition. Typically, highly graphitized carbons possess a relatively flat surface, which results in a lower surface area as shown in **Figure 25**a. On the other hand, more amorphous carbons lend themselves to a surface disordered on the nanometer scale, giving rise to much larger surface areas and higher microporosity. The morphology, porosity, and PSD for the overall CL is dependent on manufacturing, ionomer content/distribution, size/structure, and initial porosity/PSD of the support material.[64,293,351,352]

Porosity and PSD have been reported to play a large role in catalyst durability. As discussed in Section 1, the two main mechanisms of Pt loss are Ostwald ripening and particle coalescence.[71,178] Both of these degradation mechanisms result in an ECSA loss, but differ in size of the resulting catalyst particle sizes. Sneed et al.[178] reported the upper barrier to catalyst particle size growth due to AST in HSACs was much lower than LSACs. This is due to the surfaces of flat LSACs allowing for facile coalescence of the catalyst into larger particles, in contrast to isolated particles within the micropores of HSACs, which have less freedom of movement. **Figure 26** shows significant
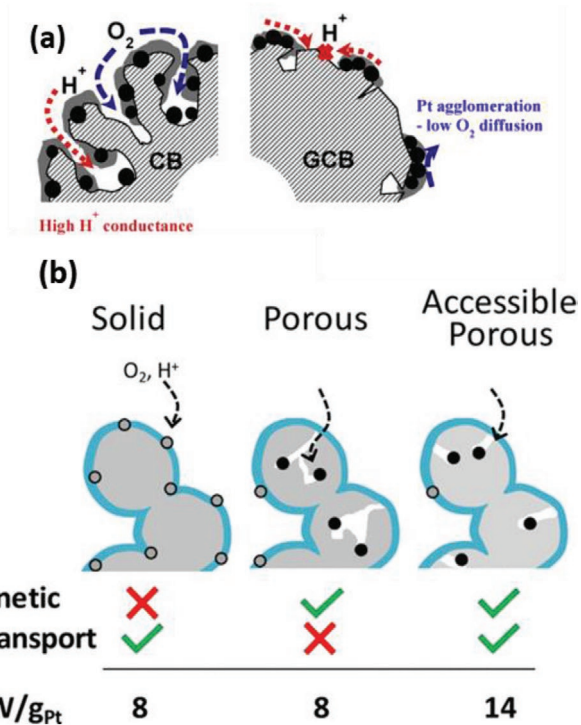
Figure 25. a) Schematic ORR models of the carbon-supported Pt catalysts. Adapted under the terms of the Creative Commons Attribution 4.0 International (CC BY 4.0) license.[64] Copyright 2016, Elsevier. b) ORR kinetic and transport (O_2 and proton) characteristics of CL structures made from three types of carbon (grey). Small black and grey circles represent relatively high and low activity Pt particles, respectively, due to ionomer (blue) adsorption. Adapted with permission.[63] Copyright 2018, American Chemical Society.

Figure 26. Violin plots of particle size distributions measured with by scanning transmission electron microscopy (STEM) in MEA cathodes with different catalysts at beginning-of-life (blue) and end-of-life (red). The distributions in (a) are simple numerical histograms, while the distributions in (b) include a volume weighting factor to show the distribution of mass between particles of different sizes. Blue "o" markers and red "x" markers show the mean size for BoL and EoL distributions. Reproduced under the terms of the Creative Commons Attribution 4.0 International (CC BY 4.0) license. Copyright 2019, Electrochemical Society.[71]

differences in the change in catalyst particle size during AST between different types of carbon supports. While this may at first imply that HSAC catalyst would lose ECSA at a slower rate, Sneed et al,[178] among others[186] reported that there was no significant difference in ECSA change during AST between LSACs and HSACs. Pt catalyst particles are protected from particle coalescence in HSACs, this benefit is offset by the increased vulnerability of the smaller catalyst particles to Ostwald ripening compared to LSACs.[71,178,186]

Mass activity of catalyst is reported to increase when the particles are deposited in the support micropores, attributed to the absence of a gas impeding ionomer coating, which cannot be deposited into the interior of small pore. Harzer et al.[353] compared catalysts deposited on exterior or interior pores, and found the ECSA and current density losses in the mass transport region were greater for exterior pore catalyst. This was reportedly due to interior pores not being poisoned from the ionomer coating.[60–66,71,186,322] Due to this effect, HSACs have often been reported to outperform LSACs.[178] However, in the absence of direct ionomer contact, catalyst particles buried in micropores are dependent on the presence of localized liquid water to transfer protons. Depending on the pore size, localized water can increase O_2 transport resistance by forcing the gas to diffuse through flooded pores to access the catalyst surface.[63] This, combined with a more tortuous

gas diffusion pathway and the possibility that the entrance to pores may be partially blocked with ionomer, further limits O_2 transport.[64,353–355] From this, solid carbon supports have been reported to possess superior current density in the mass transport region compared to porous carbons.[64,71,353] However, this general trend does not always hold true due to other differences between LSAC and HSAC, such as surface functionalization, surface area, porosity, and impacts of different testing conditions, it is therefore not clear which of these different types of carbon support consistently outperforms the others.

While the size, shape, and PSD of the carbon support is the major factor in developing the morphology of the CL, the interaction of the ionomer and catalyst particles with the support also plays a role. For example, CB powders have been reported to have pores ranging from 1 nm to several hundred μm. However, electrodes formed from these powders contain a narrower pore range between 3 and 300 nm.[351] This is due to the introduction of catalyst particles and ionomer depositing onto the support particles and modifying the pore structure, with higher ionomer contents reported to reduce peak pore diameter and porosity.[64,283,356] Andersen et al.[76] reported that the introduction of Pt NPs significantly reduces the micro- and meso-pore volumes in most samples; this was observed to be significantly worse in LSACs. Yu et al.[351] investigated the role of ionomer in pore formation and found that the incorporation of ionomer into

the CL increases the peak pore sizes, as it acts as a binder during manufacturing. However, the addition of ionomer above I/C = 0.5 causes the average pore size and porosity to significantly decrease. A high ionomer content is reported to have a more detrimental impact on graphitized carbon compared to amorphous carbon, likely due to the lack of micropores and low surface area the ionomer can occupy. Elsewhere, such as Sun et al.[288] have reported any addition of ionomer reduces the porosity with even a small addition of ionomer removing most of the microporosity. The differences between these reports we assign to the variation in support materials and fabrication methods used.

Takahashi et al.[323] have shown that an increase of porosity has large positive impacts on both kinetics and mass transport of the CL. In this case, they reported that changing the spraying deposition method from pulse to electrostatic changed the porosity from 43% to 54%. This resulted in increased ECSA, implying the Pt was more accessible, with significantly higher mass activity and current density in the mass transport region which suggests improved delivery of reagents to the surface of the catalyst. However, it has also been reported that porosity in CLs above 50% reduces the performance, as the negative impact of higher Ohmic resistance outweighs the positive impacts of improved mass transport.[357] Kjelstrup et al.[348] suggested from their simulated MEA layers that the best method to achieve an efficient low loading of Pt is by controlling the macroporosity. A balance is required between water management, oxygen supply, electrical conductivity, and proton conductivity. If the porosity is too low, O_2 transport and Pt utilization is reduced, too high and the cell has lower volumetric power and impeded proton and electron conductivity, with the optimal porosity being 50%.[348] Suzuki et al.[358] investigated the effect that drying methods and hot pressing have on PSD and porosity. They reported that larger pore size increased overpotential at 1 A cm^{-2}, however, this was only observed for hot pressed samples and may be convoluted with other factors, hence, cannot be assigned to simply changes in pore structure. Pore structure also has an impact on water management, such as by Kartouzian et al.[342] who reported that the introduction of porosity improves water management within the CLs. They showed that more porous CLs can accommodate more water within larger pores, reducing the chances of flooding. This allows for other channels to transport oxygen when the pores fill with water. The accumulated water in the larger pores of the cathode is transferred across in the membrane to the anode, facilitating better hydration of the membrane and opposite electrode. Soboleva et al.[343] compared the water management effects of solid and porous carbons, reporting that smaller mesopores (<20 nm) help facilitate WU by capillary action and help retain water.[342] It has also been reported that water can preferentially fill the larger pores, which allows the smaller pores to transport the oxygen throughout the CL.[359] While these reports highlight the role of different size pores on water management further work is required to achieve a more complete understanding, particularly the role of pore size under different environmental conditions.
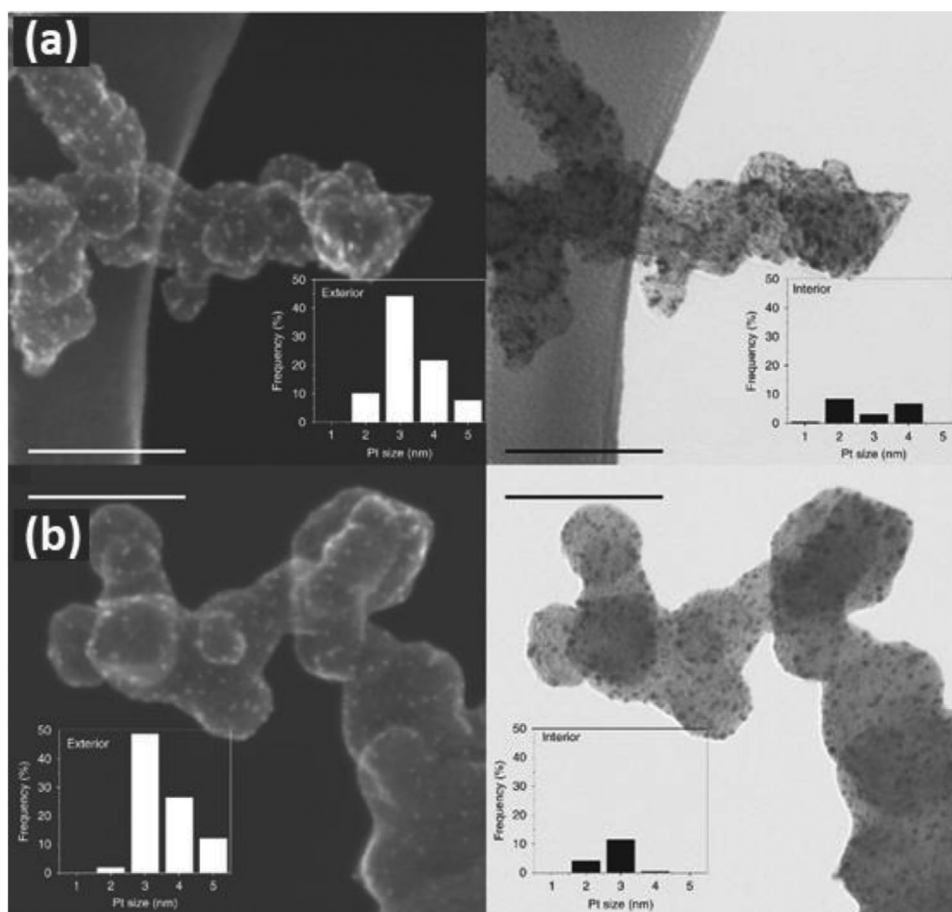
From their comparisons of the performance of different carbon supports, Yarlagadda et al.[63] suggested accessible porous carbons with 4–7 nm pore sizes are an optimum middle ground between narrower pores that limit O_2 transport and larger pores that accommodate catalyst-poisoning ionomer (Figure 25b). They reported that for porous materials, the dry proton accessibility increased and the local O_2 resistance decreased as the volume of smaller mesopores (4–7 nm) increased. This correlation led them to conclude that HSAC, which have internal mesopores 4 and 7 nm, have the ideal balance for achieving high mass activity and low local O_2 transport resistance. Ott et al.[113] reported a synthesis method that formed highly mesoporous support materials by combined acid-treating carbon and heating in ammonia gas. This resulted in a huge increase of surface nitrogen groups and mesoporosity. RDE testing of support materials with different amounts of mesoporosity were shown to have the same performance. However, with the introduction of ionomer and testing in an MEA, the more mesoporous materials possessed better mass transport and mass activity. Improved performance in the kinetic region, particularly in porous materials, is often associated with catalyst located in pore interiors with less direct ionomer contact and therefore reduced poisoning. Given these improvements were not observed in RDE tests in which ionomer is not utilized, it suggests that the origin of the mass activity and mass transport is from the lack of ionomer within the mesopores. However, TEM/SEM comparison of interior versus exterior Pt deposition suggested that the carbon supports investigated have similar exterior/interior location distribution of Pt particles (**Figure 27**). In addition, dry ionomer proton transport measurements suggested near-perfect contact of the ionomer/Pt for the best performing material. This strongly suggests that each Pt catalyst has contact with the ionomer while benefiting from reduced poisoning and improved mass transport. The explanation behind this apparent contradiction and the role of mesopores in this publication is unclear. Ott et al.[113] suggested that the Pt particles are located at the edge of the mesopores and therefore only partially in contact with the ionomer. However, no experimental evidence was used to backup this claim. Indeed, if this analysis is correct, it would require a huge degree of control over the Pt deposition position to achieve a uniform distribution. Given the report from Yarlagadda et al.[63] describing similar performance increase in both mass activity and current density in the mass transport region due to mesoporous carbon, it is clear that some aspects of mesoporosity have a positive impact on performance.[113] However, further research is required to understand the exact location of the catalyst particles with respect to the mesopores and the origin of this performance enhancement.

4.3. Functionalization of Support Materials

The surface and bulk chemistries of the support material have a significant impact on the performance and durability of a CL, which are often overlooked. For example, the exterior surfaces of the carbon supports are typically covered in oxygen functional groups, although the quantity of these groups can vary wildly depending on the material in question, with highly graphitized carbons having very few.[71,76] Functionalization is a widely used technique to selectivity introduce and control the surface chemistry of a support. In the case of high aspect ratio, nanomaterials such as graphene doping should be considered

ADVANCED
SCIENCE NEWS
www.advancedsciencenews.com

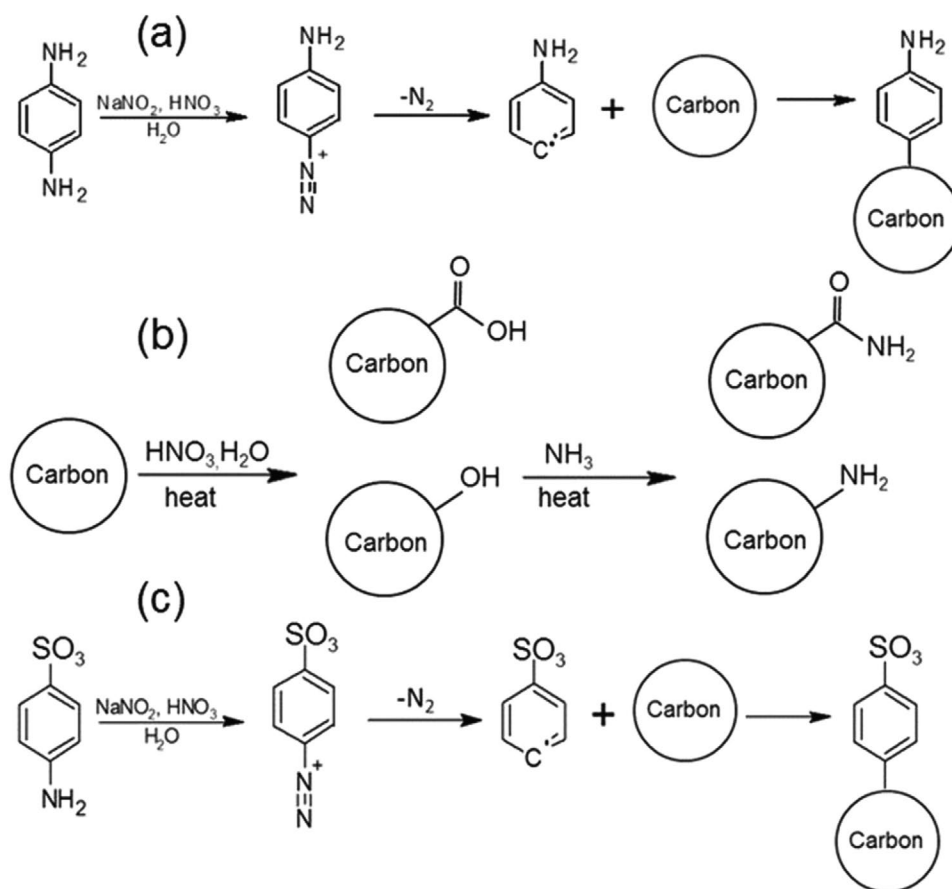ADVANCED
ENERGY
MATERIALS
www.advenergymat.de

Figure 27. Morphological and structural characterization of catalysts. Pt-particle localization of Pt/n-KB 600 °C comparing exterior and interior Pt particle applying SEM and TEM, respectively. a) Pt/n-KB 600 °C. b) Pt/KB. The insets represent a histogram of the Pt particle size distribution exterior and interior. Scale bars, 75 nm. Adapted with permission.[113] Copyright 2019, Springer Nature.

as a form of functionalization due to the surface nature of these materials. A wide variety of possible pathways by which functional groups can be added to the surface of carbon supports exist, including grafting of covalently bonded structures (as shown in **Figure 28**), adsorption of species onto the surface, or by removing the original surface chemistry via acid or heat treatment.[68] Support surface functionalization has been reported to affect catalyst activity,[334–336] catalyst particle size and distribution,[334–337,360–362] ionomer distribution,[113,334,363] durability,[69,334–338] mass transport limitations,[334,363] and CL morphology[337] and are therefore capable of enhancing performance, even at low Pt loadings.[113,334,363] The quantity of introduced functional groups has been reported to be dependent not only on the functionalization pathway but also on the nature of the support with more porous, more amorphous, and high surface area supports achieving higher degrees of functionalization.[334] Functionalization is also often concurrent with a reduction of specific surface area,[113,334,363] but has been reported to both decrease[113,334,363] or increase[113,363] ECSA. This change in ECSA is dependent on which technique is used to acquire the data. For example, Orfanidi et al.[363] reported that RDE testing showed a decrease in ECSA due to the addition

of -NH$_x$ functional groups,[335,360] while an increase in ECSA due to the same functionalization under MEA testing. This apparent contradiction is most likely due to changes in catalyst particle sizes and the changes to ionomer distribution caused by functionalization.[113]

One of the most significant performance limitations for MEAs has been attributed to inhomogeneous or inadequate ionomer distribution across the support.[64] It has been widely reported that the introduction of functional groups can have a significant impact on this.[113,334,363,364] Fang et al.,[334] among many others, have reported that functionalization increases ionomer surface coverage. This was suggested as an explanation for the observed current density improvements, and not proven by a direct measurement, although they did utilize STEM to observe the ionomer distribution with some limited success. Pramounmat et al.[68] reported the use of a polypeptide which was shown to alter the morphology of the ionomer in the CL, in particular increasing the thickness of the Nafion coating. However, the electrochemical consequences of this were not investigated and it is also not clear in what manner the polypeptide altered the ionomer structure, or whether it truly acts as an intermediary between the ionomer and the catalyst

**ADVANCED
SCIENCE NEWS**

www.advancedsciencenews.com

**ADVANCED
ENERGY
MATERIALS**

www.advenergymat.de

Figure 28. Reaction mechanisms for several functionalization schemes: a) Scheme 1 diazonium reaction with para-phenylenediamine for creating positive surface charge in solution, b) Scheme 2 amination for creating positive surface charge, and c) Scheme 3 diazonium reaction with sulfanilic acid for generating negative surface charge. Reproduced with permission.[334] Copyright 2005, IOP Publishing, Ltd.

surface. The interplay between O_2 diffusion through ionomer, film thickness, and free water is thus heavily influenced by the substrate–ionomer interactions unique to particular chemistries and operating conditions, as discussed in Section 3.[365] Functionalization, typically hydrophilic, strengthens the interaction between the functionalized support and the ionomer sulfonic head, which has been reported to create thinner and more homogenously distributed proton-conducting layer.[113,334,363] This results in improved device performance, which is credited to the reduced mass transport and O_2 diffusion resistance from homogeneous ionomer distribution. The impact of relative strengths of the functionalized support-ionomer interaction has been shown by Yang et al.[55] who reported that when simply washed with a Nafion solution, more Nafion adsorbed onto the surface of the PyPBI-coated multiwalled carbon nanotube (MWCNTs) compared to oxidized MWCNTs. While the optimization of ionomer distribution has often been suggested as the cause of performance improvements in a range of publications, there is often a lack of sufficient structural characterization such as porosity, PSD, ECSA, and electrode thickness. It is difficult to determine the exact spatial organization of ionomer/Pt catalyst as discussed in Section 3.7. Given the complexity of the Pt/ionomer/support interaction and the resulting increased

ECSA and dry proton accessibility, much more extensive microscopic, structural, and spectroscopic analysis must be completed on this topic, particularly under different environmental conditions. This would allow for the quantification of how the ionomer distribution is affected by the surface chemistry of the support, hence facilitating functionalization to become a useful tool to controlling ionomer distribution and performance.

A multitude of different functional groups could be theoretically reacted with support material, creating a huge range of functionalized materials. Although, due to the limited number of publications in this area only the use of a few different functional groups have been reported. Functional groups are best categorized by their elemental compositions; however, this is not ideal as there is variation between different functional groups of the same elemental composition. The three main types of functional groups that are reported are nitrogen, oxygen, and sulfur containing. Oxygen functional groups are the most common form of functionalization as they are often present on the exterior surfaces of as-synthesized carbon supports. They are frequency described as defects and are associated with increased carbon corrosion.[69,186,366–368] When new functionalized support materials are compared to commercial carbons, they can in effect be

**ADVANCED
SCIENCE NEWS**

www.advancedsciencenews.com

**ADVANCED
ENERGY
MATERIALS**

www.advenergymat.de

comparing with oxygen surface functional groups depending on exact commercial support material. As such, the properties of oxygen functional groups are rarely reported themselves; a notable exception to this is with reduced graphene oxide (rGO), which is often compared to traditional support materials and unfunctionalized graphene. The oxygen functional groups in rGO are widely reported to cause higher power densities due to more homogeneous ionomer distribution and improved catalyst durability as a result of anchoring interactions between surface functional groups and the catalyst particles (as detailed below); rGO is discussed in more detail in Section 4.8.[369–371]
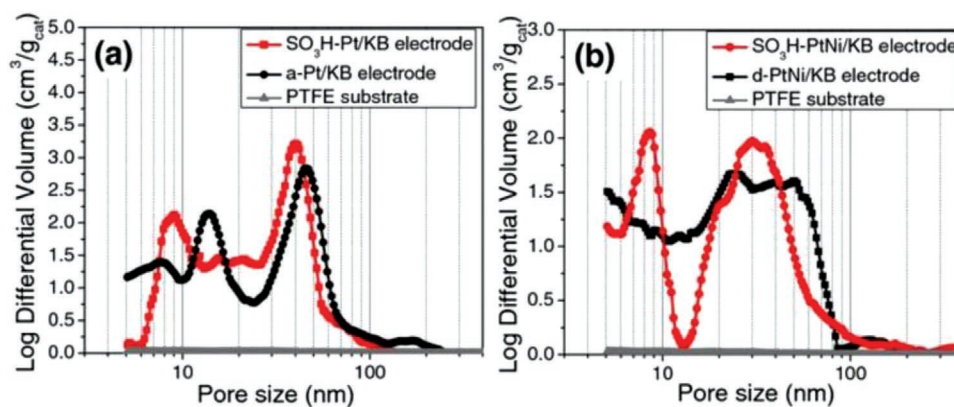
Sulfur-based functional groups are other elements that are commonly explored, partly due to their tendency to form hydrophilic surface groups that are not associated with enhanced carbon corrosion. Xin et al.[362] reported that SO_3H improved O_2 transport at mid to low RH conditions, due to the increased hydrophilicity of the support leading to more water being retained at low humidity conditions. On the other hand, Roy et al.[360] reported sulfur functional groups were detrimental for performance of a DMFC, attributed to reduced mass activity from catalyst poisoning, similar to catalyst poisoning of Pt by PFSA ionomers. This poisoning can be observed within the data reported by Fang et al.,[334] who found simple amines improved current density while phenyl-sulfonate groups caused it to decrease by over 50%. This was suggested to be due to observed increased mass transport resistances; however, the authors did not comment on the ≈50% decrease in ECSA after the sulfur functional group was introduced. This coupled with only small changes in catalyst particle size between the functionalized supports strongly suggests that the sulfur functional groups are poisoning the surface of the catalyst. Furthermore, the sulfur functional groups were found to significantly increase the rate of degradation during carbon corrosion ASTs; the origin of this performance loss was not commented upon. From this, it appears that sulfur functionalization has a negative impact on ECSA, although its hydrophilic functional groups can positively impact device performance under low humidity conditions.

Nitrogen-based groups are the most common type of functionalization, partly due to support materials being functionalized with nitrogen having fairly uniformly reported catalyst durability improvements and higher current densities.[338,363,372] For example, Ott et al.[113] reported higher performance and durability due to N-doping (in addition to other mesoporosity changes); they attributed this to a more homogenous ionomer distribution; however, experimental evidence or further discussion is lacking. Yang et al.[364] discussed the relationship between N-doping and ionomer distribution in more detail. They reported that amine surface groups have a stable interaction with the sulfuric head of the ionomer due to the attraction between NH_3^+ and SO_3^-, as observed from significant increase in carbon support aggregate size when Nafion is added to an ink. They suggested that utilizing functional surfaces, particularly those with a complimentary charge to SO_3^-, would assist in forming homogenous ionomer distribution. However, their experiments only investigated the ionomer/N-doped support interaction in an ink not an MEA and hence lacked performance data such as power density. The studies that have reported the

merits of nitrogen functionalization often lack in-depth characterization and explanation of the origin of the benefits. For example, Karuppanan et al.[373] simply reported that N-doped graphene outperforms PtC in current density, by facilitating homogenous dispersion of catalysts and enhancing electrical conductivity, although experimental evidence of this was not reported. Jung et al.[338] reported the use of graphitized nitrogen and iron-functionalized supports with significantly improved Pt stability compared to commercial PtC. The origin of this effect was reported as being due to the strong interaction between electrons delocalized between the doped graphitic support and the catalyst; however, no experimental data or model was presented to aid in the understanding of this effect. The improvements in the performance due to nitrogen functionalization, particularly in the low-voltage range, have been suggested to be partially attributed to the presence of additional non-metal catalytic C-N sites.[334,374] Lee et al.[375] reported that aniline-functionalized supports possessed higher specific activity under RDE testing, suggested to be due to the presence of catalytically active pyridinic ORR active sites. However, under MEA testing, the same material performed worse than PtC, likely due to the additional non-metal catalytic sites being unutilized in a mass transport limited MEA, although enhanced catalyst durability was observed. RDE-based reports have suggested NH_2-functionalized graphene possess only a minor improvement in initial specific activity compared to nonfunctionalized graphene.[335] However, after AST, the specific activity of the NH_2-functionalized graphene decreased significantly less than nonfunctionalized graphene. This was attributed to Pt anchoring in which improvements to the catalyst stability are associated with electron transfer between the catalyst and the support, binding the components together.[335] It is associated with changes in the binding energy of the relevant elements, measured via XPS.[335] Furthermore, higher catalyst mass activity has often been reported due to functionalization, particularly for nitrogen-based functional groups; this has been suggested to be due to electron density shifts between the Pt catalyst particle and the support functional groups.[113,334–336,360,376] While catalyst stability and mass activity improvements are often observed, it is difficult to quantify the impact and strength of these interactions. More in depth research is required to understand the relationship between changes in binding energy from XPS and performance/durability improvements.

It has been extensively reported that carbon corrosion occurs at different rates depending on the chemical structure of the support.[377] Fang et al.[334] reported the impact of functionalization with phenyl-amine, phenyl-sulfonate, and amine functional groups on the durability of HSACs and LSACs. The rate of carbon corrosion in HSAC, in this case KetjenBlack, increased with all the functionalization pathways explored in this publication. Hard carbons, such as Vulcan, showed little difference in chemical corrosion across functionalized samples. Faster corrosion of HSACs was suggested to be due to the introduction of defect sites and less chemically stable surface groups. The authors also reported an improvement to durability due to the same series of functionalization on a different highly graphitized sample, but due to its proprietary nature, the exact origin of this effect is unclear. Li et al.[337] and further work by this group[74] reported

ADVANCED
SCIENCE NEWS
www.advancedsciencenews.com

ADVANCED
ENERGY
MATERIALS
www.advenergymat.de

Figure 29. Specific pore volume distribution curves of PTFE film substrate, CLs with and without functionalization. Reproduced with permission.[362] Copyright 2017, Electrochemical Society.

a 66 mV loss at 0.8 A cm^{-2} for PBI-functionalized rGO compared to a 602 mV loss for non-functionalized rGO. They suggested that their method of functionalizing graphene with PBI targets the most active site of the graphitic materials, resulting in the most reactive parts of the supports becoming terminated with stable functional groups forcing alternative degradation routes, particularly in a highly defective material, such as rGO.
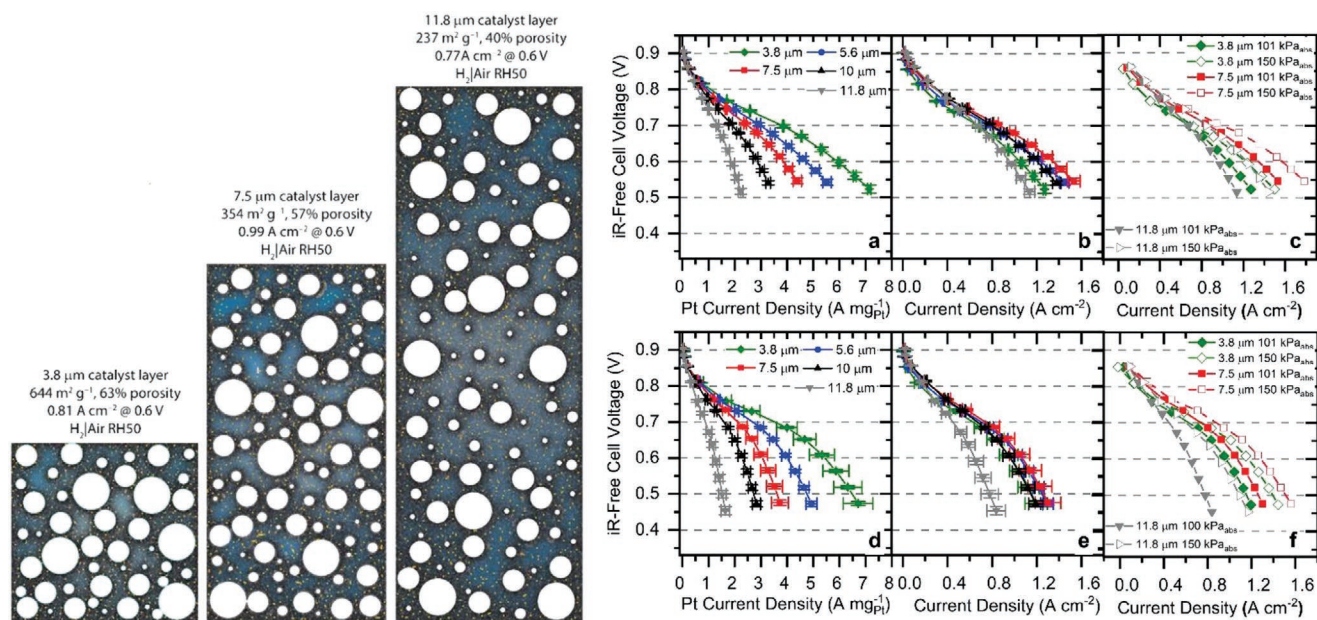
As mentioned above, variations in the local chemical structure between similar functional groups can cause a significant change in hydrophilicity, which has a significant impact on water management. Hydrophobic functionalization, typically via introduction of fluorine into the support surface chemistry, has been reported to reduce carbon corrosion by 50%.[69] Li et al.[378] reported that surface functionalization of C_6F_5 significantly changes the hydrophobicity of the carbon support. Forouzandeh et al.[330] from the same research group, tested the durability of these hydrophobic supports via CV cycling in sulfuric acid, and showed improved durability compared to non-functionalized samples. However, this measurement was taken without the presence of Pt catalyst, which also contributes to carbon corrosion mechanisms or ionomer, which will likely have disrupted surface distribution by this functionalization. Simple hydrophobic functionalization may have great potential for creating high carbon corrosion resistant supports, but more in situ MEA testing is required to investigate this. Changes in hydrophilicity have also been reported to impact other aspects of CL preparation; for example, Xin et al.[362] reported significant changes in the PSD of a functionalized CB compared to a non-functionalized material, as shown in **Figure 29**. They reported this to be due to the more hydrophilic functional groups being dispersed differently within the ink, changing CL PSD and led to enhanced fuel cell performance after deposition. Experiments attempting to measure performance changes from functionalization must be careful to keep every other variable constant, such as porosity, ionomer distribution, catalyst size, Pt loading, and ECSA, but this is not facile as all can be impacted by functional groups. It is therefore key that as much morphological and structural characterization as possible is reported, to help facilitate understanding. Furthermore, additional follow-up publications that explores the origins of

performance enhancement are strongly encouraged, as optimizing functionalization to develop next-generation materials requires this in-depth understanding that is lacking in most publications.

4.4. CL Thickness and Heterogeneous Electrodes

The thickness, Pt distribution, and catalyst loading all have an impact on performance. However, this is not a facile relationship with specific activity and Pt utilization depending on electrode thickness or Pt loading. Typical CLs range from 5 to 10 μm in thickness with uniform Pt, porosity, and ionomer distribution across the film. While this structure is widely used, heterogeneous distributions has been shown to effect performance, as discussed in Section 2.5.2. New CL structures have been explored for potential benefits, such as significantly thinner electrodes or porosity and ionomer gradients across the electrode. Owejan et al.[245] investigated how heterogeneous Pt distribution affects performance by comparing uniform PtC materials to high-loading PtC diluted with bare carbon, while maintaining overall loading and thickness. They reported that inhomogeneous Pt distribution (high loading Pt/C diluted with bare CB) had a negative impact on cell performance compared to uniform Pt distribution (across the thickness of the cathode). This was not related to the surface area of Pt which was kept roughly constant, but suggested as being a result of the higher O_2 flux through the ionomer around the Pt. It was suggested this increased transport losses through the ionomer, although this conclusion was based on the assumption that the ionomer was uniformly deposited across the CL.[245] Further research in this area is required to resolve the relationship between inhomogeneous Pt distribution and performance and how this relates to O_2 flux, as discussed in more detail in Section 3.4.

The performance of catalysts change with Pt loading in CLs where the thickness is constant. Suzuki et al.[379] reported that while reduced catalyst content caused a reduction in current density, the current density per mass of Pt (mass activity) significantly increased, particularly in the mass transport dominated region of the polarization curve. Almost identical values of ECSA for the differently loaded electrodes indicated that
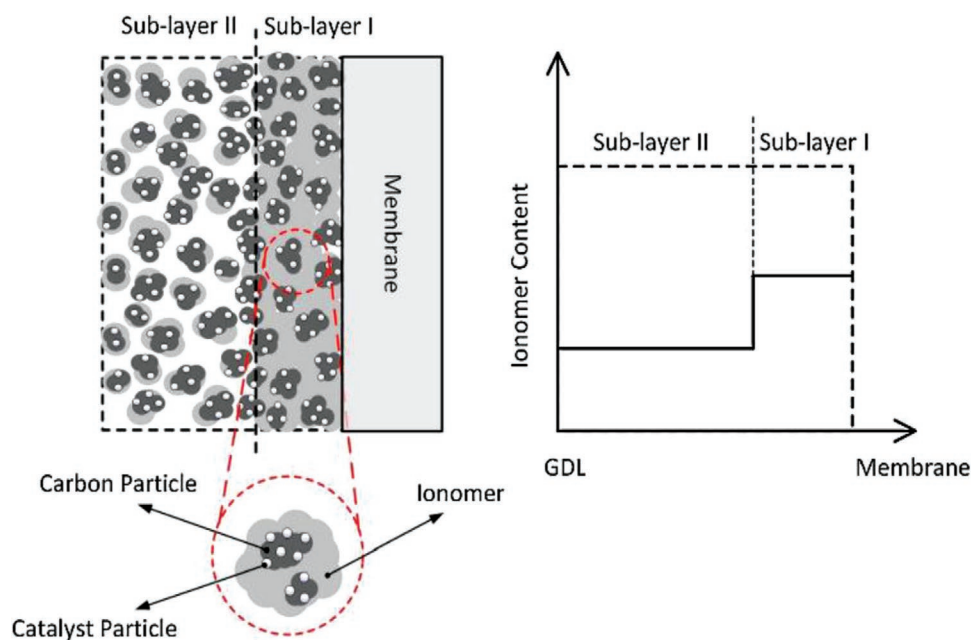
**ADVANCED
SCIENCE NEWS**

www.advancedsciencenews.com

**ADVANCED
ENERGY
MATERIALS**

www.advenergymat.de

Figure 30. Left: Schematic illustrating the porosity of 3.8, 7.5, and 11.8 μm cathode CLs. Pore size content extracted from N_2-sorption porosimetry data. Placement of pores is qualitative. Pores are white, carbon is black, Pt is yellow, and Nafion is blue. Right: Polarization curves as a function of cathode CL thickness under the following conditions: H_2|Air at stoichiometric flow of 2|2, 80 °C cell, and 64 °C gases (50% RH, top row) and 79 °C gases (100% RH, bottom row). a,d) iR-free cell voltage versus Pt mass-normalized current density; b,e) iR-free cell voltage versus current density; c,f) iR-free cell voltage versus current density at 101 kPa$_{abs}$ (solid symbols) and 150 kPa$_{abs}$ applied back-pressure (open symbols). Adapted with permission.[350] Copyright 2019, Elsevier.

these changes were not due to variation in catalyst particle size. This suggests that each Pt particle has the capacity to drive larger currents than typically utilized in high loaded electrodes. For studies in which the thickness of the electrode varies with the catalyst loading, the Pt mass normalized current is highest for very thin CLs, and decreases with thicker films, as shown by Sassin et al. (**Figure 30**b) among others.[350,379–382] Furthermore, the absolute current densities were higher for very thin (3.8 μm, 0.18 mg$_{Pt}$ cm^{-2}) CLs, compared to very thick (11.8 μm, 0.51 mg$_{Pt}$ cm^{-2}) ones. These changes in performance have been suggested to be due to limitations in the mass transport, often the rate determining process.[379] Of which, the O_2 transport limitations have been reported to be an important factor, as charge transfer resistances were similar for all CLs, apart from the very thinnest electrodes.[379,380] In addition, reduced Pt utilisation is often observed in thicker electrodes. Kriston et al.[381] reported the changes in performance and Ef$_{Pt}$ with Pt loading, observing an increase of Ef$_{Pt}$ from 48% to 82% as the catalyst loading (in this case expected to be roughly proportional to thickness) was decreased from 0.4 to 0.05 mg$_{Pt}$ cm^{-2}. This is most likely a consequence of reduced porosity in thicker electrodes.

The reduced performance of thicker electrodes is broadly appreciated across the literature as being due to an exacerbation of mass transport resistances. However, no one mechanism can be used to explain how thicker electrodes impact performance, it is best understood as a combination of factors. Some publication have explored certain aspects, for example, Sassin et al.[350] (Figure 30a) showed a correlation between the porosity of the CLs in their study with electrode thicknesses, ranging from

63% porosity in 3.8 μm electrodes to 40% porosity in 11.8 μm CLs. They reported that the highest performance was achieved at a thickness of 7.5 μm and porosity of 57%. They suggested that achieving maximum performance required finding the optimum porosity. They also suggested that the origin of the reduced porosity in thicker electrodes was due to pore collapse associated with solvent evaporation during fabrication.[350] Similarly, Talukdar et al.[383] showed that the performance of an electrode was directly related to its porosity, where a porosity change from 18.4% to 24% was associated with current density increase from 1 to 1.5 A cm^{-2} at 0.3 V. This was attributed to increased Pt utilization as shown by the ECSA increase from 17 to 29 m^2 g^{-1}. They suggest that thick CLs (>10 μm) and ultra-thin ionomer coatings limit the charge transport. The exact relationship between pore size, porosity and electrode thickness has not reached a consensus within the literature. Kriston et al.[381] reported the changes in performance and Ef$_{Pt}$ with Pt loading, observing an increase of Ef$_{Pt}$ from 48% to 82% as the catalyst loading was decreased from 0.4 to 0.05 mg$_{Pt}$ cm^{-2} (roughly proportional to thickness in this case). Sassin et al.[350] observed little change in the PSD with thickness. This in contrast to Talukdar et al.,[383] Kriston et al.[381] reported an increase in average pore diameter with higher loading. However, the manufacturing route used by Kriston et al.[381] was similar to Sassin et al.[350] who did not observe these effects; it is likely that the relatively low ionomer content used by Kriston et al.[381] helped reduced the loss of porosity in thicker electrodes.[50,380,383] As such the relationship between PSD and electrode thickness seems to depend largely on the exact manufacturing method and ionomer loading.

**ADVANCED
SCIENCE NEWS**
www.advancedsciencenews.com

**ADVANCED
ENERGY
MATERIALS**
www.advenergymat.de

Figure 31. Schematic of the ionomer-gradient cathode CL (CCL) design with ionomer loading decreasing away from the membrane interface. Reproduced with permission.[385] Copyright 2018, Elsevier.

The thickness of the electrodes also has implications on other aspects of performance; for example, thin CLs (>4 μm) typically possess higher porosity and low total pore volume (as discussed in Section 3.4); hence, they suffer from flooding, which in turn significantly increases the O_2 transport resistances.[50,245,350,380] Very thick CLs (<11 μm) are less likely to suffer from this effect but increases in O_2 transport resistance are typically observed due to the highly tortuous gas diffusion pathway.[375,380,384] The porosity of a CL is a morphological aspect that is dependent on the manufacturing techniques; hence, researchers should aim to control it through the use of alternative fabrication techniques. This raises the possibility of retaining a high porosity even with thicker electrodes, improving Pt utilization, current density, and water management, if the manufacturing methods are optimized for thicker CL design.[323,379]

CLs with a Pt distribution, support materials, or porosity gradient along the membrane-MPL axis have been suggested as a novel CL structure that could be utilized to improve performance. Typically publications use only dual CL systems formed from two layers with distinct morphologies that are combined to make up a single electrode, as shown in **Figure 31**. For example, Ye et al.[386] reported a catalyst and porosity gradient formed with one PtC layer and one carbon nanofiber (CNF)/CNT CL. This electrode system showed a 22% reduction of ECSA compared to a standard homogenous electrode but showed a ≈10% improvement in current density at 0.3 V, suggested to be due to enhanced mass transport. However, the authors utilized several testing aspects such as CV measurements being carried out on RDE while MEA data was used to report the current density, which makes comparison between samples difficult. Furthermore, the dual CL with the CNF/CNT was only compared with single-layer commercial PtC and not with single layer CNF/CNT, which would have further facilitated comparison. As a result, it is difficult to determine what

caused the performance improvements. Zhao et al.[387] reported a novel dual CL in which a hydrophilic layer containing Nafion and Pt/C was first sprayed onto a membrane followed by a hydrophobic layer which contained PTFE and Pt/C, which was achieved by depositing different thicknesses of the respective inks. They reported a performance increase of the dual-layer CL system compared to commercial PtC (≈10% current density @0.3 V) with maximum current density achieved via use of a thick hydrophilic layer (0.3 mg cm⁻²) and thin PTFE layer (0.1 mg cm⁻²), which was suggested to be due to improved water management across the cell, although this was not characterized in detail in this publication. However, in this dual CL system, the hydrophobic layer contains no ionomer, which would be expected to significantly reduce Pt utilization in this half of the electrode. Further investigation of this CL design would be required to confirm the exact source of performance improvements, and determine the Pt utilization within a dual CL in which one CL has no ionomer.

CLs manufactured with ionomer and catalyst gradients from the membrane to the GDL have been explored. Higher ionomer content nearer the membrane with a gradual reduction approaching the GDL has been widely reported to outperform uniform CLs and those with the ionomer gradient inversed.[356,385,388] Shahgaldi et al.[385] reported that this methodology resulted in a 13% higher maximum power density, Kim et al.[388] a roughly 10% increase in current density, and Xie et al.[356] a 20% improvement in current density. All of these reports were coupled with small or no changes in the ECSA of the CL and the publications broadly agree that the enhanced performance was based on improved proton conductivity at the CL/membrane interface and improved mass transport due to the reduction of ionomer near the GDL. This CL structure splits the trade-off between ionomer content and mass transport within the CL into two sections. This allows localized high
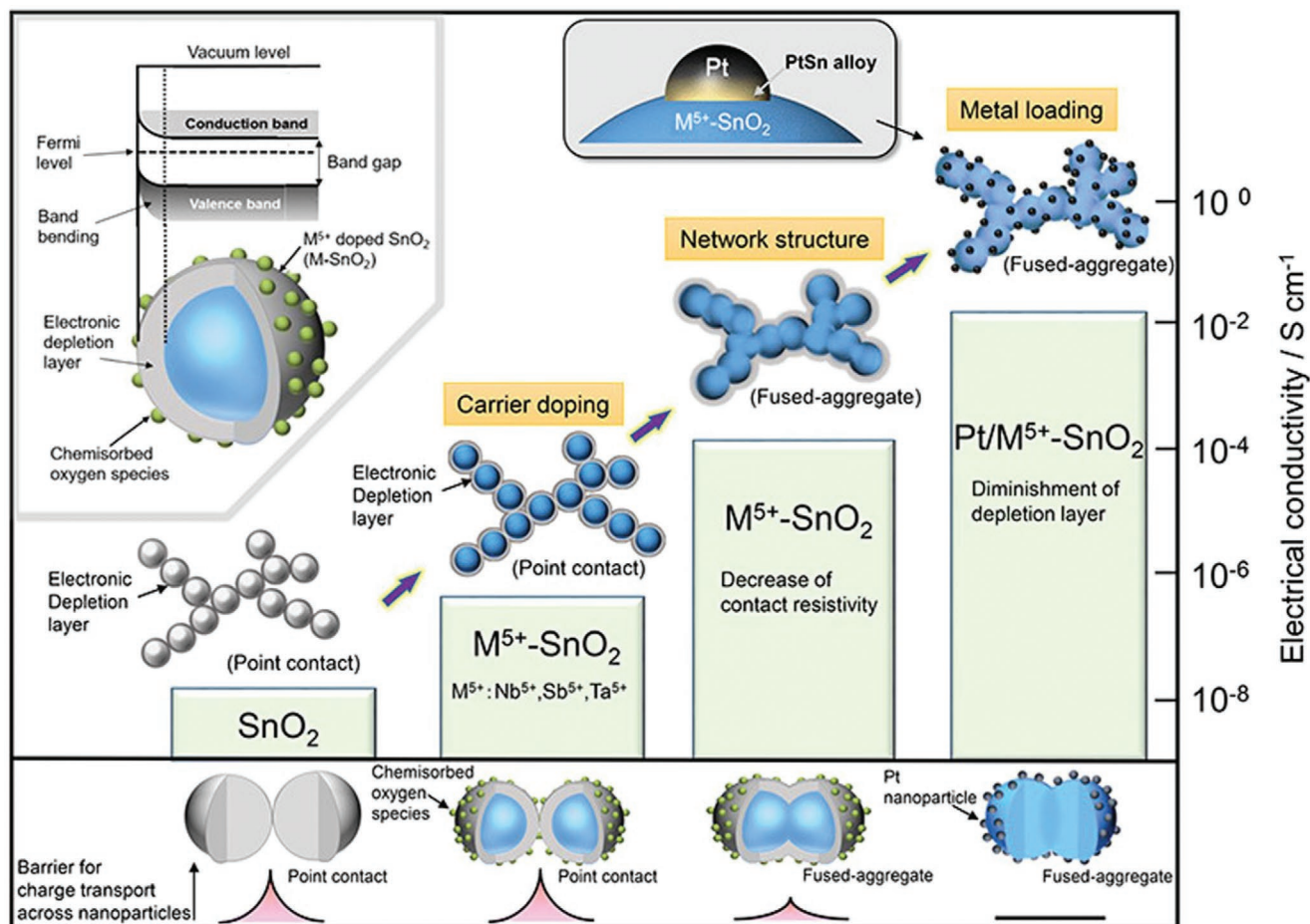
porosity near the GDL, and higher ionomer loadings near the membrane and hence improved overall mass transport and proton conductivity. The ionomer gradient with a maxima near the membrane was also used by Chen et al.,[389] although these authors also investigated the impact of a Pt gradient. They reported almost 40% increase in power density when the maxima of the Pt and ionomer gradient was highest next to the membrane compared to a uniform CL. This value of the current density was even higher under low humidity conditions. Similarly, these performance enhancements were attributed to improved mass transport and Pt utilization, although ECSA of the graded CLs were lower than the uniforms ones. The structure reported by Chen et al.[389] would be expected to significantly increase O_2 transport resistance and Pt catalyst poisoning due to high localized ionomer loading near the membrane. However, this was found not to be the case, or at least suggested that these effects are mitigated by the enhanced mass transport near the GDL side. The significant variation in reported current and power densities from the catalyst and ionomer gradients compared to other reports is most likely due to differences in ionomer content, Pt distribution, and testing conditions.

Hydrophobicity has also been introduced into the CL to improve water management, typically through the inclusion of polytetrafluoroethylene (PTFE).[331] PTFE has been widely reported to be used as a binder in CLs, which impacts the morphology of the CL during fabrication.[331,390] For example, Therdthianwong et al.[391] reported that the introduction of PTFE into the CL significantly reduces the micro- and meso-porosity and slightly increases the macro-porosity. They further reported that CLs formed with PTFE achieved higher current density by reducing activation losses and lower O_2 diffusion resistances through reduction of localized standing water.[391,392] This suggests that a hydrophobic component in the CL ensures that some regions of free volume remain during flooding and retain a pathway for gas transport through the CL. However, patterning the distribution of the PTFE in the CL has been reported to not benefit the performance.[391] It is not clear if this effect is due to morphological changes imposed by the addition of PTFE, the changes in the water distribution across the CL or a combination of both. Alternatively, Avcioglu et al.[331] reported that the introduction of PTFE causes a reduction of Pt utilization, ECSA, and a 60% loss in pore volume, which suggest the Pt utilization loss is related to the porosity reduction, although direct covering of the hydrophobic polymer on the catalyst surface could also be the cause. Nonetheless, higher loadings of PTFE, up to 30%, can significantly reduce or eliminate mass transport limitations arising due to flooding, meaning this may be a useful trade-off between performance losses for applications in high humidity environments.[331,393] Performance differences between these reports seems to be related to the electrode thickness, in which thinner electrodes benefit more from the presence of hydrophobic PTFE, as their water vaporization is limited and are more prone to flooding.[50,392] By contrast, thicker electrodes will suffer greater Ohmic resistance from a non-electrical or proton conductive phase being introduced into the CL. Other hydrophobic CL additives such as polydimethylsiloxane (PDMS) have been suggested by Ungan et al.,[332] and reported to improve current density when added to a CL. However, it is not clear why the reported ECSA of Pt/PDMS was higher than that of Pt-only under RDE testing. Furthermore, in MEA testing, all loadings of the hydrophobic polymer from 0 to 30% were shown to perform better than pure catalyst, reportedly due to improved water management and reduced O_2 diffusion limitations. This is markedly different to literature observations for other hydrophobic polymers such as PTFE.[331,391,393]

4.5. Alternative Support Materials

Due to their high electrical conductivity, ease of manufacturing and low cost, the most widely used catalyst supports in laboratory development and commercial applications are based on carbon. However, they suffer from chemical and structural corrosion in the acidic aqueous environments found in operational fuel cells, particularly during long cycling or fuel starvation conditions.[69] Graphitized carbon supports have been widely reported to possess increased carbon corrosion resistance compared to more amorphous carbon structures.[74,178,186,225,322–324] This has been taken to the logical conclusion with graphene and other graphitic nanomaterials being widely explored as support materials, as discussed in more detail in Section 4.8. Conductive ceramics have also been reported as a potential replacement for CB.[394,395] These doped metal oxide-based supports typically show lower electrical conductivity and initial performance, but higher current density after AST due to their superior corrosion resistance, particularly at high potential.[77,394–399] However, these support materials suffer from less well-understood degradation mechanics than CB, such as the loss of dopant during operation (shown in **Figure 32**), causing a reduction of electrical conductivity.[398,400] Takabatake et al.[401] compared the electrochemical activity and stability against dissolution of the Pt deposited onto several metal oxide materials, suggesting that SnO_2 was the most promising. However, the ECSA of the metal oxides including SnO_2 was significantly lower than that of PtC. Since catalyst particle size has a large impact on stability and performance, is it difficult to compare the relative catalyst stability. Kakinuma et al.[402] reported that the Pt deposited onto Nb-doped SnO_2 formed a PtSn alloy between the catalyst and the surface, which enhanced the electron transfer to the catalyst by reducing the Schottky-type barrier. They also reported that the conductivity had a significant dependence on the Pt loading. The same authors[253] found that Nafion coated the hydrophilic Nb-SnO_2 more consistently compared to hydrophobic commercial PtC, requiring significantly less ionomer. This highlights the need to reassess I/C ratio when novel catalyst or supports are used to ensure their performance is optimized in comparison to CB. The reduced but more homogeneous ionomer coatings were suggested as having the dual benefit of increasing Pt utilization and increasing pore volume, allowing for greater mass transport. However, the thickness of the Nafion layer was simply inferred from TEM images to be uniform and estimated based on the support/ionomer ratio and the support surface area; more detailed characterization of the ionomer distribution would be required to confirm this hypothesis. Dhanasekaran et al.[403] reported a composite carbon and ZrO_2 support with between 0 and 30% carbon mass. The ECSA was found to be significantly lower on metal oxides with reduced carbon content; however, the origin of this was not widely

**ADVANCED
SCIENCE NEWS**

www.advancedsciencenews.com

**ADVANCED
ENERGY
MATERIALS**

www.advenergymat.de

Figure 32. Schematic diagram of methods to enhance the electrical conductivity of tin oxide based supports. Reproduced with permission.[402] Copyright 2019, American Chemical Society.

discussed. Initial performance of the 20% carbon CL was superior to PtC (roughly 3.3 A cm^{-2} to 2.5 A cm^{-2} at 0.3 V, respectively), and showed significantly reduced performance loss after high voltage ASTs. The superior performance was suggested to be due to electron transfer between the support and the catalyst, while the durability improvements were due to reduced carbon loss and enhanced catalyst durability. While the performance and durability reported were very impressive, it is worth noting that the Pt was deposited onto both the carbon and the ZrO$_2$ and hence the origin of the durability improvement for the carbon phase is unclear. Doped metal oxides offer a worthy potential replacement to traditional carbon supports, with both support and catalyst durability improvements being reported, due to the interaction between the support and the catalyst, which modifies the electronic structure of the catalyst and potentially improves its durability.[399,404] However, they suffer from some conductivity limitations and increased difficulty of functionalization of the metal oxide surface compared to carbon based supports.

4.6. Flooded Porous Electrodes

In this case, Muzaffar et al.[50] has suggested that an instructive way to categorize CLs is into two different proton transport

designs: the common GDE, which requires ionomer, and flooded porous electrodes (FPEs), which do not require ionomer.[50,198,405] CL designs do not require support materials,[406] and others do not require ionomer as the thickness of the CL is small enough to utilize localized water to transfer protons without significant O$_2$ diffusion limitations.[61,197,200] This simplifies the CL structure, eliminating catalyst poisoning by the ionomer and the thickness of the electrode resulting in less tortuous gas transport across the CL and no O$_2$ diffusion resistance across the ionomer/catalyst boundary (as discussed in Section 3.4).[52,407] Most NSTFs are FPEs,[50,52,198,199,407] due to their very thin CL on the order of 0.5-2 μm utilizing liquid water for proton conduction.[50,384] NSTFs such as those developed by 3M have been reported to achieve high current densities, especially at low Pt loading where they outperform commercial catalysts, partially due to them being less affected by O$_2$ diffusion limitations (as discussed in Section 3.4).[52,198,199] However, due to their requirement for a very thin CL and high surface area they are sensitive to water management and RH changes.[199] The thin structure of NSTFs limits water vaporization and makes them susceptible to flooding at high current densities.[50,51] Due to their thin CL and dependence on high catalyst surface areas for high performance, NSTFs are typically highly engineered such as those shown as **Figure 33**; however, this does not
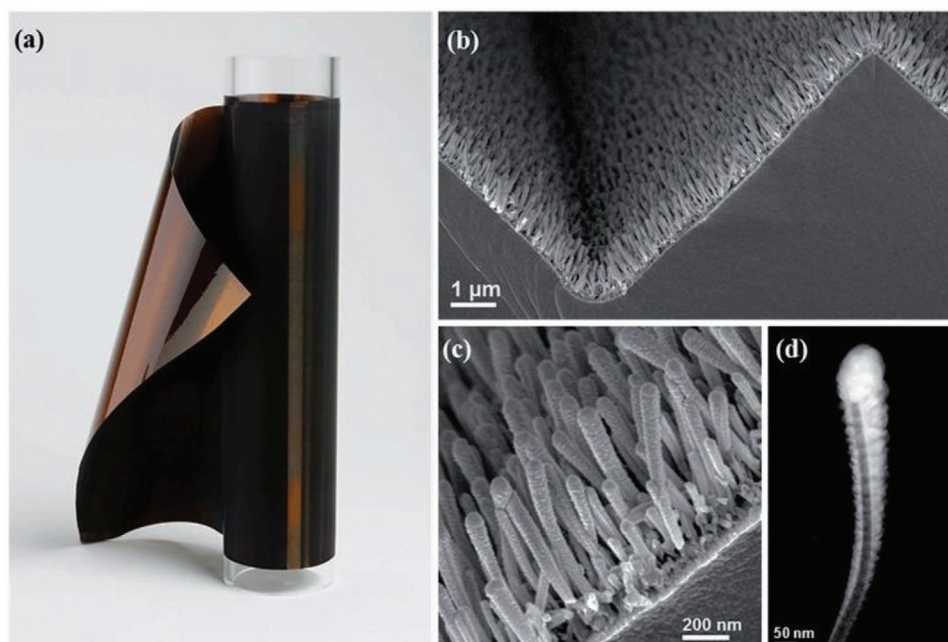
Figure 33. a) Photograph of a NSTF roll, b,c) SEM images of Pt3Ni7/NSTF, d) STEM-HAADF image of an individual Pt3Ni7/NSTF whisker. Adapted with permission.[405] Copyright 2015, Royal Society of Chemistry.
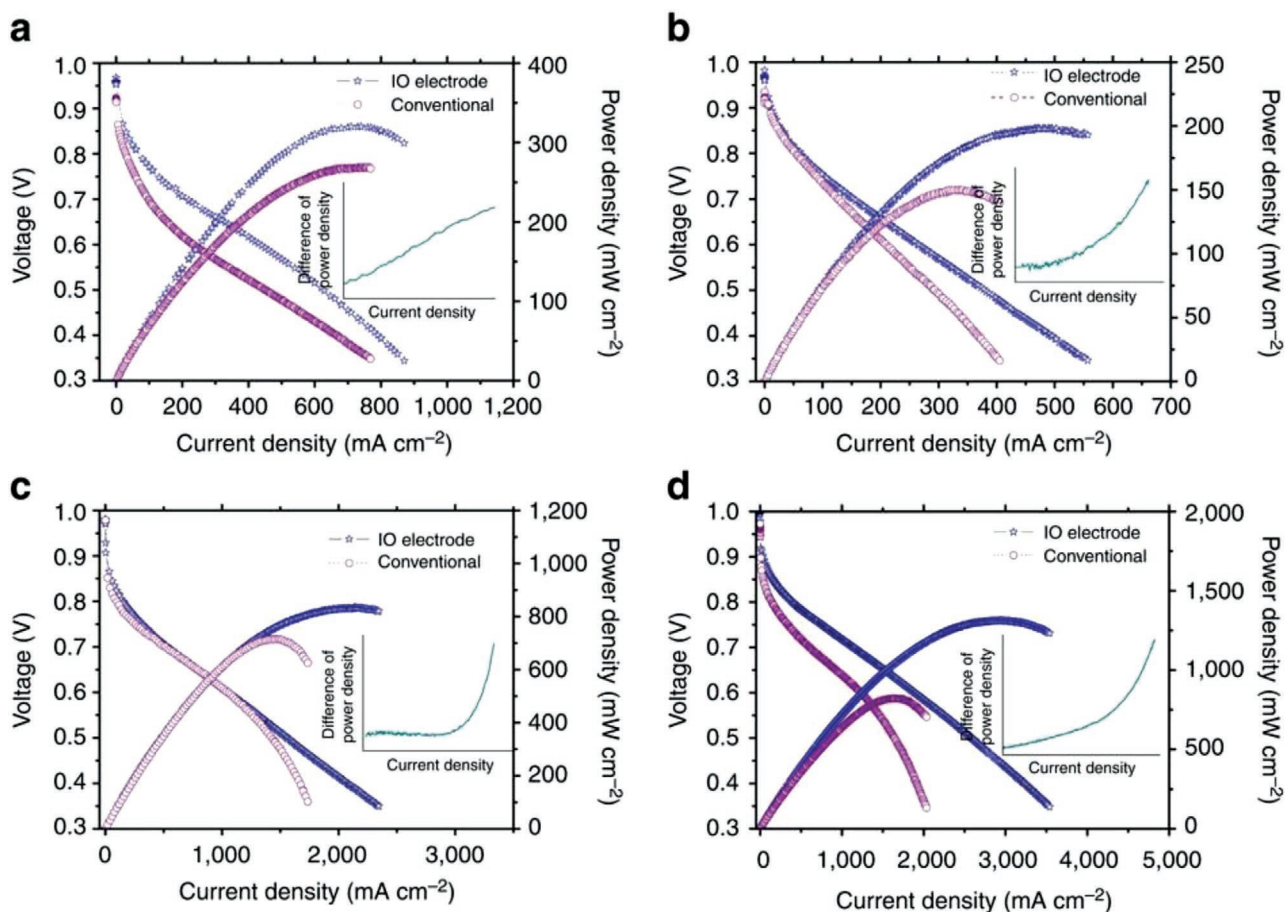
guarantee high Pt utilization. For example, Deng et al.[408] fabricated hollow nanotubes of Pt to act as the CL. The ECSA of the Pt tubes was much lower than commercial PtC, even though the experiment was undertaken on an RDE, suggesting a low Pt utilization, most likely from tubes walls excessive thickness. The performance of these structures appeared to be similar to PtC; however, given differences in Pt loading it is difficult to determine the origin of these effects in this publication.

Kinkead et al.[409] constructed a nanostructured FPE from a template of polystyrene nanospheres, creating an inverse opal (IO) structure. The resultant CL was a thin, continuous, and highly porous layer made entirely of Pt. The performance of these highly ordered FPEs was reported to be better than commercial systems, particularly in the mass transport region. Using a different manufacturing technique, but a similar CL design, Kim et al.[384] reported achieving an very impressive 3.5 A cm^{-2} at 0.35 V with a 0.2 mg Pt cm^{-2} loading (see **Figure 34**d). However, the ECSA and Pt utilization were similar or lower than commercial PtC and it is only in the mass transport regime or higher pressures that the IO structure significantly outperformed conventional materials. Since these improvements were a consequence of mass transport improvements and not catalyst kinetics, it is the reduction of CL thickness, tortuous diffusion pathways, and proton conductivity resistances that yield this higher performance. However, the durability of this CL design is not clear as Pt catalyst aggregation typically occurs as part of fuel cell operation. A CL constructed entirely from Pt catalyst would be highly susceptible to Pt agglomeration and CL thinning, which would significantly change the morphology and therefore performance. While they show excellent performance, the durability of FPE electrodes is largely unknown and ASTs on FPEs are required to understand their commercial relevance.

4.7. Imaging and Measuring Porosity

It is key to quantify the change in porosity and PSD in order to understand how the structure of a CL changes due to the materials or manufacturing methods used (as discussed further in Section 5). Typically, surface area measurements are achieved based on N_2 adsorption using Brunauer–Emmett–Teller (BET) or Barrettt–Joyner–Halenda (BJH) methods, which are also commonly used to measure PSD from 1 to 100 nm.[64,288,331,351,410] To determine the PSD of materials with larger pore sizes other techniques such as mercury porosimetry are typically used.[351,410,411] Mercury intrusion porosimetry is commonly used to measure pores sizes between 3 nm to 1 µm and may be destructive to the sample due to its high intrusion pressure.[410] It is also often the case when developing novel support materials that a qualitative investigation of the CL morphology is required. Some of the most useful tools for this are SEM and electron dispersive X-ray spectroscopy (EDS or EDX) that yield information about the surface of a sample, such as surface roughness and elemental composition.[288,386,411] Cross-sectional SEM allows imaging through a slice of the CL, which gives information about the CL morphology and allows for determination of the porosity, PSD, quantity of isolated pores, and Nafion distribution.[358] Cross-sectional SEM images are typically prepared by filling an MEA with epoxy resin, followed by polishing or microtoming, to ensure that the sample does not degrade under the electron beam.[412] This results in direct visualization of structural information from the CL, with minimal distortion from sample processing. This technique has been improved upon when used in conjunction with a focused ion beam (FIB), which allows a user to capture a series of cross-sectional images via FIB erosion.[412,413] These images

ADVANCED
SCIENCE NEWS
www.advancedsciencenews.com

ADVANCED
ENERGY
MATERIALS
www.advenergymat.de

Figure 34. Polarization curves of IO electrode-based MEAs. a) Using a fully humidified H_2/O_2 supplement and maintained at 80 °C. b) Under ambient humidity and room temperature condition. For both MEAs, the cathode catalyst loading was ≈0.12 mg_{Pt} cm^{-2}. c) Polarization curves from US Department of Energy's reference conditions with 0.12 mg_{Pt} cm^{-2} and d) 0.20 mg_{Pt} cm^{-2} of cathode catalyst loading. Test at 80 °C H_2/air in MEA; fully humidified with total outlet pressure of 150 kPa; an anode stoichiometry of 2; and a cathode stoichiometry of 2 for air. The inset show the difference between the power densities of MEAs with a conventional electrode and an IO electrode. Reproduced with permission.[384] Copyright 2013. Springer Nature.

can be reconstructed to give a 3D image of a CL. This extra dimension allows for information about pore volumes to be obtained, which provides a more realistic representation of the sample being imaged.[292,412,414,415] Furthermore, this 3D reconstruction can be used for modeling and simulations of the various transport processes present within the MEA, including O_2 transport, electron conductivity, and proton conductivity, among many others.[323,349,406,412,414] Other methods have also been utilized to resolve the pore structure, such as X-ray CT. However, the resolution of X-ray CT is currently limited, as distinguishing between the NPs of the support/Pt are beyond the resolution of the technique.[242,292,410,416] A combination of several techniques should be used when investigating CL structures to provide a more realistic representation.[349,410,417]

While SEM provides information about the bulk CL porosity, visualization of the Pt NPs or ionomer distribution is beyond the limits of the technique's resolution. Thus, TEM imaging of fuel cell components can be employed to provide information on support aggregate size, catalyst particle size, ionomer distribution, and ionomer thickness.[248,288,323,334] Typically, the ionomer shell thickness of catalyst aggregates

is estimated from visual inspection of the agglomerate edges. However, the distinction between support material and ionomer is not trivial, even if EDS spectra and maps are also obtained. It is not clear how representative estimations of the ionomer distribution and thickness are from TEM images, as they only image the edge of agglomerates, not the interior, top, or bottom surfaces. Furthermore, the preparation of samples for TEM imaging usually involves sonication or soaking in solvent, which can change the morphology of the surface ionomer distribution. The bulk structure will, of course, change structure and porosity, due to the different drying conditions and particle/particle interactions, which will change during sample preparation. Park et al.[64] reported a technique to measure and compare the ratio of interior to exterior Pt catalyst for different carbon support materials. This requires STEM with a 360° sample holder, allowing a fully representative quantification of commercial PtC, as shown in **Figure 35**. This powerful technique was used to show the superior oxygen and proton mass transport properties of surface located catalyst particles.[353] The location of the catalyst particles has been reported to play a role in performance, particularly
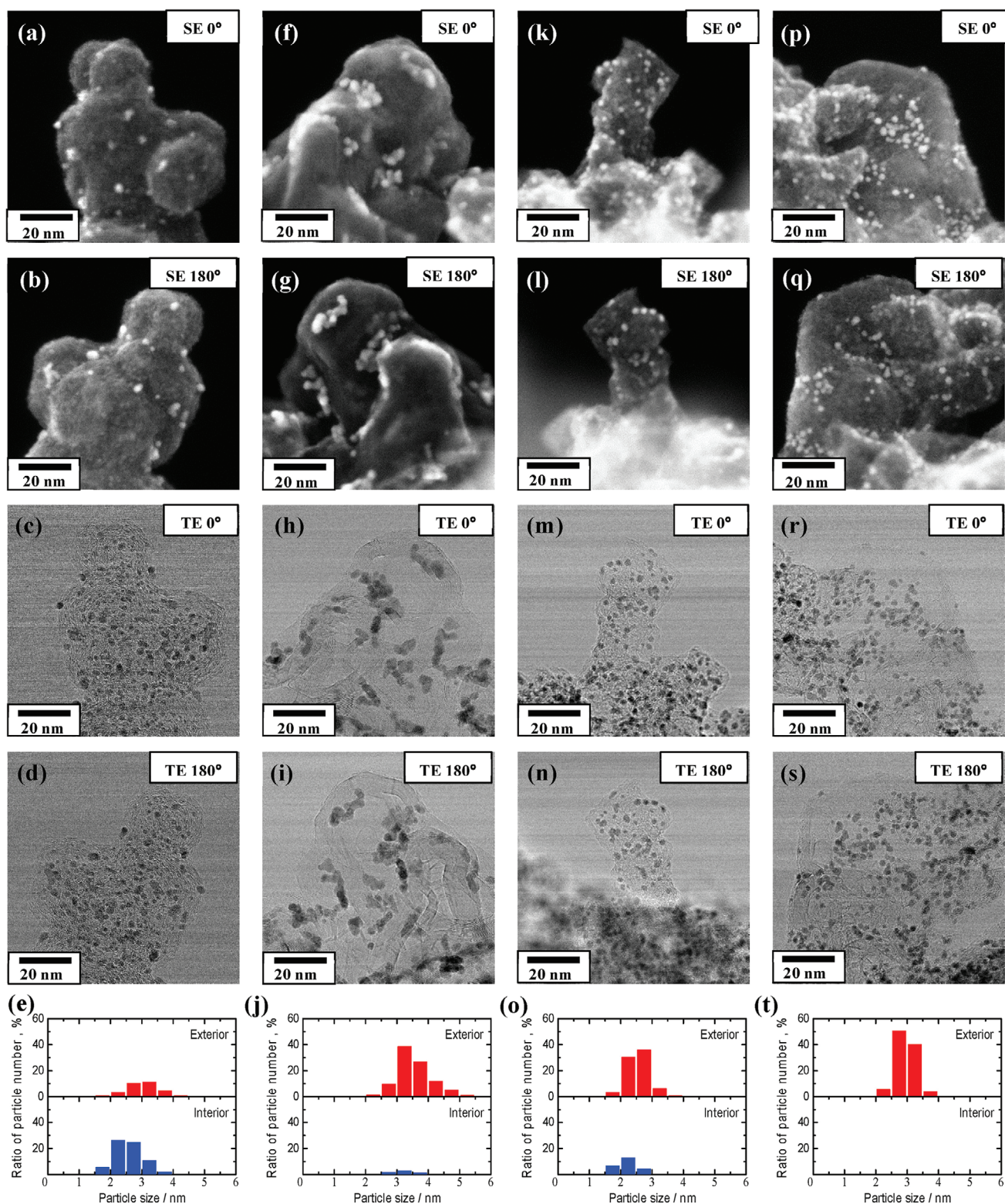
Figure 35. STEM images and Pt distributions at both interior and exterior surfaces of carbon-supported Pt catalysts (SE mode, SEM image; TE mode, TEM image): a) SE mode 0° of c-PtCB, b) SE mode 180° of c-PtCB, c) TE mode 0° of c-PtCB, d) TE mode 180° of c-PtCB, e) Pt distribution of c-PtCB, f) SE mode 0° of c-Pt/GCB, g) SE mode 180° of c-Pt/GCB, h) TE mode 0° of c-Pt/GCB, i) TE mode 180° of c-Pt/GCB, j) Pt distribution of c-Pt/GCB, k) SE mode 0° of n-Pt/AB800, l) SE mode 180° of n-Pt/AB800, m) TE mode 0° of n-Pt/AB800, n) TE mode 180° of n-Pt/AB800, o) Pt distribution of n-Pt/AB800, p) SE mode 0° of n-Pt/AB250, q) SE mode 180° of n-Pt/AB250, r) TE mode 0° of n-Pt/AB250, s) TE mode 180° of n-Pt/AB250, and t) Pt distribution of n-Pt/AB250. Reproduced under the terms of the Creative Commons Attribution 4.0 International (CC BY 4.0) license.[64] Copyright 2016, Elsevier.

**ADVANCED
SCIENCE NEWS**

www.advancedsciencenews.com

**ADVANCED
ENERGY
MATERIALS**

www.advenergymat.de

at low Pt loadings.[353] This is particularly relevant for highly porous supports, as transport resistances have been modeled to increase significantly in tortuous pores.[418]

4.8. Nanostructured Support Materials

In order to minimize the Pt loading required in fuel cells, and to enhance the lifetime of the CL, a number of carbon-based nanomaterials have been investigated as a replacement for CB. The aim is to take advantage of proposed higher conductivities, specific surface areas, and carbon corrosion resistance.[84,394,419–422] Although the field is now in its second decade of research, the majority of work focuses on material discovery and innovation. Thus, only a small minority of work has reached the maturity required to be produced in quantities suitable for MEA manufacturing and single-cell testing.[423] In this section, only works that have presented MEA testing will be reviewed.

4.8.1. Carbon Nanotubes and Nanofibers

Carbon nanotubes were the first carbon nanomaterial proposed as a replacement for CB in PEFCs, as early as the 1990s.[424] A single-wall carbon nanotube (SWCNT) can be thought of as a single sheet of graphene rolled into a complete tube, whereas MWCNT consist of multiple concentric rolls of graphene,[425] with inter-tube distances typically around 3.5 Å. Given that CNTs are expensive when compared with other carbon materials,[84] MWCNTs are typically favored for use in PEFCs over SWCNTs due to their lower synthesis costs and reduced tendency to form bundles which would reduce available surface area.[426] While the properties of MWCNTs can vary greatly depending on the synthesis procedure used,[426] they typically exhibit high conductivities and specific surface areas, while their graphitized carbon structure results in high stability across a wide voltage window,[424,426] making them potentially suitable as carbon corrosion-resistant support materials.[319] In the majority of works, MWCNTs are synthesized using chemical vapor deposition (CVD), and are then acid-treated to introduce defects that facilitate the deposition

of catalyst NPs.[394,423,424,426–429] The obtained catalyst powder is then dispersed in a solvent, deposited onto a GDL, and assembled into an MEA for testing.[394,423,424,429] However, this process can introduce functional groups onto the surface of the CNTs which will have an impact on CL performance. CNTs are widely reported to improve the durability of Pt catalysts: for example, Vinayan et al.[430] reported Pt/CNT electrodes composed of Pt NPs decorated on functionalized MWCNTs (see **Figure 36** below) with no voltage loss after 50 h at high current density. However, the observations of improved Pt catalyst durability on CNTs are among many others that are often not accompanied by an explanation of the origin of these observations. Instead, they are commonly assigned to factors independent of the support material, such a catalyst carbon shells or functionalization.[426–428,430,431]
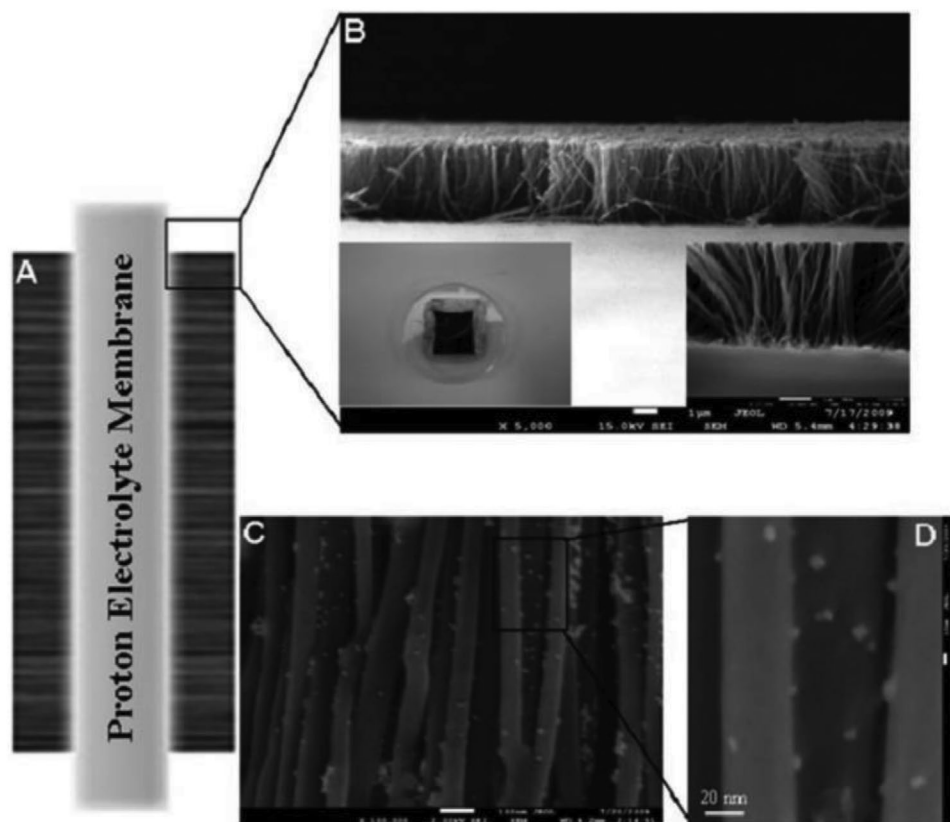
Within the literature, it is not clear if the BoL performance of CNTs is higher than that of commercial PtC. For example, Gupta et al.[426] and Matsumoto et al.[428] report higher current densities for CNTs-based electrodes, reportedly due to well-dispersed Pt NPs and improved electrical conductivity. However, both reports have significant limitations such as badly performing PtC references, limited characterization, and narrow explanations of the observed effects. Contrary to these reports, Andersen et al.[432] reported the initial performance of commercial PtC to be 393 mW cm^{-2} compared to 147 mW cm^{-2} that was observed for PtCNT. Due to their nanoscale size, CNTs can be manipulated into complex novel CL structures. This has led to reports of highly engineered CLs; for example, Zhang et al.[427] fabricated aligned CNT electrodes that were directly attached to the Nafion membrane, as shown in **Figure 37**. The authors report improved current density (605.88 mA cm^{-2}) and power density (397.23 mW cm^{-2}) at 0.65 V compared with a commercial PtC sample (285.65 mA cm^{-2}, 210.79 mW cm^{-2}). The source of this increased performance was reported to be lower kinetic resistance and a larger ECSA was measured for the aligned CNT CL when compared to the commercial sample. The source of these may be due to the limited Nafion content in the CL, resulting in it possessing a CL morphology similar to a NSTF.

CNFs are a class of nanomaterials distinct from CNTs, and are being widely investigated as replacements for CB as catalyst support.[424] CNFs are typically 10–500 nm thick[320] and
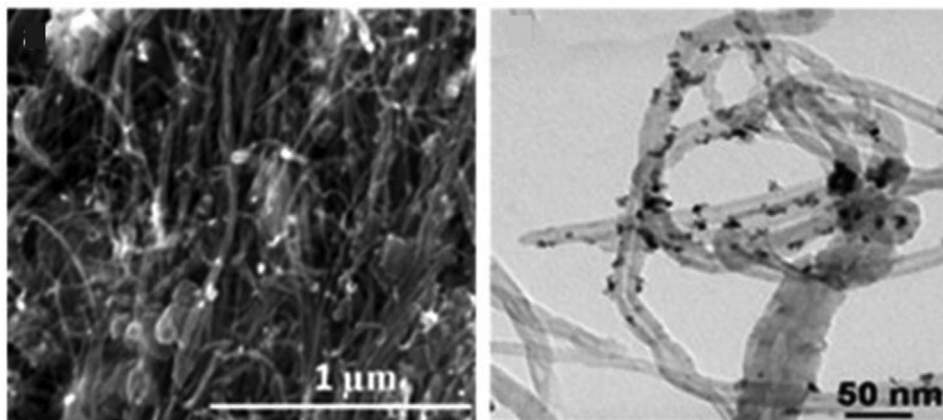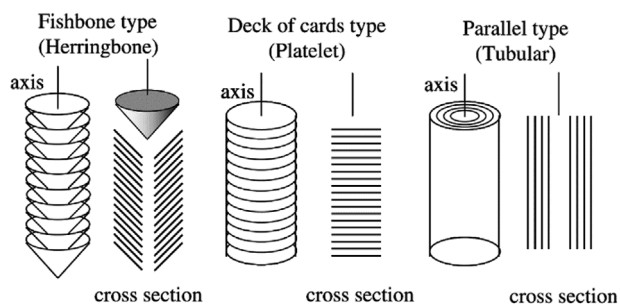

Figure 36. SEM and TEM of Pt nanoparticles on functionalized MWCNTs. Adapted with permission.[430] Copyright 2012, Elsevier.

**ADVANCED
SCIENCE NEWS**
www.advancedsciencenews.com

**ADVANCED
ENERGY
MATERIALS**
www.advenergymat.de

Figure 37. Images of Pt nanoparticles decorated on aligned carbon nanotubes directly attached to a Nafion membrane. a) Shows a schematic of the structure; b) SEM of the aligned CNT array on the Nafion membrane, with the right insert showing a cross-sectional image and the left insert showing the whole Pt-loaded structure in a single cell. c,d) SEM images of the Pt nanoparticles on aligned CNTs after a single cell test. Adapted with permission.[427] Copyright 2010, Royal Society of Chemistry.

composed of graphene layers arranged parallel, perpendicular and at 45° to the growth axis, as can be seen in **Figure 38**, with each arrangement giving rise to different properties.[424] The structure of platelet and herringbone CNFs results in a regular arrangement of nano-graphene sheets with their edges exposed along the outside of the carbon nanofibers, which serve as more favorable sites compared with the basal plane, for Pt NP anchoring.[320] As a result of their much larger size compared with CNTs, CNFs have significantly lower specific surface areas.[432] CNFs have been reported to have higher thermal stability, electrochemical durability, and similar electrical con-

ductivity compared to CNTs.[432] Wang et al.[433] reported that CNF-based CLs have almost identical performance to commercial PtC under MEA testing, although the performance of all materials in this study, including the references, were lower compared to the wider literature. These differences in reported performance make it difficult to determine which material is superior. Andersen et al.[432] reported the initial performance of commercial PtC to be 393 mW cm^{-2} compared to 195 mW cm^{-2} that was observed for PtCNF. Stevenson et al.[434] reported a similar trend with PtC achieving a maximum power density of 756 mW cm^{-2} compared to that of 490 mW cm^{-2} for CNF, although in this case the differences in Pt particle size (2.7 nm vs. 4.6 nm, respectively) may explain the origin of this performance difference.

Each nanomaterial has advantages and disadvantages that should be considered. CNTs can be manipulated into complex nanostructures with designed morphology. CNFs are resistant to carbon corrosion, significantly cheaper and can be formed into CL mats. However, they have low surface areas, less graphitization compared to CNT, and often require functionalization. Potential benefits of CNTs/CNFs are the inherent stability of graphitized carbon, and unique CL layer design that could yield highly porous electrodes. To investigate these opportunities, publications must either perform ASTs or develop and characterize engineered nanomaterial-based electrodes. Using

Figure 38. Arrangements of graphene layers in three types of CNFs. Reproduced with permission.[424] Copyright 2006, Springer Nature.

durability tests consisting of 5000 high voltage AST cycles, Andersen et al.[432] investigated the carbon corrosion of Pt/CNFs compared with Pt/MWCNTs and Pt/CB. They reported that while the commercial Pt/CB sample saw a 50% drop in ECSA and a 28% drop in maximum power density, Pt/MWCNT showed an ECSA decrease of 20% and an improvement of 6% in maximum power density after 10 000 cycles. Remarkably, the Pt/CNF ECSA showed no net change and a 12% increase in maximum power density. They suggest that the improved stability of the Pt/MWCNT and Pt/CNF samples are achieved through the reduced rate of carbon corrosion; however, further AST studies and characterization on CNF materials should be conducted to understand significantly reduced ECSA loss.[320,432]

4.8.2. Graphene, Spacers, and Novel Nanomaterial Morphologies

Since the enhanced nanoscale properties of isolated graphene were first reported in 2004, graphene has grown to become one of the largest areas of catalyst support material research.[435] Of its various properties that originate from its 2D structure, graphene's potentially very high specific surface area, electronic conductivity, and suggested chemical resistance compared to CB make it a promising candidate for fuel cells.[436,437] Of the various methods for producing graphene, the ones most commonly used in fuel cell catalysis research are liquid phase exfoliation and reduction of graphene oxide, produced using the well-established Hummer's method.[438] While graphene oxide and its derivatives have higher electrical resistivity than pristine graphene produced via methods such as CVD, its relatively low cost, facile synthesis, and solubility in water make it readily available for scale up.[438] In addition, rGO and graphene oxide (GO)-based supports are reported to improve Pt catalyst durability under catalyst stability cycling. This is typically explained by the stronger anchoring interactions between surface functional groups and the catalyst particles.[369–371] However, oxygen functional groups have been widely reported to promote carbon corrosion of the support.[69,186,366,367]

Mardle et al.[439] reported the maximum power density of rGO based electrodes was inferior compared to PtC, (128 vs. 314 mW cm^{-2}), although this can be largely explained by the eight-times lower ECSA values (2.7 vs. 19.8 m^2 g$_{Pt}^{-1}$, respectively). Ghosh et al.[370] reported the use of rGO and critic acid functionalized rGO to increase the hydrophilicity of the material, allowing for better catalyst ink dispersion. In fuel cell tests, the rGO and functionalized rGO supports had higher power density than commercial PtC (maximum power density 426 vs 455 vs 314 mW cm^{-2} respectively), with the largest improvements in power density observed in the mass transport regime. Furthermore, the catalyst durability was found to be higher in the rGO and functionalized rGO support compared to PtC (14%, 9% and 24% loss in ECSA measured on RDE respectively). However, the ECSA and MEA performance of the commercial reference material was significantly lower than other literature sources and there was minimal information on the chemical composition of the functionalized sample; hence, a more depth analysis of the role that rGO determined in this performance change is difficult. Heydari et al.[372] showed the current density of a N-doped rGO MEA was higher compared
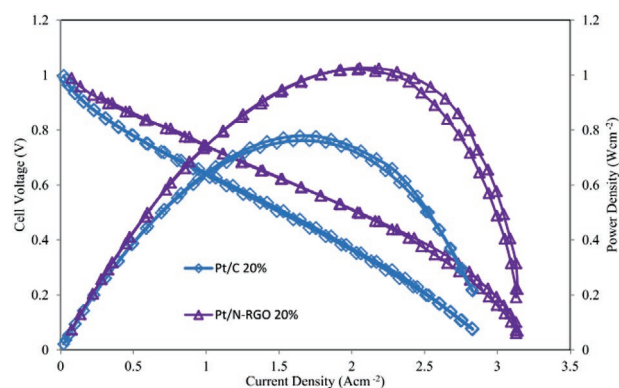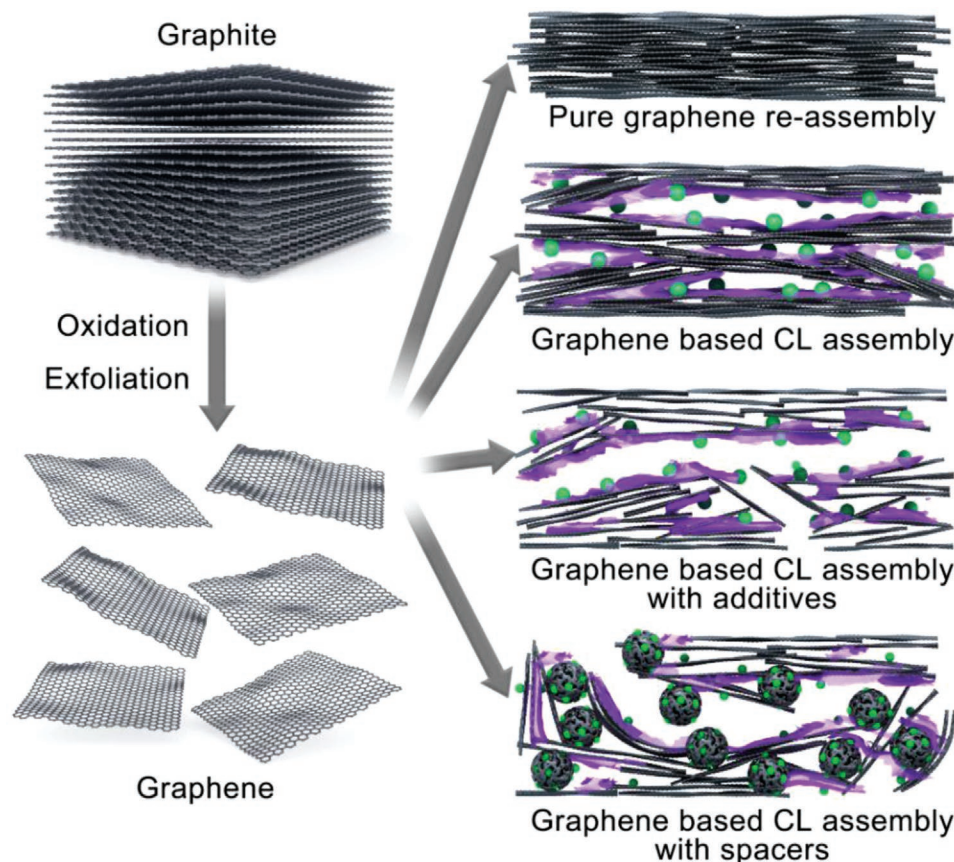

Figure 39. Polarisation curves and power curves for Pt nanoparticles supported by nitrogen doped reduced graphene oxide, compared with a commercial PtC catalyst, at 80% RH at the cathode, H$_2$/O$_2$ at flow rates of 220 and 400 mL min^{-1} at the anode and cathode, respectively, and temperature maintained at 333 K. Reproduced with permission.[372] Copyright 2016, Elsevier.

to commercial PtC (as shown in **Figure 39**); the reason for this was not explained in the publication, although in this case it can be explained by the higher ECSA of the graphene-based electrodes. Furthermore, the graphene-based electrodes were reported to possess a significantly better catalyst durability compared to commercial PtC, which showed a surprisingly large 96% loss in ECSA after 3000 AST cycles on RDE. The cause of the N-doped graphene's improved durability was not suggested, and AST comparison to other MEAs were only performed on RDE.

When reporting the performance of rGO based CLs, the current or power density is typically cited as due to the higher electrical conductivity of graphene.[440] Catalyst durability improvement are commonly reported due to the anchoring effects of surface oxygen functional groups. However, rGO and pristine graphene have very different resistivities; furthermore, the role of different catalyst NPs sizes are typically overlooked or seen as a property of rGO, not an independent variable that can be separately controlled, which has a huge impact on MEA performance and durability. Support durability would be expected to be reduced due to the presence of oxygen functionalized groups and is rarely reported on. It is not conclusive from the literature whether rGO offers better performance than existing commercial PtC catalysts. Furthermore, rGO is fundamentally limited by the high concentration of defects produced during its synthesis, from which carbon corrosion can be initiated.[321] Further research is needed to determine if functionalized rGO will surpass PtC in cost-effectiveness, usability, current density, or durability.

Pristine graphene is chemically distinct from rGO as it does not possess significant quantities of non-carbon functional groups, although they will still exist on the edges of the sheets. The lack of these groups results in pristine graphene forming unstable inks.[441] Graphene nanoplatelets (GNPs) are typically produced via the exfoliation of intercalated graphite and retain a much more graphitic structure with fewer defects than rGO, resulting in improved mechanical and electronic properties.[325] Furthermore, the reduced concentration of structural defects make it more resistant to carbon corrosion.[74,178,186,225,321–324]

**ADVANCED
SCIENCE NEWS**
www.advancedsciencenews.com
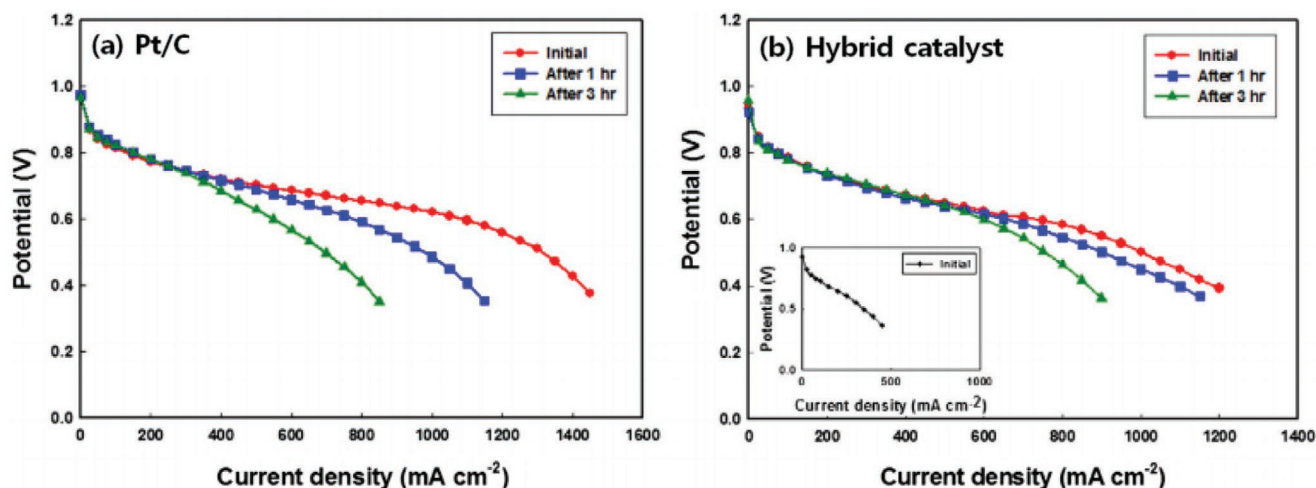
**ADVANCED
ENERGY
MATERIALS**
www.advenergymat.de

Figure 40. Schematic of the fabrication of graphene-based CLs, which typically form low porosity electrodes. Different manufacturing techniques such as the introduction of additives or spacers can increase porosity and widen the PSD.

The combination of these effects should, in theory, provide the improved corrosion resistance required.[321] Multilayer graphene (MLG) and GNPs have a strong tendency to restack due to van der Waals forces between individual sheets or groups of sheets. This inter-sheet attraction causes graphenes to agglomerate, hence when deposited they form low porosity electrodes with tortuous gas transport pathways.[371] This was highlighted by Marinkas et al.[442] who (among many others) reported the performance of entirely MLG-based MEAs was significantly worse than commercial PtC, suggested to be as a result of mass transport limitations caused by the low porosity restacked MLG CLs. One component of this reduced performance was significantly lower OCV in high MLG content electrodes, most likely due to a very low proportion of accessible Pt combined with high transport resistances causing a very low kinetic current.[443] Combinations of CB and MLG achieved higher performance compared with pure MLG, although this was not compared against CB reference. Furthermore, this report compared samples with Pt loadings from 0.1 to 4.2 mg_{Pt} cm^{-2}, with no two electrodes possessing the same loading and the lack of morphological data such as PSD or CL thickness make comparison between the different electrodes in this study very difficult. Graphene based electrode typically utilize spacers to mitigate the propensity for large sheets to restack during the manufacturing process as shown in **Figure 40**.[371,443–448] Here, spacers are defined as any additional non-graphene support material that is added to the

CL to improve performance. Adding spacers improves performance but introduces a second, potentially less stable, carbon phase.[443] This can lead to a trade-off between performance and catalyst durability.[369] The carbon corrosion performance of mixed carbon supports have not been widely investigated. Sung et al.[449] reported that the inclusion of even a small percentage of MLG improved power density of commercial PtC by roughly 20%, with 0.1 wt% being the optimum graphene content. Furthermore, they reported that the inclusion of 0.1 wt% graphene resulted in a 3.7 times slower degradation rate than without graphene. However, this performance enhancement was attributed to the higher electrical conductivity of graphene; no mechanism was suggested for how such a small amount of graphene could have such an outsized impact or the origin of the superior durability. Detailed PSD measurements, more easily comparable ASTs, and repeat measurements would be needed to clarify how and why the performance and durability of the electrode improved so significantly with only a small percentage of graphene.

The most commonly researched spacer is CB, which is used in varying amounts across many studies to alter the electrode structure and its resultant performance. Arici et al.[326] compared an in-house prepared PtC sample with Pt/GNP and a 50:50 hybrid of the two materials. Similar to their previous work, they suggested that the addition of CB effectively inhibits the restacking of the GNPs, but no morphological characterization

**ADVANCED
SCIENCE NEWS**

www.advancedsciencenews.com
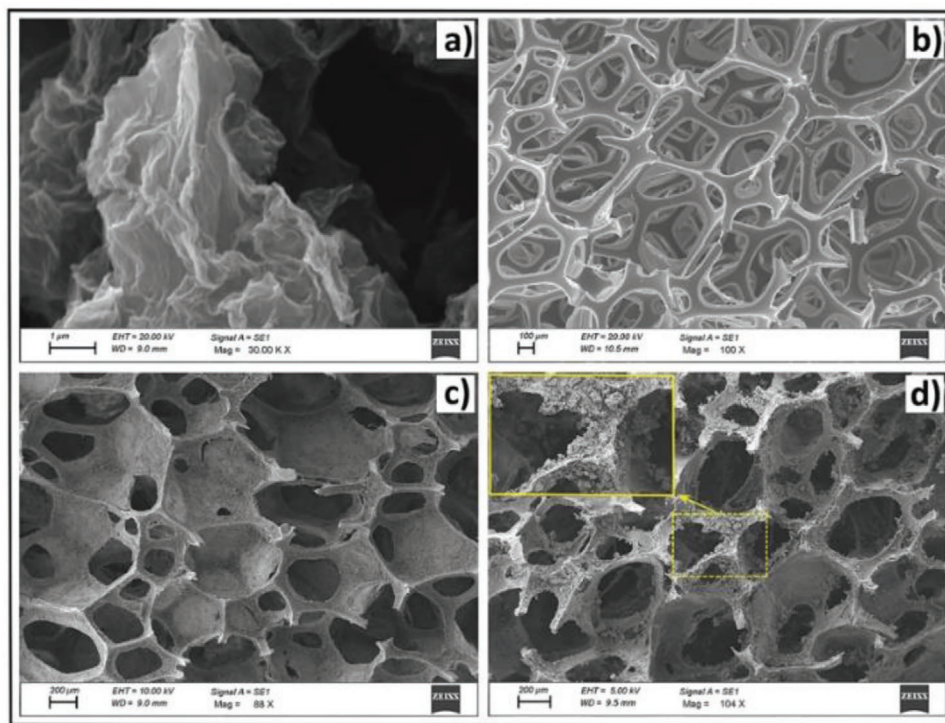
**ADVANCED
ENERGY
MATERIALS**

www.advenergymat.de

Figure 41. Polarization curves of a) PtC and of b) a hybrid mixture of PtC and Pt/graphene oxide, before and after applying a voltage of 1.4 V for 3 h. b) Inset shows activity of Pt/GO catalyst without any added PtC. Reproduced with permission.[369] Copyright 2014, Elsevier.

was performed to support this.[371,443,445] In further work by the same group, Daş et al.[325] performed a similar study, comparing the initial performance and durability of different ratios of CB to GNP. After a 24 h hold at 1.4 V, the MEA composed of 60:40 GNP:C showed the highest durability, with only half the loss of ECSA when compared with PtC. In both of these reports, the differences in Pt catalyst size between novel and commercial samples make it difficult to determine the separate contributions to durability from the novel support and smaller particle size.

The addition of spacers has been widely used to increase the performance of rGO as well as pristine graphene, due to similar enhancements of porosity and Pt utilization. Typically, varying amounts of spacer material is added to a Pt/rGO catalyst, such as in work by Park et al.,[444] who showed that spacers increase the distance between graphitic sheets and hence increase Pt utilization and mass transport. They reported that the ECSA increased from 32 to 50 m^2 g^{-1} as CB content was increased from 0 wt% up to 25 wt%, due to greater accessibility of trapped Pt particles in between graphitic sheets. Şanlı et al.[445] and others from the same group[371,443] utilized CB to reduce restacking and improve MEA performance in rGO electrodes.[371,443] They reported that the optimum CB loading was 25% and this outperformed 100% PtC. While they justify the improvement of rGO due to enhanced mass transport and Pt utilization, they did not explain why the performance of 100% rGO significantly outperforms 100% PtC. In both sets of studies, it was observed that above 25% CB, any additional CB reduced performance. This was suggested to be due to excess CB blocking Pt NPs, thereby reducing the number of active catalyst sites present in the CL. This theory has also been reported in other studies,[450] although it suggests that commercial CB-based electrodes would have a significant issue with low Pt utilization, which is not the case. This rationale has never been directly experimentally verified; a better explanation for the improved performance is that 25% CB forms a favorable CL morphology with a porosity and electrode thickness that can achieve high mass transport and Pt utilization.

Jung et al.[369] reported CLs based on mix of CB and rGO at different ratios, showing that while higher quantities of rGO

reduced ECSA, they also increased catalyst durability under RDE. After holding single cells at 1.4 V for 3 h, the PtC catalyst saw a 45.4% loss in current density at 0.6 V, compared with only a 17.7% decrease exhibited by the hybrid catalyst containing 20% Pt/rGO, although the absolute current density after 3h of ASTs were very similar (550 vs 600 mA cm^{-2} respectively). The majority of the activity loss measured in polarization curves of the PtC material was observed at high current densities as shown in **Figure 41**. This was suggested to be caused by the agglomeration or loss of Pt NPs, supported by TEM investigations, which showed reduced catalyst agglomeration in the hybrid systems. However, the activity change measured was only in the mass transport region of the polarisation curve, which would suggest it was not due to only reduced ECSA changes. It is possible that due to their ASTs employing a constant high voltage of 1.4 V, the authors were also unintentionally measuring carbon corrosion of the support. While it is clear that rGO is providing some catalyst durability enhancement, the atypical AST used and the lack of detailed morphological imaging make it difficult to determine the origin of improvements in the mass transport region. Xin et al.[74] found that CL formed from functionalization of rGO with PBI polymer had significantly reduced current density, improved durability compared with commercial PtC. Without the presence of a spacer, the mesoporosity of the graphene-based electrodes was shown to be close to zero, with the Nafion ionomer filling the gaps between graphene agglomerates and the resulting performance was very low. With the inclusion of a functionalized CB spacer, mercury porosimetry measurements showed the emergence of larger secondary pores, indicating the spacer (50 wt%) was effective in inhibiting the restacking of the graphene, which resulted in reduced mass transport losses. Initially, PtC was reported to achieve significantly higher current density, although after a 10 000-cycle carbon corrosion AST, the hybrid rGO CL impressively showed only a small change in performance and ECSA while PtC showed no electrochemical activity after the AST. The improvement in durability was suggested to be as a result of the PBI functionalization, which both stabilized Pt NPs and the highly reactive parts of the support material, thus limiting

ADVANCED
SCIENCE NEWS

www.advancedsciencenews.com

ADVANCED
ENERGY
MATERIALS

www.advenergymat.de

Figure 42. SEM micrographs of a) N-graphene, b) bare foam used as substrate, c) Pt@N-graphene on foam, and d) carbonized Pt@N-graphene foam. Adapted with permission.[373] Copyright 2016, Royal Society of Chemistry.

the number of available sites from which carbon corrosion can occur. The above studies all report performance improvements when using graphene-based CLs with a second spacer carbon support introduced. The addition of a spacer forms a more favorable CL structure and hence improved mass transport and Pt utilization. However, the publications are rarely accompanied by PSD, porosity data, or images of the morphology; therefore, the analysis is often limited and the optimized morphology of these materials remains unknown.

To circumvent the problem of graphene restacking altogether, research has been conducted into novel, 3D graphene structures,[421,451,452] which exhibit higher specific surface areas[453,454] and porosities.[373] Liu et al.[454] developed a graphene foam through a simple synthesis method via the combustion of sodium ethoxide. This produced a highly porous graphitic support, although performed worse than commercial PtC tested in an MEA. This was most likely due to the unoptimized Nafion content and homogeneity of the graphitic support, particularly in a relatively uncontrollable synthesis such as simple combustion. A more complex synthesis for a 3D graphene-based architecture and nitrogen doping was reported by Karuppanan et al.,[373] SEM of which is presented in **Figure 42**. They reported significantly improved power density from nitrogen-doped graphene (289 mW cm^{-2}) and 3D foam structure (294 mW cm^{-2}) compared to PtC (201 mW cm^{-2}). This was attributed to the improved electrical conductivity of graphene, highly porous 3D structure and nitrogen facilitating a homogenous spread of catalyst particles. A wider PSD could be expected to improve performance of the MEA, particularly in the mass transport region. However, it is unclear why the

traditionally fabricated graphene MEA so outperformed commercial PtC, which has a well-established pore structure and typically achieves very high performance. The pore structure of this CL morphology needs to be quantified in order to understand the benefits of this architecture.

4.8.3. Graphene/CNT Hybrid CLs

To take advantage of the benefits that nanomaterials present they can be combined with other materials that compliment their structure or properties, this technique has produced a number of promising hybrid CLs. The most straightforward way to achieve this is to mix exfoliated GO and CVD-grown MWCNTs before deposition of Pt NPs, producing graphene with MWCNTs between the layers.[446] Work by Aravind et al.[447] achieved a high maximum power density (675 mW cm^{-2}) from a similar system of Pt/rGO/MWCNTs, nearly double that of Pt/rGO on its own. The improvement was attributed to the CNTs acting as both a spacer and as a conductive pathway between the rGO sheets, increasing the number of available triple-phase boundaries and improving effective mass transport at high current density regions. However, this report did not compare the rGO or MWCNT/rGO CLs against commercial PtC. Further work by Aravind et al.[448] reported wrapping MWCNTs with rGO. Defects in the rGO were shown to allow for the deposition of Pt NPs on the hybrid material without the need for harsh acid treatment typically required in the functionalization of MWCNTs. They reported MWCNT/rGO composites achieving maximum power densities of 661 mW cm^{-2}, compared with
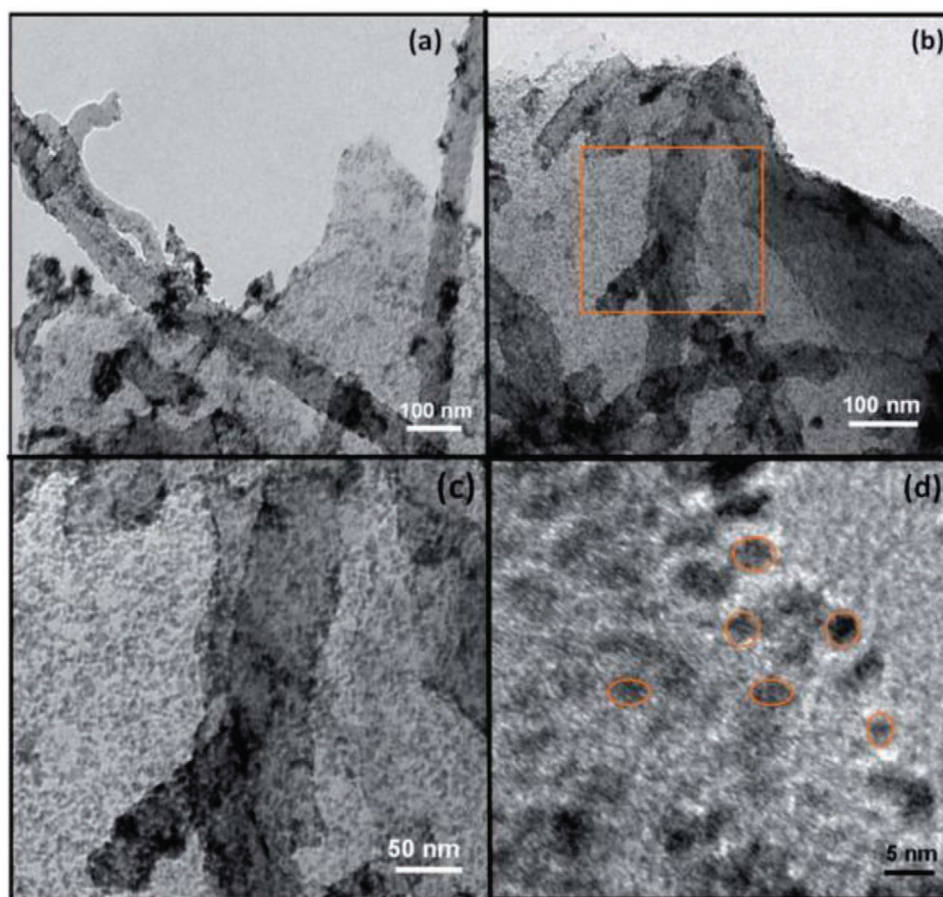
Figure 43. TEM (a–c) and HRTEM (d) of a novel MWCNT-rGO "sandwich" structure, decorated with Pt nanoparticles. Adapted with permission.[455] Copyright 2011, Royal Society of Chemistry.

376 mW cm^{-2} for a commercial PtC catalyst. The performance achieved by the reference PtC value was low, particularly given the Pt loading. The authors reported the improved performance was due to higher support conductivity and the "2D polyelectrolyte". However, it is unclear exactly what is meant by this term. While rGO is significantly more hydrophilic than CB and therefore would act to retain proton-conducting water, intrinsically it is not an electrolyte. Given this, it is unclear why rGO wrapped MWCNTs achieved such a large performance improvement compared to commercial PtC. A novel, sandwich-like structure of graphene/CNT was achieved by Sahoo et al.[455] by growing MWCNTs on functionalized GO, resulting in MWCNTs trapped between rGO sheets, displayed in **Figure 43**. Polarization curves showed an improved maximum power density for the hybrid material compared with commercial PtC and Pt/rGO samples (382 mW cm^{-2} vs. 289, 141 mW cm^{-2}, respectively), reportedly due to its decreased electrical resistance. While electrical resistance would have an impact on current density, it would not be expected to introduce this much difference between the samples. Furthermore, the OCV achieved for the PtC and rGO was 0.889 and 0.987 V, respectively; since OCV is mainly dominated by the catalyst, this significant variation can only be explained by a very low Pt utilization in their reference material. This point was not discussed in the publication or viewed as an important factor in discussing why the different support

materials achieved different power densities. Due to this oversight it is not facile to interpret and compare the data between these two materials.

4.9. Conclusion and Outlook

To achieve the highest performing and most durable PEFCs, porosity, support material, functionalization, and CL design all need to be optimized relative to each other as they are interdependent. For this reason, it would be impossible to determine a singular best performing material/CL. Different materials, morphologies, and functionalizations will each be useful at different operating conditions for different purposes. The relationship between these different aspects of CL design is important, for example, at a set ionomer ratio and Pt loading in a thicker and more porous electrode may result in improved Pt utilization and improved gas transport. However, using thicker electrodes may result in reduced proton and electrical conductivity. Understanding the interplay between these variables in each unique CL system is key to optimizing performance. Publications which compare current or power density should attempt to keep porosity, ionomer content, thickness, and catalyst size the same (if these are not being deliberately varied) when comparing different MEAs, or at least acknowledge and include

**ADVANCED
SCIENCE NEWS**

www.advancedsciencenews.com

**ADVANCED
ENERGY
MATERIALS**

www.advenergymat.de

in their analysis the role these CL properties play on performance. There are several intertwined main limitations to CL performance, catalyst utilization, proton conductivity, and mass transport. Optimizing pore structure has been shown to significantly improve catalyst utilization, mass transport, and control flooding while a homogeneous ionomer can also improve catalyst utilization, proton conductivity, flooding, and mass transport. Most importantly, these need to be optimized for the particular structure and operating conditions with performance limitations induced by too much, or too little of either. While pore structure is often a consequence of support material (as discussed in Sections 4.2 and 4.8), it is also affected by the manufacturing technique used (Section 5). Ionomer distribution is mostly governed by the nature of the support surface functional groups and the ionomer used (Section 3).
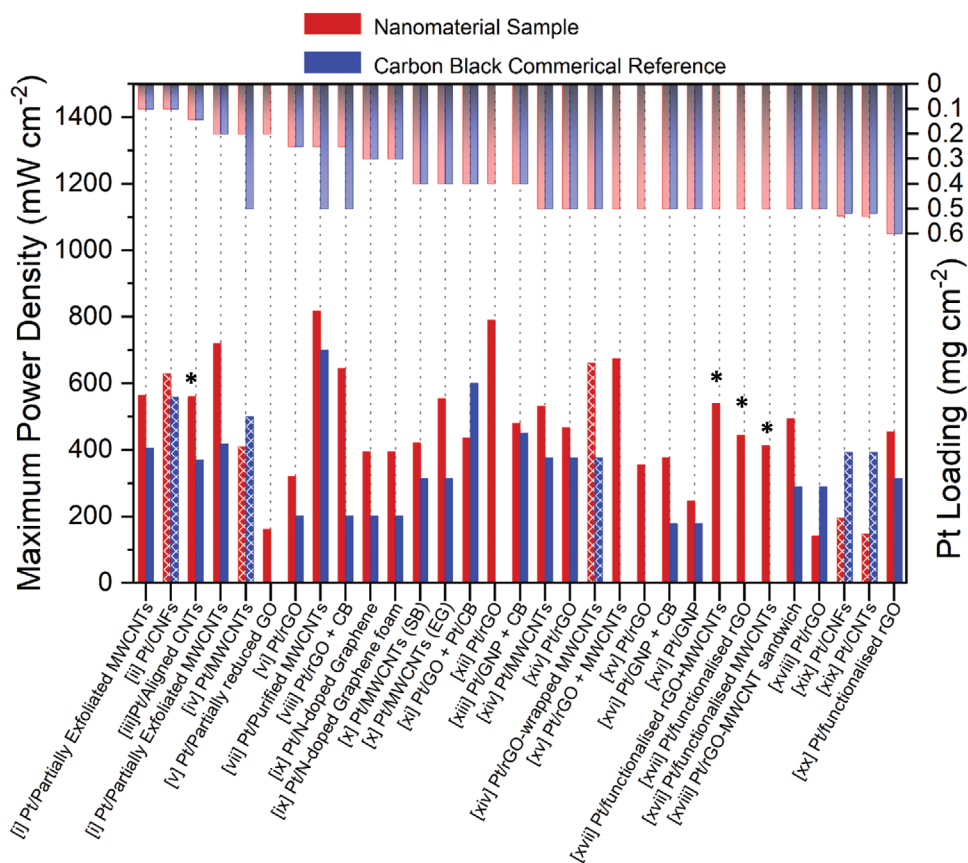
One of the requirements for wide-scale commercial uptake of fuel cells is improvements in durability. The origin of the improvements to catalyst durability by effects such as anchoring are not well understood, more fundamental investigations of these effects can yield valuable information about the optimum support material doping or functional groups. Often, reports suggest improvement to catalyst durability without mentioning potential losses to support durability, these can be estimated independently using the ASTs defined by the DoE. Furthermore, support corrosion is one of the key mechanisms of fuel cell performance degradation, and efforts should be made to report this key parameter for novel materials. It is also important to understand the impact that CL morphology has on support corrosion and electrode thinning. Studies suggest that electrode thinning is not simply due to carbon corrosion but also structural change[159,320,341] and flooding,[146] although the mechanisms are not thoroughly understood. Significantly more research is required to understand electrode thinning and how the CL morphology can be utilized to mitigate corrosion, as highlighted by Zhang et al.[341] and Brodt et al.[320] among many others. Novel support materials such as metal oxide and nanomaterials offer improved durability. As with most new materials, there are potential benefits but also drawbacks. Metal oxides have been reported to improve support durability but also possess different degradation mechanisms which need to be compared to carbon under realistic testing conditions.

A wide range of nanomaterials have been investigated as a potential solution to many of the issues facing fuel cells. Highly graphitized carbons show some promise regarding their durability, although they typically suffer from a lack of porosity and reduced ionomer coverage.[69,71,324,351] Surface functionalized materials such as rGO have been reported to outperform PtC,[370,372,440] although the origin of these effects vary and are typically associated with higher ECSA, ionomer distribution, or an anchoring effect due to oxygen functional groups. The potential support durability ramifications of these functional groups needs to be further explored. This is highlighted by catalyst and support durability of rGO being rarely reported in the same publication. The catalyst and support corrosion mechanisms are distinct and are affected by different aspects of support material chemistry and CL morphology, so must be considered independently. However, they are concurrent, and both impact the real-world operational durability of a PEFC. Publications should attempt to describe at least briefly all aspects of a

materials performance rather than ignoring parts that do not fit the narrative.

It is key for the fast development of fuel cells that experimental results are published in a manner that allows easy comparison between different materials, while this should be the priority of any publication, it is often not the case. For example, reports can fail to consider the impact of particle size as a separate issue when considering the impact of functionalization or choice of nanomaterials. While size[178,394] and location[394,456] of deposited catalyst particles is a property of support material, it can also be independently controllable. This review has discussed several examples where the role of catalyst size variation between different samples on performance and durability is not discussed, which makes interpretting these results not facile. Some publications, due to the lack of characterization and explanation of the observed performance changes, do not aid in the widespread understanding and development of PEFCs. The lack of comparability between results is likely to have played a significant role in the fact that, despite two decades of research and the development of large scale graphene manufacturing, there is no clear consensus if graphene is superior to commercial CB. It is therefore suggested that every study should contain at least one standardized polarization curve for both the novel material and a commercial PtC catalyst, obtained under parameters described by an established reputable body such that it is possible to make quantitative comparisons with existing literature. Ultimately, it is the goal of a publication to facilitate understanding, this requires thorough explanation of observed effects or enough ancillary data to build a complete picture of the system in question. Furthermore, it is the role of authors, editors, and reviewers to insist upon higher standards for comparative materials and to expect more detailed structural characterization in publications. Particularity those that help to deconvolute the various parameters that impact performance. For example, CO_2 exhaust measurements can be used to directly compare the levels of carbon corrosion occurring for commercial catalysts and novel catalysts. TEM and SEM have been used to identify changes in NP and ionomer distribution. Porosity, PSD, and X-ray CT measurements are used to establish changes to macroscale morphology that occur as a result of degradation. Investigation of these processes in-operando would also help understand the changes ongoing in MEAs. In-depth characterization of novel materials and functionalization strategies will allow the scientific community to understand the tools at our disposal. Understanding the tools and the limitations will permit the development of next-generation electrode morphologies, materials, functionalization, and structures, which will in turn allow the development of durable, high-performing MEAs, changing the future energy landscape.

Some publications discussed within this section have very poor performing reference materials, making comparison with literature non-trivial. This problem is particularly acute in the nanomaterials segment of PEFC literature. A true assessment of which support nanomaterials are best performing from the literature is very difficult not only due to the hugely varying parameters used when testing novel catalysts, but also due to a lack of clear trends in materials performance. This is best conveyed by a direct comparison of both novel and references materials, as shown in **Figure 44**. This figure attempts

ADVANCED
SCIENCE NEWS
www.advancedsciencenews.com

ADVANCED
ENERGY
MATERIALS
www.advenergymat.de

Figure 44. Maximum power densities and Pt loading of novel carbon nanomaterial MEAs, compared with commercial PtC MEAs where applicable. Solid bars represent samples that were tested using oxygen at the cathode; cross-filled bars used air at the cathode. Examples marked with an *applied a back pressure during the polarisation curve tests. The references are as follows: i,[457] ii,[431] iii,[427] iv,[428] v,[458] vi,[371] vii,[426] viii,[445] ix,[373] x (One power density reported for each Pt deposition method),[430] xv (Power densities calculated form reported current densities at 0.6 V),[369] xi (Power densities calculated form reported current densities at 0.6 V),[369] xii,[459] xiii,[325] xiv,[448] xv,[447] xvi,[326] xvii (Power densities reported from voltage at 1 A cm−2),[446] xviii,[455] xix,[432] and xx.[370]

to show the disparate nature of published MEA test results for both nanomaterials and their commercial PtC references. Despite various standardized testing protocols put forward by bodies such as the US DoE, in the studies detailed here, only rarely did studies use identical sets of parameters for obtaining polarization curves, with operating temperatures ranging from 40 to 80 °C, cathode gases differing between pure oxygen and air, and catalyst Pt loading differing in almost every instance. This is most clearly reflected in the power densities obtained not for the novel materials themselves, but in the commercial PtC samples used to benchmark their activity. Several authors did not report a reference material,[459] used a pure Pt electrode instead of a typically carbon black one,[458] or used literature data instead of measuring their own.[447] The current densities reported for the reference materials for nanomaterial PEFC based publications have a huge variation and are typically lower than that achieved by commercial CB reported from other sources. This issue is highlighted when observing the lack of a trend between Pt/C reference power densities and Pt loading. While it is only natural for research groups to only spend time optimizing the novel structure and material they are working on, using a reference sample that achieves a lower than typically observed current density significantly devalues the whole

experiment. This can be due to many factors, such as particular MEA design, testing systems, and flow-field design, among many other factors. Broadly speaking, it is not in the interest of research groups to optimize the commercial reference material, and groups new to the fuel cell field have less historic data to compare to. The values presented for PtC vary across the studies from ≈178 to 700 mW cm−2, as can be seen in Figure 44. Furthermore, despite the corrosion resistance of carbon nanomaterials being a key property that drives the motivation for research into their use, only two studies were found to have followed well defined corrosion testing protocols, while 4 used in-house cycling protocols, 6 used constant voltage protocols, and 17 omitted corrosion testing. Suggestions for making future publications significantly more easy to compare are discussed in Section 6.

5. Catalyst Layer Preparation Methods

5.1. Introduction

Manufacturing the CL and the MEA are essential steps in the process of creating a working fuel cell. Once the catalyst ink

has been prepared, it is adhered onto a substrate to form an electrode. The two electrodes are assembled on either side of the membrane to prepare the MEA and then the cell can be tested. Within this process, there are a large number of variables that can lead to changes in the final performance of the MEA. This includes the ink composition, the substrate used, the CL manufacturing method, if the MEA is hot pressed, and the pressure applied in the cell assembly. Critical for the performance is the choice of manufacturing technique, for which there are a wide range of options depending on the application and target end-use.

The first choice to be made in the manufacturing process is the ink composition, which depends on the specific catalyst, support and ionomer used, and the solvent chosen must be appropriate for the manufacturing and CL substrate. The CL can be applied directly onto the membrane producing a catalyst coated membrane (CCM), whereas applying it to the gas diffusion medium (GDM) produces a gas diffusion electrode (GDE), sometimes called a catalyst coated substrate (CCS). As mentioned in the Section 1, the GDM consists of the GDL as well as the microporous layer (MPL), which is a carbon and PTFE containing layer that aids with water management and physical integration between the GDL and CL. Next, the MEA is prepared, hot pressing is a common choice of method, with either the GDM being pressed onto the CCM or the GDEs being pressed onto the membrane. Finally, the MEA is assembled in the fuel cell casing for operation, with clamping pressure being applied. Each step in this workflow has the potential to change the morphology of the electrode, as well as its performance (especially given the intrinsic link between micro-/nanostructure and performance) and they will be analyzed in turn below.

5.2. The Role of Ink Formulations

As detailed in Section 3.6, the ink composition has a significant impact on the surface and internal structure of the prepared CL. This has an effect on gas penetration, proton-conduction pathway, catalyst utilization, and durability.[201] The solvent, which determines the ionomer conformation and ion-pair clustering, directs the size, shape, and dispersion of aggregates and thus must be well considered. Ionomer solubility generally increases with solvent polarity, which causes a decrease in primary aggregate size.[365] Greater solvation of both the ionomer main and side chains (such as in NMP) result in homogenous aggregation producing tough, crack-free, and coarse microstructure of cast CL.[56] Main- and side-chain mobility in the solvent influences how ionomer interacts with the catalyst and support particles, effecting ionomer distribution, thickness, and phase separation on the surface and within pores of the PtC agglomerates, or remaining as free ionomer.[267] Therdthianwong et al.[460] reported on the effect of solvent on the performance of CLs, finding that IPA formed the highest power density electrodes. CCM electrodes prepared using IPA were proposed to benefit from the low ε solvent interaction, allowing superior attachment and surface coverage of CL to the membrane, minimizing contact resistance between the two phases.[264] Low ε solvent was also directly observed via SEM to facilitate impregnation

of ionomer into the hydrophobic GDL during fabrication, providing a well-distributed, porous, and uniform structure, rather than highly polar solvents that remained at the surface of the GDL.[266] Further work by Takahashi et al.[461] hypothesized that having a larger alcohol content in the ink resulted in a dried CL with high ionomer coverage but slightly inferior performance. By contrast, a high water-content ink resulted in dried CLs with heterogeneous and low ionomer coverage but slighter better performance. From this, they concluded that a near equal mix of alcohol and water had the best performance, with optimized pore structures, ionomer distribution, and catalyst activity. This shows that the ink properties that induce appropriate bulk structure of the CL must also be optimized with consideration of the interaction at the interfaces of GDL and PEM.

Changing the ionomer conformation and assembly can cause the PtC/ionomer agglomerate particles to form tightly bound structures, with little to no porosity, or form large, connected agglomerates with significant internal pore structure. Aggregate size within ionomer–solvent dispersions has been reported to increase with ionomer concentration because of reduced electrostatic repulsion between sulfonate groups.[275] In addition, low pH solvents favor side-chain extension into the solvent, due to electrostatic attraction, reducing particle aggregation, and inducing linear conformation.[277] Through the use of cryo-TEM and ultra-SAXS, surface functionalization has been shown to allow control over agglomerate stabilization. Yang et al.[364] reported different-sized aggregates form after the addition of Nafion ionomer to functionalized and non-functionalized CB dispersed in water:IPA (3:1). The electrostatic interactions between CB and ionomer dominated the aggregate-forming mechanics and was found to be heavily influenced by the CB surface functionalities. NH_2-functionalized CB led to 58% aggregate size increase as Nafion was added to the dispersion. This was ascribed to the attraction between the positive charge that can occupy the NH_3^+ functional groups and the negative charge on the SO^{3-}. Interestingly, when Nafion was added to negatively charged SO_3H-functionalized CB, aggregate size change was negligible (–1%).[364] ^{19}F NMR and XPS studies showed that sulfonate group interaction with the support increased with degree of oxygen surface functionalization, and was even greater for carbon supports with nitrogen-containing functional groups.[284,285] Larger agglomerates formed from these stronger support-ionomer interactions will significantly impact CL structure and likely induce greater pore volumes for gas transport.[265]

An appropriate final CL structure also requires the solvent system to be used with complementary deposition parameters. An important relation between ink and CL morphological changes occurring within the meso- and nanopores of the CL during ink drying, was monitored with SANS by Kusano et al.[462] It was found that the dehydration of the ionomer and loss of solvent during drying partially collapses the pore structure of the CL.[462] The group found that by using PFSI ionomer, the mesoporosity of the CL could be somewhat retained during ink drying; however, the effect this had on performance was not reported. Suzuki et al.[358] reported that this porosity and PSD were affected by the ink drying rates, with slower drying reducing porosity. The capillary force was found to have more time to displace aggregates into low contact regions with slower rates and resulted in a loss of porosity

during long drying times. In contrast, comparably fast solvent removal during deposition largely improved the distribution and adherence of the CL, reducing the mass transport resistance. A comprehensive investigation by Therdthianwong et al.[460] on CCMs revealed some key solvent parameters to be considered for optimal CL performance. Very low solvent boiling points can impact structural properties, inducing cracking in CL prepared with acetone due to rapid evaporation. Efforts should be taken to ensure all residual solvent has been removed, particularly for high boiling point solvents, as residual solvent has been reported to inhibit agglomerate structure formation by residing in the pores after drying, with a resultant increase in mass transport resistance.[279] The CL performance also benefited when using solvents with viscosity ≈ 1 cP, this was suggested to be due to improved CL homogeneity and good adhesion to the membrane, compared to solvents with lower or higher viscosities. The combination of solvent properties such as viscosity, dielectric constant and ionomer swelling ratio were all shown to impact the resultant CL distribution, membrane adhesion and cracking.[460] While this performance-based study provides insight into optimal solvent choice, they fail to consider a multitude of competing factors. For example, using a constant casting and drying temperature did not provide a fair comparison of the vastly differing boiling point solvents. Based on the importance of drying time and solvent removal, a fairer procedure may have kept the drying temperatures constant relative to solvent, that is, 10 °C below the specific solvent boiling point. In addition, the ink fabrication commonly uses a commercial Nafion in alcohol dispersion, which may contribute to enhanced performance in pure alcohol inks, while small alcohol content could negatively affect other solvent systems.[279] As highlighted by Talkudar et al.,[383] there is limited research into drying techniques and it is recommended as an area for future research.
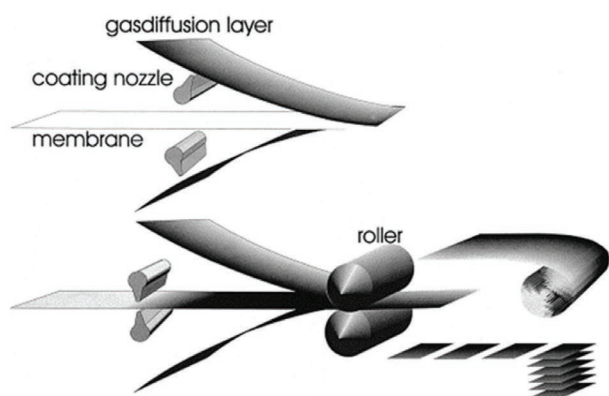
5.3. Manufacturing Method

The manufacturing process used to form the MEA can significantly influence the structure of the CL and hence the fuel cell performance. There are a wide range of manufacturing techniques available for CL preparation such as rolling, spray coating, and screen-printing among many others. Lee et al.[315] emphasized that the method used for CL preparation has a significant impact on the final CL morphology, including porosity and thickness. The critical interplay between morphology and performance was also highlighted by Khandavalli et al.,[283] who showed that the CL microstructure is primarily controlled by the fabrication process, which includes the ink dispersion. As outlined by Kundu et al.,[463] morphological defects in the CL arise during manufacture and can be classified into various groups, like cracking, catalyst/ionomer clusters, or variable thickness (**Figure 45**a–c). These defects are expected to negatively affect fuel cell performance and degradation; manufacturing techniques can be carefully selected to minimize such defects. However, Kim et al.[464] suggested that a certain level of cracking was beneficial for fuel cell performance. By mechanically stretching the membrane to induce cracking of the CL, the authors found that some cracking improved mass transport
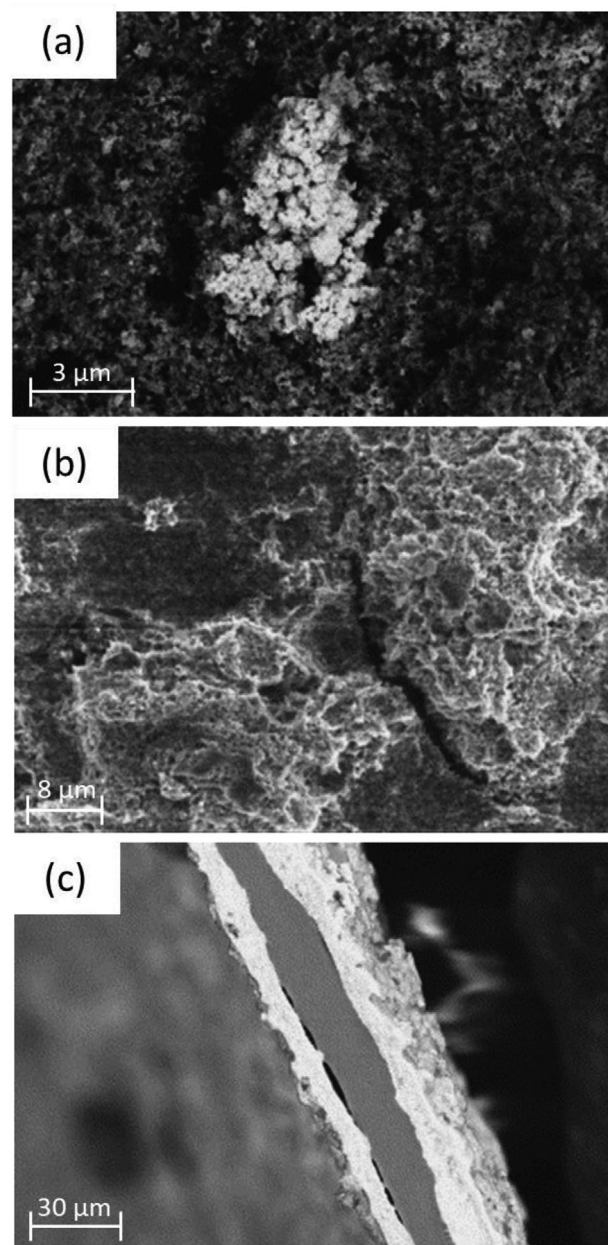
Figure 45. SEM images showing various CL defects, such as a) catalyst clustering, b) cracking, and c) thickness variations. Adapted with permission.[463] Copyright 2006, Elsevier.

losses of the cell, while ECSA stayed constant. Further work is required to understand the nanoporosity and durability changes occurring as a result of different degrees of cracking.

Early CLs were prepared by hand-painting the ink onto the substrate using a brush,[465] but disadvantages of hand-painting techniques include a low level of precision and poor reproducibility. This method could result in CLs with uneven thicknesses, as shown in Figure 45c, which could affect the localized performance and current distribution of the MEA. Other CL manufacture techniques have been developed that possess a large increase in availability and scalability of different processes. Descriptions of preparation methods have been

ADVANCED
SCIENCE NEWS
www.advancedsciencenews.com

ADVANCED
ENERGY
MATERIALS
www.advenergymat.de

(a) Roll-to-roll production method

(b) Ultrasonic spraying head

Figure 46. Schemes of several electrode manufacturing methods. a) Scheme of roll-to-roll production technique for PEFC and DMFC MEAs. Adapted with permission.[468] Copyright 2000, Elsevier. b) Sono-Tek Ultrasonic Spray system. Adapted with permission.[382] Copyright 2011, Elsevier.

reviewed elsewhere[466,467] and are widely classified into categories such as spreading and spraying methods. Although from the perspective of this review, manufacturing is best considered from the relative ease and cost of use in an academic or commercial environment and the impact that techniques have on CL morphology.

A factor in the choice of electrode preparation technique is the application; industrial applications will generally use a method like roller applied deposition, doctor blading, or screen printing to quickly deposit the correct amount of ink onto the substrate in a single action. This simplified and quick approach to fabrication makes it attractive for commercial MEA manufacturing. Roller-applied methods involve the deposition of the ink onto the membrane through a nozzle followed by feeding through a roller to smooth out the ink (**Figure 46**a).[468] In doctor blade techniques, a well of ink is fed down onto the substrate behind a blade, with a gap between the blade edge and the substrate. The blade is then pulled across the substrate (or vice versa), forming a CL with a smooth consistent thickness.[278] Owing to the ability to feed large volumes of substrate

through the mechanical rollers, there have been efforts to demonstrate efficient roll-to-roll MEA preparation techniques using these methods,[469] which improves the efficiency and cost of the manufacturing process. Recently, Mauger et al.[470] reported the use of roll-to-roll coated GDEs to manufacture CLs that had performance almost matching that of spray-coated CLs with an additional ionomer layer. They also reported that, due to the different drying mechanics between layer-by-layer and a thick liquid film, an ionomer gradient was observed in the roll-to-roll coated GDEs, similar to those discussed in Section 4.4, reducing CL/membrane interface resistance. This demonstrates the structural implications of different manufacturing techniques, in particular how it impacts the complex drying mechanics of the different components of the CL. Screen printing is another typically single action manufacturing technique, achieved by selecting a mesh of the desired thickness, through which the ink is stamped onto the electrode surface to achieve a uniform pore distribution.[411] Varying the size of the mesh allows for different loadings to be applied. This can be extended to the creation of variable loading CLs, where the CL thickness changes across the surface of the CL, with the aim of evening out the current density across the MEA.[471] While better than hand-painting in terms of precision,[472] this method for CL preparation is quite complex and it has been highlighted that it would not be especially useful for industrial applications.[472] These single action printing techniques require pre-existing knowledge of the material ratio to achieve particular thickness or Pt loading. To achieve this requires trial and error experiments to make MEAs at different thicknesses, the Pt loading of each MEA is then measured to determine the correct thickness. If there is a significant change in the CL composition, such as a change in support material or Nafion ratio; this trial and error approach must be repeated with the new formulation to determine the correct loading and thickness. As such, single action printing methods are not the most agile research tool but are potentially more commercially relevant.

Layer-by-layer techniques offer the advantage that practitioners have greater control over the resulting loading of the CL, and importantly for laboratory-based research can stop part way to evaluate the manufacturing progress. Spraying methods are one of the most common layer-by-layer depositions methods, as spraying machines and technologies have improved and become more readily available (Figure 46b). In these methods, the properties of the jet of ink being directed at the substrate are tuned to optimize the deposition. Spray systems can handle a range of materials, thus the MPL, CL, and membrane can all be deposited in order to create a CCM. Although automated systems are now common, handheld airbrush methods where the operator controls the speed and direction of the spraying onto the substrate are still widely used, partly due to their low cost and ease of use.[411,473–475] Work by both Mack et al.[474] and Hwang et al.[411] have demonstrated that spraying of the CL onto the substrate results in an electrode with fewer cracks than those prepared using doctor blade or screen-printed techniques. Spray-deposited MEAs are also reported to outperform painted MEAs due to homogeneous distribution of the CL across the substrate.[315,382] Parameters such as the spray gun inlet pressure, annulus, drying rates, and ink composition have shown to alter the performance of the MEA by changing the resultant pore structure,

Pt, and ionomer distribution of the CL.[315,475] Reports also indicate that a mist-like spray and smaller droplet size gives a better performance due to improved porosity.[323,475] While hand-held techniques are not suitable for scale-up, automated spray systems are widely available for industrial scale manufacturing procedures of scalable uniform MEAs. This is particularly advantageous in the research laboratory, where reproducibility is crucial when screening novel catalyst materials. The tunability of spraying techniques makes them good candidates for the production of uniform CLs, and obtained understanding could easily be applied to automated adaptations. Recent advances in spraying methods have seen the development and use of ultrasonic spraying techniques (Figure 46b),[382,476–478] which can produce high-performance electrodes.[393] The advantage of using an ultrasonic nozzle is that the highly uniform spray of small droplet sizes can be produced at low flow rates.[479] Examples of ultrasonic spraying include the use of the technique for deposition of Ni nanowire containing catalysts,[477] fine-tuning of the CL properties,[382] and understanding how the solvent of choice affects fuel cell performance.[476] Ultrasonic spray techniques have also allowed for the creation of MEAs that are entirely spray-coated, such as that reported by Klingele et al.[480] Electrostatic spraying is another spray method for preparing CLs,[323,481] where a potential is applied between a spray head containing the ink and the substrate, such that the negative charge of the ink is attracted to the positive charge of the substrate. This principle is applied in a number of industries where good control of ink spraying is required, such as the spraying of car bodies in vehicle manufacture,[482] which highlights the suitability of the technique for industrial manufacture of CLs. The main advantage of electrostatic methods is that only areas that have an electric charge are sprayed, which improves ink utilization since less material is lost by overspray around the CL edges.[482] Electrosprayed MEAs have been reported to show improved performance compared to other spraying methods, partly due to higher pore fractions facilitating mass transport within the CL.[323,483] Takahashi et al,[323] reported that changing the manufacturing method from pulse spray to electrospraying increased porosity and pore size, which resulted in a higher performing MEA. However, it is not clear what fundamental aspect of the electrospraying process caused this change in porosity. They found that electrospray allowed use of a lower ionomer content, which resulted in higher ECSA due to better ionomer distribution and improved porosity. Interest has also arisen in the use of inkjet printing for preparation of CLs, partly due to its commercial potential and ease of upscaling. Furthermore, inkjet printing allows for greater automation and a large degree of control over CL thickness and Pt loading, particularly at ultra-low loading.[415,484–486] Shulka et al.[484] reported that inkjet printing achieved higher performance compared to traditional spraying methods due to improved proton and oxygen transport. However, in this report, the Pt loading and thicknesses of the compared MEAs were quite different, with the most loaded screen printed CCM being 0.031 mg_{Pt} cm^{-2} (1.68 μm) while the spray-coated CCM was 0.1 or 0.4 mg_{Pt} cm^{-2} with only the most loaded CL thickness of these two being reported (10 μm). Given the unequal catalyst loadings, it is not clear in this comparison what is the resultant morphological and subsequent performance difference between these two techniques.

Electrospinning is another commonly utilized manufacturing route that has been shown to have great potential. For example, Zhang et al.,[341] and later Brodt et al.[320] from the same group, prepared a CL based on electrospun commercial PtC, which formed into strands. These were ambiguously referred to in these publication as carbon nanofibers. This should be considered an erroneous designation as the materials are significantly different from the CNFs discussed in Section 4.8. They reported a 40–50% drop in ECSA after AST, and a 5–10% loss in power density at 0.65 V after 10 000 cycles for both electrospun catalyst and a commercial sprayed catalyst. With cathode exhaust CO_2 levels during ASTs being similar for both electrodes, however, the electrospun catalyst only experienced a 15% reduction in maximum power density, compared with the commercial sprayed catalyst, which lost 41%. The electrospun PtC would be expected to have no chemical variation compared to sprayed PtC. This observed durability increase is likely due to morphological change induced by the electrospun manufacturing method which creates intra- and inter-fiber porosity, allowing for the expulsion of water, preventing flooding. The improved water management could be the cause of the observed reduction of carbon corrosion,[320] however, given the same measure CO_2 exhaust this is unlikely. A better explanation is that the electrospun CL morphology has resulted in reduced electron thinning, cracking or other structural changes, although further analysis would be required to confirm this. This better retention of the nanofiber structure even during carbon corrosion may explain the superior durability and performance.

It is widely reported that due to the inherent differences in fabrication methods, the resultant CLs possess distinct morphologies.[315,323,482,483] These include porosity, PSD, CL thickness, and ionomer distribution. It is not yet clear which fabrication method results in the best performing MEA. Since no one manufacturing route will be perfect for all situations, understanding how each manufacturing route impacts the CL morphology and performance is key to the widespread improvement of this technology; this, however, is not trivial. Different fabrication routes require different ink formulations; for example, ultrasonic spray systems typically require a dilute ink compared to hand-sprayed. This change in ink formulation has a largely unknown impact on the CL layer morphology. While there are many reports that do explore these themes, they are limited in their scope and depth of understanding. For example, when comparing different fabrication methods, a full study of PSD, porosity, Pt utilization, and CL imagining would be required to understand the differences in CL morphology. Some articles have published reports comparing manufacturing methods using CL with different Pt loadings, which lead to inconclusive data. Comparing different manufacturing routes requires the use of the same loading Pt, same ionomer ratio, and catalyst support. To achieve this requires not only significantly more research comparing different manufacturing techniques but also a shift in the expectations that authors and reviewers have towards CL morphological data.

5.4. Techniques to Modify CL Morphology

Typical commercial electrodes are formed by co-drying nanosized particles with ionomer, creating a porous but
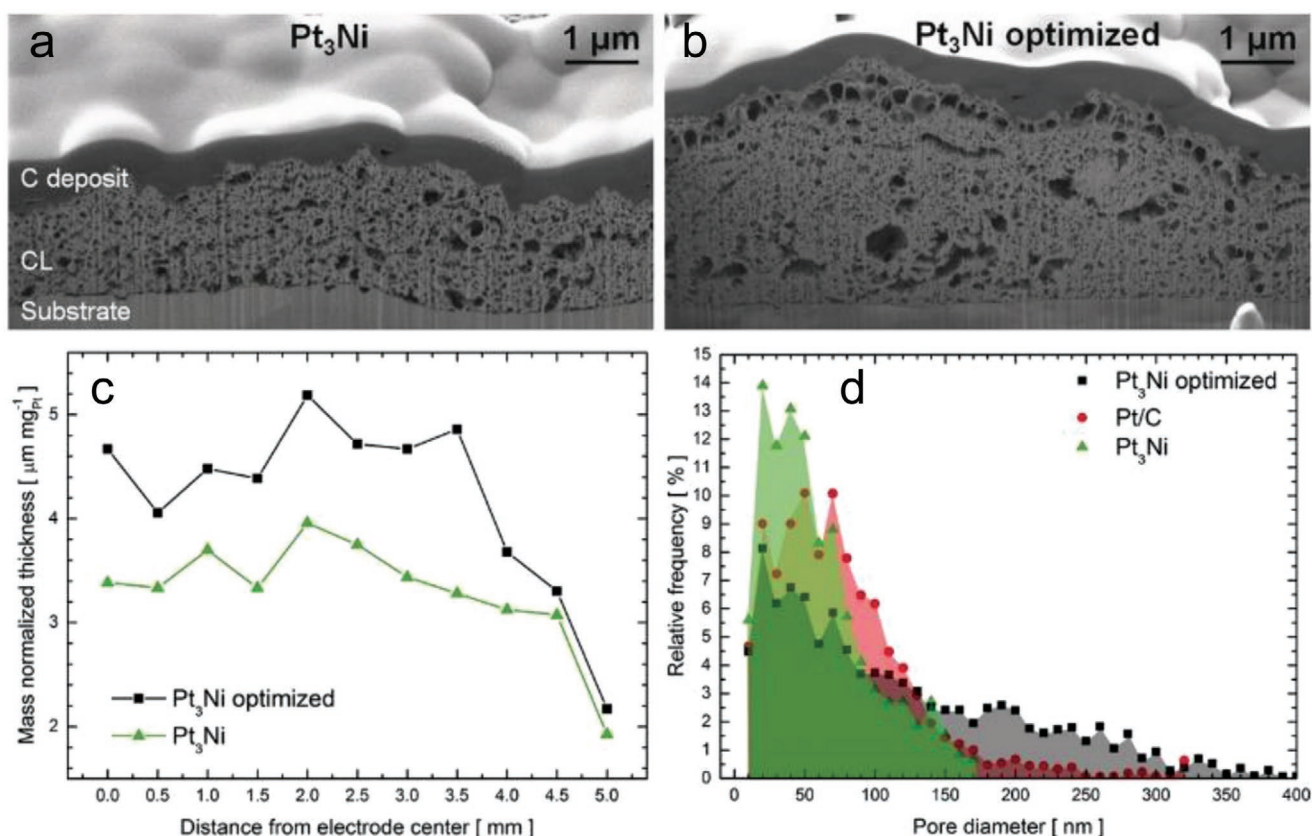
Figure 47. a,b) Representative cross-section SEM images and c) thickness as a function of the distance from the electrode center for CLs of Pt_3Ni (0.48 $mg_{Pt} cm_{geom}^{-2}$) and Pt_3Ni optimized (0.53 $mg_{Pt} cm_{geom}^{-2}$). d) PSD derived from FIB SEM tomography for Pt_3Ni, Pt_3Ni optimized, and PtC CLs. Reproduced with permission.[487] Copyright 2018, John Wiley and Sons.

interconnected network. Additional techniques and methods can be employed to further develop upon the standard manufacturing techniques and allow for precise engineering of the CL structure. This is done to enhance the natural pores formed in CLs or to introduce a beneficial PSD onto support materials without inherent porosity.

As discussed in Section 4.8, graphene has been reported to form dense, low-porosity CLs, which is alleviated by introduction of spacers.[371,443–448] However, since the spacers themselves become part of the overall CL, it is best considered as a dual support CL structure rather. Fabrication methods that modify the hierarchal pore structure of a CL without changing the overall composition have been reported. For example, simple salts can be added to the catalyst ink before manufacturing and easily removed after fabrication. Henning et al.[487] and later work by Ishikawa et al.[406] reported the use of unsupported Pt_3Ni aerogel as a CL. The nanochain Pt_3Ni structure adopted a tortuous gas diffusion pathway that limited performance. The initial performance of Pt_3Ni is significantly lower than that of PtC, but with the introduction of K_2CO_3 additive, the performance was reported to exceed that of commercial PtC. K_2CO_3 is facile to remove after MEA fabrication by simple washing or soaking in water. This increase in performance was attributed to changes in CL morphology, particularly, the significant increase in macropores which improves mass transport of gases as shown in **Figure 47**. This resulted in a thicker electrode with

improved mass transport and water management. While typically a thicker electrode has associated performance limitations, the thinner, unsupported Pt_3Ni benefited from the increased thickness. A reduction of micro and mesoporosity was observed to accompany this change in CL morphology, which may explain the significantly lower ECSA compared to commercial PtC. However, the distribution of salt during deposition can be hard to control and form a homogeneous engineered CL.

Alternative manufacturing techniques, such as colloid templating, have been suggested to improve performance by a similar introduction of porosity and chosen PSD allowing for greater Pt utilization.[84,488] Colloid templating typically uses silica as an additive to form a defined structure, which is followed by catalyst and ink impregnation. Banham et al.[456] heat treated a mixture of pitch and colloidal silica followed by reflux in NaOH to create a templated, highly porous, and nanostructured CL.[456] Controlling the size of the templating material and the manner in which it is deposited gives a huge degree of control over the final nanostructure. However, the complex and chemically extreme manufacturing method required to remove the silica requires the catalyst and ionomer to be impregnated after the morphology of the CL is created.[489–491] This can result in systems in which the ionomer cannot penetrate into the entire pore structure, resulting in a loss of catalyst utilization.[488] Efforts have been made to increase pore size and therefore Pt utilization and performance, but this will come at the
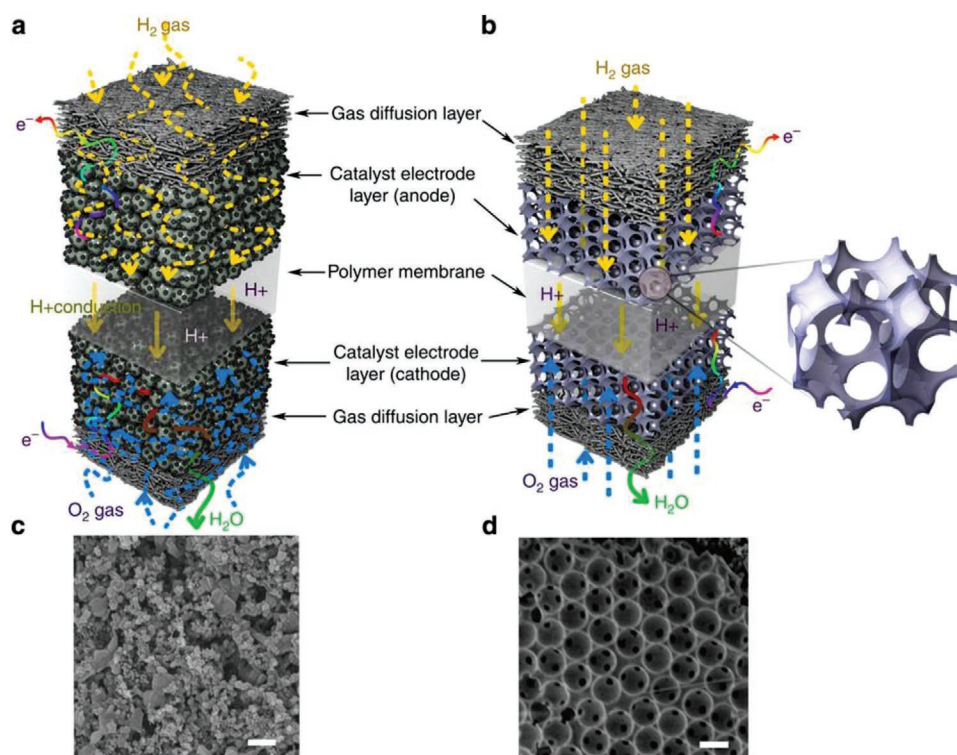
Figure 48. a) Conventional MEA with CCM; b) modified MEA with inverse-opal-structure (IO) electrode examined in this study. c) FE-SEM image of a CCM surface prepared by commercial PtC ink spraying. d) FE-SEM image of an IO electrode surface prepared by pulse electrodeposition according to colloidal crystal templating methods. Scale bar, 500 nm. Reproduced with permission.[384] Copyright 2013, Springer Nature.

cost of either surface area or thicker electrodes.[456] This technique is particularly useful for FPE in which maximized ECSA requires a uniformly nanostructured CL without the need for ionomer incorporation.

A range of other templating methods have been utilized, such as the use of polystyrene nanospheres (**Figure 48**).[342,384,492] These are easier to remove by simple washing in ethyl acetate and hence are more widely used. For example, Zlotorowicz et al.[492] reported that by introducing polystyrene nanosphere additives into a PtC ink, macroporosity and performance can be introduced. They reported that nanosphere incorporation up to 70% of the weight of the PtC performed best. However, they also changed the Pt loading across each sample and did not analyze the pore size or distribution due to the addition of additives, meaning it is unclear how exactly these additives affected the CL structure. Kartouzian et al.[342] reported the use of polystyrene to control the pore size and porosity improves the water management of the system, as discussed in Section 4.2.

Nanopatterning is a process to introduce nanoscale texture and patterns typically onto the membrane; it uses techniques such as proximity field patterning (PnP) and lithography, among many others.[493,494] Nanopatterning can lead to a significant increase in surface area and control over porosity and PSD in CLs, resulting in highly engineered structures.[493,494] These techniques can be used to benefit water management within the CL and overall fuel cell performance, but can result in higher hydrogen cross-over due to the induced mechanical thinning of the membrane.[494] Nanopatterning is a potential

tool for nanoengineering CLs, but further research is required to determine the optimum pore distribution and porosity without disturbing membrane or CL integrity.

5.5. Catalyst-Coated Membranes and Gas Diffusion Electrodes

Before the MEA can be assembled, the electrodes must be prepared. There are multiple routes to achieving this, including CCMs, GDEs, and decal transfers. Decal transfer, while not a CL fabrication method, is a technique to prepare MEAs in which a CL is deposited onto an inert substrate then adhered onto the membrane by hot pressing.[496] This has been shown to improve charge transfer resistances and performance within the MEA.[497,498] Decal transfer methods have been reported to form CLs with a more homogeneous distribution of ionomer as GDEs can lose significant amounts of ink permeating into the MPL. Although, as highlighted by Shahgaldi et al.,[82] this is an extra processing step, so may be less suitable for industrial applications.

There are several opinions within the community as to whether GDE or CCM performs better. It is thought that the deposition of the CL directly onto the membrane reduces the contact resistances by direct lamination, as well as providing more proton-conducting pathways through the CL to the membrane (or vice versa on the cathode); however, the deposition can cause the membrane to deform. Investigations carried out by Tang et al.[499] showed that the CCM performs better than the GDE. EIS highlighted more efficient charge transfer of species

ADVANCED
SCIENCE NEWS

www.advancedsciencenews.com

ADVANCED
ENERGY
MATERIALS

www.advenergymat.de

in the CCM, with the cathode charge transfer arc being smaller for all CCM samples than for GDE samples. Wang et al.[500] reported that CCMs generally out perform GDEs, although this is dependent on Pt loading, as discussed later.

Reasons for the improved performance of the CCM over the GDE are typically attributed to multiple factors, including lower cell resistances and improved ECSA.[82,495] This was even shown for high-temperature PEFCs, where the lowered Ohmic and charge transfer resistances of the CCM resulted in an increased power density.[495] Using a CCM preparation technique was also shown to be effective for increasing catalyst utilization, suggested to be arising from better contact between the CL and the ionomer.[501] Further insight into the differences between CCM and GDE preparation methods were shown by Thanasilp and Hunsom,[497] who found that while CCM showed little improvement in Ohmic resistance compared with GDE, there was a significant improvement in charge transfer resistance, ECSA, and OCV when using a CCM.[497] This improved performance of the CCM was assigned partly due to its significantly lower average pore diameter which may be a consequence of a more connected (less resistive) membrane and CL contact, which is often referred to as "better contact" although, this term is loosely defined. A more rigorous measurable definition is required to more clearly understand and compare this structure–performance relationship. While it is reasonable that the CL morphology would change depending on the nature of the substrate it is deposited into, in-depth structural comparisons between CCMs and GDEs are required to understand the origin of this performance difference. Direct membrane deposition (DMD) is a development on the CCM approach whereby a GDE is first prepared, followed by deposition of the membrane (from solution) on to the GDE, and finally the opposite electrode is sprayed on to the membrane. The superior power density from DMD was thought to arise due to improved water management and reduced ionic resistance, even compared with a CCM.[502] However, limited characterization and comparable literature results lead to an inadequate understanding of the origin of this performance difference. The additional step of directly applying the membrane constitutes an extra step in the manufacturing process, which must be balanced against whether a high power density is required for the desired application.

While more publications seem to suggest that CCMs outperform GDEs, this not always the case. For example, Liang et al.[495] and Shahgaldi et al.[82] have reported that under some conditions, such as with higher Pt loading electrodes, or when following specific fabrication methods, the GDEs have similar performance to or outperform CCMs (**Figure 49**). However, this is in contrast to Wang et al.[500] found that the screen-printed CCM outpeformed GDEs when above Pt loadings of $0.3~mg_{Pt}~cm^{-2}$. The origin of this reported performance difference is not clear and not widely discussed in this publication; further in-depth structural analysis such as PSD may be required. The difficulty in determining the relative performance of CCMs and GDEs is likely due to variation in the preparation methods and ink composition.[460] It has been shown that by adding a thin layer of ionomer and then hot pressing onto the membrane, an improved GDE performance can be achieved, matching that of the CCM, as shown in Figure 49a.[82,498] This approach benefits in the same way as the DMD MEA, but avoids issues of limited
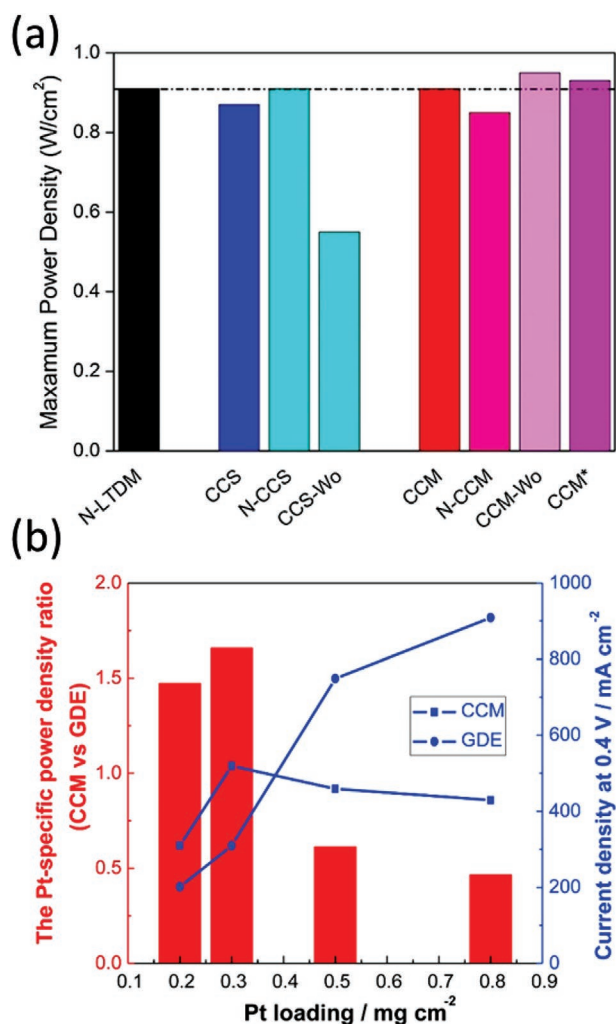
Figure 49. a) Histogram comparing the maximum power density of the MEAs prepared by the range of the variations deployed in the three different MEA manufacturing methods ($0.5~mg_{Pt}~cm^{-2}$, 75 °C, 35 kPa back pressure, 100% RH air/H_2). Reproduced with permission.[82] Copyright 2018, Elsevier. b) The Pt utilization ratio and the current density at 0.4 V comparison of MEAs prepared by CCM and GDE. Reproduced with permission.[495] Copyright 2014, Elsevier.

dispersion cast membrane stability. Results showed that it was possible to achieve comparable performance to a CCM, which highlights that preparation of the CL using a GDE method is still a viable option for achieving high-performance MEAs. A similar trade-off also exists for CCM preparation; because the membrane is not as rigid as a GDM and rapidly swells in the presence of solvent, when depositing the ink onto the membrane, the surface can become rippled or wrinkled causing it to become uneven. This is a particular problem when using inks with high solvent contents, or high boiling points solvents, resulting in prolonged drying duration that gives the membrane more time to morph. This is another issue that DMD can mitigate as the benefits of CCM are realized but wrinkling is avoided due to the rigid GDL substrate. Tuning the method used for drying the CL can also help mitigate these drying effects.

**ADVANCED
SCIENCE NEWS**

www.advancedsciencenews.com

**ADVANCED
ENERGY
MATERIALS**

www.advenergymat.de

5.6. Hot Pressing

The most common method for preparation of the MEA is by hot pressing the two GDEs onto either side of the membrane (or two GDMs onto either side of the CCM) by placing them between two heated plates and applying a specified pressure, as first discussed by Ticianelli et al. in 1988.[503] The temperature of the plates and the pressure applied depend on the practitioner, with conditions commonly being determined using iterative testing approaches.[504,505] Hot pressing can affect the structure and morphology of the materials within the MEA, with the main aim being to improve the contact between the membrane and CL. However, work done by Suzuki et al.[358] has shown that high amounts of pressure during hot pressing can significantly decrease porosity and average pore size, hence reducing performance, with 2 MPa on a 5 cm² MEA found to achieve the highest current density. Any significant loss of porosity will impede both access of gas to active sites, as well as water expulsion from the pores, and will ultimately reduce the performance of the cell.

No consensus of the performance improvements observed from hot pressing has been reached in the literature, with the necessity and pressure of hot pressing having been reported to be different for CCM compared to GDEs.[82,504] The need to hot press GDEs has been found to be pronounced, particularly at lower catalyst loadings.[82,498] Andersen et al.[504] compared ten different GDEs hot pressed with varying temperatures, pressures, and duration of pressing. It was suggested that a pressure of 7 bar at 150 °C for 3 min were the optimum conditions. However, this is in contrast with the findings of Meyer et al.,[506] who showed that the optimum hot pressing temperature for GDEs is slightly lower at 130 °C (**Figure 50**a). Alternatively, Hack et al.[507] suggested that there was no improvement in performance with hot pressing the
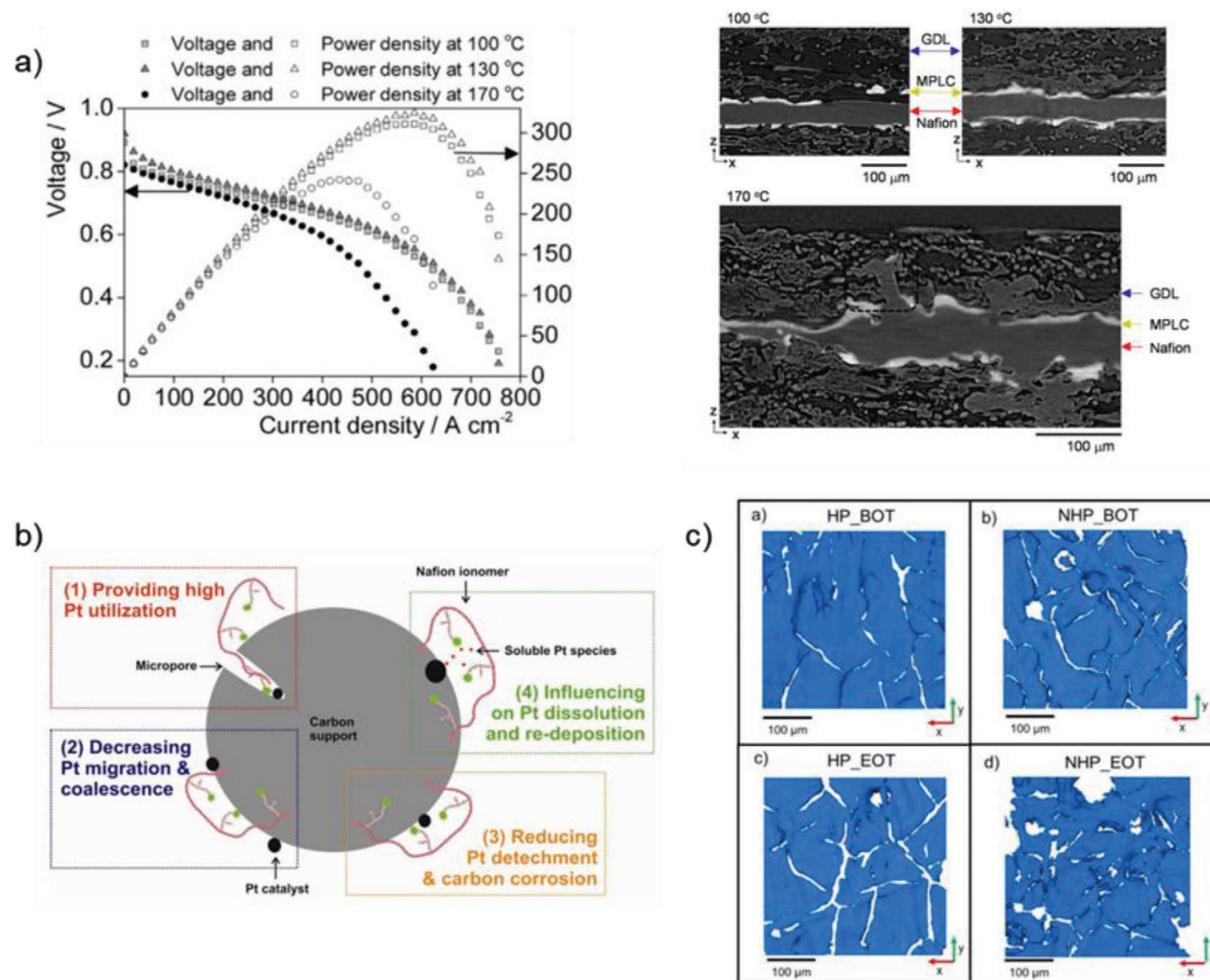
Figure 50. a) Polarization curves of MEAs hot pressed at different temperatures (right) X-ray CT images of hot pressing, showing severe disfiguration of the sample HP at 170 °C. Adapted with permission.[506] Copyright 2017, Elsevier. b) Schematic showing the role of the ionomer in CL performance and how improving this is linked to reduced degradation. Reproduced with permission.[504] Copyright 2015, Elsevier. c) X-ray CT volume renderings of comparing catalyst layers hot pressed (HP) and not hot pressed (NHP), at the start and end of the test. Adapted under the terms of the Creative Commons Attribution 4.0 International (CC BY 4.0) license.[507] Copyright 2018, Electrochemical Society.

MEA prior to operation, with the heat and pressure applied by the cell during operation thought to provide an in situ lamination effect. Finally, by the three key variables of their models (temperature, pressure, and duration) Okur et al.[505] suggested optimum conditions of 97 °C, 65 bar, and 3.56 min for their GDEs. As shown in Figure 49a, an additional thin ionomer layer deposited onto GDEs before assembly has been reported to improve performance. These conflicting reports from literature emphasize that each MEA setup will perform differently due to inherent differences in microstructure in different commercial or in-house manufactured CLs and MPLs. While the exact optimized conditions are not clear, GDEs do broadly appear to improve upon hot pressing; however, operating conditions and MEA cell compression may have similar effects. Practitioners should ensure they spend time finding the optimum conditions when working with new MEA architectures and materials.

CCMs have been reported to show little improvement after hot pressing, or with the introduction of a thin ionomer layer.[82,498] Roudbari et al.[508] reported that in half-cell experiments, CCMs hot-pressed at 110 °C resulted in the best performance. Again, these conflicting reports highlight that the performance of a particular MEA system is highly dependent on the materials of choice and operating conditions. Universal optimization of hot-pressing cannot occur due to the intrinsic differences between MPLs, membranes, and CLs, but a more coherent understanding of the mechanism occurring during hot pressing would help elucidate optimization parameters. In-house optimization procedures must be developed by research groups based on their commonly used materials. However, when investigating new CL morphologies or changes in other components, these procedures must be re-evaluated to achieve optimum performance.

The increasing availability of laboratory-based 3D imaging has seen a growth in the use of techniques like X-ray CT to elucidate the effect of hot pressing on the microstructure of the MEA.[506,507] Paul et al.[302] reported that Nafion membranes undergo restructuring when annealed at 140–160 °C, temperature similar to those used for hot pressing. Using X-ray CT, Meyer et al.[506] reported that when hot-pressed at temperatures well above the glass transition temperature of Nafion (123 °C) there was significant disfiguration of the membrane (Figure 50a). In particular, a highly irregular membrane thickness was observed and some parts of the membrane were found to have flowed into the pores of the GDL. However, at temperatures below the glass transition temperature, there is only partial lamination of the membrane to the CL, which increases Ohmic resistances. Hack et al.[507] compared X-ray CT of hot-pressed and non-hot pressed MEAs, showing that the non-hot-pressed samples had more cracks and depressions in the electrode surface (Figure 50c). However, it was concluded that the differences in the microstructure of the CL were not sufficient to affect the MEA performance. Despite the knowledge of the importance of the membrane and ionomer in the CL (as shown in Figure 50b), there has been little work that elucidates the chemical changes that arise in the membrane during the hot pressing process. It is unknown whether the bonds within the membrane material are altered, even if hot pressing at temperatures below the glass transition temperature of the ionomer, and for very short periods of time, and whether this has an effect on the MEA performance.

5.7. Pressure During Assembly

The assembly of a fuel cell and the optimal MEA compression presents a crucial step to achieving maximum performance and avoiding irreversible morphological damage. In conventional PEFCs, the MEA is first placed between two flow-field plates, ensuring good alignment and correct orientation prior to compression. Custom-designed gaskets provide a gas seal around the MEA perimeter and come under two main categories: compressible (EPDM rubber) and incompressible (silicone, PTFE). Preference between the two gasket types is at the discretion of the manufacturer and studies into gasket durability within a fuel cell environment consider the impurities formed during degradation, which may contaminate the MEA.[511–514] MEA compression is imposed by the mechanical compaction of the PEFC and the thickness of the sealing gaskets. The most common assembly approach uses compression tie-bolts to hold the fuel cell fixture together, torqued to a pre-set value that establishes a desired contact pressure on the MEA. The number of bolts and their arrangement can have a significant impact on the pressure distribution across the MEA but is dependent on the size and geometry of the fuel cell fixture.[515] A non-uniform pressure distribution can result in a lack of electrical contact toward the MEA center, which can have a significant effect on the local performance.[516,517] This can be solved by using thicker endplates,[517,518] bladder cells,[519] or increasing the clamping pressure.[520]

Adequate cell compression is essential to ensure sufficient electrical contact of the GDL with the flow-field plates and effective gas sealing of the gaskets. However, over-compression can lead to significant and irreversible deformations to the MEA. GDL fibers are soft and brittle and their morphological structure is easily influenced by compression, forming structural deformations by the land/channel imprint of the flow-field (**Figure 51**). Under the land, increasing compression crushes the GDL to the flow-field, decreasing GDL porosity and increasing the tortuosity factor.[521–523] The reduced pore diameter alters the capillary pressure, increasing water retention, resulting in a higher water presence in the cell.[524,525] Kulkarni et al.[510] investigated the effect of compressive loads on the contact surface between a current collector (piston) and GDL fibers using X-ray CT (**Figure 52**). Non-uniform MEA compression results in heterogeneous transport properties as the GDL phase density and fiber cracking increases with compression, exhibiting the "tenting" phenomenon within the channels. The interfacial contact area between the lands and the GDL increases by 11% at the higher compression, which resulted in improved Ohmic resistance but at the cost of a reduction of free gas flow. Poor water removal efficiency then ensued, which resulted in an early onset of flooding phenomena. In another report, Kulkarni et al.[521] also observed a 27% increase in water accumulation in a PEFC when GDL compression increased from 25% to 35% (**Figure 53**), particularly under the lands, with significant performance loss at high current densities. The severe flooding of the GDL under the land with increasing current density resulted in a loss of reactant supply to the electrodes and thus an uneven current density distribution. The RH of the inlet gases also played a role in the GDL flooding and it was suggested to decrease the compression ratio with higher gas humidity.[526]
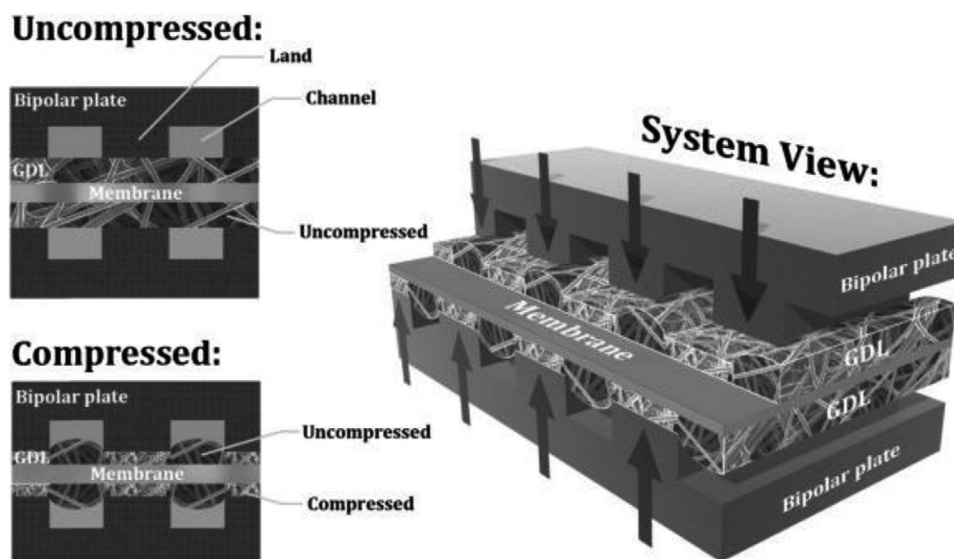
Figure 51. Image of the compression processes; as the fuel cell is compressed, a loss in thickness occurs as the land compresses the GDL beneath it. Adapted with permission.[509] Copyright 2013, Elsevier.
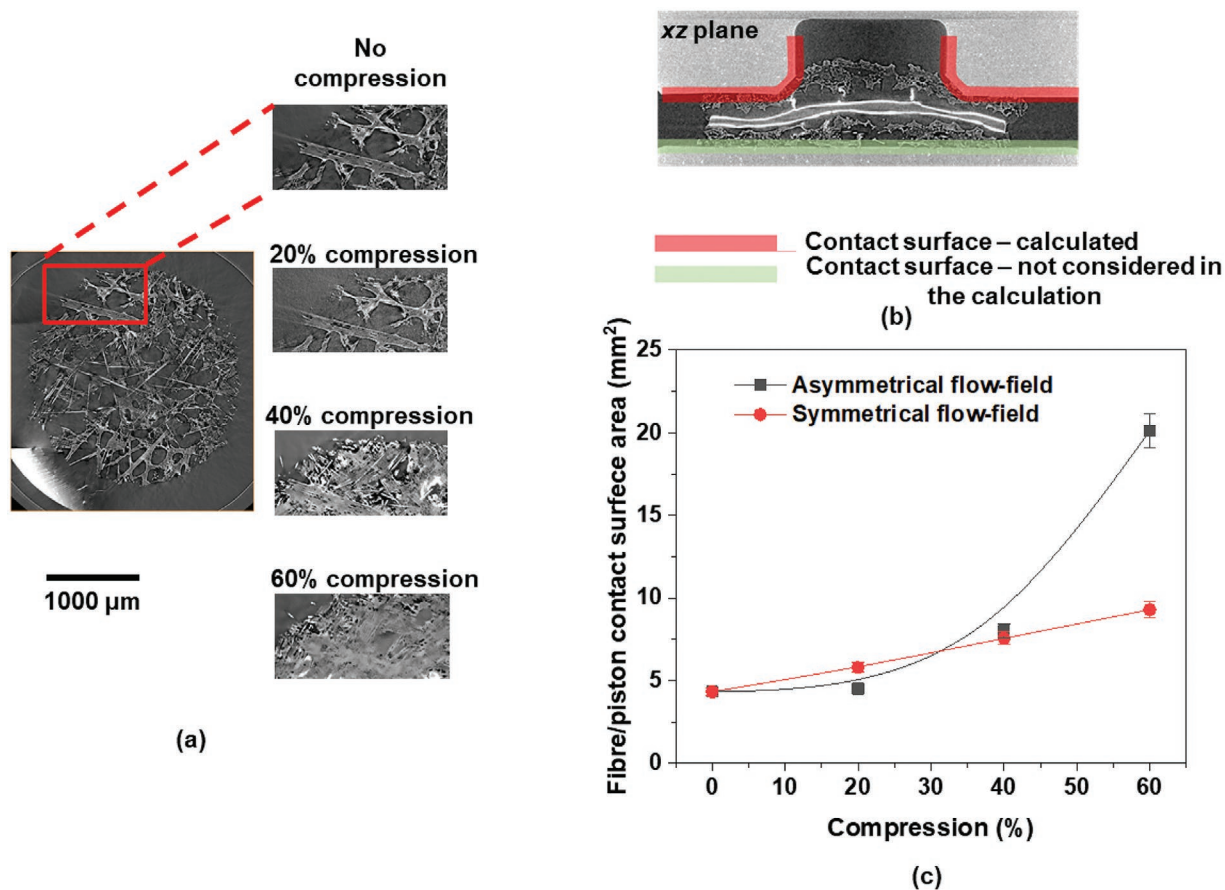
Figure 52. Effect of compressive load on the contact surface area between the current collector (piston) and GDL fibers; a) ortho-slice showing the interfacial surface for the asymmetrical flow field, the area under the red square shows an increase in fiber phase density with compression, b) the contact sub-domain of GDL fibers and the top piston (red) was considered for the quantification of the contact area, and c) the change in the interfacial contact area between GDL fibers and piston with compression. B-spline passing through the data points is included as a guide to the eye. Reproduced with permission.[510] Copyright 2019, Elsevier.

**ADVANCED
SCIENCE NEWS**

www.advancedsciencenews.com

**ADVANCED
ENERGY
MATERIALS**

www.advenergymat.de
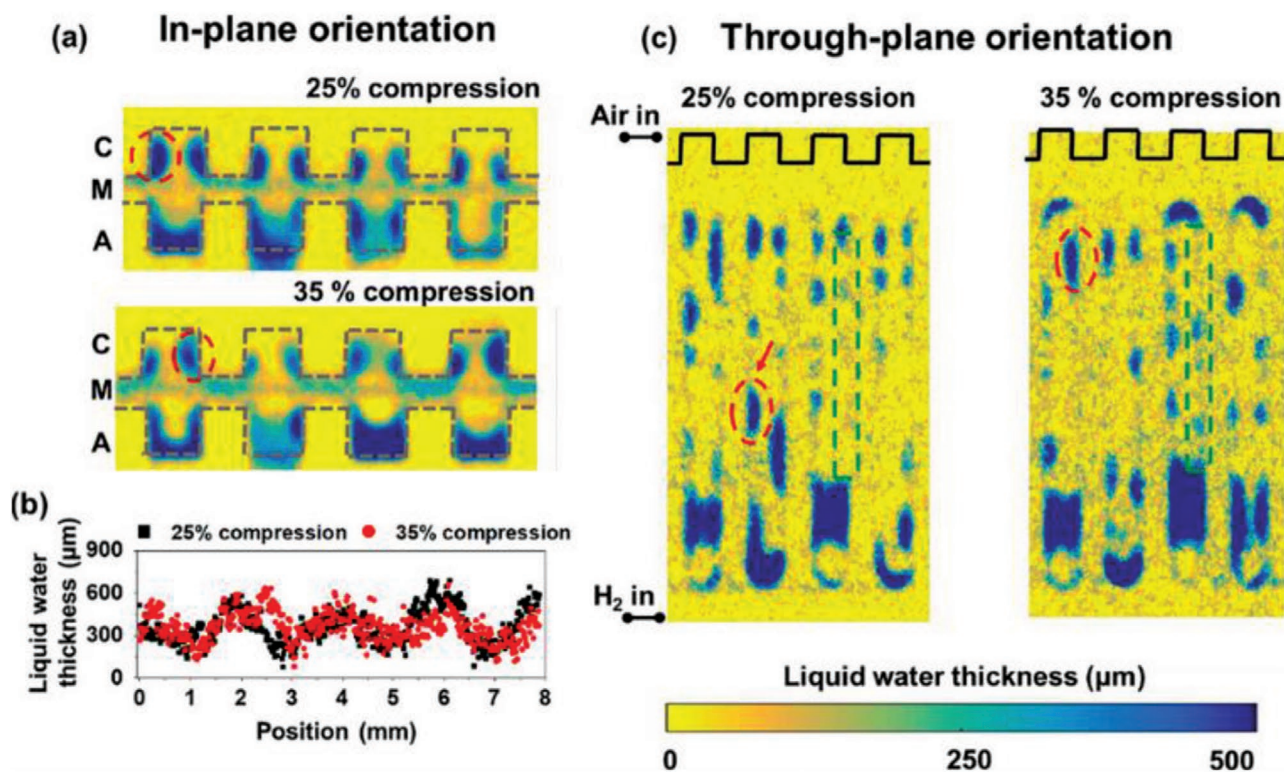
Figure 53. Effect of compression on the water distribution in the mass transport region, $j = 1$ A cm^{-2} (a) in-plane radiographs measured at $t = 300$ s, "C" is the cathode flow channels, "M" is MEA (GDLs + CLs + membrane), and "A" is the anode flow channels. Grey dashed lines showing the flow field outline is included as a guide to the eye. b) Liquid water thickness profile in the in-plane orientation measured at the membrane/CL showing the effect of channel/land geometry on the water retention. c) Through-plane radiographs measured at $t = 300$ s. Panels (a) and (c) share the same color bar. Reproduced with permission.[521] Copyright 2019, Elsevier.

GDL within the channels experience a smaller compressive force compared to that in direct contact with the flow field; however, the lateral displacement of GDL from the compressed regions under the land create a "tenting" effect under the channel.[528] The effects of PTFE treatment have a notable effect on this "tenting" phenomena, where an increase in the hydrophobic agent which binds the carbon fibers together improves the mechanical strength of the GDL.[527] Thus, when the GDL is compressed, the microstructure profile results in a flatter land/channel deformation and less porosity loss (**Figure 54**). In situ diagnostic techniques have also been utilized to study the effects of compression, predominantly through polarization curves (**Figure 55**a).[529] Compression has little impact on performance at low current densities. As higher current densities are reached and more water is produced, water management complications arise, with earlier onsets of flooding for increasing GDL compression.[530,531] Mason et al.[509] used EIS to separate the effects of compression on the contact resistance and mass transport losses (Figure 55b,c bottom). Increasing compression resulted in a non-linear decrease in the Ohmic resistance but was found to most severely impact the mass transport region, particularly the cathode GDL. They found that the optimal compression on the MEA was 0.5 MPa. A trade-off is required in PEFC design between decreased contact resistance, resulting in better Ohmic performance and decreased porosity which aggravates the effects of flooding and ultimately leads to performance loss.

5.8. Conclusion and Outlook

Manufacture of the CL and subsequent preparation of the MEA is intrinsically linked to the final fuel cell performance and it is key that factors like hot-pressing parameters, CL preparation, and assembly in the cell are fully optimized in order to achieve the best performance. However, different fabrication methods and conditions will have different impacts depending on the structure and chemistry of the materials used. Given the wide range of materials and preparation techniques available, it is imperative that practitioners spend time tuning the fabrication method to their unique materials. Fabrication method has a large impact on the morphology and performance of the CL. This is problematic when comparing publications with different manufacturing routes, and a significant morphological characterization is required to achieve a clear comparison between CLs prepared differently.

Preparation of the CL is a complex balancing act between practicality and achieving the highest performing devices. Advanced CL manufacturing techniques, like ultrasonic spray coaters, produce top-performing high-throughput electrodes, but require more expensive equipment. Industrially friendly fabrication processes such as roll-to-roll, doctor blade, and slot die coating are typically difficult research tools due to their inflexibility. Colloidal templating is not well suited for scaleup and highthroughput manufacturing, but have been shown

ADVANCED
SCIENCE NEWS
www.advancedsciencenews.com

ADVANCED
ENERGY
MATERIALS
www.advenergymat.de
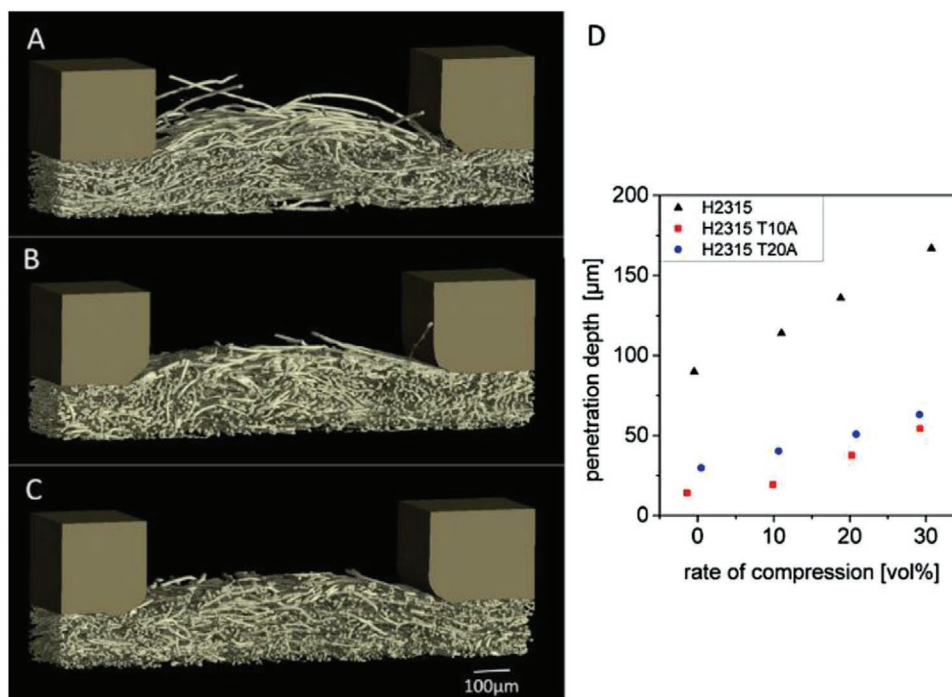
Figure 54. Perspective 3D-view on the sample compressed by about 30 vol%, rendered on a section of channel and the adjacent land area. a) H2315 (no PTFE); b) H2315 T10A (10 wt% PTFE); c) H2315 (20 wt% PTFE). d) Penetration of the flow field channel by fiber material measured along the centre line of the channel at increasing rates of compression. Reproduced with permission.[527] Copyright 2016, Elsevier.

to produce very high performing electrodes. However, there are very little comparison in the literature between different manufacturing methods and the subsequent changes in CL morphology that they cause. This is problematic as the manufacturing route should be considered another tool with which researchers can control the CL morphology and therefore performance. We encourage more detailed investigation of different manufacturing routes and the structure of the resulting CLs. Comparison between these different manufacturing pathways is not facile due to differences in the porosity, PSD, and thickness of the resultant electrodes. Furthermore, feedback from industrial CL manufactures about the most commercially relevant manufacturing method would allow researchers to prioritize which technique to investigate.

Ink formulations, solvent type, and, Nafion concentration all have been shown to play a role in CL layer morphology. It is clear that there is a need for literature to critically analyze and explore manufacturing techniques without bias. In particular, more experimental studies in which the structure of the CL is the feature of interest when using manufacturing methods. In addition, improved transparency surrounding the choice of parameters like hot pressing conditions or CL preparation and drying techniques is needed. A range of tools from removable salt filler to polystyrene nanospheres and silica templating can be used in conjunction with standard manufacturing to tune and control the CL morphology. The catalogue of different sacrificial additives that can be used for this purpose is currently limited in the literature, but may have the potential to allow significant control over porosity and PSD. Further research on different sacrificial additives and their impact on CL morphology and performance is required. The method in which the testing cell is assembled,

such as hot pressing and cell compression, has a large role to play on the resulting performance. Different morphologies are created depending on whether deposition is onto a membrane or an MPL, with the impact of the substrate on CL morphology not widely investigated. The process of CL fabrication, be it CCM or GDE, has been reported to affect performance and morphology. However, there is no consensus about which of the two methods forms the highest performing MEA. Further highlighting this, it has been reported that the Pt loading impacts performance differently depending on whether CCM or GDE has been used. Further research is required to understand the morphological impacts of CCMs versus GDEs, allowing the fabrication method to tailor this aspect of fuel cell fabrication to match the desired morphologies. The role of hot pressing in improving MEA performance is also not clear; this is again likely due to difference in testing regimes and a range of different CL morphologies being tested. This highlights that much more morphological based CL research is required to understand the impact these assembly methods have on performance, and therefore find the optimum fabrication method for each unique CL design. The effects of cell compression can have a detrimental impact on MEA morphology and overall cell performance. The imprint of the flow-field design on the GDL results in varying porosity across the structure, which can significantly impact both the gas flow to the electrode or effectuate local flooding. Conversely, a lack of compression will increase Ohmic overpotentials and fuel efficiency due to the lack of electrical contact between the plates and MEA and poor gas sealing from uncompressed gaskets. Side-reactions from leaking gases may ensue, further degrading the membrane and GDE due to mixed potentials. Optimizing the compressive load is crucial for effective design and will differ between
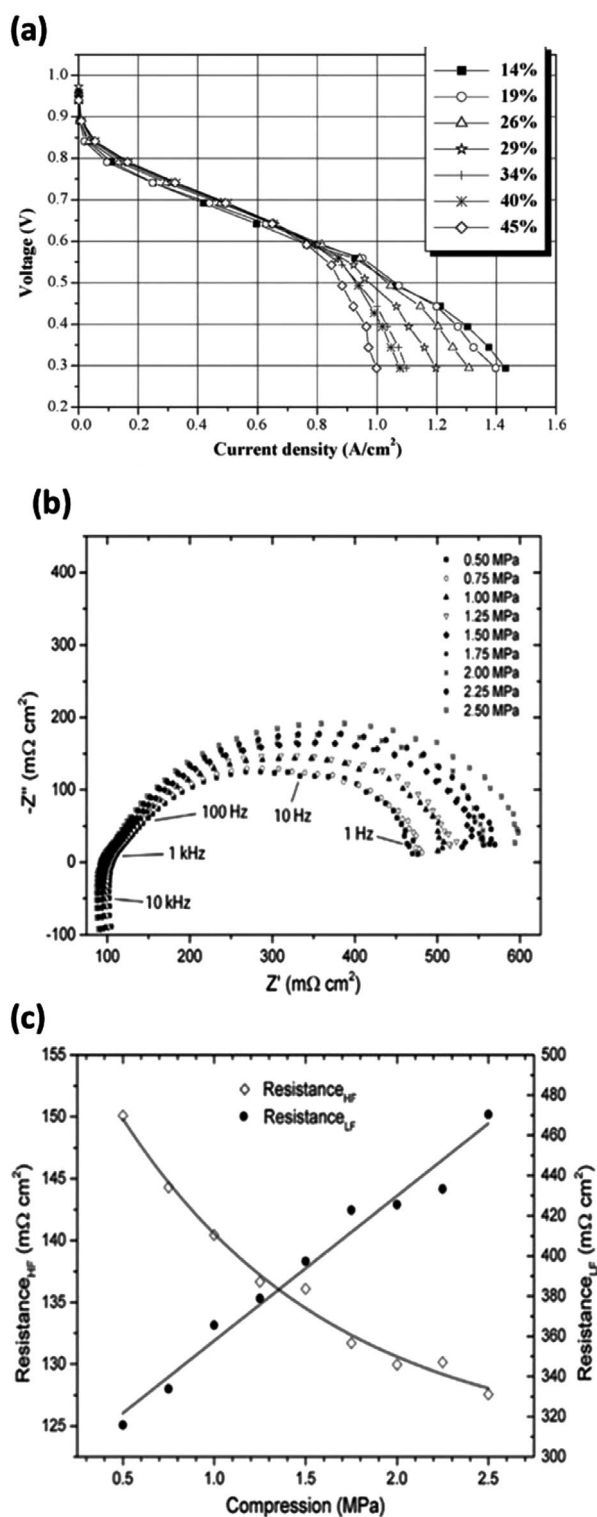
Figure 55. a) Polarization curves for carbon cloth GDL at different compression ratios. Cell temperature 65 °C, cathode and anode flow rates 1200 and 2200 sccm, respectively. Anode and cathode humidifier temperatures set to 80 °C. Adapted with permission.[531] Copyright 2006, Elsevier. Bottom: b) EIS plots of a PEFC under mechanical compression ranging from 0.5 to 2.5 MPa. c) Relationship between high (contact resistance) and low frequency (mass transport) resistances as a function of compression. Adapted with permission.[122] Copyright 2013, Elsevier.

systems due to: active area, cell geometry, number of cells, MEA materials, and operating humidity environment. The impact of these different MEA fabrication and assembly methods is highly dependant on the structure of the electrodes used, and as a result there is and cannot be one optimum testing system. Publications focusing on MEA fabrication and assembly should make significant efforts to report CL morphological data such as porosity and PSD before and after assembly. This will greatly expand discussion and aid understanding of the impact of CCM/GDE, hot pressing, and cell assembly pressure.

6. Perspective

With the urgent need to decarbonize, and limitations with existing low-carbon technologies, such as the insufficient energy density of batteries, there is increasing demand for hydrogen and fuel cell technologies. This is especially true for long-distance heavy goods vehicles and shipping applications.[5] The implication of this is that, fuel cell systems should not just be seen as an academic curiosity, but a race against time to optimize and increase roll out of this desperately needed technology. While the technology itself is not new, it is entering a new age of maturing as it becomes increasingly commercialized. However, to accelerate this process, research on this topic must match the increased specific demands of the industry, who are not only concerned with power density, but also cost, durability, and efficiency under commercially viable operating conditions. To achieve this goal, closer interactions between commercial interests and research institutions with published feedback is required. A trade-off between high Pt mass activity and high volumetric current density can exist with different catalyst loading; larger stacks with a more efficient use of Pt would be required to achieve the same current density with smaller, more high performing PEFCs. The cost benefit analysis of Pt costs versus other fuel cell components is not clear, and insights such as desired stack volumetric current density at set catalyst loadings from industrial bodies are required to optimize CL design.

The CL morphology itself has a large role on the performance and durability of a fuel cell and should not be viewed as the consequence of a particular fabrication method or support material but as an aspect of the CL design that need to be actively controlled. With the maturation of fuel cell research, a significant number of new tools and designs have emerged that have yet to be fully utilized in optimizing CL performance and durability. These tools are all key pathways to significantly improving MEA performance and durability and should receive expanded research effort. The choice of fabrication method significantly impacts the structure and performance of the CL, as a result of differences in the PSD and CL morphology. Furthermore, other manufacturing aspects such as ink composition, concentration, and solvent have an impact on CL formation as it impacts ionomer and support aggregate properties in the ink. However, such relations between manufacture method and morphology are not widely reported in detail. Utilizing different fabrication methods result in changes to the final morphology and therefore, changes to the performance. With further understanding, a fabrication method could be chosen

to tune and control a particular CL morphology. A wide range of other techniques can be utilized to influence device performance and durability.

Functionalization offers tunability and control over the hydrophilicity, ionomer wetting, catalyst interactions, and support inter-particle spacing of the support material, but only a small range of the multitude of potential functional groups have been published, with the performance impact of those that have been reported often lacking in understanding. The introduction of heteroatoms modifies the ionomer/support interaction and can poison the catalyst but can also anchor the catalyst, improving Pt durability. Optimization of these effects requires understanding their underlying causes, which in turn requires more thorough and detailed testing than is typically reported. Changes in hydrophobicity, either by functionalization or introduction of PTFE, shows great potential for aiding water management and ionomer distribution. Dual, multiple sectioned, or graded CL systems offer a structure to split the trade-off between thickness, porosity, ionomer loading, and Pt utilization into different sections and thereby increase the overall performance. Although, cotemporary results show only modest improvements, there is significant scope for more research in this area. Different CL designs such as NSTF and FPEs have shown to be incredibly high performing. Despite their significant limitations, they can be further modified or utilized in particular environmental conditions to outperform standard commercial materials. Control over ionomer nanostructures and the development of low O_2 resistance ionomers have the potential to form homogeneous ionomer distribution and alleviate O_2 transport resistances, which are some of the leading causes of performance limitations, particularly for low loading Pt electrodes. Novel supports such as metal oxides have shown great potential due to their higher durability compared to CB. As these materials are relatively immature compared to CB, significant research is required under a variety of ASTs and drive cycles to understand their degradation and their impact on catalyst durability. Nanomaterials, such as graphene, rGO, CNTs among many others offer great potential if their nanoscale properties can be utilized in a bulk electrode; however, this appears to require highly engineered CLs to observe any clear benefit. As the fuel cell sector grows into new commercial sectors, the requirements for fuel cells will broaden with their more varied use. These tools mentioned above offer the ability to tailor CLs to fit particular application, and will need to be much more widely investigated, their impact on performance and durability fully characterized and understood.

Increased commercialization requires enhanced durability of both the catalyst and the support as well as increasing the achievable current density. Methods to mitigate these limitations have been widely reported. However, publications are typically limited in scope and focus on specific changes to materials and have often missed the impact of the CL morphology on performance. Catalyst durability is not just an inherent property of the catalyst in question but is also significantly impacted by the support material it is deposited onto and the surrounding environment such as ionomer content and porosity. Support durability, while highly dependent on the chemical structure of the material, can be improved by controlling aspects of the CL structure such a hydrophobicity, water distribution, and fuel starvation.

Electrode thinning is a poorly understood process which also has a significant impact on cell deterioration, which demands much wider investigation, and this process appears to be alleviated by careful CL design. Current density is typically divided into two aspects both of which are impacted by CL structure, specific current density, which is a product of the catalysts' inherent properties and catalyst utilization. Catalyst utilization is entirely dependent on high porosity for gas transport, and ionomer coverage for proton access to the active site, although direct coating of ionomer can reduce catalyst utilization by blocking active sites. The specific current density has been shown to be highly dependent on mass transport and the availability of reactants. Mass transport is one of the biggest issues within the fuel cell; it requires balance between all the competing reactant pathways. While it could be stated that mass transport improvements will only affect the mass transport regime of the polarisation curve which is often below the intended operating voltage of a fuel cell, higher current densities, increased catalyst utilization, and reduced resistances are observed with better CL mass transport in all regions of the polarization curve.

Given the performance interoperability of all the components and structure of a CL, to achieve an enhanced understanding requires published scientific works to spread their focus on the CL as a whole, not simply the one aspect authors are focused on. For example, consider the comparison of a CL with a novel nanomaterial to a CL with traditional CB at the same Pt loading. This may at first appear to be a simple comparison of different materials, but the morphologies of resulting CLs manufactured either with or without the new nanomaterial will be significantly different, with changes in the PSD, the Pt utilization, and mass transport. The nuanced properties of the nanomaterial could be lost in the analysis, with the impact on performance of this new structure being falsely assigned as a property of the nanomaterial rather than a change in structure induced by the nanomaterial. Distinguishing the origin of performance changes is important as a change in structure that yields improved performance could be achieved via different manufacturing methods or a multitude of other techniques. Unfortunately, few publications present this nuanced viewpoint, with several examples having been discussed in this review, and authors attributing performance enhancements to the new materials under investigation rather than the consequences of the new materials on CL morphology or catalyst size. It is important for the future understanding of the novel materials to distinguish between these factors; likewise, it is key that the differences between the CL structures are thoroughly investigated and reported in publications.

Variations in MEA performance is expected from small unintentional differences in the manufacturing and testing process, such as GDE alignments during hot pressing, conditioning, and accidental damage to the electrode. This is particularly acute when investigating CLs that have been fabricated in-house, as these electrodes can have significant variation in morphology and composition depending on the fabrication process. Typically, publications reporting MEA data will only present data from a single MEA, showing only a single test, or performing multiple tests and only reporting the highest performance. This can lead to misrepresentation of results and muddying the literature, slowing the development of fuel cells. Within the wider

scientific community, repeat measurements with average results and appropriate error analysis are a well-accepted practice. However, within MEA testing, this is a rare observation. Averaged data across multiple polarization curves for MEAs, or preferably multiple tests on different MEAs prepared the same way, should become necessary for publication and reported within the paper's methods, particularly, for in-house manufacturing methods.

Although (or perhaps because of) the multitude of accepted testing procedures, MEA publications still use a variety of operating parameters and protocols. As widely discussed in this review, this makes comparison between different publications difficult. A push toward unifying testing protocols around the world should be made. Achieving this would require a significant worldwide effort, and would need to be take into account the variations in laboratory capabilities across the world. In the interim, we suggest in the aid of data comparison that those who utilize O_2 for the oxidant should also make efforts to report air oxidant data even if these are only included in the supporting information. Similarly, publications that report electrochemical data taken with back pressure applied should also include the same data performed at atmospheric pressure within the publication. For ease of comparison, all reports should include current density at 0.3 V, maximum power density, and ECSA measurements, written within the text or tabulated. Furthermore, data from a reference material should be provided from every aspect of change from commercial PtC; for example, if a new catalyst is being prepared on a novel nanomaterial, a reference should be provided for both the support material and the novel catalyst. The protocols for ASTs should be based on those suggested by large institutions such as the DoE, EU, JARI, FCCJ, among many others. However, there is no one set protocol that will be optimized for every potential fuel cell application. Systems from CHP to automotive to backup power will have different system requirements and operating conditions. It is not enough to understand and control the performance–structure relationship of a given material for one system; it is equally as important to understand how the different aspects of the CL work together under any operating conditions. As such, when testing novel materials or CL structures, a multitude of different operating conditions should be tested, such as dry and flooded electrodes. Furthermore, significant effort by academics and journals should be made to include negative results, which are often not published due to their perceived lack of value. Assembling this knowledge will make it significantly easier to choose a material, fabrication method, and CL morphology to design a system with set operating parameters, and make comparison of publications significantly easier. Facilitating the faster rate of improvement of much needed fuel cell technologies.

Acknowledgements

Conflict of Interest

The authors declare no conflict of interest.

Keywords

[1] D. P. van Vuuren, E. Stehfest, D. E. H. J. Gernaat, J. C. Doelman, M. van den Berg, M. Harmsen, H. S. de Boer, L. F. Bouwman, V. Daioglou, O. Y. Edelenbosch, B. Girod, T. Kram, L. Lassaletta, P. L. Lucas, H. van Meijl, C. Müller, B. J. van Ruijven, S. van der Sluis, A. Tabeau, *Global Environ. Change* **2017**, *42*, 237.

[2] IEA, *World Energy Outlook 2018: Highlights*, Vol. *1*, International Energy Agency, Paris **2018**.

[3] COM, A policy framework for climate and energy in the period from 2020 to 2030, European Commission **2014**.

[4] C. A. Horowitz, *Int. Leg. Mater.* **2016**, *55*, 740.

[5] I. Staffell, D. Scamman, A. Velazquez Abad, P. Balcombe, P. E. Dodds, P. Ekins, N. Shah, K. R. Ward, *Energy Environ. Sci.* **2019**, *12*, 463.

[6] K. Ukena, K. Tsutsui, *A New Member of the Hypothalamic RF-Amide Peptide Family, LPXRF-Amide Peptides: Structure, Localization, and Function*, Vol. *24*, Springer, London, **2005**.

[7] Y. Wang, K. S. Chen, J. Mishler, S. C. Cho, X. C. Adroher, *Appl. Energy* **2011**, *88*, 981.

[8] Q. Li, J. O. Jensen, R. F. Savinell, N. J. Bjerrum, *Prog. Polym. Sci.* **2009**, *34*, 449.

[9] J. S. Wainright, *J. Electrochem. Soc.* **1995**, *142*, L121.

[10] G. Merle, M. Wessling, K. Nijmeijer, *J. Membr. Sci.* **2011**, *377*, 1.

[11] N. J. Cherepy, R. Krueger, K. J. Fiet, A. F. Jankowski, J. F. Cooper, *J. Electrochem. Soc.* **2005**, *152*, A80.

[12] N. Mahato, A. Banerjee, A. Gupta, S. Omar, K. Balani, *Prog. Mater. Sci.* **2015**, *72*, 141.

[13] S. Wasmus, A. Küver, *J. Electroanal. Chem.* **1999**, *461*, 14.

[14] A. S. Aricò, S. Srinivasan, V. Antonucci, *Fuel Cells* **2001**, *1*, 133.

[15] R. Lan, S. Tao, *J. Power Sources* **2011**, *196*, 5021.

[16] R. Lan, S. Tao, J. T. S. Irvine, *Energy Environ. Sci.* **2010**, *3*, 438.

[17] K. W. Harrison, R. Remick, A. Hoskin, G. D. Martin, in *18th World Hydrogen Energy Conference*, Essen, Germany **2010**.

[18] N. Ge, S. Chevalier, J. Lee, R. Yip, R. Banerjee, M. G. George, H. Liu, C. H. Lee, M. Fazeli, P. Antonacci, T. Kotaka, Y. Tabuchi, A. Bazylak, *Int. J. Heat Mass Transfer* **2017**, *107*, 418.

[19] M. Wei, M. Jiang, X. Liu, M. Wang, S. Mu, *J. Power Sources* **2016**, *327*, 384.

[20] D. Hart, F. Lehner, R. Rose, J. Lewis, *The Fuel Cell Industry Review*, E4Tech **2019**, https://fuelcellindustryreview.com/archive/TheFuelCellIndustryReview2019.pdf.

[21] R. E. Rosli, A. B. Sulong, W. R. W. Daud, M. A. Zulkifley, T. Husaini, M. I. Rosli, E. H. Majlan, M. A. Haque, *Int. J. Hydrogen Energy* **2017**, *42*, 9293.

**ADVANCED
SCIENCE NEWS**

www.advancedsciencenews.com

**ADVANCED
ENERGY
MATERIALS**

www.advenergymat.de

[22] S. S. Araya, F. Zhou, V. Liso, S. L. Sahlin, J. R. Vang, S. Thomas, X. Gao, C. Jeppesen, S. K. Kær, *Int. J. Hydrogen Energy* **2016**, *41*, 21310.

[23] J. S. Yang, L. N. Cleemann, T. Steenberg, C. Terkelsen, Q. F. Li, J. O. Jensen, H. A. Hjuler, N. J. Bjerrum, R. H. He, *Fuel Cells* **2014**, *14*, 7.

[24] A. Kusoglu, A. Z. Weber, *Chem. Rev.* **2017**, *117*, 987.

[25] J. Garche, L. Jörissen, *Electrochem. Soc. Interface* **2015**, *24*, 39.

[26] Z. Zhang, R. Miyajima, T. Inada, D. Miyagi, M. Tsuda, *Int. J. Hydrogen Energy* **2018**, *43*, 6879.

[27] F. Zhang, P. Zhao, M. Niu, J. Maddy, *Int. J. Hydrogen Energy* **2016**, *41*, 14535.

[28] Y. Kumar, J. Ringenberg, S. S. Depuru, V. K. Devabhaktuni, J. W. Lee, E. Nikolaidis, B. Andersen, A. Afjeh, *Renewable Sustainable Energy Rev.* **2016**, *53*, 209.

[29] N. P. Brandon, Z. Kurban, *Phil. Trans. R. Soc. A* **2017**, *375*, 20160400.

[30] N. Konno, S. Mizuno, H. Nakaji, Y. Ishikawa, *SAE Int. J. Altern. Powertrains* **2015**, *4*, 123.

[31] Global Honda Website, Clarity Fuel Cell, https://global.honda/innovation/FuelCell/Clarity-Fuel-Cell-picturebook.html (accessed: December 2020).

[32] Hyundai Website, ix35 HFCV, https://www.hyundai.co.uk/about-us/environment/hydrogen-fuel-cell (accessed: December 2020).

[33] I. E. L. Stephens, J. Rossmeisl, I. Chorkendorff, *Science* **2016**, *354*, 1378.

[34] E. J. Carlson, K. Kopf, S. Sinha, *Cost Analysis of PEM Fuel Cell Systems for Transportation. Subcontract Report NREL/SR-560-39104*, National Renewable Energy Lab.(NREL), Golden, CO **2005**.

[35] Y. Sun, M. Delucchi, J. Ogden, *Int. J. Hydrogen Energy* **2011**, *36*, 11116.

[36] T. Abdel-Baset, T. Benjamin, R. Borup, K. E. Martin, N. Garland, S. Hirano, J. Kopasz, B. Lakshmanmn, D. Masten, M. Mehall, D. Myers, D. Papageorgopoulos, W. Podolski, T. Trabold, B. Vermeersch, J. Waldecker, The US Deparment of Energy (DOE). Energy Efficiency and Renewable Energy, https://www.energy.gov/sites/prod/files/2017/11/f46/FCTT_Roadmap_Nov_2017_FINAL.pdf.

[37] P. E. Dodds, P. Ekins, *Int. J. Hydrogen Energy* **2014**, *39*, 13941.

[38] B. James, *2018 Cost Projections of PEM Fuel Cell Systems for Automobiles and Medium-Duty Vehicles*, Office of Energy Efficiency & Renewable Energy, Washington, DC **2018**.

[39] METI, *The Strategic Road Map for Hydrogen and Fuel Cells*, Tokyo, Japan **2019**, https://www.meti.go.jp/english/press/2019/0312_002.html.

[40] U. S. Department of Energy, *Hydrogen Strategy, Enabling A Low-Carbon Economy*, Washington, DC **2020**, https://www.energy.gov/sites/prod/files/2020/07/f76/USDOE_FE_Hydrogen_Strategy_July2020.pdf.

[41] The EU, TheEuropean Green Deal, **2019**.

[42] K. Kodama, T. Nagai, A. Kuwaki, R. Jinnouchi, Y. Morimoto, *Nat. Nanotechnol.* *16*, 140.

[43] D. Banham, S. Y. Ye, *ACS Energy Lett.* **2017**, *2*, 629.

[44] Y. Bing, H. Liu, L. Zhang, D. Ghosh, J. Zhang, *Chem. Soc. Rev.* **2010**, *39*, 2184.

[45] Y. Shao, J. P. Dodelet, G. Wu, P. Zelenay, *Adv. Mater.* **2019**, *31*, 1807615.

[46] F. Jaouen, D. Jones, N. Coutard, V. Artero, P. Strasser, A. Kucernak, *Johnson Matthey Technol. Rev.* **2018**, *62*, 231.

[47] H. Mistry, A. S. Varela, S. Kühl, P. Strasser, B. R. Cuenya, *Nat. Rev. Mater.* **2016**, *1*, 16009.

[48] M. Shao, Q. Chang, J.-P. Dodelet, R. Chenitz, *Chem. Rev.* **2016**, *116*, 3594.

[49] S. Sui, X. Wang, X. Zhou, Y. Su, S. Riffat, C. jun Liu, *J. Mater. Chem. A* **2017**, *5*, 1808.

[50] T. Muzaffar, T. Kadyk, M. Eikerling, *Sustainable Energy Fuels* **2018**, *2*, 1189.

[51] M. K. Debe, A. J. Steinbach, *ECS Trans.* **2019**, *11*, 659.

[52] M. K. Debe, *J. Electrochem. Soc.* **2011**, *159*, B53.

[53] G. Doo, J. H. Lee, S. Yuk, S. Choi, D. H. Lee, D. W. Lee, H. G. Kim, S. H. Kwon, S. G. Lee, H. T. Kim, *ACS Appl. Mater. Interfaces* **2018**, *10*, 17835.

[54] E. C. S. Transactions, T. E. Society, *ECS Trans.* **2017**, *77*, 1273.

[55] Z. Yang, T. Fujigaya, N. Nakashima, *J. Power Sources* **2015**, *300*, 175.

[56] Y. S. Kim, C. F. Welch, N. H. Mack, R. P. Hjelm, E. B. Orler, M. E. Hawley, K. S. Lee, S. D. Yim, C. M. Johnston, *Phys. Chem. Chem. Phys.* **2014**, *16*, 5927.

[57] E. Passalacqua, F. Lufrano, G. Squadrito, A. Patti, L. Giorgi, *Electrochim. Acta* **2001**, *46*, 799.

[58] W. Yoon, A. Z. Weber, *J. Electrochem. Soc.* **2011**, *158*, B1007.

[59] M. Eikerling, *J. Electrochem. Soc.* **2006**, *153*, E58.

[60] K. Shinozaki, Y. Morimoto, B. S. Pivovar, S. S. Kocha, *J. Power Sources* **2016**, *325*, 745.

[61] R. Jinnouchi, K. Kudo, N. Kitano, Y. Morimoto, *Electrochim. Acta* **2016**, *188*, 767.

[62] R. Subbaraman, D. Strmcnik, A. P. Paulikas, V. R. Stamenkovic, N. M. Markovic, *ChemPhysChem* **2010**, *11*, 2825.

[63] V. Yarlagadda, M. K. Carpenter, T. E. Moylan, R. S. Kukreja, R. Koestner, W. Gu, L. Thompson, A. Kongkanand, *ACS Energy Lett.* **2018**, *3*, 618.

[64] Y. C. Park, H. Tokiwa, K. Kakinuma, M. Watanabe, M. Uchida, *J. Power Sources* **2016**, *315*, 179.

[65] A. Kongkanand, V. Yarlagadda, T. R. Garrick, T. E. Moylan, W. Gu, *ECS Trans.* **2016**, *75*, 25.

[66] T. R. Garrick, T. E. Moylan, V. Yarlagadda, A. Kongkanand, *J. Electrochem. Soc.* **2017**, *164*, F60.

[67] K. Kodama, A. Shinohara, N. Hasegawa, K. Shinozaki, R. Jinnouchi, T. Suzuki, T. Hatanaka, Y. Morimoto, *J. Electrochem. Soc.* **2014**, *161*, F649.

[68] N. Pramounmat, C. N. Loney, C. Kim, L. Wiles, K. E. Ayers, A. Kusoglu, J. N. Renner, *ACS Appl. Mater. Interfaces* **2019**, *11*, 43649.

[69] F. Forouzandeh, X. Li, D. W. Banham, F. Feng, S. Ye, V. Birss, *J. Electrochem. Soc.* **2018**, *165*, F3230.

[70] T. Kim, T. Xie, W. Jung, F. Gadala-Maria, P. Ganesan, B. N. Popov, *J. Power Sources* **2015**, *273*, 761.

[71] E. Padgett, V. Yarlagadda, M. E. Holtz, M. Ko, B. D. A. Levin, R. S. Kukreja, J. M. Ziegelbauer, R. N. Andrews, J. Ilavsky, A. Kongkanand, D. A. Muller, *J. Electrochem. Soc.* **2019**, *166*, F198.

[72] L. Zhang, L. Wang, C. M. B. Holt, B. Zahiri, Z. Li, K. Malek, T. Navessin, M. H. Eikerling, D. Mitlin, *Energy Environ. Sci.* **2012**, *5*, 6156.

[73] J. C. Meier, C. Galeano, I. Katsounaros, J. Witte, H. J. Bongard, A. A. Topalov, C. Baldizzone, S. Mezzavilla, F. Schüth, K. J. J. Mayrhofer, *Beilstein J. Nanotechnol.* **2014**, *5*, 44.

[74] L. Xin, F. Yang, Y. Qiu, A. Uzunoglu, T. Rockward, R. L. Borup, L. A. Stanciu, W. Li, J. Xie, *J. Electrochem. Soc.* **2016**, *163*, F1228.

[75] S. M. Andersen, M. Borghei, R. Dhiman, H. Jiang, V. Ruiz, E. Kauppinen, E. Skou, *Carbon* **2014**, *71*, 218.

[76] S. M. Andersen, *Appl. Catal. B Environ.* **2016**, *181*, 146.

[77] M. Uchida, *Curr. Opin. Electrochem.* **2020**, *21*, 209.

[78] G. Wang, L. Zou, Q. Huang, Z. Zou, H. Yang, *J. Mater. Chem. A* **2019**, *7*, 9447.

[79] D. L. Wood, J. Chlistunoff, J. Majewski, R. L. Borup, *J. Am. Chem. Soc.* **2009**, *131*, 18096.

[80] G. Inoue, T. Ohnishi, M. So, K. Park, M. Ono, Y. Tsuge, *J. Power Sources* **2019**, *439*, 227060.

[81] G. Lee, H. Choi, Y. Tak, *Nanotechnology* **2019**, *30*, 085402.

[82] S. Shahgaldi, I. Alaefour, X. Li, *Appl. Energy* **2018**, *225*, 1022.

2101025 (73 of 82)

**ADVANCED
SCIENCE NEWS**

www.advancedsciencenews.com

**ADVANCED
ENERGY
MATERIALS**

www.advenergymat.de

[83] E. Negro, R. Latsuzbaia, M. Dieci, I. Boshuizen, G. J. M. Koper, *Appl. Catal. B Environ.* **2015**, *166-167*, 155.

[84] E. Antolini, *Appl. Catal. B Environ.* **2012**, *123-124*, 52.

[85] S. Martens, L. Asen, G. Ercolano, F. Dionigi, C. Zalitis, A. Hawkins, A. Martinez Bonastre, L. Seidl, A. C. Knoll, J. Sharman, P. Strasser, D. Jones, O. Schneider, *J. Power Sources* **2018**, *392*, 274.

[86] S. Proch, M. Stenström, L. Eriksson, J. Andersson, G. Sjöblom, A. Jansson, J. Westlinder, *Int. J. Hydrogen Energy* **2020**, *45*, 1313.

[87] D. Franzen, B. Ellendorff, M. C. Paulisch, A. Hilger, M. Osenberg, I. Manke, T. Turek, *J. Appl. Electrochem.* **2019**, *49*, 705.

[88] M. Li, K. Duanmu, C. Wan, T. Cheng, L. Zhang, S. Dai, W. Chen, Z. Zhao, P. Li, H. Fei, Y. Zhu, R. Yu, J. Luo, K. Zang, Z. Lin, M. Ding, J. Huang, H. Sun, J. Guo, X. Pan, W. A. Goddard, P. Sautet, Y. Huang, X. Duan, *Nat. Catal.* **2019**, *2*, 495.

[89] S. Chen, in *Handbook of Electrochemistry* (Ed: C. G. Zoski), Elsevier, Amsterdam **2007**, pp. 33–56.

[90] K. Shinozaki, J. W. Zack, R. M. Richards, B. S. Pivovar, S. S. Kocha, *J. Electrochem. Soc.* **2015**, *162*, F1144.

[91] S. Li, A. Thomas, in *Advanced Nanomaterials for Electrochemical-Based Energy Conversion and Storage*, Elsevier, New York **2020**, pp. 393-423.

[92] S. Srinivasan, O. A. Velev, A. Parthasarathy, D. J. Manko, A. J. Appleby, *J. Power Sources* **1991**, *36*, 299.

[93] A. Parthasarathy, B. Davé, S. Srinivasan, A. J. Appleby, C. R. Martin, *J. Electrochem. Soc.* **1992**, *139*, 1634.

[94] J. Chlistunoff, *J. Power Sources* **2014**, *245*, 203.

[95] J. G. Petrovick, G. C. Anderson, D. I. Kushner, N. Danilovic, A. Z. Weber, *J. Electrochem. Soc.* **2021**, *168*, 056517.

[96] G. Bontempelli, N. Dossi, R. Toniolo, *Reference Module in Chemistry, Molecular Sciences and Chemical Engineering*, Elsevier, New York **2016**.

[97] K. Wandelt, *Encyclopedia of Interfacial Chemistry: Surface Science and Electrochemistry*, Elsevier Science, New York **2018**.

[98] A. J. R. Botz, M. Nebel, R. A. Rincón, E. Ventosa, W. Schuhmann, *Electrochim. Acta* **2015**, *179*, 38.

[99] C. Ponce-De-León, R. W. Field, *J. Appl. Electrochem.* **2000**, *30*, 1087.

[100] F. J. Vidal-Iglesias, J. Solla-Gullón, V. Montiel, A. Aldaz, *Electrochem. Commun.* **2012**, *15*, 42.

[101] S. Xu, Y. Kim, D. Higgins, M. Yusuf, T. F. Jaramillo, F. B. Prinz, *Electrochim. Acta* **2017**, *255*, 99.

[102] S. S. Kocha, J. W. Zack, S. M. Alia, K. C. Neyerlin, B. S. Pivovar, *ECS Trans.* **2013**, *50*, 1475.

[103] S. S. Kocha, K. Shinozaki, J. W. Zack, D. J. Myers, N. N. Kariuki, T. Nowicki, V. Stamenkovic, Y. Kang, D. Li, D. Papageorgopoulos, *Electrocatalysis* **2017**, *8*, 366.

[104] Y. Garsany, J. Ge, J. St-Pierre, R. Rocheleau, K. E. Swider-Lyons, *J. Electrochem. Soc.* **2014**, *161*, F628.

[105] Y. Garsany, O. A. Baturina, K. E. Swider-Lyons, S. S. Kocha, *Anal. Chem.* **2010**, *82*, 6321.

[106] I. Takahashi, S. S. Kocha, *J. Power Sources* **2010**, *195*, 6312.

[107] D. Kumsa, N. Bhadra, E. Hudak, S. Kelley, D. Untereker, J. Mortimer, *J. Neural Eng.* **2016**, *13*, 052001.

[108] R. N. Carter, S. S. Kocha, F. Wagner, M. Fay, H. A. Gasteiger, *ECS Trans.* **2019**, *11*, 403.

[109] Z. Chen, M. Waje, W. Li, Y. Yan, *Angew. Chem., Int. Ed.* **2007**, *46*, 4060.

[110] E. Brightman, G. Hinds, R. O'Malley, *J. Power Sources* **2013**, *242*, 244.

[111] F. Barbir, *PEM Fuel Cells*, 2nd ed., Academic Press, San Diego, CA **2012**.

[112] M. Lee, M. Uchida, H. Yano, D. A. Tryk, H. Uchida, M. Watanabe, *Electrochim. Acta* **2010**, *55*, 8504.

[113] S. Ott, A. Orfanidi, H. Schmies, B. Anke, H. N. Nong, J. Hübner, U. Gernert, M. Gliech, M. Lerch, P. Strasser, *Nat. Mater.* **2020**, *19*, 77.

[114] J. Wu, X. Z. Yuan, H. Wang, M. Blanco, J. J. Martin, J. Zhang, *Int. J. Hydrogen Energy* **2008**, *33*, 1735.

[115] J. Zhang, H. Zhang, J. Wu, J. Zhang, *PEM Fuel Cell Testing and Diagnosis: Fuel Cell Open Circuit Voltage*, Elsevier, Amsterdam **2013**, pp. 187–200, Ch. 7.

[116] J. Zhang, H. Zhang, J. Wu, J. Zhang, *PEM Fuel Cell Testing and Diagnosis: Hydrogen Crossover*, Elsevier, Amsterdam, **2013**, pp. 171–185, Ch. 6.

[117] S. Ueda, S. Koizumi, Y. Tsutsumi, *Results Phys.* **2019**, *12*, 1871.

[118] X. Z. Yuan, J. C. Sun, H. Wang, H. Li, *J. Power Sources* **2012**, *205*, 340.

[119] Z. Qi, A. Kaufman, *J. Power Sources* **2002**, *109*, 227.

[120] M. Zhiani, I. Mohammadi, S. Majidi, *Int. J. Hydrogen Energy* **2017**, *42*, 4490.

[121] X. Z. Yuan, S. Zhang, J. C. Sun, H. Wang, *J. Power Sources* **2011**, *196*, 9097.

[122] T. J. Mason, J. Millichamp, T. P. Neville, P. R. Shearing, S. Simons, D. J. L. Brett, *J. Power Sources* **2013**, *242*, 70.

[123] W. Schmittinger, A. Vahidi, *J. Power Sources* **2008**, *180*, 1.

[124] A. Taniguchi, T. Akita, K. Yasuda, Y. Miyazaki, *J. Power Sources* **2004**, *130*, 42.

[125] A. Taniguchi, T. Akita, K. Yasuda, Y. Miyazaki, *Int. J. Hydrogen Energy* **2008**, *33*, 2323.

[126] C. He, Z. Qi, M. Hollett, A. Kaufman, *Electrochem. Solid-State Lett.* **2002**, *5*, 181.

[127] M. Zhiani, S. Majidi, *Int. J. Hydrogen Energy* **2013**, *38*, 9819.

[128] M. Zhiani, S. Majidi, M. M. Taghiabadi, *Fuel Cells* **2013**, *13*, 946.

[129] M. M. Taghiabadi, M. Zhiani, V. Silva, *Appl. Energy* **2019**, *242*, 602.

[130] Z. Qi, A. Kaufman, *J. Power Sources* **2002**, *111*, 181.

[131] Z. Qi, A. Kaufman, *J. Power Sources* **2003**, *114*, 21.

[132] G. Gupta, B. Wu, S. Mylius, G. J. Offer, *Int. J. Hydrogen Energy* **2017**, *42*, 4320.

[133] C. V. Chi (Fuelcell Energy Inc), *US4397918A*, **1983**.

[134] C. G. Hochgraf, R. S. Foley, M. K. Hortop, B. Lakshmanan, (GM Global Technology Operations LLC), *US7968240B2*, **2009**.

[135] Z. Xie, X. Zhao, M. Adachi, Z. Shi, T. Mashio, A. Ohma, K. Shinohara, S. Holdcroft, T. Navessin, *Energy Environ. Sci.* **2008**, *1*, 184.

[136] P. Trogadas, J. I. S. Cho, N. Kapil, L. Rasha, A. Corredera, D. J. L. Brett, M.-O. Coppens, *Sustainable Energy Fuels* **2020**, *4*, 5739.

[137] US Fuel Cell Council, *Single Cell Test Protocol*, USFCC, Washington, DC **2006**.

[138] Q. Meyer, L. Rasha, H. M. Koegeler, S. Foster, P. Adcock, P. R. Shearing, D. J. L. Brett, *Int. J. Powertrains* **2018**, *7*, 118.

[139] Q. Yan, H. Toghiani, H. Causey, *J. Power Sources* **2006**, *161*, 492.

[140] H. Sun, G. Zhang, L.-J. Guo, H. Liu, *J. Power Sources* **2006**, *158*, 326.

[141] M. Noorkami, J. B. Robinson, Q. Meyer, O. A. Obeisun, E. S. Fraga, T. Reisch, P. R. Shearing, D. J. L. Brett, *Int. J. Hydrogen Energy* **2014**, *39*, 1439.

[142] S. Wasterlain, D. Candusso, D. Hissel, F. Harel, P. Bergman, P. Menard, M. Anwar, *J. Power Sources* **2010**, *195*, 984.

[143] J. H. Jang, H. C. Chiu, W. M. Yan, W. L. Sun, *J. Power Sources* **2008**, *180*, 476.

[144] L. Wang, A. Husar, T. Zhou, H. Liu, *Int. J. Hydrogen Energy* **2003**, *28*, 1263.

[145] P. Gazdzicki, J. Mitzel, A. M. Dreizler, M. Schulze, K. A. Friedrich, *Fuel Cells* **2018**, *18*, 270.

[146] B. Chen, J. Wang, T. Yang, Y. Cai, C. Zhang, S. H. Chan, Y. Yu, Z. Tu, *Energy* **2016**, *106*, 54.

[147] S. Ohyagi, T. Matsuda, Y. Iseki, T. Sasaki, C. Kaito, *J. Power Sources* **2011**, *196*, 3743.

[148] K. C. Neyerlin, H. A. Gasteiger, C. K. Mittelsteadt, J. Jorne, W. Gu, *J. Electrochem. Soc.* **2005**, *152*, A1073.

[149] S. Jomori, K. Komatsubara, N. Nonoyama, M. Kato, T. Yoshida, *J. Electrochem. Soc.* **2013**, *160*, F1067.

[150] D. J. L. Brett, S. Atkins, N. P. Brandon, N. Vasileiadis, V. Vesovic, A. R. Kucernak, *J. Power Sources* **2007**, *172*, 2.

[151] L. Fan, G. Zhang, K. Jiao, *Energy Convers. Manage.* **2017**, *150*, 763.

[152] G. Tsotridis, A. Pilenga, G. De Marco, T. Malkow, *EU Harmonised Test Protocols for PEMFC MEA Testing in Single Cell Configuration for Automotive Applications; JRC Science for Policy Report*, Publications Office of the European Union, Luxembourg **2015**.

[153] Q. Meyer, S. Ashton, O. Curnick, T. Reisch, P. Adcock, K. Ronaszegi, J. B. Robinson, D. J. L. Brett, *J. Power Sources* **2014**, *254*, 1.

[154] J. Yu, Z. Jiang, M. Hou, D. Liang, Y. Xiao, M. Dou, Z. Shao, B. Yi, *J. Power Sources* **2014**, *246*, 90.

[155] S. Strahl, A. Husar, J. Riera, *J. Power Sources* **2014**, *248*, 474.

[156] S. Chevalier, N. Ge, J. Lee, P. Antonacci, R. Yip, M. G. George, H. Liu, R. Banerjee, M. Fazeli, A. Bazylak, *Electrochem. Commun.* **2015**, *59*, 16.

[157] R. O'Hayre, S.-W. Cha, W. Colella, F. B. Prinz, in *Fuel Cell Fundamentals*, Wiley, New York **2016**, p. 25.

[158] J. Kim, J. Lee, Y. Tak, *J. Power Sources* **2009**, *192*, 674.

[159] N. Macauley, D. D. Papadias, J. Fairweather, D. Spernjak, D. Langlois, R. Ahluwalia, K. L. More, R. Mukundan, R. L. Borup, *J. Electrochem. Soc.* **2018**, *165*, F3148.

[160] Y. B. Kim, *Int. J. Energy Res.* **2012**, *36*, 509.

[161] T. Van Nguyen, M. W. Knobbe, *J. Power Sources* **2003**, *114*, 70.

[162] K. Tüber, D. Pócza, C. Hebling, *J. Power Sources* **2003**, *124*, 403.

[163] B. Chen, J. Wang, T. Yang, Y. Cai, M. Pan, Z. Tu, C. Zhang, S. H. Chan, Y. Yu, *Energy Convers. Manage.* **2016**, *119*, 60.

[164] D. J. L. Brett, S. Atkins, N. P. Brandon, V. Vesovic, N. Vasileiadis, A. R. Kucernak, *Electrochem. Commun.* **2001**, *3*, 628.

[165] N. Yousfi-Steiner, P. Moçotéguy, D. Candusso, D. Hissel, *J. Power Sources* **2009**, *194*, 130.

[166] Z. Y. Liu, B. K. Brady, R. N. Carter, B. Litteer, M. Budinski, J. K. Hyun, D. A. Muller, *J. Electrochem. Soc.* **2008**, *155*, B979.

[167] P. Mandal, B. K. Hong, J.-G. Oh, S. Litster, *J. Power Sources* **2018**, *397*, 397.

[168] D. Liang, Q. Shen, M. Hou, Z. Shao, B. Yi, *J. Power Sources* **2009**, *194*, 847.

[169] F. Nandjou, J.-P. Poirot-Crouvezier, M. Chandesris, J.-F. Blachot, C. Bonnaud, Y. Bultel, *J. Power Sources* **2016**, *326*, 182.

[170] G. Zhang, S. Shen, L. Guo, H. Liu, *Int. J. Hydrogen Energy* **2012**, *37*, 1884.

[171] J. Zhang, C. Song, J. Zhang, R. Baker, L. Zhang, *J. Electroanal. Chem.* **2013**, *688*, 130.

[172] J. Zhang, H. Zhang, J. Wu, J. Zhang, *PEM Fuel Cell Testing and Diagnosis: Pressure Effects on PEM Fuel Cell Performance*, Amsterdam **2013**, pp. 225–241, Ch. 9.

[173] M. A. R. S. Al-Baghdadi, H. A. K. S. Al-Janabi, *Int. J. Hydrogen Energy* **2007**, *32*, 4510.

[174] DOE, *Hydrogen and Fuel Cell Technologies Office Multi-Year Research, Development, and Demonstration Plan - 3.4 Fuel Cells*, **2016**, https://www.energy.gov/eere/fuelcells/downloads/hydrogen-and-fuel-cell-technologies-office-multi-year-research-development.

[175] M. Bodner, J. Senn, V. Hacker, *Fuel Cells and Hydrogen: From Fundamentals to Applied Research*, Elsevier, Amsterdam **2018**, pp. 139–154.

[176] L. Dubau, L. Castanheira, F. Maillard, M. Chatenet, O. Lottin, G. Maranzana, J. Dillet, A. Lamibrac, J.-C. Perrin, E. Moukheiber, A. ElKaddouri, G. De Moor, C. Bas, L. Flandin, N. Caqué, *WIREs Energy Environ.* **2014**, *3*, 540.

[177] Q. Meyer, Y. Zeng, C. Zhao, *J. Power Sources* **2019**, *437*, 226922.

[178] B. T. Sneed, D. A. Cullen, K. S. Reeves, O. E. Dyck, D. A. Langlois, R. Mukundan, R. L. Borup, K. L. More, *ACS Appl. Mater. Interfaces* **2017**, *9*, 29839.

[179] D. J. S. Sandbeck, N. M. Secher, F. D. Speck, J. E. Sørensen, J. Kibsgaard, I. Chorkendorff, S. Cherevko, *ACS Catal.* **2020**, *10*, 6281.

[180] S. Shahgaldi, A. Ozden, X. Li, F. Hamdullahpur, *Appl. Energy* **2020**, *268*, 114956.

[181] F. A. de Bruijn, V. A. T. Dam, G. J. M. Janssen, *Fuel Cells* **2008**, *8*, 3.

[182] Y. Yamashita, S. Itami, J. Takano, K. Kakinuma, H. Uchida, M. Watanabe, A. Iiyama, M. Uchida, *J. Electrochem. Soc.* **2017**, *164*, F181.

[183] A. Pandy, Z. Yang, M. Gummalla, V. V. Atrazhev, N. Y. Kuzminyh, V. I. Sultanov, S. Burlatsky, *J. Electrochem. Soc.* **2013**, *160*, F972.

[184] R. T. White, A. Wu, M. Najm, F. P. Orfino, M. Dutta, E. Kjeang, *J. Power Sources* **2017**, *350*, 94.

[185] J. Hack, L. Rasha, P. L. Cullen, J. J. Bailey, T. P. Neville, P. R. Shearing, N. P. Brandon, D. J. L. Brett, *Electrochim. Acta* **2020**, *352*, 136464.

[186] L. Castanheira, W. O. Silva, F. H. B. Lima, A. Crisci, L. Dubau, F. Maillard, *ACS Catal.* **2015**, *5*, 2184.

[187] Z. Fang, A. G. Star, T. F. Fuller, *J. Electrochem. Soc.* **2019**, *166*, F709.

[188] P. Ren, P. Pei, Y. Li, Z. Wu, D. Chen, S. Huang, *Prog. Energy Combust. Sci.* **2020**, *80*, 100859.

[189] J. Zhao, X. Li, *Energy Convers. Manage.* **2019**, *199*, 112022.

[190] D. Novitski, S. Holdcroft, *ACS Appl. Mater. Interfaces* **2015**, *7*, 27314.

[191] P. Choi, N. H. Jalani, R. Datta, *J. Electrochem. Soc.* **2005**, *152*, E123.

[192] D. K. Paul, K. Karan, A. Docoslis, J. B. Giorgi, J. Pearce, *Macromolecules* **2013**, *46*, 3461.

[193] A. Kusoglu, D. Kushner, D. K. Paul, K. Karan, M. A. Hickner, A. Z. Weber, *Adv. Funct. Mater.* **2014**, *24*, 4763.

[194] L. Liu, W. Chen, Y. Li, *J. Memb. Sci.* **2016**, *504*, 1.

[195] B. Choi, D. A. Langlois, N. Mack, C. M. Johnston, Y. S. Kim, *J. Electrochem. Soc.* **2014**, *161*, F1154.

[196] M. Breitwieser, M. Klingele, S. Vierrath, R. Zengerle, S. Thiele, *Adv. Energy Mater.8*, 1701257.

[197] K. Chan, M. Eikerling, *J. Electrochem. Soc.* **2011**, *158*, B18.

[198] M. K. Debe, *J. Electrochem. Soc.* **2013**, *160*, F522.

[199] P. K. Sinha, W. Gu, A. Kongkanand, E. Thompson, *J. Electrochem. Soc.* **2011**, *158*, B831.

[200] J. Huang, J. Zhang, M. Eikerling, *Faraday Discuss.* **2016**, *193*, 427.

[201] S. Holdcroft, *Chem. Mater.* **2014**, *26*, 381.

[202] T. D. Gierke, G. E. Munn, F. C. Wilson, *J. Polym. Sci. Part A-2, Polym. Phys.* **1981**, *19*, 1687.

[203] K. Schmidt-Rohr, Q. Chen, *Nat. Mater.* **2008**, *7*, 75.

[204] P. C. Van Der Heijden, L. Rubatat, O. Diat, *Macromolecules* **2004**, *37*, 5327.

[205] A. L. Rollet, O. Diat, G. Gebel, *J. Phys. Chem. B* **2002**, *106*, 3033.

[206] K. Karan, *Langmuir* **2019**, *35*, 13489.

[207] M. A. Modestino, D. K. Paul, S. Dishari, S. A. Petrina, F. I. Allen, M. A. Hickner, K. Karan, R. A. Segalman, A. Z. Weber, *Macromolecules* **2013**, *46*, 867.

[208] D. K. Paul, A. Fraser, K. Karan, *Electrochem. Commun.* **2011**, *13*, 774.

[209] K. Malek, M. Eikerling, Q. Wang, T. Navessin, Z. Liu, *J. Phys. Chem. C* **2007**, *111*, 13627.

[210] U. N. Shrivastava, K. Suetsugu, S. Nagano, H. Fritzsche, Y. Nagao, K. Karan, *Soft Matter* **2020**, *16*, 1190.

[211] S. C. DeCaluwe, A. M. Baker, P. Bhargava, J. E. Fischer, J. A. Dura, *Nano Energy* **2018**, *46*, 91.

[212] J. A. Dura, V. S. Murthi, M. Hartman, S. K. Satija, C. F. Majkrzak, *Macromolecules* **2009**, *42*, 4769.

[213] S. A. Eastman, S. Kim, K. A. Page, B. W. Rowe, S. Kang, C. L. Soles, K. G. Yager, *Macromolecules* **2012**, *45*, 7920.

[214] T. J. Zimudzi, M. A. Hickner, *ACS Macro Lett.* **2016**, *5*, 83.

[215] S. C. DeCaluwe, P. A. Kienzle, P. Bhargava, A. M. Baker, J. A. Dura, *Soft Matter* **2014**, *10*, 5763.

**ADVANCED
SCIENCE NEWS**

www.advancedsciencenews.com

**ADVANCED
ENERGY
MATERIALS**

www.advenergymat.de

[216] S. M. Andersen, M. Borghei, R. Dhiman, V. Ruiz, E. Kauppinen, E. Skou, *J. Phys. Chem. C* **2014**, *118*, 10814.

[217] S. K. Dishari, M. A. Hickner, *Macromolecules* **2013**, *46*, 413.

[218] S. Kim, J. A. Dura, K. A. Page, B. W. Rowe, K. G. Yager, H. J. Lee, C. L. Soles, *Macromolecules* **2013**, *46*, 5630.

[219] Y. Ogata, T. Abe, S. Yonemori, N. L. Yamada, D. Kawaguchi, K. Tanaka, *Langmuir* **2018**, *34*, 15483.

[220] X. Y. Zhang, Y. H. Ding, *RSC Adv.* **2014**, *4*, 44214.

[221] Z. Siroma, R. Kakitsubo, N. Fujiwara, T. Ioroi, S. ichi Yamazaki, K. Yasuda, *J. Power Sources* **2009**, *189*, 994.

[222] A. Kongkanand, *J. Phys. Chem. C* **2011**, *115*, 11318.

[223] S. K. Dishari, M. A. Hickner, *ACS Macro Lett.* **2012**, *1*, 291.

[224] C. Zhang, M. Davies, K. Karan, *J. Polym. Sci. Part B Polym. Phys.* **2019**, *57*, 343.

[225] Q. He, N. S. Suraweera, D. C. Joy, D. J. Keffer, *J. Phys. Chem. C* **2013**, *117*, 25305.

[226] M. E. Selvan, Q. He, E. M. Calvo-Muñoz, D. J. Keffer, *J. Phys. Chem. C* **2012**, *116*, 12890.

[227] X. Cheng, B. Yi, M. Han, J. Zhang, Y. Qiao, J. Yu, *J. Power Sources* **1999**, *79*, 75.

[228] N. Nonoyama, S. Okazaki, A. Z. Weber, Y. Ikogi, T. Yoshida, *J. Electrochem. Soc.* **2011**, *158*, B416.

[229] Y. Ono, A. Ohma, K. Shinohara, K. Fushinobu, *J. Electrochem. Soc.* **2013**, *160*, F779.

[230] A. Ohira, S. Kuroda, H. F. M. Mohamed, B. Tavernier, *Phys. Chem. Chem. Phys.* **2013**, *15*, 11494.

[231] N. E. De Almeida, D. K. Paul, K. Karan, G. R. Goward, *J. Phys. Chem. C* **2015**, *119*, 1280.

[232] S. C. DeCaluwe, J. A. Dura, *ECS Trans.* **2017**, *80*, 619.

[233] R. Gao, M. A. Edwards, Y. Qiu, K. Barman, H. S. White, *J. Am. Chem. Soc.* **2020**, *142*, 8890.

[234] U.S. Department of Energy, DOE Technical Targets for Polymer Electrolyte Membrane Fuel Cell Components | Department of Energy, https://www.energy.gov/eere/fuelcells/doe-technical-targets-polymer-electrolyte-membrane-fuel-cell-components (accessed: December 2020).

[235] A. Kongkanand, M. F. Mathias, *J. Phys. Chem. Lett.* **2016**, *7*, 1127.

[236] Y. Ono, T. Mashio, S. Takaichi, A. Ohma, H. Kanesaka, K. Shinohara, *ECS Trans.* **2019**, *28*, 69.

[237] A. Z. Weber, A. Kusoglu, *J. Mater. Chem. A* **2014**, *2*, 17207.

[238] N. P. Subramanian, T. A. Greszler, J. Zhang, W. Gu, R. Makharia, *J. Electrochem. Soc.* **2012**, *159*, B531.

[239] T. Reshetenko, A. Kulikovsky, *RSC Adv.* **2019**, *9*, 38797.

[240] S. Jomori, N. Nonoyama, T. Yoshida, *J. Power Sources* **2012**, *215*, 18.

[241] K. Sakai, K. Sato, T. Mashio, A. Ohma, K. Yamaguchi, K. Shinohara, *ECS Trans.* **2019**, *25*, 1193.

[242] F. C. Cetinbas, X. Wang, R. K. Ahluwalia, N. N. Kariuki, R. P. Winarski, Z. Yang, J. Sharman, D. J. Myers, *J. Electrochem. Soc.* **2017**, *164*, F1596.

[243] K. Kudo, R. Jinnouchi, Y. Morimoto, *Electrochim. Acta* **2016**, *209*, 682.

[244] K. Kudo, Y. Morimoto, *ECS Trans.* **2013**, *50*, 1487.

[245] J. P. Owejan, J. E. Owejan, W. Gu, *J. Electrochem. Soc.* **2013**, *160*, F824.

[246] W. Yoshimune, M. Harada, *Chem. Lett.* **2019**, *48*, 487.

[247] S. Ma, Q. Chen, F. H. Jøgensen, P. C. Stein, E. M. Skou, *Solid State Ionics* **2007**, *178*, 1568.

[248] T. Schuler, A. Chowdhury, A. T. Freiberg, B. Sneed, F. B. Spingler, M. C. Tucker, K. L. More, C. J. Radke, A. Z. Weber, *J. Electrochem. Soc.* **2019**, *166*, F3020.

[249] M. Hwang, Y. A. Elabd, *Int. J. Hydrogen Energy* **2019**, *44*, 6245.

[250] U. N. Shrivastava, H. Fritzsche, K. Karan, *Macromolecules* **2018**, *51*, 9839.

[251] A. Ohma, K. Fushinobu, K. Okazaki, *Electrochim. Acta* **2010**, *55*, 8829.

[252] K. Karan, *Curr. Opin. Electrochem.* **2017**, *5*, 27.

[253] K. Kakinuma, R. Kobayashi, A. Iiyama, M. Uchida, *J. Electrochem. Soc.* **2018**, *165*, J3083.

[254] M. Lopez-Haro, L. Guétaz, T. Printemps, A. Morin, S. Escribano, P. H. Jouneau, P. Bayle-Guillemaud, F. Chandezon, G. Gebel, *Nat. Commun.* **2014**, *5*, 5229.

[255] T. Soboleva, X. Zhao, K. Malek, Z. Xie, T. Navessin, S. Holdcroft, *ACS Appl. Mater. Interfaces* **2010**, *2*, 375.

[256] A. Kulikovsky, *Electrochem. Commun.* **2019**, *103*, 61.

[257] C. H. Ma, T. L. Yu, H. L. Lin, Y. T. Huang, Y. L. Chen, U. S. Jeng, Y. H. Lai, Y. Sen Sun, *Polymer* **2009**, *50*, 1764.

[258] N. Kumano, K. Kudo, A. Suda, Y. Akimoto, M. Ishii, H. Nakamura, *J. Power Sources* **2019**, *419*, 219.

[259] M. B. Dixit, B. A. Harkey, F. Shen, K. B. Hatzell, *J. Electrochem. Soc.* **2018**, *165*, F264.

[260] S. Woo, S. Lee, A. Z. Taning, T. H. Yang, S. H. Park, S. D. Yim, *Curr. Opin. Electrochem.* **2020**, *21*, 289.

[261] C. H. Song, J. S. Park, *Energies* **2019**, *12*, 549.

[262] H. L. Lin, T. L. Yu, C. H. Huang, T. L. Lin, *J. Polym. Sci. Part B Polym. Phys.* **2005**, *43*, 3044.

[263] P. J. Dudenas, A. Kusoglu, *Macromolecules* **2019**, *52*, 7779.

[264] M. Uchida, *J. Electrochem. Soc.* **1995**, *142*, 463.

[265] J. H. Kim, H. Y. Ha, I. H. Oh, S. A. Hong, H. I. Lee, *J. Power Sources* **2004**, *135*, 29.

[266] R. Fernández, P. Ferreira-Aparicio, L. Daza, *J. Power Sources* **2005**, *151*, 18.

[267] A. Tarokh, K. Karan, S. Ponnurangam, *Macromolecules* **2020**, *53*, 288.

[268] A. Eisenberg, *Macromolecules* **1970**, *3*, 147.

[269] C. Welch, A. Labouriau, R. Hjelm, B. Orler, C. Johnston, Y. S. Kim, *ACS Macro Lett.* **2012**, *1*, 1403.

[270] M. Yamaguchi, T. Matsunaga, K. Amemiya, A. Ohira, N. Hasegawa, K. Shinohara, M. Ando, T. Yoshida, *J. Phys. Chem. B* **2014**, *118*, 5752.

[271] P. Aldebert, B. Dreyfus, M. Pineri, *Macromolecules* **1986**, *19*, 2651.

[272] S. Li, K. Terao, T. Sato, *Polymers* **2018**, *10*, 72.

[273] L. Rubatat, G. Gebel, O. Diat, *Macromolecules* **2004**, *37*, 7772.

[274] T. Mabuchi, S. F. Huang, T. Tokumasu, *Macromolecules* **2020**, *53*, 3273.

[275] T. Mabuchi, S. Huang, T. Tokumasu, *J. Polym. Sci.* **2020**, *58*, 487.

[276] T. T. Ngo, T. L. Yu, H. L. Lin, *J. Power Sources* **2013**, *238*, 1.

[277] S. A. Berlinger, B. D. McCloskey, A. Z. Weber, *J. Phys. Chem. B* **2018**, *122*, 7790.

[278] J. Li, X. Yang, H. Tang, M. Pan, *J. Memb. Sci.* **2010**, *361*, 38.

[279] H.-D. Nguyen, T. K. L. Nguyen, E. Planes, J. Jestin, L. Porcar, S. Lyonnard, C. Iojoiu, *J. Phys. Chem. C* **2020**, *124*, 13071.

[280] C. Y. Ahn, J. Ahn, S. Y. Kang, O. H. Kim, D. W. Lee, J. H. Lee, J. G. Shim, C. H. Lee, Y. H. Cho, Y. E. Sung, *Sci. Adv.* **2020**, *6*, eaaw0870.

[281] T. H. Kim, J. H. Yoo, T. Maiyalagan, S. C. Yi, *Appl. Surf. Sci.* **2019**, *481*, 777.

[282] J. H. Lee, G. Doo, S. H. Kwon, S. Choi, H. T. Kim, S. G. Lee, *Sci. Rep.*, https://doi.org/10.1038/s41598-018-28779-y.

[283] S. Khandavalli, J. H. Park, N. N. Kariuki, D. J. Myers, J. J. Stickel, K. Hurst, K. C. Neyerlin, M. Ulsh, S. A. Mauger, *ACS Appl. Mater. Interfaces* **2018**, *10*, 43610.

[284] K. Artyushkova, M. J. Workman, I. Matanovic, M. J. Dzara, C. Ngo, S. Pylypenko, A. Serov, P. Atanassov, *ACS Appl. Energy Mater.* **2018**, *1*, 68.

[285] K. Artyushkova, P. Atanassov, M. Dutta, S. Wessel, V. Colbow, *J. Power Sources* **2015**, *284*, 631.

[286] T. H. Kim, J. Y. Yi, C. Y. Jung, E. Jeong, S. C. Yi, *Int. J. Hydrogen Energy* **2017**, *42*, 478.

[287] K. H. Kim, K. Y. Lee, H. J. Kim, E. A. Cho, S. Y. Lee, T. H. Lim, S. P. Yoon, I. C. Hwang, J. H. Jang, *Int. J. Hydrogen Energy* **2010**, *35*, 2119.

[288] C.-N. Sun, K. L. More, G. M. Veith, T. A. Zawodzinski, *J. Electrochem. Soc.* **2013**, *160*, F1000.

[289] S. Martin, P. L. Garcia-Ybarra, J. L. Castillo, *J. Power Sources* **2010**, *195*, 2443.

[290] M. R. Lee, H. Y. Lee, S. D. Yim, C. S. Kim, Y. G. Shul, A. Kucernak, D. Shin, *Fuel Cells* **2018**, *18*, 129.

[291] T. Morawietz, M. Handl, C. Oldani, K. A. Friedrich, R. Hiesgen, *ACS Appl. Mater. Interfaces* **2016**, *8*, 27044.

[292] S. Komini Babu, H. T. Chung, P. Zelenay, S. Litster, *ACS Appl. Mater. Interfaces* **2016**, *8*, 32764.

[293] T. Mashio, A. Ohma, S. Yamamoto, K. Shinohara, *ECS Trans.* **2019**, *11*, 529.

[294] M. Tesfaye, A. N. MacDonald, P. J. Dudenas, A. Kusoglu, A. Z. Weber, *Electrochem. Commun.* **2018**, *87*, 86.

[295] K. Kodama, R. Jinnouchi, T. Suzuki, H. Murata, T. Hatanaka, Y. Morimoto, *Electrochem. Commun.* **2013**, *36*, 26.

[296] Y. Yin, R. Li, F. Bai, W. Zhu, Y. Qin, Y. Chang, J. Zhang, M. D. Guiver, *Electrochem. Commun.* **2019**, *109*, 106590.

[297] S. Jomori, K. Komatsubara, N. Nonoyama, M. Kato, T. Yoshida, *J. Electrochem. Soc.* **2013**, *160*, X14.

[298] R. Jinnouchi, K. Kudo, N. Kitano, Y. Morimoto, *Electrochim. Acta* **2018**, *287*, 160.

[299] Y. Chang, J. Liu, R. Li, J. Zhao, Y. Qin, J. Zhang, Y. Yin, X. Li, *Energy Convers. Manage.* **2019**, *189*, 24.

[300] H. Y. Jung, K. Y. Cho, Y. M. Lee, J. K. Park, J. H. Choi, Y. E. Sung, *J. Power Sources* **2007**, *163*, 952.

[301] B. R. Frieberg, K. A. Page, J. R. Graybill, M. L. Walker, C. M. Stafford, G. R. Stafford, C. L. Soles, *ACS Appl. Mater. Interfaces* **2016**, *8*, 33240.

[302] D. K. Paul, K. Karan, *J. Phys. Chem. C* **2014**, *118*, 1828.

[303] A. Katzenberg, A. Chowdhury, M. Fang, A. Z. Weber, Y. Okamoto, A. Kusoglu, M. A. Modestino, *J. Am. Chem. Soc.* **2020**, *142*, 3742.

[304] S. Y. Kim, M. J. Park, N. P. Balsara, A. Jackson, *Macromolecules* **2010**, *43*, 8128.

[305] V. V. Atrazhev, T. Y. Astakhova, V. I. Sultanov, M. L. Perry, S. F. Burlatsky, *J. Electrochem. Soc.* **2017**, *164*, F1265.

[306] A. Kusoglu, T. J. Dursch, A. Z. Weber, *Adv. Funct. Mater.* **2016**, *26*, 4961.

[307] M. Breitwieser, T. Bayer, A. Büchler, R. Zengerle, S. M. Lyth, S. Thiele, *J. Power Sources* **2017**, *351*, 145.

[308] C. H. Park, C. H. Lee, M. D. Guiver, Y. M. Lee, *Prog. Polym. Sci.* **2011**, *36*, 1443.

[309] L. Zhang, C. Ma, S. Mukerjee, *Electrochim. Acta* **2003**, *48*, 1845.

[310] T. Astill, Z. Xie, Z. Shi, T. Navessin, S. Holdcroft, *J. Electrochem. Soc.* **2009**, *156*, B499.

[311] K. Miyatake, T. Omata, D. A. Tryk, H. Uchida, M. Watanabe, *J. Phys. Chem. C* **2009**, *113*, 7772.

[312] K. D. Kreuer, *J. Memb. Sci.* **2001**, *185*, 29.

[313] T. Shimura, K. Miyatake, M. Watanabe, *Eur. Polym. J.* **2008**, *44*, 4054.

[314] E. B. Easton, T. D. Astill, S. Holdcroft, *J. Electrochem. Soc.* **2005**, *152*, A752.

[315] H. K. Lee, J. H. Park, D. Y. Kim, T. H. Lee, *J. Power Sources* **2004**, *131*, 200.

[316] O. D. Payton, L. Picco, T. B. Scott, *Int. Mater. Rev.* **2016**, *61*, 473.

[317] M. J. Eslamibidgoli, J. Huang, T. Kadyk, A. Malek, M. Eikerling, *Nano Energy* **2016**, *29*, 334.

[318] A. Nouri-Khorasani, K. Malek, A. Malek, T. Mashio, D. P. Wilkinson, M. H. Eikerling, *Catal. Today* **2016**, *262*, 133.

[319] E. Akbari, Z. Buntat, *Int. J. Energy Res.* **2017**, *41*, 92.

[320] M. Brodt, T. Han, N. Dale, E. Niangar, R. Wycisk, P. Pintauro, *J. Electrochem. Soc.* **2015**, *162*, F84.

[321] Y. Shao, S. Zhang, C. Wang, Z. Nie, J. Liu, Y. Wang, Y. Lin, *J. Power Sources* **2010**, *195*, 4600.

[322] T. Kim, T. Xie, W. S. Jung, B. N. Popov, *Int. J. Hydrogen Energy* **2017**, *42*, 12507.

[323] K. Takahashi, R. Koda, K. Kakinuma, M. Uchida, *J. Electrochem. Soc.* **2017**, *164*, F235.

[324] P. Liu, J. Kong, Y. Liu, Q. Liu, H. Zhu, *J. Power Sources* **2015**, *278*, 522.

[325] E. Daş, B. Y. Kaplan, S. A. Gürsel, A. B. Yurtcan, *Renewable Energy* **2019**, *139*, 1099.

[326] E. Arici, B. Y. Kaplan, A. M. Mert, S. Alkan Gursel, S. Kinayyigit, *Int. J. Hydrogen Energy* **2019**, *44*, 14175.

[327] S. Mezzavilla, S. Cherevko, C. Baldizzone, E. Pizzutilo, G. Polymeros, K. J. J. Mayrhofer, *ChemElectroChem* **2016**, *3*, 1524.

[328] S. V. Venkatesan, M. Dutta, E. Kjeang, *Electrochem. Commun.* **2016**, *72*, 15.

[329] O. Lori, L. Elbaz, *Catalysts* **2015**, *5*, 1445.

[330] F. Forouzandeh, X. Li, D. W. Banham, F. Feng, A. J. Kakanat, S. Ye, V. Birss, *J. Power Sources* **2018**, *378*, 732.

[331] G. S. Avcioglu, B. Ficicilar, A. Bayrakceken, I. Eroglu, *Int. J. Hydrogen Energy* **2015**, *40*, 7720.

[332] H. Ungan, A. Bayrakçeken Yurtcan, *Int. J. Energy Res.* **2019**, *43*, 5946.

[333] B. J. Hsieh, M. C. Tsai, C. J. Pan, W. N. Su, J. Rick, H. L. Chou, J. F. Lee, B. J. Hwang, *Electrochim. Acta* **2017**, *224*, 452.

[334] Z. Fang, M. S. Lee, J. Y. Kim, J. H. Kim, T. F. Fuller, *J. Electrochem. Soc.* **2020**, *167*, 064506.

[335] L. Xin, F. Yang, S. Rasouli, Y. Qiu, Z. F. Li, A. Uzunoglu, C. J. Sun, Y. Liu, P. Ferreira, W. Li, Y. Ren, L. A. Stanciu, J. Xie, *ACS Catal.* **2016**, *6*, 2642.

[336] Y. Zhou, K. Neyerlin, T. S. Olson, S. Pylypenko, J. Bult, H. N. Dinh, T. Gennett, Z. Shao, R. O'Hayre, *Energy Environ. Sci.* **2010**, *3*, 1437.

[337] Z. F. Li, L. Xin, F. Yang, Y. Liu, Y. Liu, H. Zhang, L. Stanciu, J. Xie, *Nano Energy* **2015**, *16*, 281.

[338] W. S. Jung, B. N. Popov, *Carbon* **2017**, *122*, 746.

[339] A. Pokhrel, M. El Hannach, F. P. Orfino, M. Dutta, E. Kjeang, *J. Power Sources* **2016**, *329*, 330.

[340] R. L. Borup, D. D. Papadias, R. Mukundan, D. Spernjak, D. A. Langlois, R. Ahluwalia, K. L. More, S. Grot, *ECS Trans.* **2015**, *69*, 1029.

[341] W. Zhang, P. N. Pintauro, *ChemSusChem* **2011**, *4*, 1753.

[342] D. Kartouzian, A. Mohseninia, H. Markötter, P. Langner, J. Scholta, I. Manke, *ECS Trans.* **2019**, *92*, 135.

[343] T. Soboleva, K. Malek, Z. Xie, T. Navessin, S. Holdcroft, *ACS Appl. Mater. Interfaces* **2011**, *3*, 1827.

[344] M. R. Benzigar, S. N. Talapaneni, S. Joseph, K. Ramadass, G. Singh, J. Scaranto, U. Ravon, K. Al-Bahily, A. Vinu, *Chem. Soc. Rev.* **2018**, *47*, 2680.

[345] J. Rouquerol, D. Avnir, C. W. Fairbridge, D. H. Everett, J. M. Haynes, N. Pernicone, J. D. F. Ramsay, K. S. W. Sing, K. K. Unger, *Pure Appl. Chem.* **1994**, *66*, 1739.

[346] J. Zhao, A. Ozden, S. Shahgaldi, I. E. Alaefour, X. Li, F. Hamdullahpur, *Energy* **2018**, *150*, 69.

[347] J. Haber, *Pure Appl. Chem.* **1991**, *63*, 1227.

[348] S. Kjelstrup, M. O. Coppens, J. G. Pharoah, P. Pfeifer, *Energy and Fuels* **2010**, *24*, 5097.

[349] G. Inoue, M. Kawase, *J. Power Sources* **2016**, *327*, 1.

[350] M. B. Sassin, Y. Garsany, R. W. Atkinson, R. M. E. Hjelm, K. E. Swider-Lyons, *Int. J. Hydrogen Energy* **2019**, *44*, 16944.

[351] Z. Yu, R. N. Carter, J. Zhang, *Fuel Cells* **2012**, *12*, 557.

[352] E. Padgett, N. Andrejevic, Z. Liu, A. Kongkanand, W. Gu, K. Moriyama, Y. Jiang, S. Kumaraguru, T. E. Moylan, R. Kukreja, D. A. Muller, *J. Electrochem. Soc.* **2018**, *165*, F173.

[353] G. S. Harzer, A. Orfanidi, H. El-Sayed, P. Madkikar, H. A. Gasteiger, *J. Electrochem. Soc.* **2018**, *165*, F770.

[354] M. Uchida, *J. Electrochem. Soc.* **1996**, *143*, 2245.

[355] H. Yu, J. M. Roller, W. E. Mustain, R. Maric, *J. Power Sources* **2015**, *283*, 84.

[356] Z. Xie, T. Navessin, K. Shi, R. Chow, Q. Wang, D. Song, B. Andreaus, M. Eikerling, Z. Liu, S. Holdcroft, *J. Electrochem. Soc.* **2005**, *152*, A1171.

2101025 (77 of 82)

**ADVANCED
SCIENCE NEWS**

www.advancedsciencenews.com

**ADVANCED
ENERGY
MATERIALS**

www.advenergymat.de

[357] A. Suzuki, T. Hattori, R. Miura, H. Tsuboi, N. Hatakeyama, H. Takaba, M. C. Williams, A. Miyamoto, *Int. J. Electrochem. Sci.* **2010**, *5*, 1948.

[358] T. Suzuki, H. Tanaka, M. Hayase, S. Tsushima, S. Hirai, *Int. J. Hydrogen Energy* **2016**, *41*, 20326.

[359] A. Mohseninia, D. Kartouzian, M. Eppler, P. Langner, H. Markötter, F. Wilhelm, J. Scholta, I. Manke, *Fuel Cells* **2020**, *20*, 469.

[360] S. C. Roy, *J. Electrochem. Soc.* **1997**, *144*, 2323.

[361] W. Zhang, A. I. Minett, M. Gao, J. Zhao, J. M. Razal, G. G. Wallace, T. Romeo, J. Chen, *Adv. Energy Mater.* **2011**, *1*, 671.

[362] L. Xin, F. Yang, J. Xie, Z. Yang, N. N. Kariuki, D. J. Myers, J.-K. Peng, X. Wang, R. K. Ahluwalia, K. Yu, P. J. Ferreira, A. M. Bonastre, D. Fongalland, J. Sharman, *J. Electrochem. Soc.* **2017**, *164*, F674.

[363] A. Orfanidi, P. Madkikar, H. A. El-Sayed, G. S. Harzer, T. Kratky, H. A. Gasteiger, *J. Electrochem. Soc.* **2017**, *164*, F418.

[364] F. Yang, L. Xin, A. Uzunoglu, Y. Qiu, L. Stanciu, J. Ilavsky, W. Li, J. Xie, *ACS Appl. Mater. Interfaces* **2017**, *9*, 6530.

[365] K. Malek, T. Mashio, M. Eikerling, *Electrocatalysis* **2011**, *2*, 141.

[366] L. Castanheira, L. Dubau, M. Mermoux, G. Berthomé, N. Caqué, E. Rossinot, M. Chatenet, F. Maillard, *ACS Catal.* **2014**, *4*, 2258.

[367] Y.-J. Ko, H.-S. Oh, H. Kim, *J. Power Sources* **2010**, *195*, 2623.

[368] H.-S. Oh, K. Kim, Y.-J. Ko, H. Kim, *Int. J. Hydrogen Energy* **2010**, *35*, 701.

[369] J. H. Jung, H. J. Park, J. Kim, S. H. Hur, *J. Power Sources* **2014**, *248*, 1156.

[370] A. Ghosh, S. Basu, A. Verma, *Fuel Cells* **2013**, *13*, 355.

[371] L. I. Şanli, V. Bayram, B. Yarar, S. Ghobadi, S. A. Gürsel, *Int. J. Hydrogen Energy* **2016**, *41*, 3414.

[372] A. Heydari, H. Gharibi, *J. Power Sources* **2016**, *325*, 808.

[373] K. K. Karuppanan, A. V. Raghu, M. K. Panthalingal, V. Thiruvenkatam, P. Karthikeyan, B. Pullithadathil, *Sustainable Energy Fuels* **2019**, *3*, 996.

[374] E. F. Holby, P. Zelenay, *Nano Energy* **2016**, *29*, 54.

[375] H. Lee, Y. E. Sung, I. Choi, T. Lim, O. J. Kwon, *J. Power Sources* **2017**, *362*, 228.

[376] R. Chetty, S. Kundu, W. Xia, M. Bron, W. Schuhmann, V. Chirila, W. Brandl, T. Reinecke, M. Muhler, *Electrochim. Acta* **2009**, *54*, 4208.

[377] H. Schmies, E. Hornberger, B. Anke, T. Jurzinsky, H. N. Nong, F. Dionigi, S. Kühl, J. Drnec, M. Lerch, C. Cremers, P. Strasser, *Chem. Mater.* **2018**, *30*, 7287.

[378] X. Li, F. Forouzandeh, A. J. Kakanat, F. Feng, D. W. H. Banham, S. Ye, D. Y. Kwok, V. Birss, *ACS Appl. Mater. Interfaces* **2018**, *10*, 2130.

[379] T. Suzuki, S. Tsushima, S. Hirai, *J. Power Sources* **2013**, *233*, 269.

[380] T.-H. Huang, H.-L. Shen, T.-C. Jao, F.-B. Weng, A. Su, *Int. J. Hydrogen Energy* **2012**, *37*, 13872.

[381] Á. Kriston, T. Xie, D. Gamliel, P. Ganesan, B. N. Popov, *J. Power Sources* **2013**, *243*, 958.

[382] B. Millington, V. Whipple, B. G. Pollet, *J. Power Sources* **2011**, *196*, 8500.

[383] K. Talukdar, M. A. Ripan, T. Jahnke, P. Gazdzicki, T. Morawietz, K. A. Friedrich, *J. Power Sources* **2020**, *461*, 228169.

[384] O. H. Kim, Y. H. Cho, S. H. Kang, H. Y. Park, M. Kim, J. W. Lim, D. Y. Chung, M. J. Lee, H. Choe, Y. E. Sung, *Nat. Commun.* **2013**, *4*, 2473.

[385] S. Shahgaldi, A. Ozden, X. Li, F. Hamdullahpur, *Energy Convers. Manage.* **2018**, *171*, 1476.

[386] L. Ye, Y. Gao, S. Zhu, J. Zheng, P. Li, J. P. Zheng, *Int. J. Hydrogen Energy* **2017**, *42*, 7241.

[387] B. Zhao, L. Sun, L. Ran, Z. Shao, *Solid State Ionics* **2014**, *262*, 313.

[388] K.-H. Kim, H.-J. Kim, K.-Y. Lee, J. H. Jang, S.-Y. Lee, E. Cho, I.-H. Oh, T.-H. Lim, *Int. J. Hydrogen Energy* **2008**, *33*, 2783.

[389] G.-Y. Chen, C. Wang, Y.-J. Lei, J. Zhang, Z. Mao, Z.-Q. Mao, J.-W. Guo, J. Li, M. Ouyang, *Int. J. Hydrogen Energy* **2017**, *42*, 29960.

[390] T. V. Nguyen, D. Natarajan, R. Jain, *ECS Trans.* **2019**, *1*, 501.

[391] A. Therdthianwong, P. Saenwiset, S. Therdthianwong, *Fuel* **2012**, *91*, 192.

[392] G. S. Avcioglu, B. Ficicilar, I. Eroglu, *Int. J. Hydrogen Energy* **2018**, *43*, 18632.

[393] G. S. Avcioglu, B. Ficicilar, I. Eroglu, *Int. J. Hydrogen Energy* **2016**, *41*, 10010.

[394] L. Du, Y. Shao, J. Sun, G. Yin, J. Liu, Y. Wang, *Nano Energy* **2016**, *29*, 314.

[395] T. Yoshizumi, M. Nagamine, Z. Noda, J. Matsuda, A. Hayashi, K. Sasaki, *ECS Trans.* **2019**, *92*, 479.

[396] K. Kakinuma, M. Uchida, T. Kamino, H. Uchida, M. Watanabe, *Electrochim. Acta* **2011**, *56*, 2881.

[397] K. Kakinuma, Y. Chino, Y. Senoo, M. Uchida, T. Kamino, H. Uchida, S. Deki, M. Watanabe, *Electrochim. Acta* **2013**, *110*, 316.

[398] G. Cognard, G. Ozouf, C. Beauger, G. Berthomé, D. Riassetto, L. Dubau, R. Chattot, M. Chatenet, F. Maillard, *Appl. Catal. B Environ.* **2017**, *201*, 381.

[399] T. Arai, O. Takashi, K. Amemiya, T. Takahashi, *SAE Int. J. Alt. Power.* **2017**, *6*, 145.

[400] C. Takei, R. Kobayashi, Y. Mizushita, Y. Hiramitsu, K. Kakinuma, M. Uchida, *J. Electrochem. Soc.* **2018**, *165*, F1300.

[401] Y. Takabatake, Z. Noda, S. M. Lyth, A. Hayashi, K. Sasaki, *Int. J. Hydrogen Energy* **2014**, *39*, 5074.

[402] K. Kakinuma, K. Suda, R. Kobayashi, T. Tano, C. Arata, I. Amemiya, S. Watanabe, M. Matsumoto, H. Imai, A. Iiyama, M. Uchida, *ACS Appl. Mater. Interfaces* **2019**, *11*, 34957.

[403] P. Dhanasekaran, S. R. Williams, D. Kalpana, S. D. Bhat, *RSC Adv.* **2018**, *8*, 472.

[404] Z. Zhang, J. Liu, J. Gu, L. Su, L. Cheng, *Energy Environ. Sci.* **2014**, *7*, 2535.

[405] D. A. Cullen, M. Lopez-Haro, P. Bayle-Guillemaud, L. Guetaz, M. K. Debe, A. J. Steinbach, *J. Mater. Chem. A* **2015**, *3*, 11660.

[406] H. Ishikawa, S. Henning, J. Herranz, A. Eychmüller, M. Uchida, T. J. Schmidt, *J. Electrochem. Soc.* **2018**, *165*, F7.

[407] M. K. Debe, *Nature* **2012**, *486*, 43.

[408] R. Deng, Z. Xia, R. Sun, S. Wang, G. Sun, *J. Energy Chem.* **2020**, *43*, 33.

[409] B. Kinkead, J. van Drunen, M. T. Y. Paul, K. Dowling, G. Jerkiewicz, B. D. Gates, *Electrocatalysis* **2013**, *4*, 179.

[410] F. C. Cetinbas, R. K. Ahluwalia, N. Kariuki, V. De Andrade, D. Fongalland, L. Smith, J. Sharman, P. Ferreira, S. Rasouli, D. J. Myers, *J. Power Sources* **2017**, *344*, 62.

[411] D. S. Hwang, C. H. Park, S. C. Yi, Y. M. Lee, *Int. J. Hydrogen Energy* **2011**, *36*, 9876.

[412] S. Ghosh, H. Ohashi, H. Tabata, Y. Hashimasa, T. Yamaguchi, *Int. J. Hydrogen Energy* **2015**, *40*, 15663.

[413] T. Terao, G. Inoue, M. Kawase, N. Kubo, M. Yamaguchi, K. Yokoyama, T. Tokunaga, K. Shinohara, Y. Hara, T. Hara, *J. Power Sources* **2017**, *347*, 108.

[414] R. Singh, A. R. Akhgar, P. C. Sui, K. J. Lange, N. Djilali, *J. Electrochem. Soc.* **2014**, *161*, F415.

[415] M. Sabharwal, L. M. Pant, A. Putz, D. Susac, J. Jankovic, M. Secanell, *Fuel Cells* **2016**, *16*, 734.

[416] Q. Meyer, J. Hack, N. Mansor, F. Iacoviello, J. J. Bailey, P. R. Shearing, D. J. L. Brett, *Fuel Cells* **2019**, *19*, 35.

[417] S. Thiele, S. Vierrath, K. Matthias, R. Zengerle, *ECS Meet. Abstr.* **2015**, MA2015-02, 1344.

[418] L. Chen, Q. Kang, W. Tao, *Electrochim. Acta* **2019**, *306*, 454.

[419] Z. Yang, H. Nie, X. Chen, X. Chen, S. Huang, *J. Power Sources* **2013**, *236*, 238.

[420] M. Hu, Z. Yao, X. Wang, *Ind. Eng. Chem. Res.* **2017**, *56*, 3477.

[421] S. Nardecchia, D. Carriazo, M. L. Ferrer, M. C. Gutiérrez, F. Del Monte, *Chem. Soc. Rev.* **2013**, *42*, 794.

[422] N. Seselj, C. Engelbrekt, J. Zhang, *Sci. Bull.* **2015**, *60*, 864.

[423] X. Zhou, J. Qiao, L. Yang, J. Zhang, *Adv. Energy Mater.* **2014**, *4*, 1301523.

[424] K. Lee, J. Zhang, H. Wang, D. P. Wilkinson, *J. Appl. Electrochem.* **2006**, *36*, 507.

[425] A. J. Clancy, M. K. Bayazit, S. A. Hodge, N. T. Skipper, C. A. Howard, M. S. P. Shaffer, *Chem. Rev.* **2018**, *118*, 7363.

[426] C. Gupta, P. H. Maheshwari, D. Sachdev, A. K. Sahu, S. R. Dhakate, *RSC Adv.* **2016**, *6*, 32258.

[427] W. Zhang, J. Chen, A. I. Minett, G. F. Swiegers, C. O. Too, G. G. Wallace, *Chem. Commun.* **2010**, *46*, 4824.

[428] T. Matsumoto, T. Komatsu, K. Arai, T. Yamazaki, M. Kijima, H. Shimizu, Y. Takasawa, J. Nakamura, *Chem. Commun.* **2004**, *4*, 840.

[429] W. Wang, F. Lv, B. Lei, S. Wan, M. Luo, S. Guo, *Adv. Mater.* **2016**, *28*, 10117.

[430] B. P. Vinayan, R. I. Jafri, R. Nagar, N. Rajalakshmi, K. Sethupathi, S. Ramaprabhu, *Int. J. Hydrogen Energy* **2012**, *37*, 412.

[431] M. Karuppannan, Y. Kim, S. Gok, E. Lee, J. Y. Hwang, J. H. Jang, Y. H. Cho, T. Lim, Y. E. Sung, O. J. Kwon, *Energy Environ. Sci.* **2019**, *12*, 2820.

[432] S. M. Andersen, M. Borghei, P. Lund, Y. R. Elina, A. Pasanen, E. Kauppinen, V. Ruiz, P. Kauranen, E. M. Skou, *Solid State Ionics* **2013**, *231*, 94.

[433] Y. Wang, J. Jin, S. Yang, G. Li, J. Qiao, *Electrochim. Acta* **2015**, *177*, 181.

[434] M. L. Stevenson, G. Pattrick, *J. South. Afr. Inst. Min. Metall.* **2017**, *117*, 989.

[435] K. S. Novoselov, A. K. Geim, S. V. Morozov, D. Jiang, Y. Zhang, S. V. Dubonos, I. V. Grigorieva, A. A. Firsov, *Science* **2004**, *306*, 666.

[436] N. M. Julkapli, S. Bagheri, *Int. J. Hydrogen Energy* **2015**, *40*, 948.

[437] M. Liu, R. Zhang, W. Chen, *Chem. Rev.* **2014**, *114*, 5117.

[438] D. R. Kauffman, A. Star, *Analyst* **2010**, *135*, 2790.

[439] P. Mardle, O. Fernihough, S. Du, *Coatings* **2018**, *8*, 48.

[440] Y. Devrim, A. Albostan, *J. Electron. Mater.* **2016**, *45*, 3900.

[441] U. R. Farooqui, A. L. Ahmad, N. A. Hamid, *Renewable Sustainable Energy Rev.* **2018**, *82*, 714.

[442] A. Marinkas, R. Hempelmann, A. Heinzel, V. Peinecke, I. Radev, H. Natter, *J. Power Sources* **2015**, *295*, 79.

[443] B. Yarar Kaplan, N. Haghmoradi, E. Biçer, C. Merino, S. Alkan Gürsel, *Int. J. Hydrogen Energy* **2018**, *43*, 23221.

[444] S. Park, Y. Shao, H. Wan, P. C. Rieke, V. V. Viswanathan, S. A. Towne, L. V. Saraf, J. Liu, Y. Lin, Y. Wang, *Electrochem. Commun.* **2011**, *13*, 258.

[445] L. Işıkel Şanlı, V. Bayram, S. Ghobadi, N. Düzen, S. A. Gürsel, *Int. J. Hydrogen Energy* **2017**, *42*, 1085.

[446] R. I. Jafri, T. Arockiados, N. Rajalakshmi, S. Ramaprabhu, *J. Electrochem. Soc.* **2010**, *157*, B874.

[447] S. S. Jyothirmayee Aravind, R. Imran Jafri, N. Rajalakshmi, S. Ramaprabhu, *J. Mater. Chem.* **2011**, *21*, 18199.

[448] S. S. J. Aravind, S. Ramaprabhu, *ACS Appl. Mater. Interfaces* **2012**, *4*, 3805.

[449] C.-C. Sung, C.-Y. Liu, C. C. J. Cheng, *Int. J. Hydrogen Energy* **2014**, *39*, 11706.

[450] S. H. Cho, H. N. Yang, D. C. Lee, S. H. Park, W. J. Kim, *J. Power Sources* **2013**, *225*, 200.

[451] S. Han, D. Wu, S. Li, F. Zhang, X. Feng, *Adv. Mater.* **2014**, *26*, 849.

[452] Z. Yan, W. Yao, L. Hu, D. Liu, C. Wang, C. S. Lee, *Nanoscale* **2015**, *7*, 5563.

[453] X. Zhou, S. Tang, Y. Yin, S. Sun, J. Qiao, *Appl. Energy* **2016**, *175*, 459.

[454] J. Liu, D. Takeshi, K. Sasaki, S. M. Lyth, *J. Electrochem. Soc.* **2014**, *161*, F838.

[455] M. Sahoo, B. P. Vinayan, S. Ramaprabhu, *RSC Adv.* **2014**, *4*, 26140.

[456] D. Banham, F. Feng, T. Fürstenhaupt, K. Pei, S. Ye, V. Birss, *Catalysts* **2015**, *5*, 1046.

[457] M. Sahoo, K. Scott, S. Ramaprabhu, *Int. J. Hydrogen Energy* **2015**, *40*, 9435.

[458] B. Seger, P. V. Kamat, *J. Phys. Chem. C* **2009**, *113*, 7990.

[459] C. V. Rao, A. L. M. Reddy, Y. Ishikawa, P. M. Ajayan, *Carbon* **2011**, *49*, 931.

[460] A. Therdthianwong, P. Ekdharmasuit, S. Therdthianwong, *Energy Fuels* **2010**, *24*, 1191.

[461] S. Takahashi, T. Mashio, N. Horibe, K. Akizuki, A. Ohma, *ChemElectroChem* **2015**, *2*, 1560.

[462] T. Kusano, T. Hiroi, K. Amemiya, M. Ando, T. Takahashi, M. Shibayama, *Polym. J.* **2015**, *47*, 546.

[463] S. Kundu, M. W. Fowler, L. C. Simon, S. Grot, *J. Power Sources* **2006**, *157*, 650.

[464] S. M. Kim, C. Y. Ahn, Y. H. Cho, S. Kim, W. Hwang, S. Jang, S. Shin, G. Lee, Y. E. Sung, M. Choi, *Sci. Rep.* **2016**, *6*, 26503.

[465] M. S. Wilson, *J. Electrochem. Soc.* **1992**, *139*, L28.

[466] V. Mehta, J. S. Cooper, *J. Power Sources* **2003**, *114*, 32.

[467] A. Strong, C. Thornberry, S. Beattie, R. Chen, S. R. Coles, *J. Fuel Cell Sci. Technol.*, https://doi.org/10.1115/1.4031961.

[468] E. Gülzow, M. Schulze, N. Wagner, T. Kaz, R. Reissner, G. Steinhilber, A. Schneider, *J. Power Sources* **2000**, *86*, 352.

[469] J. Chen, X. Jiang, W. Tang, L. Ma, Y. Li, Y. A. Huang, Z. Yin, *Proc. Inst. Mech. Eng. Part B* **2020**, *234*, 66.

[470] S. A. Mauger, M. Wang, F. C. Cetinbas, M. J. Dzara, J. Park, D. J. Myers, R. K. Ahluwalia, S. Pylypenko, L. Hu, S. Litster, K. C. Neyerlin, M. Ulsh, *J. Power Sources* **2021**, *506*, 230039.

[471] Y. Zhang, A. Smirnova, A. Verma, R. Pitchumani, *J. Power Sources* **2015**, *291*, 46.

[472] G. Bender, T. A. Zawodzinski, A. P. Saab, *J. Power Sources* **2003**, *124*, 114.

[473] C. H. Hsu, C. C. Wan, *J. Power Sources* **2003**, *115*, 268.

[474] F. Mack, M. Klages, J. Scholta, L. Jörissen, T. Morawietz, R. Hiesgen, D. Kramer, R. Zeis, *J. Power Sources* **2014**, *255*, 431.

[475] R. P. Brooker, M. P. Rodgers, L. J. Bonville, H. R. Kunz, D. K. Slattery, J. M. Fenton, *ECS Trans.* **2019**, *28*, 51.

[476] B. Millington, S. Du, B. G. Pollet, *J. Power Sources* **2011**, *196*, 9013.

[477] S. A. Mauger, K. C. Neyerlin, S. M. Alia, C. Ngo, S. K. Babu, K. E. Hurst, S. Pylypenko, S. Litster, B. S. Pivovar, *J. Electrochem. Soc.* **2018**, *165*, F238.

[478] M. Wang, J. H. Park, S. Kabir, K. C. Neyerlin, N. N. Kariuki, H. Lv, V. R. Stamenkovic, D. J. Myers, M. Ulsh, S. A. Mauger, *ACS Appl. Energy Mater.* **2019**, *2*, 6417.

[479] B. G. Pollet, *Int. J. Hydrogen Energy* **2010**, *35*, 11986.

[480] M. Klingele, B. Britton, M. Breitwieser, S. Vierrath, R. Zengerle, S. Holdcroft, S. Thiele, *Electrochem. Commun.* **2016**, *70*, 65.

[481] B. S. Koh, J. H. Yoo, E. K. Jang, V. R. Jothi, C. Y. Jung, S. C. Yi, *Electrochem. Commun.* **2018**, *93*, 76.

[482] S. Poozesh, K. Akafuah, K. Saito, *Proc. Inst. Mech. Eng. Part D* **2018**, *232*, 282.

[483] L. I. Şanlı, B. Yarar, V. Bayram, S. A. Gürsel, *J. Mater. Sci.* **2017**, *52*, 2091.

[484] S. Shukla, K. Domican, K. Karan, S. Bhattacharjee, M. Secanell, *Electrochim. Acta* **2014**, *156*, 289.

[485] A. D. Taylor, E. Y. Kim, V. P. Humes, J. Kizuka, L. T. Thompson, *J. Power Sources* **2007**, *171*, 101.

[486] M. Klingele, M. Breitwieser, R. Zengerle, S. Thiele, *J. Mater. Chem. A* **2015**, *3*, 11239.

[487] S. Henning, H. Ishikawa, L. Kühn, J. Herranz, E. Müller, A. Eychmüller, T. J. Schmidt, *Angew. Chem., Int. Ed.* **2017**, *56*, 10707.

[488] S. H. Joo, S. J. Choi, I. Oh, J. Kwak, Z. Liu, O. Terasaki, R. Ryoo, *Nature* **2001**, *412*, 169.

[489] U. B. Suryavanshi, T. Iijima, A. Hayashi, Y. Hayashi, M. Tanemura, *Chem. Commun.* **2011**, *47*, 10758.

[490] C. Liang, K. Hong, G. A. Guiochon, J. W. Mays, S. Dai, *Angew. Chem., Int. Ed.* **2004**, *43*, 5785.

[491] A. Arunchander, K. G. Nishanth, K. K. Tintula, S. G. Peera, A. K. Sahu, *Bull. Mater. Sci.* **2015**, *38*, 451.

[492] A. Zlotorowicz, K. Jayasayee, P. I. Dahl, M. S. Thomassen, S. Kjelstrup, *J. Power Sources* **2015**, *287*, 472.

**ADVANCED
SCIENCE NEWS**

www.advancedsciencenews.com

**ADVANCED
ENERGY
MATERIALS**

www.advenergymat.de

[493] C. Ahn, J. Park, D. Cho, G. Hyun, Y. Ham, K. Kim, S.-H. Nam, G. Bae, K. Lee, Y.-S. Shim, J. N. S. Ang, S. Jeon, *Funct. Compos. Struct.* **2019**, *1*, 032002.

[494] M. T. Y. Paul, D. Kim, M. S. Saha, J. Stumper, B. D. Gates, *ACS Appl. Energy Mater.* **2020**, *3*, 478.

[495] H. Liang, H. Su, B. G. Pollet, V. Linkov, S. Pasupathi, *J. Power Sources* **2014**, *266*, 107.

[496] S. H. Akella, D. Ebenezer, S. S. Sai, A. Ahire, N. K. Mal, *Sci. Rep.* **2018**, *8*, 12082.

[497] S. Thanasilp, M. Hunsom, *Fuel* **2010**, *89*, 3847.

[498] S. A. Mauger, J. R. Pfeilsticker, M. Wang, S. Medina, A. C. Yang-Neyerlin, K. C. Neyerlin, C. Stetson, S. Pylypenko, M. Ulsh, *J. Power Sources* **2020**, *450*, 227581.

[499] H. Tang, S. Wang, S. P. Jiang, M. Pan, *J. Power Sources* **2007**, *170*, 140.

[500] W. Wang, S. Chen, J. Li, W. Wang, *Int. J. Hydrogen Energy* **2015**, *40*, 4649.

[501] B. Wu, B. Li, W. Liu, J. Liu, M. Zhao, Y. Yao, J. Gu, Z. Zou, *Int. J. Hydrogen Energy* **2013**, *38*, 10978.

[502] S. Vierrath, M. Breitwieser, M. Klingele, B. Britton, S. Holdcroft, R. Zengerle, S. Thiele, *J. Power Sources* **2016**, *326*, 170.

[503] E. A. Ticianelli, *J. Electrochem. Soc.* **1988**, *135*, 2209.

[504] S. M. Andersen, R. Dhiman, M. J. Larsen, E. Skou, *Appl. Catal. B Environ.* **2015**, *172-173*, 82.

[505] O. Okur, Ç. Iyigün Karadağ, F. G. Boyaci San, E. Okumuş, G. Behmenyar, *Energy* **2013**, *57*, 574.

[506] Q. Meyer, N. Mansor, F. Iacoviello, P. L. Cullen, R. Jervis, D. Finegan, C. Tan, J. Bailey, P. R. Shearing, D. J. L. Brett, *Electrochim. Acta* **2017**, *242*, 125.

[507] J. Hack, T. M. M. Heenan, F. Iacoviello, N. Mansor, Q. Meyer, P. Shearing, N. Brandon, D. J. L. Brett, *J. Electrochem. Soc.* **2018**, *165*, F3045.

[508] M. Najafi Roudbari, R. Ojani, J. B. Raoof, *Energy* **2017**, *140*, 794.

[509] T. J. Mason, J. Millichamp, P. R. Shearing, D. J. L. Brett, *Int. J. Hydrogen Energy* **2013**, *38*, 7414.

[510] N. Kulkarni, M. D. R. Kok, R. Jervis, F. Iacoviello, Q. Meyer, P. R. Shearing, D. J. L. Brett, *J. Power Sources* **2019**, *426*, 97.

[511] M. Zhiani, S. Majidi, V. B. Silva, H. Gharibi, *Energy* **2016**, *97*, 560.

[512] J. Tan, Y. J. Chao, H. Wang, J. Gong, J. W. Van Zee, *Polym. Degrad. Stab.* **2009**, *94*, 2072.

[513] J. Tan, Y. J. Chao, M. Yang, W. K. Lee, J. W. Van Zee, *Int. J. Hydrogen Energy* **2011**, *36*, 1846.

[514] S. Pehlivan-Davis, J. Clarke, S. Armour, *J. Appl. Polym. Sci.* **2013**, *129*, 1446.

[515] C. Y. Wen, Y. S. Lin, C. H. Lu, *J. Power Sources* **2009**, *192*, 475.

[516] P. Zhou, P. Lin, C. W. Wu, Z. Li, *Int. J. Hydrogen Energy* **2011**, *36*, 6039.

[517] E. Alizadeh, M. Ghadimi, M. M. Barzegari, M. Momenifar, S. H. M. Saadat, *Energy* **2017**, *131*, 92.

[518] T. Dey, J. Deshpande, D. Singdeo, P. C. Ghosh, *J. Energy* **2019**, *2019*, 3821082.

[519] X. Wang, Y. Song, B. Zhang, *J. Power Sources* **2008**, *179*, 305.

[520] R. Montanini, G. Squadrito, G. Giacoppo, in *Proc. 19th IMEKO World Congress 2009*, Curran Associates, Redhook, NY **2009**, pp. 920–925.

[521] N. Kulkarni, J. I. S. Cho, L. Rasha, R. E. Owen, Y. Wu, R. Ziesche, J. Hack, T. Neville, M. Whiteley, N. Kardjilov, H. Markötter, I. Manke, P. R. Shearing, D. J. L. Brett, *J. Power Sources* **2019**, *439*, 227074.

[522] T. J. Mason, J. Millichamp, T. P. Neville, A. El-Kharouf, B. G. Pollet, D. J. L. Brett, *J. Power Sources* **2012**, *219*, 52.

[523] W. R. Chang, J. J. Hwang, F. B. Weng, S. H. Chan, *J. Power Sources* **2007**, *166*, 149.

[524] S. Litster, D. Sinton, N. Djilali, *J. Power Sources* **2006**, *154*, 95.

[525] A. Turhan, S. Kim, M. Hatzell, M. M. Mench, *Electrochim. Acta* **2010**, *55*, 2734.

[526] N. K. Shrivastava, A. Chatterjee, T. A. L. Harris, *Int. J. Energy Res.* **2020**, *44*, 370.

[527] C. Tötzke, G. Gaiselmann, M. Osenberg, T. Arlt, H. Markötter, A. Hilger, A. Kupsch, B. R. Müller, V. Schmidt, W. Lehnert, I. Manke, *J. Power Sources* **2016**, *324*, 625.

[528] J. Millichamp, T. J. Mason, T. P. Neville, N. Rajalakshmi, R. Jervis, P. R. Shearing, D. J. L. Brett, *J. Power Sources* **2015**, *284*, 305.

[529] E. M. Khetabi, K. Bouziane, N. Zamel, X. François, Y. Meyer, D. Candusso, *J. Power Sources* **2019**, *424*, 8.

[530] V. Senthil Velan, G. Velayutham, N. Rajalakshmi, K. S. Dhathathreyan, *Int. J. Hydrogen Energy* **2014**, *39*, 1752.

[531] J. Ge, A. Higier, H. Liu, *J. Power Sources* **2006**, *159*, 922.

[532] C. Yang, M. Hu, C. Wang, G. Cao, *J. Power Sources* **2012**, *197*, 180.

Theo A. M. Suter is a postdoctoral researcher in the electrochemical innovation laboratory at UCL focusing on fuel cell fabrication, testing, and characterization. He completed his Ph.D. in nanomaterial chemistry at UCL in 2018 and now specializes in nanoengineering of the fuel cell catalyst layer, particularly via the use of nanomaterials and heterogeneous catalyst layer fabrication. His interests focus on how the fuel cell catalyst layer morphology and microstructure impacts the performance of fuels cells, and how different fabrication techniques can be used as a tool to improve device durability.

**ADVANCED
SCIENCE NEWS**

www.advancedsciencenews.com

**ADVANCED
ENERGY
MATERIALS**

www.advenergymat.de

Keenan Smith is a Ph.D. student in the Electrochemical Innovation Lab at University College London, having obtained his Chemistry MSci at the University of Nottingham in 2018. His research utilizes advanced microscopy and scattering techniques to probe nanoscale structure-property relationships within novel polymer electrolyte materials and membrane-electrode assembly architectures, enabling development of high-performance fuel cells.

Jennifer Hack is an EPSRC Doctoral Prize Fellow working in the field of electrochemical energy at the Electrochemical Innovation Lab (EIL), University College London. During her Ph.D., Jennifer worked on using X-ray and neutron imaging techniques to understand the operation and degradation of polymer electrolyte fuel cells, and she is currently working on applying these techniques to zinc–air batteries. Her interests lie in using 3- and 4D characterization methods to understand the relation between the complex morphology and microstructure of these systems and their electrochemical performance.

Lara Rasha obtained her Ph.D. at the Electrochemical Innovation Laboratory at UCL. Lara's research focuses on developing advanced diagnostic techniques for electrochemical devices and exploring the intrinsic relationship between electrical performance, thermal and water management in polymer electrolyte fuel cells. Lara has also done work on powertrains and hybridizing fuel cells with batteries and supercapacitors for a range of applications (Photo not shown at the request of the author).

Zahra Rana is a Ph.D. student at the Electrochemical Innovation Lab (EIL) at UCL working on low-cost non-PGM electrocatalysts for the oxygen reduction reaction in PEM fuel cells. Her work involves the synthesis, detailed characterization, and subsequent ex situ RRDE electrochemical testing of new materials, with the aim of producing a catalyst with increased performance, selectivity, and durability. Zahra's work explores materials ranging from MOFs to biomass precursors to achieve this goal.

Gyen Ming A. Angel is a Ph.D. student working between the Electrochemical Innovation Laboratory and Condensed Matter and Material Physics groups at UCL. His research has centered around the intercalation and exfoliation of layered materials for electrochemical applications such as fuel cell and electrolyzer catalysis, including developing a patented method for the scalable synthesis of graphene-supported nanoparticles.

Paul R. Shearing is a Royal Academy of Engineering Chair in Emerging Technologies at University College London. His research interests cover a broad range of electrochemical engineering with a particular interest in the relationship between performance and microstructure for energy materials: an area in which he has published more than 250 papers (>6000 citations, h = 43). He is a pioneer of "4D Tomography" to study microstructure in electrochemical materials. He is a founding investigator of the Faraday Institution, and leads the STFC Global Challenge Network in Batteries and Electrochemical Energy Devices.

Thomas S. Miller is a Lecturer in Chemical Engineering at UCL and is a member of the Electrochemical Innovation Lab (EIL), specializing in materials science and electrochemistry. In his work, he has developed new and important nanomaterial processing methods and applied novel electrochemical techniques to projects in areas, including energy storage/conversion, nanoparticle catalysis, and sensing. In the field of fuel cells, Tom is exploring the creation of new catalysts, the utilization of advanced methods for electrode engineering, and the development of in-line diagnostic tools, moving fundamental discoveries toward industrial relevance.

Dan. J. L. Brett is a professor in Electrochemical Engineering in the Department of Chemical Engineering at UCL. He specializes in electrochemical engineering, including the modeling, testing, design, device fabrication, materials development, and techno-economic analysis. He has published over 350 peer reviewed papers in leading international journals (h = 50), and holds five patent families, based on which he is commercializing two spin-out companies. He is the UCL Director of the National Centre for Grid Scale Energy Storage and the UCL Director of the Centre for Doctoral Training in Fuel Cells and their Fuels.